0 0 0 0 4 0 0 1 4 9 7

LBL-2016
c.1

RECEIVED
LAWRENCE
RADIATION LABORATORY

OCT 22 1973

LIBRARY AND
DOCUMENTS SECTION

Radiobiological Experiments using Accelerated Heavy Ions at the Bevatron

For Reference

Not to be taken from this room

Donner Laboratory — Lawrence Berkeley Laboratory
University of California
Berkeley, California

DISCLAIMER

This document was prepared as an account of work sponsored by the United States Government. While this document is believed to contain correct information, neither the United States Government nor any agency thereof, nor the Regents of the University of California, nor any of their employees, makes any warranty, express or implied, or assumes any legal responsibility for the accuracy, completeness, or usefulness of any information, apparatus, product, or process disclosed, or represents that its use would not infringe privately owned rights. Reference herein to any specific commercial product, process, or service by its trade name, trademark, manufacturer, or otherwise, does not necessarily constitute or imply its endorsement, recommendation, or favoring by the United States Government or any agency thereof, or the Regents of the University of California. The views and opinions of authors expressed herein do not necessarily state or reflect those of the United States Government or any agency thereof or the Regents of the University of California.

0 0 0 0 4 0 0 1 4 9 8

LBL-2016

RADIOBIOLOGICAL EXPERIMENTS USING ACCELERATED HEAVY IONS AT THE BEVATRON

September 1973

Donner Laboratory-Lawrence Berkeley Laboratory
University of California
Berkeley, California 94720

Work done under the auspices of the U.S. Atomic Energy Commission
and the National Aeronautics and Space Administration

0 0 0 0 4 0 0 1 4 9 9

RADIOBIOLOGICAL EXPERIMENTS USING ACCELERATED HEAVY IONS AT THE BEVATRON

Contents

Introduction v

A NEW METHOD FOR HEAVY-PARTICLE RADIOGRAPHY
Eugene V. Benton, Richard P. Henke,
Cornelius A. Tobias 1

RELATIONSHIPS BETWEEN TRACK STRUCTURE AND BIOLOGICAL EFFECTS OF HEAVY CHARGED PARTICLES
Aloke Chatterjee, Cornelius A. Tobias 30

CELL SURVIVAL AS A FUNCTION OF DEPTH FOR A 220-MeV/NUCLEON OXYGEN-ION BEAM
Robert Roisman, Bambino Martins,
Dionysios Kalofonos, Cornelius A. Tobias 49

EFFECTS OF HEAVY-ION, HIGH-ENERGY PARTICLES UPON THE RETINAL VASCULATURE OF THE RHESUS MONKEY
Fred N. Beckman, David M. Hunter,
Charles H. Bonney 63

FRAGMENTATION OF HIGH-ENERGY, OXYGEN-ION BEAMS IN WATER
Howard D. Maccabee, Mark Ritter 75

EXPERIMENTAL SETUP AND PHYSICAL MEASUREMENTS OF THE HEAVY-ION BEAMS USED FOR BIOLOGICAL IRRADIATIONS
John T. Lyman, Jerry Howard, Graeme P. Welch,
Walter Schimmerling, Cornelius A. Tobias 100

INITIAL STUDIES ON OER, RBE, AND DEVELOPMENT OF TRIBOLIUM EGGS USING AN OXYGEN BEAM
Chui-hsu (Tracy) Yang, Laurie Craise,
Graeme P. Welch, Cornelius A. Tobias 102

STUDIES OF THE DEVELOPMENT OF ZEA MAYS IRRADIATED WITH ACCELERATED OXYGEN IONS
Chui-hsu (Tracy) Yang, Eugene V. Benton, Laurie Craise, Cornelius A. Tobias 130

COMPARATIVE EFFECTS IN IRRADIATION OF SKIN OF THE MOUSE LEG WITH X RAYS, HELIUM IONS, OR OXYGEN IONS
John T. Leith, Wolfgang A. Schilling, John T. Lyman, Jerry Howard, Walter Schimmerling, Graeme P. Welch, Donald G. Baker 153

ULTRASTRUCTURAL INVESTIGATION OF THE "LIGHT FLASH" PHENOMENON SEEN BY OUR ASTRONAUTS THROUGH EXPOSURE OF POCKET MOUSE AND RABBIT RETINA TO X-RAY, NITROGEN AND OXYGEN IRRADIATION
Delbert E. Philpott, R. Corbett, Sam Black, Charles Turnbill 172

0 0 0 0 4 0 0 1 5 0 0

RADIOBIOLOGICAL EXPERIMENTS USING ACCELERATED HEAVY IONS AT THE BEVATRON

Contents

Introduction v

A NEW METHOD FOR HEAVY-PARTICLE RADIOGRAPHY
Eugene V. Benton, Richard P. Henke,
Cornelius A. Tobias 1

RELATIONSHIPS BETWEEN TRACK STRUCTURE AND BIOLOGICAL EFFECTS OF HEAVY CHARGED PARTICLES
Aloke Chatterjee, Cornelius A. Tobias 30

CELL SURVIVAL AS A FUNCTION OF DEPTH FOR A 220-MeV/NUCLEON OXYGEN-ION BEAM
Robert Roisman, Bambino Martins,
Dionysios Kalofonos, Cornelius A. Tobias 49

EFFECTS OF HEAVY-ION, HIGH-ENERGY PARTICLES UPON THE RETINAL VASCULATURE OF THE RHESUS MONKEY
Fred N. Beckman, David M. Hunter,
Charles H. Bonney 63

FRAGMENTATION OF HIGH-ENERGY, OXYGEN-ION BEAMS IN WATER
Howard D. Maccabee, Mark Ritter 75

EXPERIMENTAL SETUP AND PHYSICAL MEASUREMENTS OF THE HEAVY-ION BEAMS USED FOR BIOLOGICAL IRRADIATIONS
John T. Lyman, Jerry Howard, Graeme P. Welch,
Walter Schimmerling, Cornelius A. Tobias 100

INITIAL STUDIES ON OER, RBE, AND DEVELOPMENT OF TRIBOLIUM EGGS USING AN OXYGEN BEAM
Chui-hsu (Tracy) Yang, Laurie Craise,
Graeme P. Welch, Cornelius A. Tobias 102

STUDIES OF THE DEVELOPMENT OF ZEA MAYS IRRADIATED WITH ACCELERATED OXYGEN IONS
Chui-hsu (Tracy) Yang, Eugene V. Benton, Laurie Craise, Cornelius A. Tobias 130

COMPARATIVE EFFECTS IN IRRADIATION OF SKIN OF THE MOUSE LEG WITH X RAYS, HELIUM IONS, OR OXYGEN IONS
John T. Leith, Wolfgang A. Schilling, John T. Lyman, Jerry Howard, Walter Schimmerling, Graeme P. Welch, Donald G. Baker 153

ULTRASTRUCTURAL INVESTIGATION OF THE "LIGHT FLASH" PHENOMENON SEEN BY OUR ASTRONAUTS THROUGH EXPOSURE OF POCKET MOUSE AND RABBIT RETINA TO X-RAY, NITROGEN AND OXYGEN IRRADIATION
Delbert E. Philpott, R. Corbett, Sam Black, Charles Turnbill 172

RADIOBIOLOGICAL EXPERIMENTS USING ACCELERATED HEAVY IONS AT THE BEVATRON

INTRODUCTION

This report describes work in progress using accelerated heavy-ion beams at the Berkeley Bevatron; in particular it contains preliminary results in a series of exposures performed in September 1972 and February 1973. In addition to reports from the Donner Laboratory, work from the USAF School of Aerospace Medicine, San Antonio, Texas; the University of San Francisco; NASA-Ames Research Laboratory, Moffett Field; and Mount Zion Hospital, San Francisco, is also presented.

The authors are grateful to the staff of the Bevatron: Herman A. Grunder, Walter D. Hartsough, Richard E. Morgado and Don M. Evans, under the leadership of Edward J. Lofgren, for their assistance.

Radiological physics measurements for most of the experiments were performed by John T. Lyman, Jerry Howard, Graeme P. Welch, Walter Schimmerling, Howard D. Maccabee and Stanley B. Curtis.

We are pleased to acknowledge support of the US Atomic Energy Commission, NASA and the National Cancer Institute.

September 1973 The Authors

0 0 0 0 4 0 0 1 5 0 1

A NEW METHOD FOR HEAVY-PARTICLE RADIOGRAPHY

Eugene V. Benton and Richard P. Henke

Physics Department, University of San Francisco
San Francisco, CA 94117

and

Cornelius A. Tobias

Donner Laboratory—Lawrence Berkeley Laboratory
University of California, Berkeley, CA 94720

Abstract.

Energetic heavy ions may be used to produce high resolution, high contrast radiographs. A uniform, monoenergetic beam of particles, such as 250 MeV/nucleon ^{16}O ions, passes through the object under investigation and slight differences in the internal structure produce differences in particle stopping power. The stopping point distribution as recorded in plastic nuclear track detectors reflects the internal structure of the object. It is found that density differences as small as 0.03 g/cm^2 or about 0.3% of the total thickness, in regions of relatively small size (< 1 cm in diameter) can be detected with ease, making possible radiography of objects not detectable using conventional, "x-ray" techniques. The method has potential applications in diagnostic localization of tumors in cases where the density difference between tumor tissue and normal tissue is too small to be detected by conventional methods. The use of plastic detectors also lends itself to quantitative three-dimensional reconstruction of tissue architecture.

Introduction.

Previously, it was suggested that a number of problems existing in diagnostic roentgenology might be solved through the use of energetic, heavy-particle beams such as those presently available at the LBL Bevatron:[1]

1) Adipose-tissue or soft-tissue tumors are often not detectable with x-rays or other conventional techniques. The tumor is detected by x-rays generally only when it has grown to a rather large size.

2) It is difficult to detect and localize air pockets which sometimes occur in parts of the body such as the brain.

3) It is well known that diagnostic x-rays are relatively insensitive in the detection of small metastatic lesions invading the bone.

It has also been pointed out that heavy-particle beams can be used as a more sensitive "thickness gauge" than either x-rays or electrons.[1] Also, it was realized that the measurement of the particle residual range after they cross an object can be used in determining the density distribution inside of the object, which is often not possible with x-ray roentgenography.[2] We have recently carried out experiments which clearly show that high resolution, high contrast radiographs can be produced utilizing heavy-particle beams in conjunction with either photographic film or plastic nuclear track detectors.[3] The emphasis has been on using plastics in that they offer some unique advantages over the photographic film. For this purpose, the main limitations of the photographic emulsions consist of the following: emulsions have a logarithmic response, they record electrons producing an unwanted "halo" effect, and they record all charged secondaries. On the other hand, plastic detectors are insensitive to electrons and being effectively "threshold" type detectors will record only the heavy component of the secondaries. Also, since they record tracks only at the end of the particle range, it is possible to detect very small variations in the stopping power of the object. Since each layer of a stack of exposed plastics may have unique information recorded on it, it then becomes possible to reconstruct the three-dimensional structure of the target object.

The terms "radiography" or "roentgenography" usually refer to producing a record of the internal structure of an object by passing short wavelength electromagnetic radiation through it. This radiation is selectively absorbed by internal regions of different composition and therefore (hopefully) different absorption coefficients for the radiation in question. Thus a "shadow"

is produced by regions which may often have an absorption coefficient only slightly different from the rest of the object. In some cases the region cannot be detected at all even though it is quite well biologically differentiated because of its small size or because of the similarity of its absorption coefficient to that of the rest of the object. This is illustrated by the three cases previously mentioned.

In many cases a much more sensitive detection of slight differences in specimen composition is afforded by using the particle stopping power variation of the specimen produced by these differences rather than the variation in the absorption coefficient. The increased resolution derives from the fact that the ionization produced by a heavy ion beam varies from a small value to its maximum value for a displacement of the beam stopping point of only the order of 1% of the range of the beam, where the range of the beam must only slightly exceed the thickness of the specimen. For an attenuated beam radiogram (x-ray), the electromagnetic radiation must be able to penetrate the entire specimen and still retain adequate intensity to sufficiently expose the film without unduly exposing the entrance side of the specimen. Thus, the distance scale for a large variation in the radiation intensity is of the order of the thickness of the specimen. This yields a sensitivity increase of the order of 100 fold for a specimen where the percentage change in the stopping power is the same as the percentage change in the absorption coefficient.

The contrast between conventional, "x-ray" radiography and heavy ion radiography with plastic detectors is illustrated in Figure 1. Here the x-ray mean free path length and the heavy particle range are the same. The x-ray intensity (the processed film reproduces this intensity) and the Lexan response to the heavy ion beam are normalized to one at their peak values. As the tissue composition changes the water equivalent path length for either absorption or stopping varies with lateral position in the beam. As can be seen from the figure the resulting fractional change in Lexan response, $\Delta R_T/R_T$ is much greater than the fractional change in the x-ray intensity, $\Delta I_x/I_x$. The "noise" with plastic detectors is generally very low and typically represents the development of a small density of background etch pits as well as the fragment induced tracks.

Previously, protons have been used successfully to produce radiographs.[3-6] However, for heavy ions, the range straggling and scattering is smaller allowing better resolution of both thickness differences and spatial

features. Also, since with plastics a considerable magnification of tracks is achieved during processing, considerably lower doses can be used to achieve good radiographs.

Basic considerations.

A. The particle beam.

The idealized beam for particle range radiography is a parallel beam of monoenergetic, heavy particles of uniform intensity over the entire area to be radiographed. Preferably, the energy of the beam should be adjustable at the source, rather than through the use of degrading material. This is desirable to provide for the minimum longitudinal spread in the particle stopping points due to range straggling. The idealized beam is assumed to have a Gaussian distribution in particle range, R, about a nominal range $R_0 = \overline{R}$. Thus, if the x, y plane is perpendicular to the beam direction (z axis) and the fluence of particles is F, the stopping density, ρ_s, is given by

$$\rho_s = \frac{d^3N}{dxdydz} = \frac{F}{\sigma_R\sqrt{2\pi}} \frac{dR}{dz} e^{-\frac{1}{2}\left(\frac{R(z)-R_0}{\sigma_R}\right)^2} . \qquad (1)$$

Here R and R_0 are the ranges in water, z is the physical longitudinal position in the beam, and σ_R is the standard deviation in particle range (H_2O equivalent) due to range straggling. The approximate values of the range straggling are given in Table I. Here σ_R for water, given as a function of the particle type, and the particle range, R, is the emulsion result [after Barkas,[7]] scaled to other materials using Eqn. 5.66 of Burcham.[8] Since the straggling goes as $A^{-1/2}$, heavy particles provide a much narrower stopping point distribution than protons and result in greater resolution. This situation can be illustrated as follows.

In critical cases where very small changes in the specimen are to be resolved, particles heavier than ^1H or ^4He are necessary. For example, a 1 cm diameter, 5% density difference soft-tissue tumor provides a relative beam displacement of only 0.5 mm of water. If this tumor occurs somewhere within a body, the particle range may be somewhere between 20 and 30 cm. In Table I, it is shown that for this range particles at least as heavy as ^{16}O must be used if the range straggling is to be 0.5 mm or smaller.

The particle beam (of the LBL Bevatron) deviates significantly from the idealized beam in several respects. 1) The intensity is generally not uniform

over the area of interest. 2) Although at a given point in the beam a single beam pulse is fairly monoenergetic (most of the spread in the stopping points is due to range straggle), the energy may vary somewhat with lateral position. Therefore, the stopping point surface is not a plane perpendicular to the beam direction but is a slightly curved surface, typically convex downstream. 3) The beam energy may vary slightly from pulse to pulse. The evidence for this is that the width of the stopping point distribution is greater for multi-pulse exposures, and subsidiary peaks appear at different longitudinal positions. 4) Initial contamination of the beam and nuclear interactions with the stopping material alter the charge composition of the beam by producing lighter particles. These particles stop over a much greater longitudinal distance than the idealized beam.

A beam pattern profile for stopping ^{16}O particles in a 30-layer (10-mil thick each) stack of Lexan plastic is shown in Figure 2. Each white dot represents a track of a particle which stopped in that layer. Dark regions represent the absence of stopping particles. The particle beam enters layer No. 1; the particle stopping point distribution can be observed in layers 10-16 with the center of the Bragg peak in layers Nos. 13 and 14. The incident beam first passes through 7.20 cm of H_2O before entering the detector stack. A 10-pulse exposure representing a total of approximately 5×10^6 particles was used. This exposure should be compared with that shown in Figure 4. Here a single pulse of 4×10^5 particles was used yielding a standard deviation for the stopping particle distribution of approximately a single layer (≈ 250 μm). The stopping particles in Figure 2 are distributed over a somewhat larger distance.

B. Effect of specimen on the particle beam.

In the following discussion it will be assumed that the beam is idealized. The motivation behind this is that: 1) the idealized beam is in a mathematically tractable form, 2) the departures from the idealized beam due to physically insurmountable causes (nuclear disintegration, etc.) are small, and 3) future improvements in the accelerator technique will probably significantly improve characteristics such as uniformity in intensity, constancy of energy, etc.

The fundamental equation expressing the displacement of the nominal beam stopping point is

$$R_0 = \int_{\text{Bevatron}}^{\text{stopping point}} f\rho dz = \int_{\text{auxiliary equipment}} f\rho dz + \int_{\text{specimen}} f\rho dz + \int_{\text{detector}} f\rho dz \qquad (2)$$

The quantity $\rho(x, y, z)$ is the physical density (g/cm^3), $f(x, y, z)$ is the water equivalence factor correcting the range in g/cm^2 to a range in water, and $R_0(x, y)$ is the nominal (not affected by straggling) particle range in water. It is assumed that f is independent of particle energy. Although this is not strictly true, it is a good approximation. For the idealized beam R_0 is constant and since the auxiliary equipment, including air, is plane parallel, the first term in the right side of Eqn. (2) is a constant. Therefore, if z_e is the z of the entrance surface of the detector stack, and f_d and ρ_d are constant values of f and ρ for the detector, Eqn. (2) can be written

$$f_d\rho_d(z_0 - z_e) + \int_{\text{specimen}} f\rho dz = R_e \qquad (3)$$

where $z_0(x, y)$ is the nominal stopping z, and

$$R_e = R_0 - \int_{\text{auxiliary equipment}} f\rho dz$$

is a constant.

The preceding discussion of the derivation of the relatively simple operational Eqn. (3) was included to indicate its various elements, and the assumptions and requirements of the method. From Eqn. (3) it can be seen that either a change in chemical composition (through f) or a change in the density of a region of the specimen can displace the nominal stopping point z_0. The distribution in the stopping point given in Eqn. (1) is now given as

$$\rho_s, H_2O = \frac{1}{f_d\rho_d}\,\rho_s = \frac{F}{\sigma_R\sqrt{2\pi}}\, e^{-\frac{[f_d\rho_d(z-z_0)]^2}{2\sigma R^2}} \qquad (4)$$

where ρ_s, H_2O is the water equivalent stopping density.

As an example, a displaced particle stopping point distribution is shown in Figure 3. Here, a Lucite block with a 1 cm diameter spherical cavity filled with a sucrose solution of 5% lower stopping power served as a tumor model. The shaded region in the detector stack of Figure 3 is the $\pm\sigma_R$ region of the stopping, idealized beam as displaced by the model tumor model. This "tumor" which probably would not be detectable with x-rays (particularly if it were located inside a larger "body") causes an approximately $2\sigma_R$ displacement in the stopping point and is readily detectable using heavy-ion radiography. This can be seen in Figure 4 (the central circular feature) which shows the response of a Lexan detector stack exposed to the 250 MeV/nuc ^{16}O beam. The "negative" character of the image produced in, for example layer No. 10 as compared with that in layer No. 14, results from their being located on the opposite side of the peak of the stopping-particle distribution. Two small air bubbles located almost diagonally with respect to the square plastic can also be readily observed. The bubbles are about 5 mm in diameter and are approximately 0.3 mm thick. The outline of a paper gasket (~ 0.3 mm thick) used in between the two halfs of the Lucite block is also clearly visible. The air bubbles represent a change of about 0.03 g/cm^2 or about 0.3% change in total thickness. The gasket produces a lesser change because its density is only slightly smaller than that of the sucrose solution. Clearly, even smaller density changes can be observed, however, some improvement in the beam characteristics is definitely desirable.

C. Detector characteristics.

The object here is to compute the detector response curve as a function of the distance from the nominal stopping point. This is accomplished by folding the stopping point distribution with the detector response as a function of residual range. For example, the familiar Bragg curve results when the detector is an ionization chamber. Here, the detector response is the total particle ionization.

The plastic nuclear track detector response can be characterized by the chemical etch rate along the particle trajectory, V_T, as a function of the particle restricted energy loss rate (LET).[9] For normally incident tracks, a very good approximation to the Lexan detector response and a reasonably good approximation to the Cellulose Nitrate, (CN) detector response is

$$V_T = \begin{cases} V_G & LET_{350} < LET_{crit} \\ V_G \left(\frac{LET_{350}}{LET_{crit}}\right)^{\psi} & LET_{350} \geq LET_{crit} \end{cases} \quad (5)$$

where V_G is the bulk etch rate of the detector surface. For Lexan (without UV sensitization), $LET_{crit} \approx 300$ keV/μ (H_2O) and $\psi \approx 2$. For CN, $LET_{crit} \approx 80$ keV/μ (H_2O) and $\psi \approx 4$. It can be seen the CN is much more sensitive than Lexan.

Two significant aspects of the plastic response canbe seen from Eqn. (5). 1) The threshold nature of the detection implies that no particle tracks will be produced if the particle range is greater than a registration range. R_{reg}, derived from the values of LET_{crit}. 2) The track etch rate, hence the track size and the macroscopically observable response, increases rapidly as the stopping point is approached and LET_{350} increases. This places the effective response point very close to the stopping point, particularly in the case of Lexan. In fact, it occurs at a residual range of somewhat less than $R_{reg}/2$, the effective response range for detectors with constant response in the region $LET_{350} > LET_{crit}$. For example, $R_{reg} \approx 0.015$ cm (H_2O) in Lexan.

In Figures 5 and 6 are shown the normalized Lexan and CN response curves as a function of the water equivalent distance downstream from the nominal stopping point. Here the Lexan response is taken to be the total track open-in area on both surfaces of the detector. This should approximate the macroscopic response given by observing the layers with scattered light (dark field illumination).

In Figure 5, two response curves are shown for the CN detector. One gives the response as seen by light transmitted through the central opening areas of tracks etched completely through the plastic. The other gives the response that would be obtained by counting the tracks (which is a large task for large numbers of detector layers or particle radiographs with much detail). The assumed amount of surface bulk etch for the central opening area response is only 8.6 μ. For longer etch times, the central opening curve will approach the track count curve in appearance.

It can be seen that the Lexan response curve approximates the stopping point distribution quite well. The track hole opening area CN response curve

has approximately the same width as the stopping point distribution, even though it is shifted slightly upstream. These threshold detectors can therefore be assumed to be measuring the stopping point distribution without introducing any more than a negligible amount of longitudinal spread.

Radiography methods and results.

The basic approach is to interpose the specimen to be radiographed between the accelerator and the detector stack. The beam energy is adjusted either internally or externally by a variable degrader to place the beam stopping point approximately in the center of the detector stack. Also, an important requirement is that the specimen be placed in a bath of liquid with volume stopping power approximately equal to the average specimen stopping power. This procedure is necessary to remove as much of the external specimen geometry effect as possible.

Several quite different types of radiographs can be obtained depending on the detector type and processing. One is the conventional "picture" type of radiographs in which the density of the radiograph monotonically increases with the nominal stopping point displacement, $\int f\rho dz$. This type of radiograph can only be achieved by having a detector response curve with a width greater than the displacement variation over the region of interest. Only one detector layer could be used—the one placed on the side of the response peak (as a function of z) for particles passing through this specimen region (x, y). A shift in the displacement from point to point in the x, y plane would cause a corresponding change in the detector response. To meet the above requirement, either the displacement variation must be quite small or the response curve must be broadened. The most reasonable ways to broaden the peak are: 1) to use a more sensitive detector with a response which varies with ionization rate and position the stopping point somewhat downstream from the detector or 2) to increase σ_R by using a fine porous degrader placed some distance from the specimen to "scramble" the details of the degrader. The second approach is the better one because contrast is retained without sacrificing linearity in the response. That is, the detector can still be placed at the inflection point of the response curve.

The second type of radiograph is a "contour radiograph". This is the natural form to be used with narrow response curves. In this case, a "response band" is seen on a given detector layer. The line through the center of this band is the contour line corresponding to the displacement consistent

with the z_0 of this layer [see Eqn. (3)]. Combining the contour lines from different detector layers then gives a contour map of the displacement.

Using the stopping ^{16}O beam with cellulose nitrate and Lexan as detectors, a series of radiographs were made which are shown in Figures 7-14. In all cases, the radiographs were obtained using a single beam pulse of about 10^6 particles, corresponding to an absorbed dose of about 1 rad. All detectors were processed in an aqueous solution of 6.25 N NaOH. The corresponding temperatures and etch times were: Lexan—70°C, 8.0 hr; CN—40°C, 4.0 hr.

In Figure 7 is shown a radiogram of an unfertilized chicken egg using the CN detector. The photograph was made by shining transmitted light through the etched-through tracks onto a photographic plate. An outline of the yolk is clearly visible. The same egg can be observed in Figure 8. Here, a stack of 30, 10-mil thick Lexan sheets was used. Layer No. 10 is upstream of the others. The photograph was made using light scattered by particle tracks.

Radiographs of a fourteen-day-old, fertilized chicken egg are shown in Figures 9 and 10, with an x-ray of the same egg shown on the right-hand side of Figure 9. A four-layer sequence of the egg using the CN detector is shown in Figure 9, while Figure 10 is an eight-layer sequence using Lexan. In both cases considerable detail of the distribution of the soft tissue can be observed. The head of the embryo is on the left. The dots which appear on these radiographs, particularly near the edges of the egg are air bubbles trapped in the foam rubber that was used to position the egg in the water container.

A small (4 cm. long) tropical fish was also radiographed. In Figure 11 is shown a four-layer sequence using CN while in Figure 12 the same fish is observed in a seven-layer sequence in Lexan. An x-ray of the fish taken inside the water box appears on the bottom right-hand side of Figure 12. The two black dots appearing in the x-ray of the head of the fish, Figure 12, can also be seen in layer No. 9 of Figure 11. Since no effort was made to remove air bubbles, several appear. A sharp, high contrast image of the air bladder is observed, however the skeletal bone structure is not recorded. This illustrates the complimentary nature of the technique to x-ray radiography.

In Figures 13 and 14 are observed four-layer sequences of the bottom portion of a live mouse in the CN and Lexan detectors, respectively. The water level is observed near the top of each picture. A variety of detail can

be observed in each picture. Of particular interest is the large tumor that is observed just to the left of the lower hind leg.

Conclusion.

Of the two detectors used, the CN detector is more sensitive and therefore offers a broader response, i.e., a greater latitude. Therefore, the radiographs produced with this detector have the more standard appearance of conventional pictures. The response of Lexan, however, is much narrower, i.e., the detector has a very narrow latitude. It is expected that this detector will be quite useful in situations requiring the three-dimensional reconstruction of radiographed objects. Of course, it should be noted that other detector types are also available, and that it is possible to significantly alter the response of any of the detectors through a variation in processing. Thus, a wide spectrum of techniques can be achieved.

Although many experimental details remain yet to be worked out, heavy-ion radiography shows great promise for revealing previously undetectable internal regions of only slightly varying chemical composition or structure. Plastic nuclear track detectors arrayed in stacks can be conveniently utilized in permanently storing this information. Both particle radiographs and laminar roentgenographs can be made in this manner. Since "exposure" times for radiographs can be very short, of the order of a millisecond or even shorter, the technique is also applicable in obtaining "blur-free" radiographs of biological specimens in motion.

REFERENCES

1. C. A. Tobias, T. L. Hayes, H. D. Maccabee, and R. M. Glaeser, "Heavy Ion Radiography and Microscopy" in Biomedical Studies with Heavy-ion Beams, UCRL-17357, p. 108 (1967).
2. C. A. Tobias and H. D. Maccabee, "Accelerated Particles in Biological Research" in Elementary Particles: Science, Technology, and Society. Academic Press (1971).
3. E. V. Benton, R. P. Henke and C. A. Tobias, Heavy-Particle Radiography (to be published in Science).
4. H. L. Anderson, U. S. Paten No. 2,953,510 (1960).
5. A. M. Koehler, Science 160, 303 (1968).
6. D. West and A. C. Sherwood, Nature 239, 157 (1972).
7. V. W. Steward and A. M. Koehler, Science 179, 913 (1973).
8. W. H. Barkas, Nuclear Research Emulsions, Academic Press (1963).
9. W. E. Burcham, Nuclear Physics, p. 177, McGraw-Hill (1963).
10. E. V. Benton, A Study of Charged Particle Tracks in Cellulose Nitrate, USNRDL-TR-68-14 (1968).

TABLE I

Range Straggle in Water
(mm)

Range/Particle	^{1}H	^{4}He	^{16}O	^{40}Ar
1 cm	0.120	0.0599	0.0282	0.0172
2	0.232	0.116	0.0546	0.0333
5	0.558	0.540	0.130	0.0792
10	1.08	0.540	0.251	0.152
20	2.08	1.04	0.481	0.292
50	4.95	2.48	1.14	0.692

Acknowledgments.

We thank J. Lyman, J. Howard, G. Welch, D. Palmer, W. Shimmerling, R. Walton and the Bevatron crew for their generous help. This work is supported in part by the AEC.

FIGURE CAPTIONS

Fig. 1. Illustration of the different situations in the depth resolution capability between x-rays and stopping heavy ions.

Fig. 2. A beam pattern profile for stopping ^{16}O particles in a 30-layer stack of Lexan. Each plastic is approximately 3 inches on the side.

Fig. 3. Scale diagram of exposed model tumor. The Lucite block cavity contains a sucrose solution of 5% lower stopping power than the Lucite. The shaded region shows the $\pm\sigma_R$ portion of the stopping point distribution.

Fig. 4. The contour radiogram of the model tumor diagrammed in Figure 3. The 10-mil Lexan detector layers were exposed to a single pulse (~ 10^5 of ^{16}O ions cm^{-2}), etched in 6.25 N NaOH with 0.5% Benax at 70.4°C, and photographed with dark field illumination. Each small white dot represents a track. Two small air bubbles are also present. The holes in the corners of each detector were used for supporting the layers during processing. Numbers correspond to adjacent detector layers.

Fig. 5. Normalized Lexan and CN detector response curves. The normalized stopping distribution producing these curves is also shown. The Lexan response is the total track opening area on both detector surfaces. The CN responses are the track count on the downstream surface and the total area of the central openings of etched-through tracks. All layer positions are for the center of the layer.

Fig. 6. Expanded response curve for Lexan. The shaded areas are the portions of the stopping point distribution that contribute to the response for the indicated layer position.

Fig. 7. "Picture" radiograph of a fertilized egg using light transmitted by etched-through tracks in CN. Some detail of the embryo can be seen at the edge of the response band. The detector was etched for 20 hours in a 40°C, 6.25 N NaOH solution. The exposure consisted of two pulses.

Fig. 8. Contour radiogram of the egg shown in Figure 7. Successive layers of a stack of 10-mil thick Lexan layers show the response bands corresponding to contours for various nominal stopping point displacements.

Fig. 9. A four-layer sequence of a 14-day-old fertilized chicken egg in CN. The layer thickness used was 10 mil; individual layer numbers appear on the left. The picture on the right is a x-ray of the same egg taken using optimum conditions: 21 cm focus to Cronex film, 35-kv potential, 50 ma, 24 sec with 0.8 inherent filtration.

Fig. 10. Same egg as in Figure 9 except Lexan detector was used. Several air bubbles can also be seen.

Fig. 11. A four-layer sequence of a small tropical fish in CN.

Fig. 12. A seven-layer sequence of the same fish as in Figure 11 in Lexan. The bottom right-hand photograph is an x-ray of the fish taken inside the water box used in these experiments; conditions are same as for Figure 9 except 1.5 sec exposure.

Fig. 13. A four-layer CN sequence of the bottom portion of a live mouse, partially submerged in water. Note the large tumor just to the left and slightly above the hind leg.

Fig. 14. A four-layer Lexan sequence of the same mouse as in Figure 13.

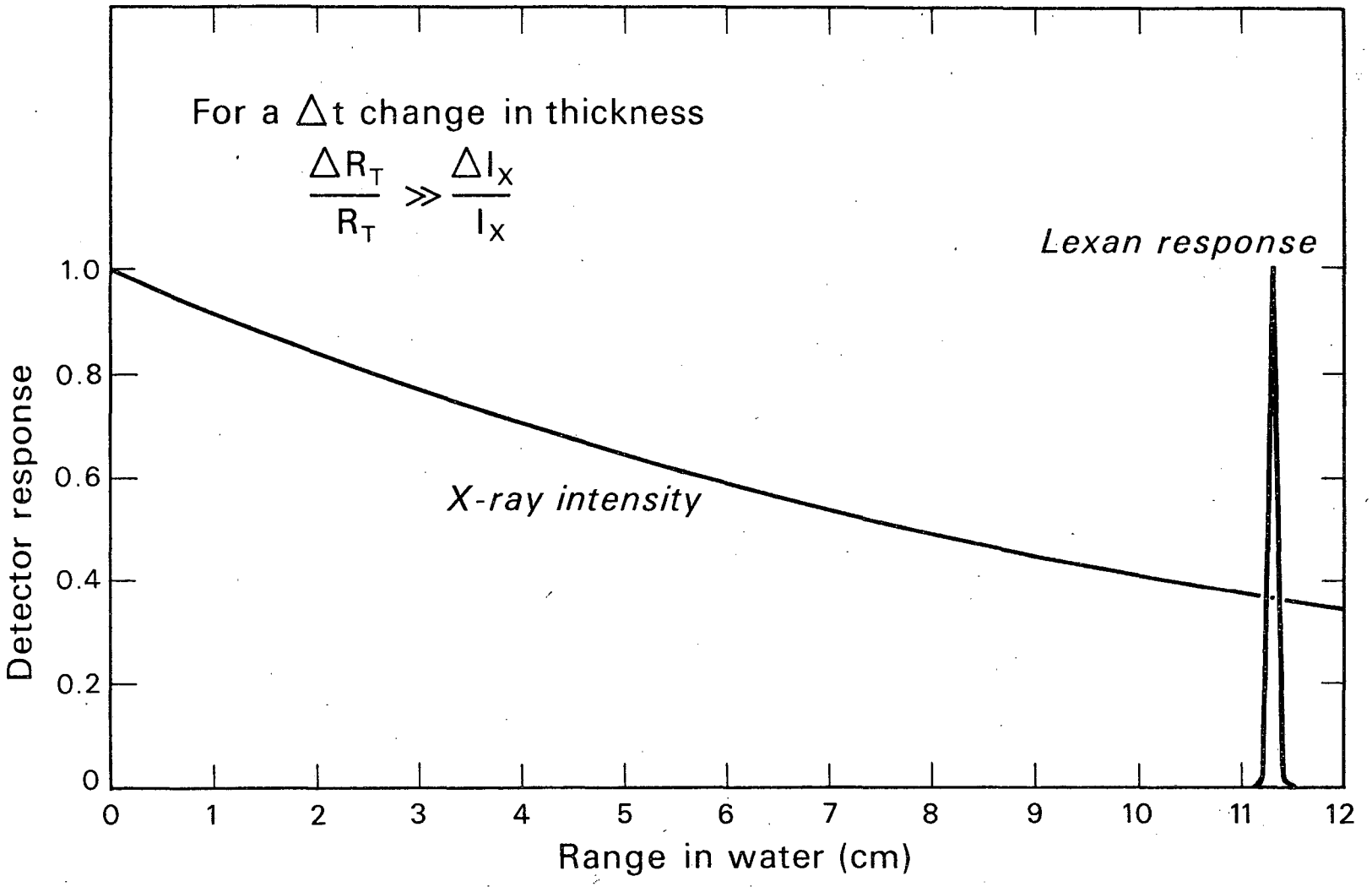

DBL 732-5053

Figure 1

0 0 0 0 4 0 0 1 5 0 9

10

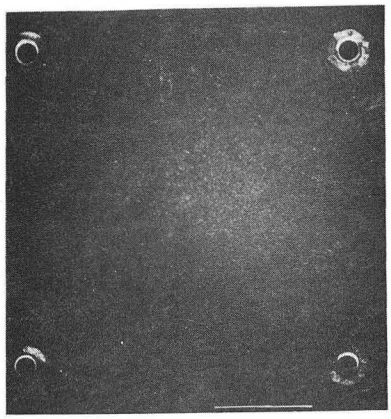

11

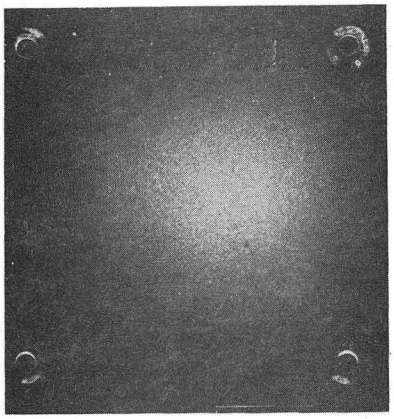

12

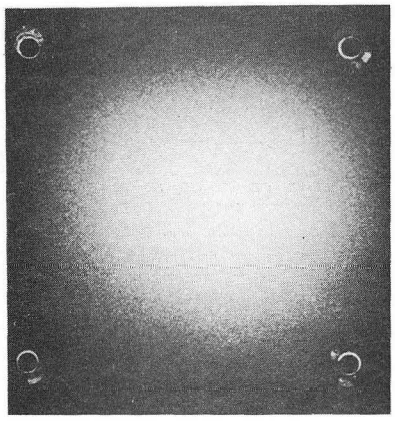

13

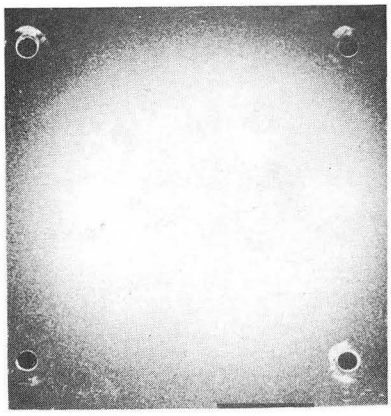

14

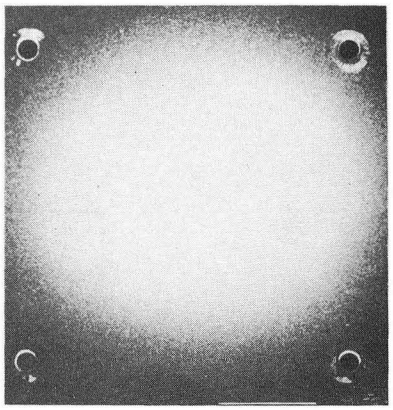

15

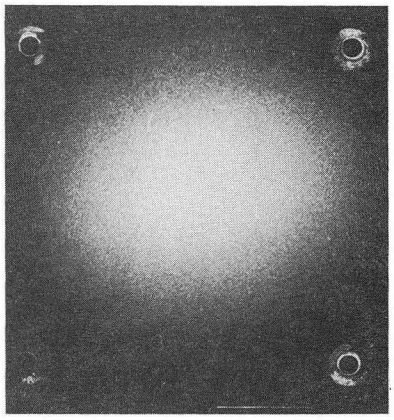

16

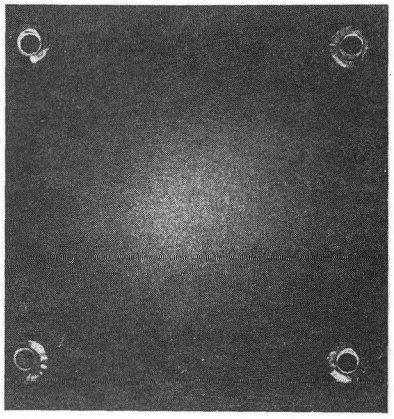

XBB 733-2163

Figure 2

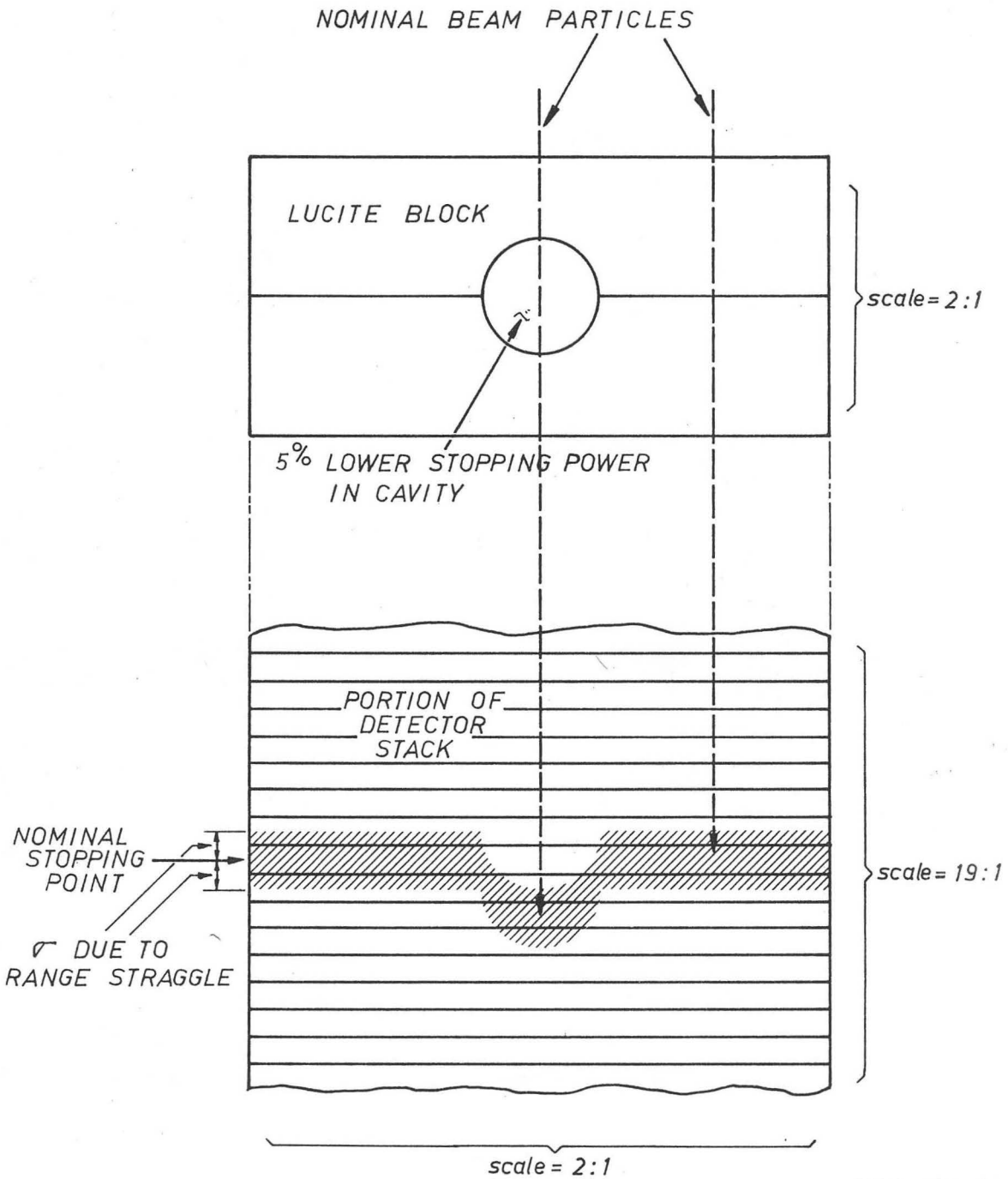

XBL 731-47

Figure 3

0 0 0 0 4 0 0 1 5 1 0

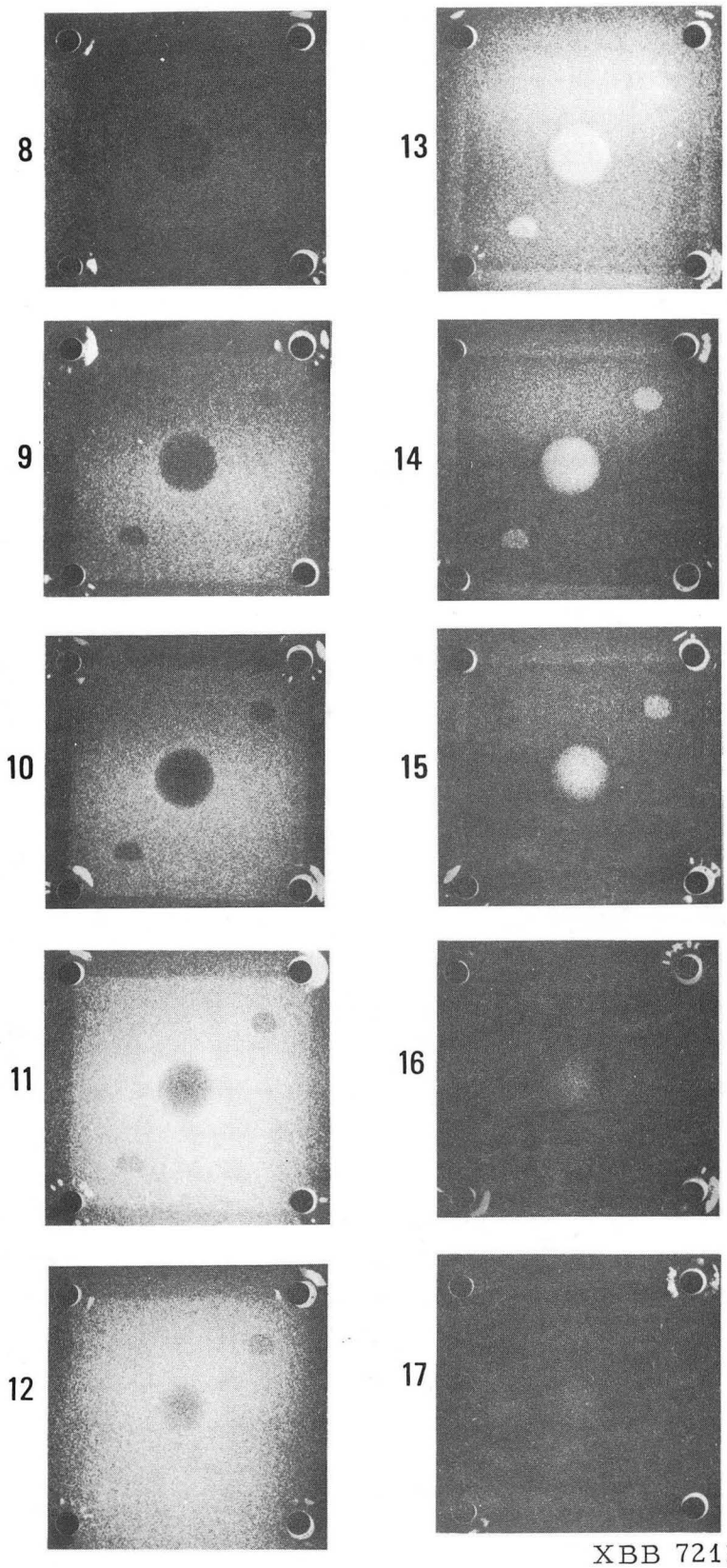

XBB 7212-6108A

Figure 4

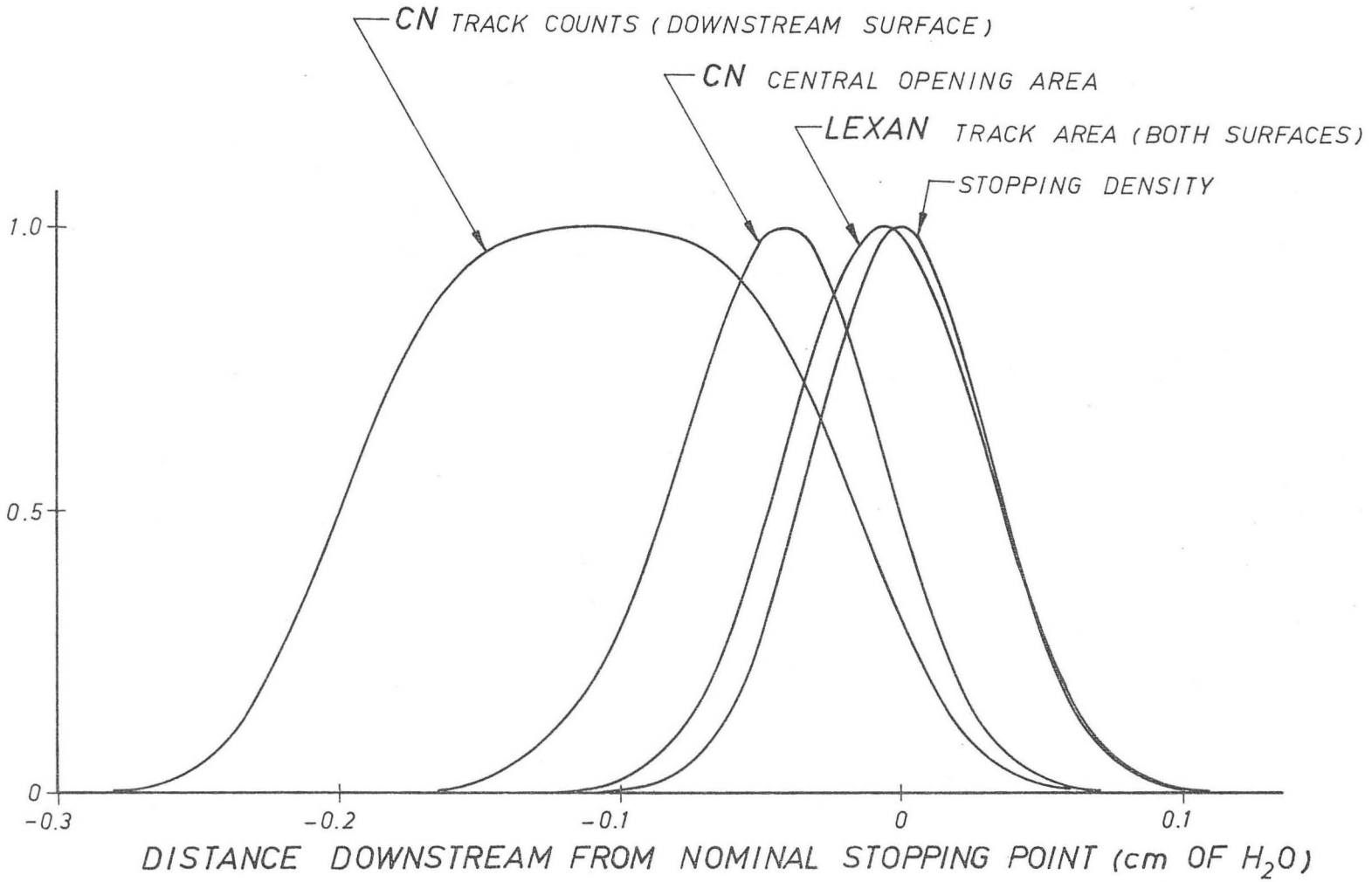

XBL 731-48

Figure 5

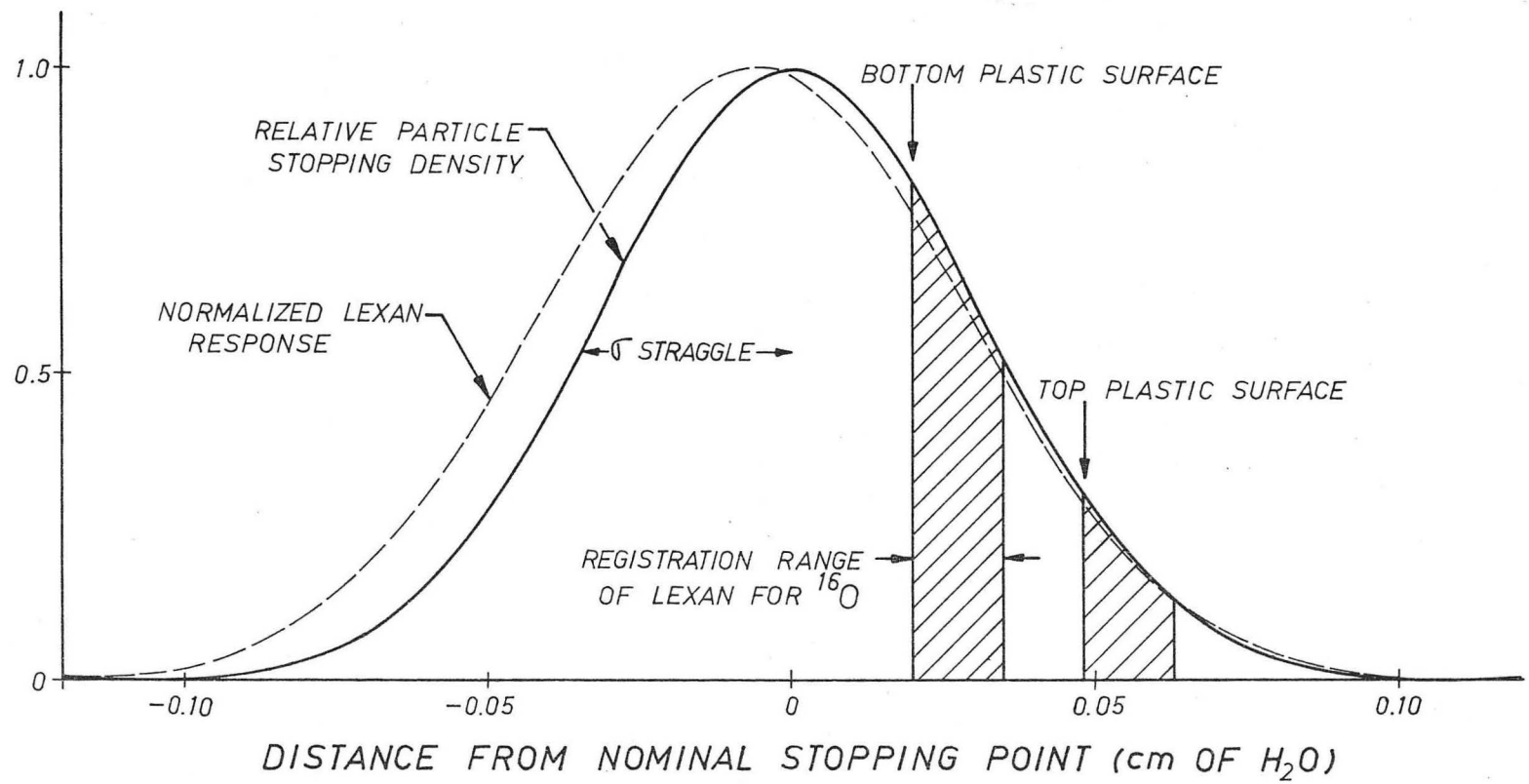

XBL 731-49

Figure 6

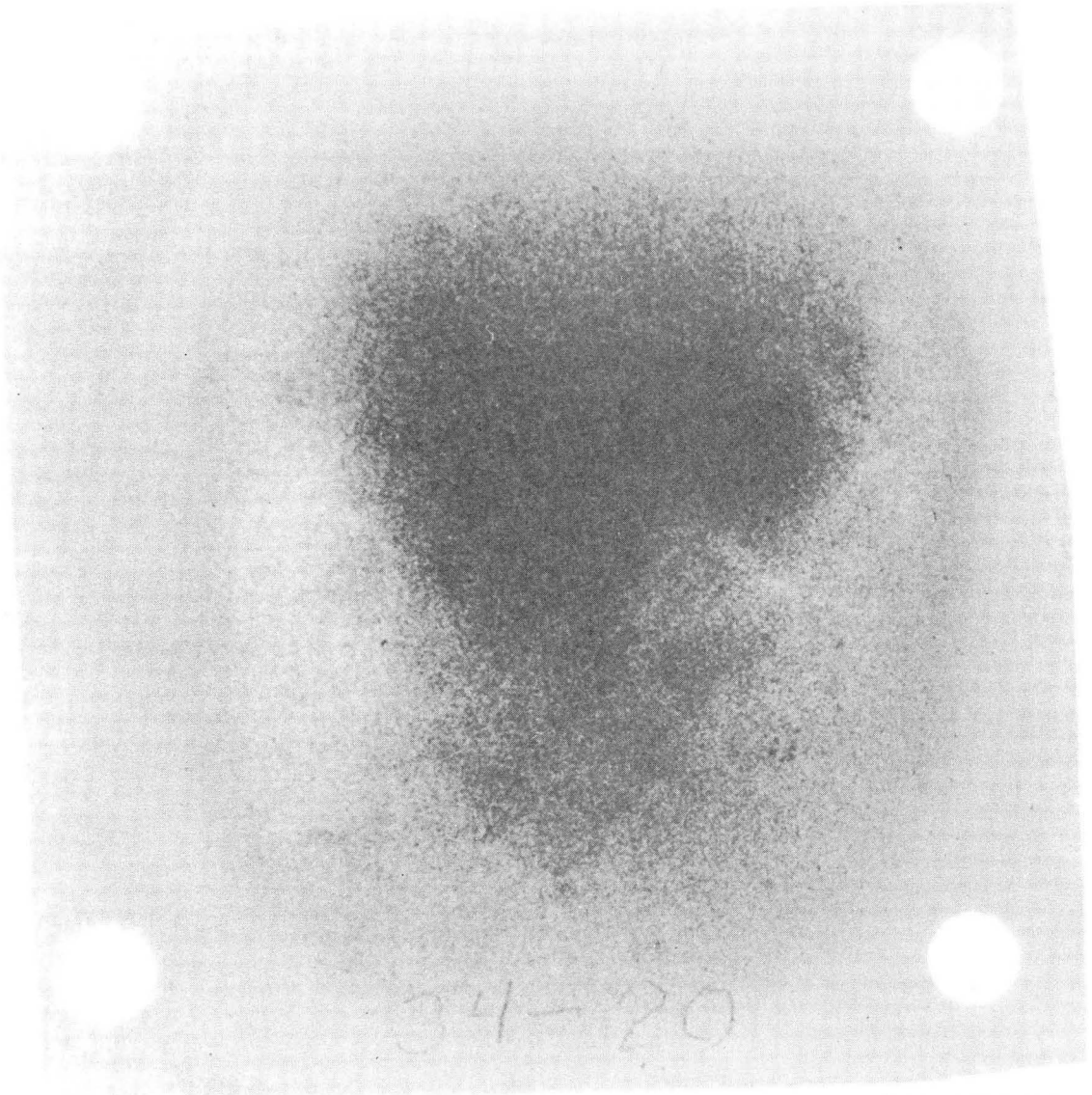

XBB 7212-6110

Figure 7

0 0 0 0 4 0 0 1 5 1 2

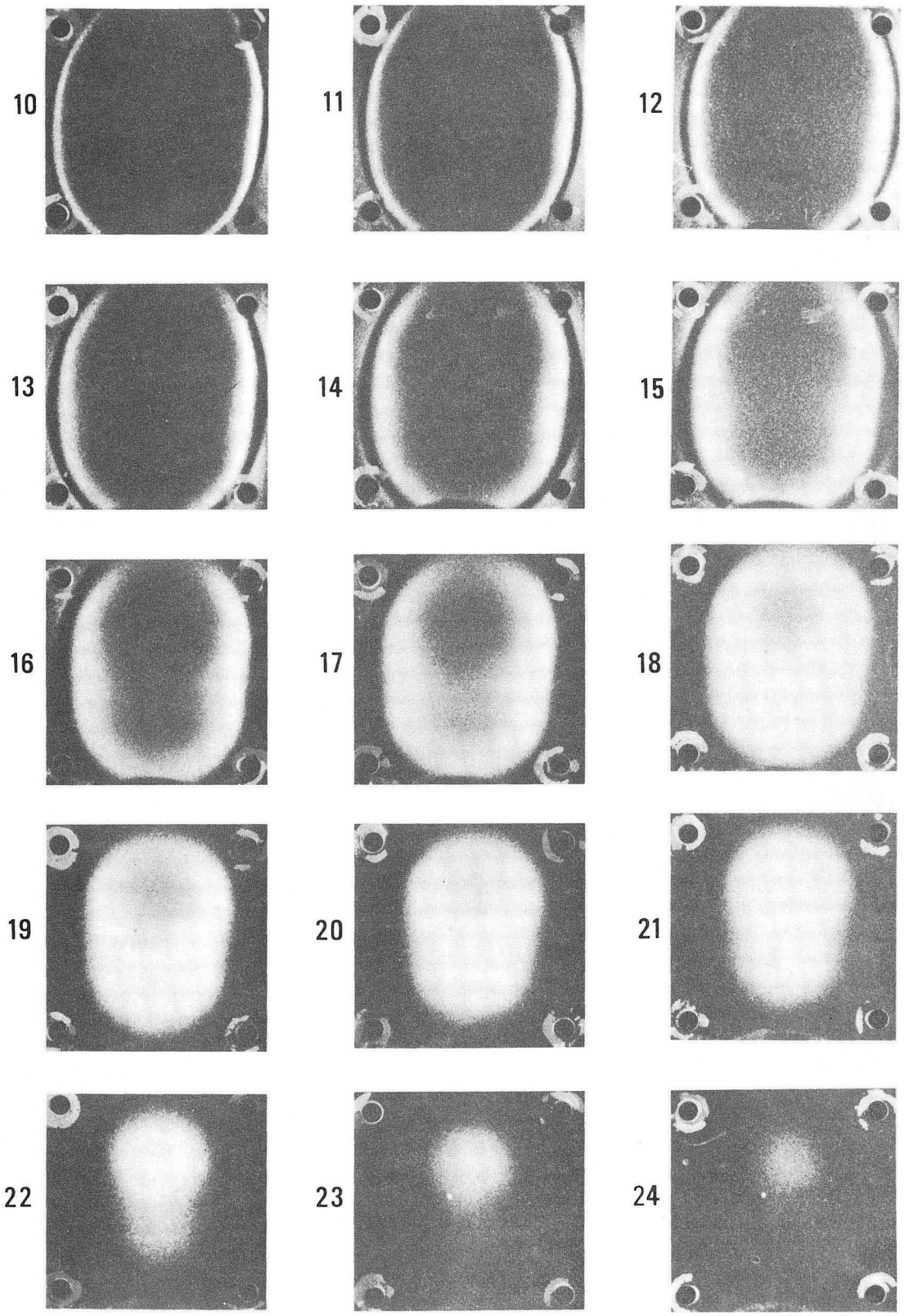

XBB 7212-6109A

Figure 8

1

2

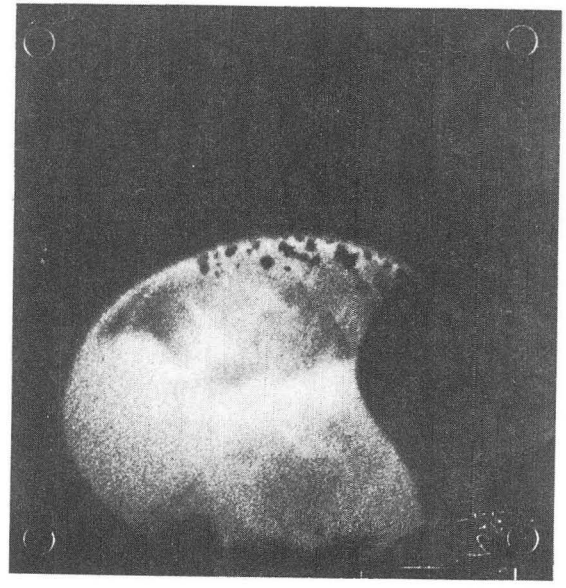

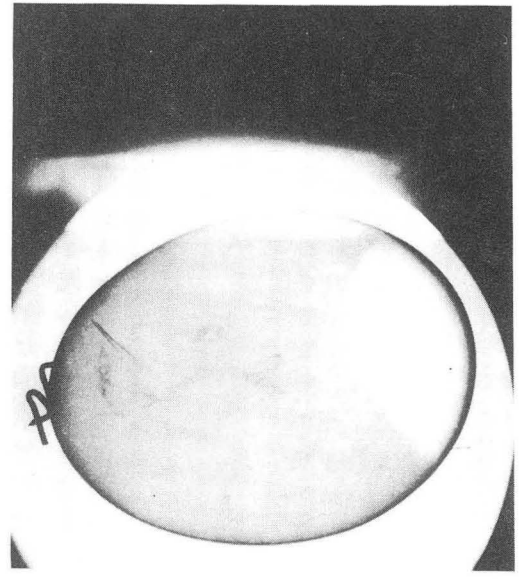

6

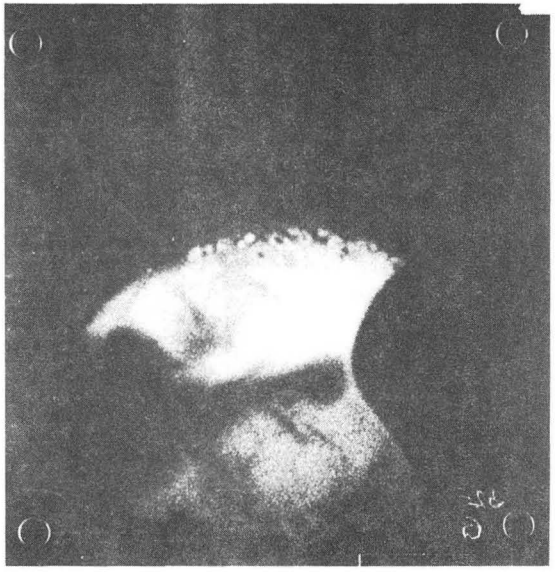

7

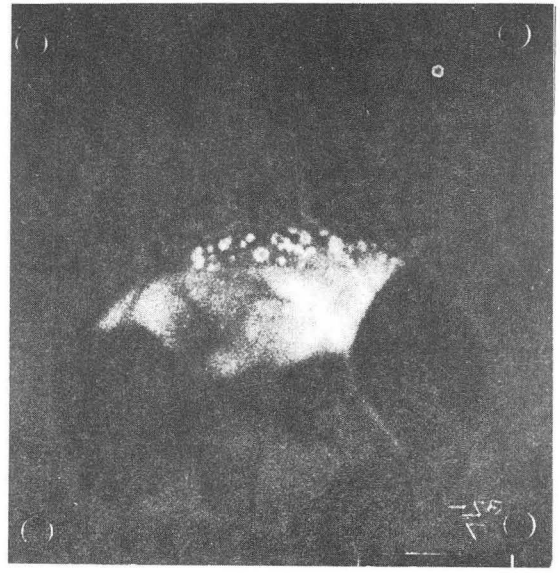

Figure 9

XBB 734-2552

0 0 0 0 4 0 0 1 5 1 3

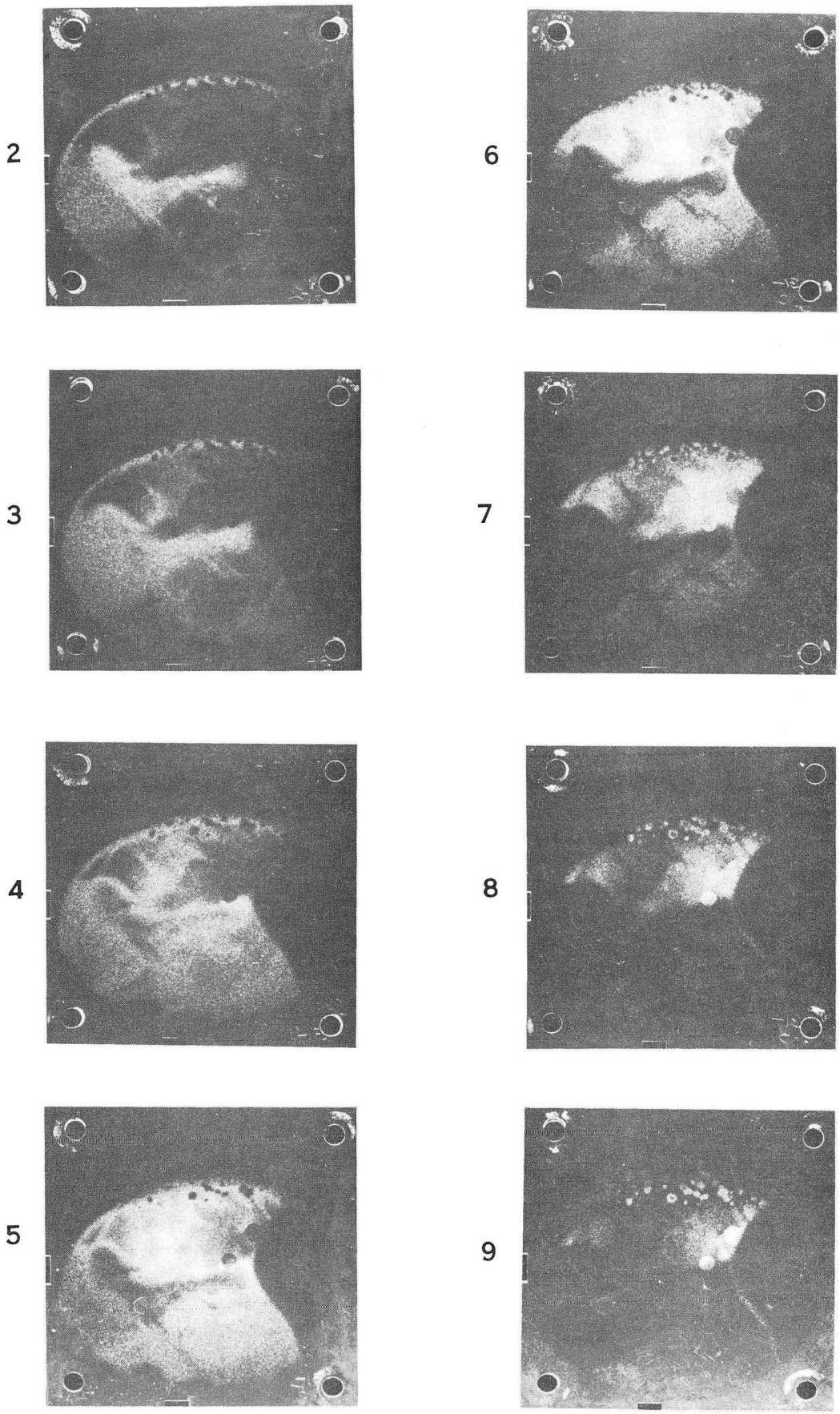

XBB 733-2164

Figure 10

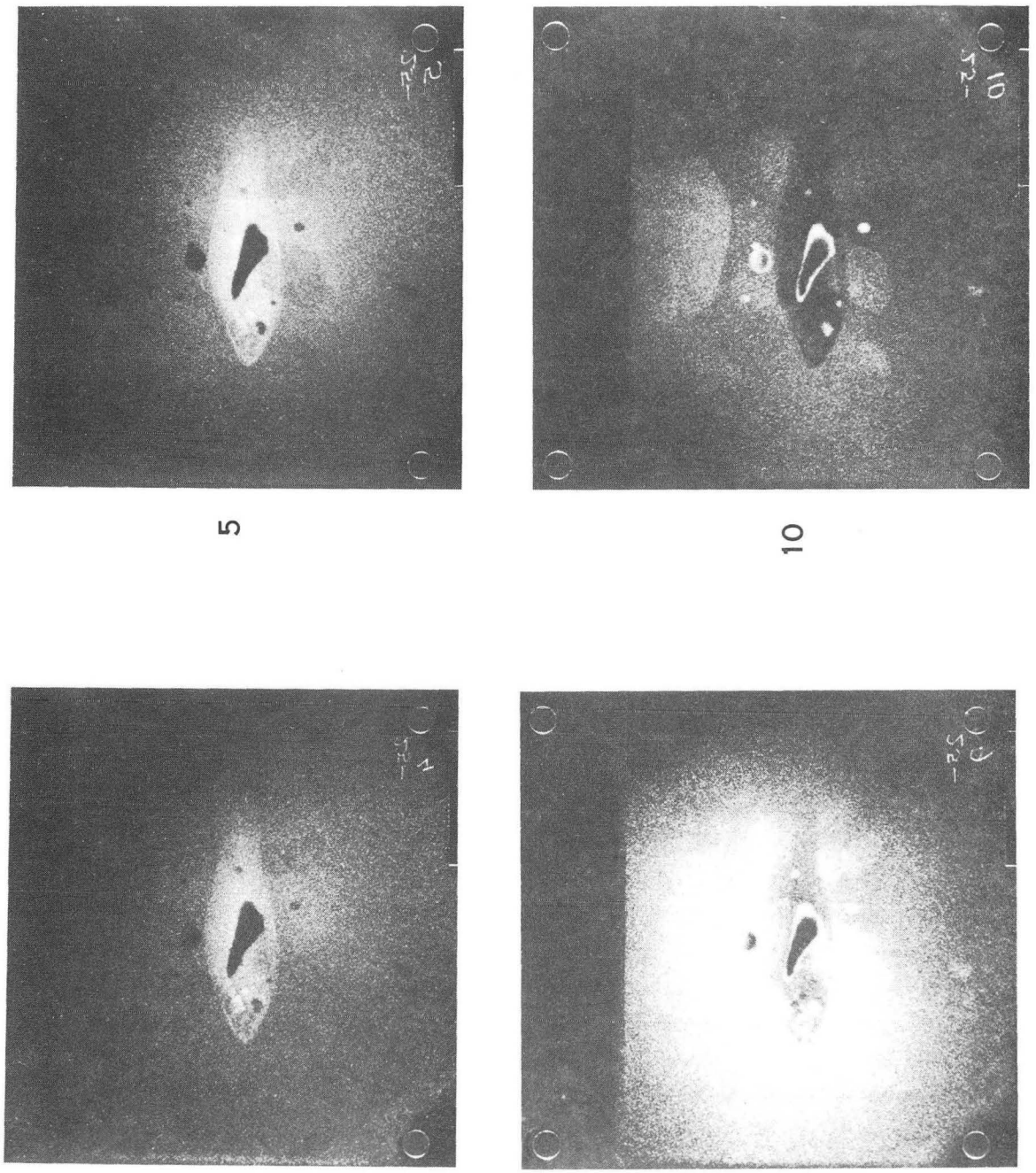

XBB 734-2550

Figure 11

0 0 0 0 4 0 0 1 5 1 4

7

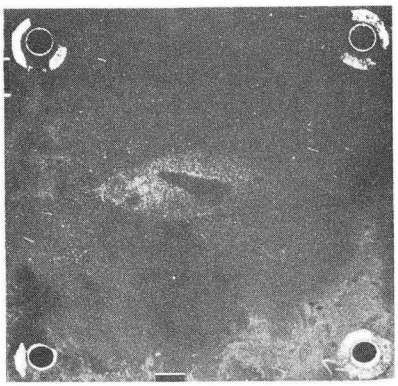

11

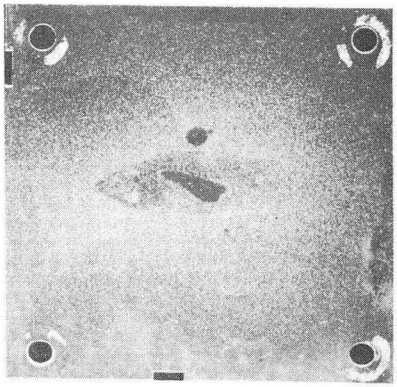

8

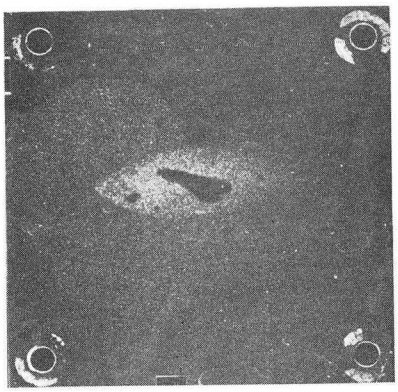

12

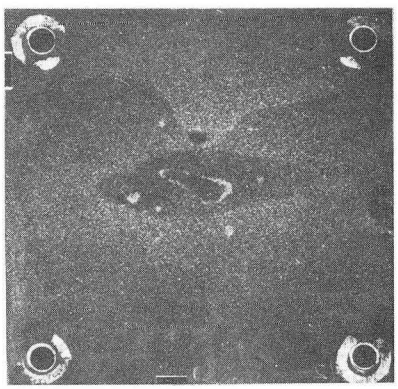

9

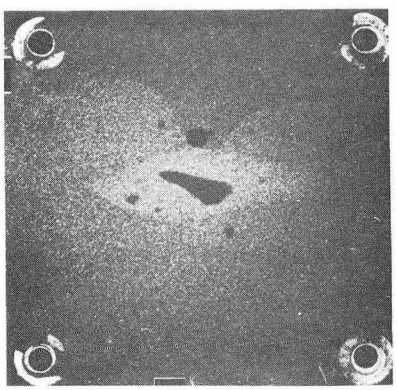

13

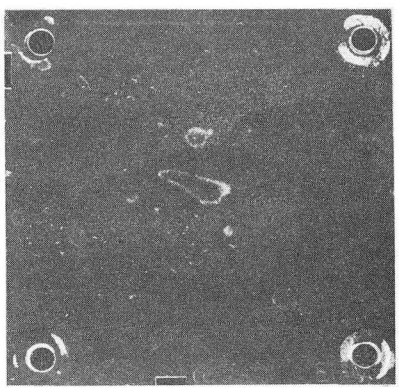

10

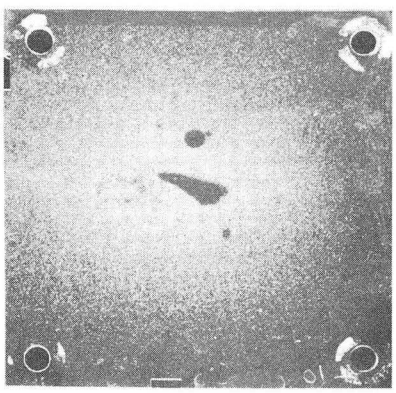

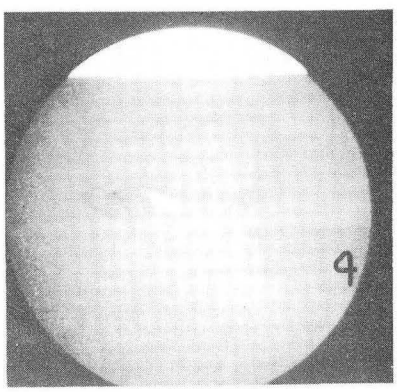

Figure 12 XBB 733-2162

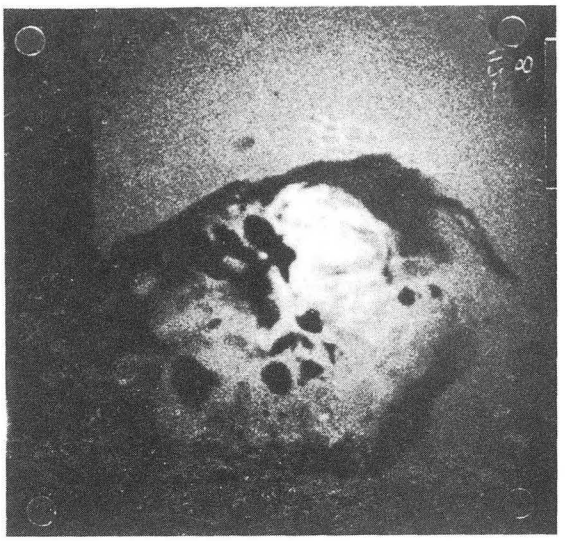

8

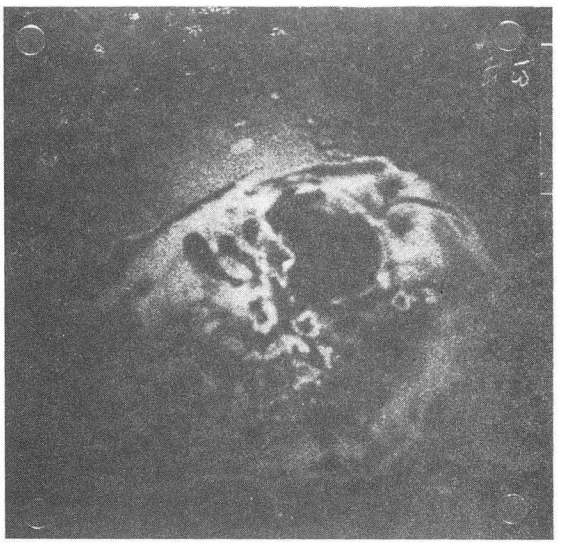

13

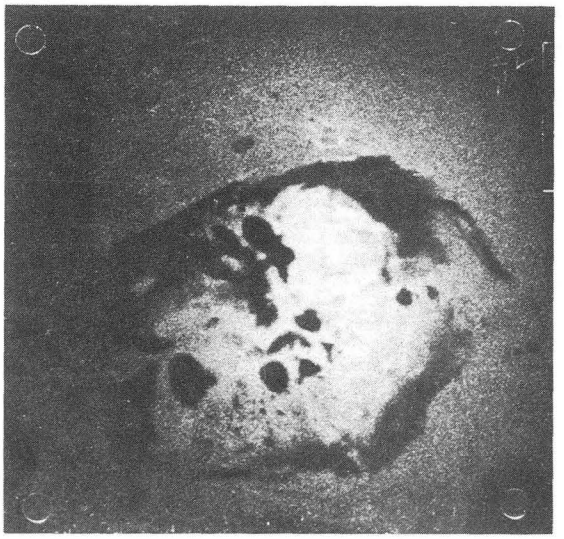

7

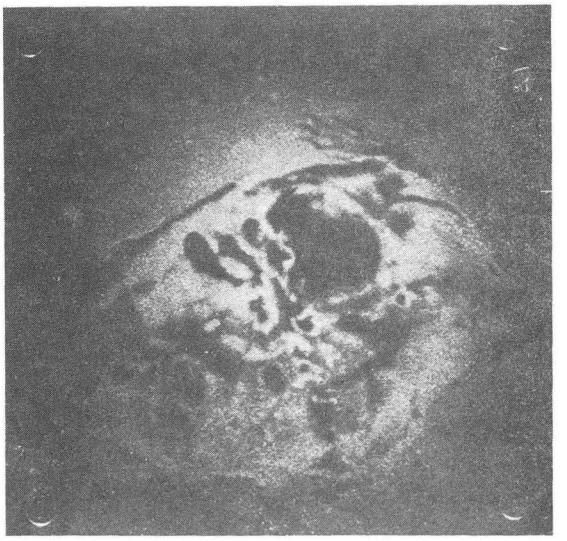

12

XBB 733-2551

Figure 13

0 0 0 0 4 0 0 1 5 1 5

9

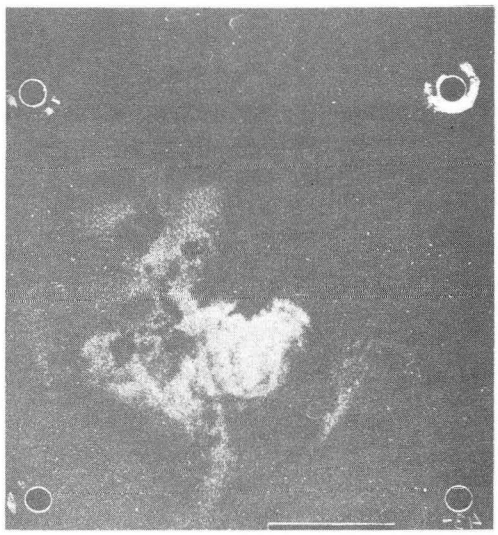

10

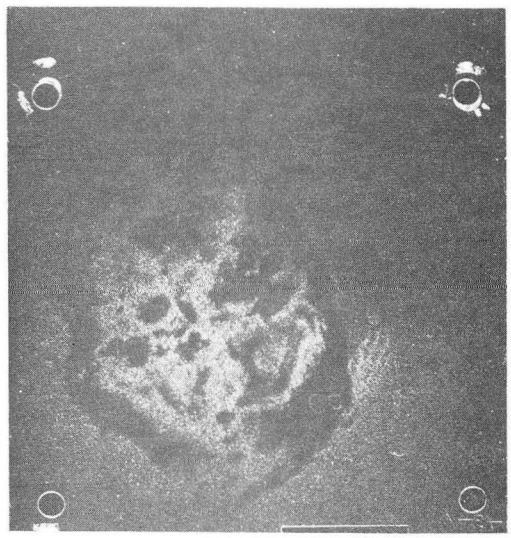

11

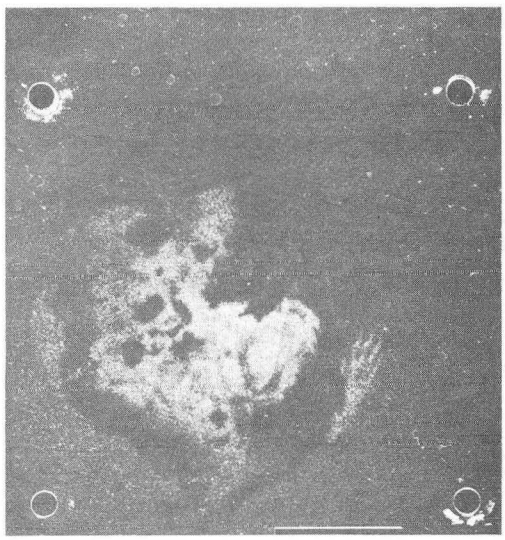

12

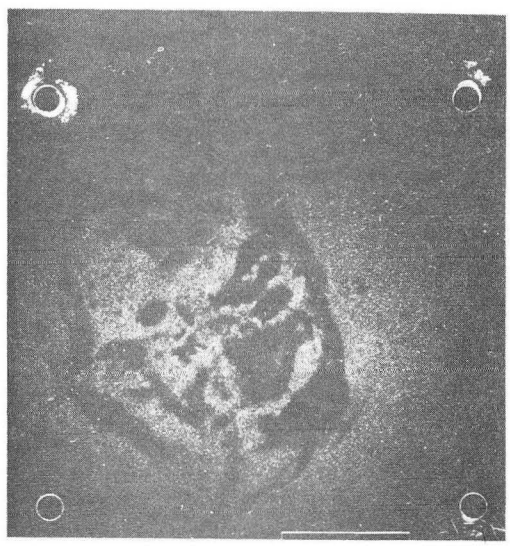

Figure 14

XBB 733-2161

RELATIONSHIPS BETWEEN TRACK STRUCTURE AND BIOLOGICAL EFFECTS OF HEAVY CHARGED PARTICLES

Aloke Chatterjee and Cornelius A. Tobias

Donner Laboratory—Lawrence Berkeley Laboratory
University of California, Berkeley, CA 94720

Abstract.

During the last two years, with availability of high-energy, heavy-ion beams at the Berkeley Bevatron, numerous experiments have been performed on the effects of high-speed (about 260 MeV/nucleon) oxygen and nitrogen ions on the survival of T-1 human kidney cells. Preliminary data from these experiments are now available (13).

An analysis of these data shows that the cross-section expressed in Equation 1 (in the text) with constants used at 6.6 MeV/nucleon does not fit the higher-energy data. It seems necessary to augment the model by demonstrating how the cross-section depends on the kinetic energy per nucleon of the bombarding particles explicitly, besides being dependent on LET. Our initial approach has provided such a modification. At the same time, it has become apparent that modification is closely related to high-LET radiation chemistry of aqueous systems.

Introduction.

With the availability of high velocity and high Z particles in the laboratory, quantitative understanding of their effects on living cells is of paramount importance. Of particular interest is the effect of heavy particles on normal cells and cancer cells. It has been proposed that heavy ions such as neon (Z = 10) could be used in cancer therapy and that such heavy ions might, in large measure, eliminate the oxygen effect (1).

Up until now, data on mammalian cell radiobiology were available only at low energies. The most complete set of such data is given by Paul Todd (2). His study involves "Reversible and Irreversible Effects of Ionizing Radiations on the Reproductive Integrity of T-1 Human Kidney Cells" with particles studied ranging from deuterons to argon, all of them having the same velocity corresponding to an energy of 6.6 MeV/nucleon. In order to explain such data, specifically, the shape of survival curves, oxygen effect and RBE and also some additional data on bacteria (3) and phage (4), Tobias et al. (5) have suggested that a portion of the cross-section for inactivation is proportional to the square of linear energy transfer. The other portion of the cross-section, which relates to effects modifiable by presence of oxygen and chemical protection, is proportional to linear energy transfer. At the same time, Kondo (6) independently suggested that biological effects were possibly related to higher powers of LET. A detailed model has been worked out (7) particularly suitable for the effects of monoenergetic ions. In this model, the probabilities for producing two types of lesions are expressed in terms of cross-section:

$$\sigma_i = \sigma_{i\infty} [p_i(1-e^{-\alpha_i \epsilon}) + q_i(1-e^{-\beta_i \epsilon})^2] \qquad (1)$$

where $\sigma_{i\infty}$ "limiting" cross-section at very large LET, ϵ, p_i and q_i are the probability factors so that $p_i + q_i = 1$. α_i is a constant relating to repairable lesion, which can be modified by the presence of chemical sensitizers or protectors. β_i is a constant relating to "co-operative effects" usually not chemically modifiable. i takes the value of 1 and 2 for two kinds of damge: the exponential region of the survival curve and the sigmoidal region of the survival curve.

With the above cross-sections, the effects on reproductive integrity of human T-1 kidney cells in asynchronous mode can be expressed by:

$$N = N_0 [1-(1-e^{-\sigma_1 F})^m] e^{-\sigma_2 F} \qquad (2)$$

where F is the flux density of monoenergetic particles of LET, ϵ. m is a constant for each system and usually varies from 3 to 6, depending upon the system.

By comparing data of Todd (2) and Barendsen (8) at various energies less than 10 MeV/nucleon, Curtis (9) came to the conclusion that the oxygen effect cannot be described adequately by using LET as a parameter. The results should probably be interpreted in terms of a new parameter, Z^{*2}/β^2, where Z^* is the effective charge of the particle and β is its velocity in units of velocity of light, C.

Recently, additional authors have discussed higher order components producing effects of high-LET radiation. For example, Neary (1) demonstrated that production of chromosome breaks relates to square of LET. Katz and Butts (11) produced a model in which the effects of high-LET particles are described in terms of "gamma kill" and "ion kill"; one of these in effect depends on the square of LET. Rossi and Kellerer (12) suggest that an aspect of biological effect depends on the square of "microdose"--a quantity which, of course, also relates to LET.

So far, no such theory is available in the literature which takes into account the effect of radiation chemistry in the understanding of consequential biological change. Such consideration is almost essential to the basic understanding of biological damage due to radiation.

Theoretical approach.

It would be logical to begin with a physical model of the structure of ionizing particle tracks, statistical in nature, and using a complete description of delta-ray distribution together with distribution of ion clusters and excitation clusters. Since such a model is not available, instead, at this time, we are using a different approach, i.e., a smoothed distribution of the radial distribution of energy transfer in monoenergetic particle tracks as developed by Chatterjee, et al. (14). The structure of heavy charged-particle tracks

can be visualized in terms of "core" (a high-energy density region) and "penumbra" (a low-density energy region). The region of core extends to a few nanometers, and energy is deposited in this region due to collective oscillations of the electron medium by the passage of heavy charged particles. Experimental demonstration of such a region is not presently feasible. The idea of collective oscillation stems from the work of Luntz (15) and others, as well as being outlined in the present paper. Most of the energy deposited by generated secondary electrons is in the penumbra region which extends possibly to micrometers. Secondary electrons deposit some energy in the region of core also.

Quantitative aspect of track structure.

Radial cut-off LET and radial cut-off dose calculations for heavy charged particles (energy range 0.25 MeV/nucleon to 600 MeV/nucleon) in water have been carried out. There is good agreement between the calculations and experimental results (16) at low energies (3 MeV/nucleon and below). Experimental results are not available at higher energies. According to Luntz, radial energy density function $\rho(Z, v, r)$, for a particle with charge Z, velocity v, and radial distance r, can be expressed by:

$$\rho(Z, v, r) = \frac{dE/dx}{2\pi r^2 \ln(\sqrt{e}\ r_{max}/r_{min})} . \qquad (3)$$

This relation agrees very well with the theoretical calculations of Chatterjee et al., provided r_{max}, the maximum extent of penumbra, is given by:

$$r_{max} = aE + b\sqrt{E} + \gamma \qquad (4)$$

where r_{max} is expressed in microns and E is the energy of the particle in MeV/nucleon. $a = 0.768$, $b = -1.925$ and $\gamma = 1.257$. r_{max} as expressed in Equation 4 is the result of calculations performed by Chatterjee et al. and differs from that given by Luntz. r_{min} is the size of the core and, according to Luntz, can be expressed as:

$$r_{min} = v/\omega_0 \qquad (5)$$

where v is the velocity of the incident particle and ω_0 is the natural frequency of oscillation, $\frac{ne^2}{m}$, and can be calculated by assuming a plasma comprised of medium electrons of density n, mass m and charge e.

According to Equation 3, we find that the energy density function varies as $1/r^2$. But, in any event, $\rho(Z, v, r)$ close to the track must be finite and hence cannot go down to $r = 0$, as does $1/r^2$. This leads to the following two questions: a) to what lower limit must we carry the $1/r^2$ distribution of energy density? b) how do we represent $\rho(Z, v, r)$ beyond that limit? As pointed out by Luntz (16), in order to answer the first question, one has to consider the possible discontinuity (physical) occurring close to the track which relates to energy deposition. There seems to be a discontinuity in direct excitation by the incident particle. The latter may be approximated by the plasma-screening distance v/ω_0 beyond which the field of the particle is totally cancelled by the induced polarization field of the medium. If one employs Bohr's criterion for adiabaticity, it yields a cut-off distance which is larger than that given by v/ω_0 by a factor of 2. The spatial extent of core is given by v/ω_0. Because of two physically differing mechanisms of energy deposition inside the core and in the penumbra, we would not expect the same spatial variation of $\rho(Z, v, r)$ inside the core as outside it (i.e., in the penumbra). It seems that plasma oscillations will <u>smooth out</u> energy deposition inside the core.

Thus the present understanding of track structure would indicate that there is a flat distribution of energy density within the core, and in the penumbra, it varies as $1/r^2$.

The model.

The distribution of energy density discussed in the preceding section is established within about 10^{-15} seconds. Evolution of the track structure with time, and subsequent changes in energy density, form an important consideration in the present model.

Our initial quantitative studies (to be reported elsewhere) convinced us that physical distributions of ionizations and excitations acting in a direct manner cannot be used for adequate explanation of either RBE or OER values. It has become necessary to consider radial redistribution of energy during the brief intervals between energy deposition and the time when damage becomes more or less permanent within biological macromolecules. In other

words, we must consider the time dependence of radial energy density distribution.

Let us denote the time-dependent radial energy density by $\rho(Z, v, r, t)$ in the track segment where the energy is E(MeV/nucleon) and the corresponding velocity is v, with linear energy transfer ϵ.

$$\epsilon = 2\pi \int_0^{r_{max}(t=10^{-15})} \rho(Z, v, r, t = 10^{-15})\, r dr \qquad (6)$$

In the present model, it is assumed that the density of free radicals, $R(Z, v, r, t)$ is directly proportional to energy density at time, t. We know that the high density of free radicals in the core can lead to radical-radical interactions; these are called co-operative events in the present model. In pure water, for example, interaction of radicals among themselves may lead to the formation of H_2O_2 in the core. Such reactions are also possible in the penumbra but perhaps to a lesser extent. It seems relevant that the co-operative terms in the cross-section of Equation 1 correspond to such interactions.

In a radial location, r, and at a time, t, we may expect that the number of relevant interactions in a thin segment, $\Delta\chi$, of the nucleus of the cell can be expressed by:

$$\kappa \rho^2 (Z, v, r, t)\, (\Delta\chi)^2$$

where κ is a proportionality constant for relating radical density to energy density. Thus the total number of events in a track segment of thickness $\Delta\chi$ can be obtained by integrating the above expression over time as well as radial extension of the track. Hence, the total number of events, ν, is given by:

$$\nu = 2\pi\kappa \int_0^t dt \int_0^{r_{max}(t)} \rho^2 (Z, v, r, t) r dr \cdot (\Delta\chi)^2 . \qquad (7)$$

As demonstrated by Equation 7, a more correct approach to the problem involves integration over time. This requires solution of the following equation for free radical density:

$$\frac{dR}{dt} = D\nabla^2 R + k_1(t)R^2 + k_2 R \qquad (8)$$

where k_1 is the nonlinear rate constant for radical-radical interaction and is a function of time, and k_2 is the linear rate constant for radical-solute interaction and is independent of time. Even if one assumes that radical density is proportional to energy density at all times, one needs to know the time evolution of energy density function. But such an expression is not at present available, as can be seen from Equation 3.

The actual problem is much more complex even than Equation 8 would indicate; one should know the distribution of all free radicals produced, their rates of interaction with each other and with specific molecules within the cellular milieu. In a way it is actually surprising that the simplified model presented here appears to approximate the experimental results. Further experimental and theoretical work may shed some light on the problem of which are the more relevant free radical processes. It is a future goal to use results of radiation chemistry as elaborated by various groups (for example, Kupperman, et al. (17)(18)). Future experiments with radiation chemistry using the fast heavy-ion beams are also planned.

Thus to arrive at a workable procedure for Phase 1 of our model, we have considered an average time, $\langle t \rangle = 10^{-9}$ seconds, which seems reasonable in terms of radiation chemistry. Thus Equation 7 now takes on the following aspect:

$$\nu = 2\pi\kappa \int^{r_{max}(\langle t \rangle)} \rho^2(Z, v, r)\, 2r dr\, (\Delta\chi)^2 . \qquad (7')$$

Now one has to consider the temporal evolution of the sizes of track core and penumbra. This can be expressed as:

$$r^2(t) = r_0^2\,(t = 10^{-15}) + 4Dt \qquad (9)$$

where D is the diffusion constant and is taken as 2×10^{-5} cm^2/sec, and r_0 is the size at $t = 10^{-15}$ sec.

Equation 9 describes the sizes of the core or penumbra at any time, and Figure 1 represents the various dimensions of the core at different times. As can be seen in Equation 5, the size of core is also velocity-dependent. Time dependence, however, tends to smooth out this dependency, as shown in Figure 1. Due to the phenomenon of track volume expansion, at an average

time, $\langle t \rangle$, energy density function can be expressed as:

$$\rho(r) = \left(\frac{r_0^2}{r^2 + 4D\langle t \rangle}\right) \rho_0 (Z, v, r_0) \tag{10}$$

where ρ_0 is the energy density at $t \simeq 10^{-15}$ seconds.

The above-mentioned considerations and simplifications lead us to the following equations which represent contributions by the core and penumbra with respect to Equation 7'.

$$\nu = \nu_{core} + \nu_{penumbra}$$

$$\kappa(\Delta\chi)^2 \left[\frac{\epsilon^2}{4\pi\beta^2} \frac{1}{r_{min}^2 + 4D\langle t \rangle} + \frac{\epsilon^2}{4\pi\beta^2} \frac{1}{r_{min}^2 + 8D\langle t \rangle}\right] \tag{11}$$

where $\beta = \ln(\sqrt{e}\, r_{max}/r_{min})$, r_{max} and r_{min} are given by Equations 4 and 5, respectively.

In order to calculate $\kappa(\Delta\chi)^2$ we followed an empirical procedure. We used as a reference point, an energy already determined, i.e., the appropriate constant of Equation 1, or 6.6 MeV/nucleon. We now introduce a new parameter as follows:

$$K = \frac{\delta(E)}{\delta_0}$$

where

$$\delta_0 = \frac{\epsilon^2}{4\pi\beta^2} \left[\frac{1}{(r_{min}^2 + 4D\langle t \rangle)} + \frac{1}{(r_{min}^2 + 8D\langle t \rangle)}\right]$$

is evaluated at $E_0 = 6.6$ MeV/nucleon, and $\delta(E)$ is that evaluated at any other energy, E. Every other constant in the co-operative terms of Equation 1, namely the reversible term, depends linearly on ϵ. Analysis shows that the cooperative effects occur at intervals on the order of 10^{-9} seconds long, whereas, at densities of ordinary chemical modifiers such as oxygen, these effects may take place in about 10^{-6} or 10^{-7} seconds. In the first term of Equation 1, it was also assumed that the number of free radicals participating is propor-

tional to $\alpha\epsilon$, where α is a constant. Actually, the number of free radicals available is less than the total number produced initially: some radicals are lost in co-operative interactions. A correction coefficient is needed for each energy, which can be evaluated from the total number of free radicals and free radicals consumed in co-operative interaction. Taking all these into consideration, we arrive at a new velocity-dependent formulation for cross-section which is given as:

$$\sigma_i = \sigma_{i\infty} \left[1 - \exp\left(-p\alpha_0 (1-K')\,\epsilon - q\delta_0 K \epsilon^2\right)\right] \qquad (1'')$$

where K' and K are dependent on energy of the particle.

In actual practice we have replaced $(1-K')$ by $\frac{1-KK_0}{K_0}$, where K_0 is another correction term that relates to free radicals in the penumbra of 6.6 MeV/nucleon in a similar way that K relates to a correction for the higher energy E and the reference energy of 6.6 MeV/nucleon.

In Figure 2 variation of K with energy has been plotted. It should be noted that, for an oxygen beam of 0 - 260 MeV/nucleon, the value of K decreases from 1.0 at 6.6 MeV/nucleon to about 0.5 at 209 MeV/nucleon. Thus a 209 MeV/n oxygen beam seems to behave, as far as co-operative effects are concerned, like a 6.6 MeV/n beam of about half the LET of the oxygen beam.

Results.

Using the various procedures outlined above, as well as some necessary assumptions, survival curves were calculated at oxic and anoxic conditions of T-1 human kidney cell systems. In the calculations, we have used $D = 2\times10^{-5}\ cm^2 sec^{-1}$, with $\langle t \rangle = 10^{-9}$ seconds. Various constants in the formula for cross-section were analyzed using 6.6 MeV/nucleon as the reference point.

In Figure 3, the curve shows how $\frac{1-KK_0}{K_0}$ changes with energy. The coefficient in Figure 3 shows that the free radicals available for the "reversible" component comprise about half of all free radicals produced by the particles at 6.6 MeV/nucleon. The coefficient is a measure of the availability of free radicals initially produced in the track for reversible action. This coefficient increases with the kinetic energy per nucleon.

In Figure 4, the curves show calculated RBE values at different depths of water for a 260-MeV/nucleon oxygen beam with a 10-cm. range. Results have been obtained from the present model, both in nitrogen and oxygen atmospheres.

In Figure 5, dose vs. surviving fractions have been plotted for a T-1 human kidney cell system irradiated with an oxygen beam of 260 MeV/nucleon energy. In order to compare OER values at two different residual ranges (R = 7.0 cm. and R = 0.6 cm.), surviving fractions are given in both nitrogen and oxygen atmospheres.

In order to provide a comparison with experiments carried out, OER values have been calculated for an oxygen beam irradiating a T-1 human kidney cell system. These values are shown in Figure 6. There is reasonable agreement between the OER values obtained experimentally and those calculated on the basis of the present model.

Acknowledgments.

The research described here is supported by the AEC and NASA.

REFERENCES

1. Tobias, C.A. and Todd, P.W. Heavy charged particles in cancer therapy, in: Radiobiology and Radiotherapy, U.S. National Cancer Inst. Monograph No. 24, Bethesda, NCI (1967), p. 1-21.
2. Todd, P.W. Reversible and Irreversible Effects of Ionizing Radiations on the Reproductive Integrity of Mammalian Cells Cultured in Vitro, (Ph.D. Thesis), University of California, Berkeley (1964).
3. Powers, E.L., Lyman, J.T. and Tobias, C.A., Int. J. Radiat. Biol. 14:4, 313-330 (1969).
4. Fluke, D.J., Brustad, T. and Birge, A.C., Radiat. Res. 13, 788-808 (1960).
5. Tobias, C.A. and Todd, P.W., Analysis of the effects of high-LET radiations on various strains of cells, in: Biological Effects of Neutron and Proton Irradiations, International Atomic Energy Agency, Vienna, Vol. 2, (1964), p. 410-418.
6. Kondo, S. Fundamental Aspects of Relative Biological Effectiveness, Proceedings of the Japanese Radioisotope Conference (5th), Tokyo, Japan (1963).
7. Tobias, C.A. and Manney, T.R., Ann., NY Acad. of Sci. 114, 16 (1964).
8. Barendsen, G. W., Walter, M.D.M., Fowler, J.F. and Bewley, D.K., Radiat. Res. 18, 106 (1963).
9. Curtis, S.B., The effect of track structure on OER at high LET, in: Charged Particle Tracks in Liquids and Solids, The Institute of Physics and the Physical Society (Eng.), Conf. Series No.8 (1970), p. 140-142.
10. Neary, G. J., Int. J. Radiat. Biol. 9, 477-502 (1965).
11. Katz, R., et al., Radiat. Res. 47, 402-425 (1971).
12. Kellerer, A.M. and Rossi, H.H., Current Topics in Radiation Research Quarterly 8, 85-158 (1972).
13. Roisman, R. et al., Cell Survival as a Function of Depth for a 220-MeV/Nucleon Oxygen-Ion Beam (to be presented at 21st Radiation Research Society Meeting, April, 1973).
14. Chatterjee, A., Maccabee, H. and Tobias, C.A., Radial Cut-off LET and Radial Cut-off Dose Calculations for Heavy Charged Particles in Water, Radiat. Res. 54, 479 (1973).

15. Luntz, M., Phys. Rev. B. 4, 2857-2868 (1972).

16. Luntz, M. (private communication).

17. Kuppeman, A. in: Radiation Research (G. Silini, ed.) North-Holland Publ., Amsterdam, 1967; see also: Kuppeman, A., Radiat. Res. Suppl. 4, 69 (1964).

18. Kuppeman, A. and Belford, G. G., J. Chem. Phys. 36, 1412 (1962).

FIGURE CAPTIONS

Fig. 1. At $\langle t \rangle = 10^{-15}$, the size of the core varies a great deal with velocity. However, because of core diffusion, the extent of variation is reduced.

Fig. 2. Variation in the values of K with energy of the particle. Effect of change in the values of $4D\zeta$ is also shown. K = 1 at E = 6.6 MeV/nucleon.

Fig. 3. Availability of free radicals for the "reversible" component comprising about half of all free radicals produced by the particles at 6.6 MeV/nucleon. The coefficient $(1 - KK_0)/K_0$ is a measure of the availability of free radicals initially produced in the track for reversible reaction.

Fig. 4. The curves show calculated values of RBE at different depths of water for a 260 MeV/nucleon oxygen beam with a 10-cm. range. Results are plotted both in nitrogen and oxygen atmospheres.

Fig. 5. Plot shows dose vs. surviving fractions for T-1 human kidney cell system irradiated with a 260 MeV/nucleon oxygen beam. In order to compare OER values at two different residual ranges (R = 7.0 cm. and R = 0.6 cm., respectively), surviving fractions are given for both nitrogen and oxygen atmospheres.

Fig. 6. Estimation of OER values for T-1 human kidney cell system irradiated with oxygen beam. There is a reasonable agreement between the exponential values and calculated values.

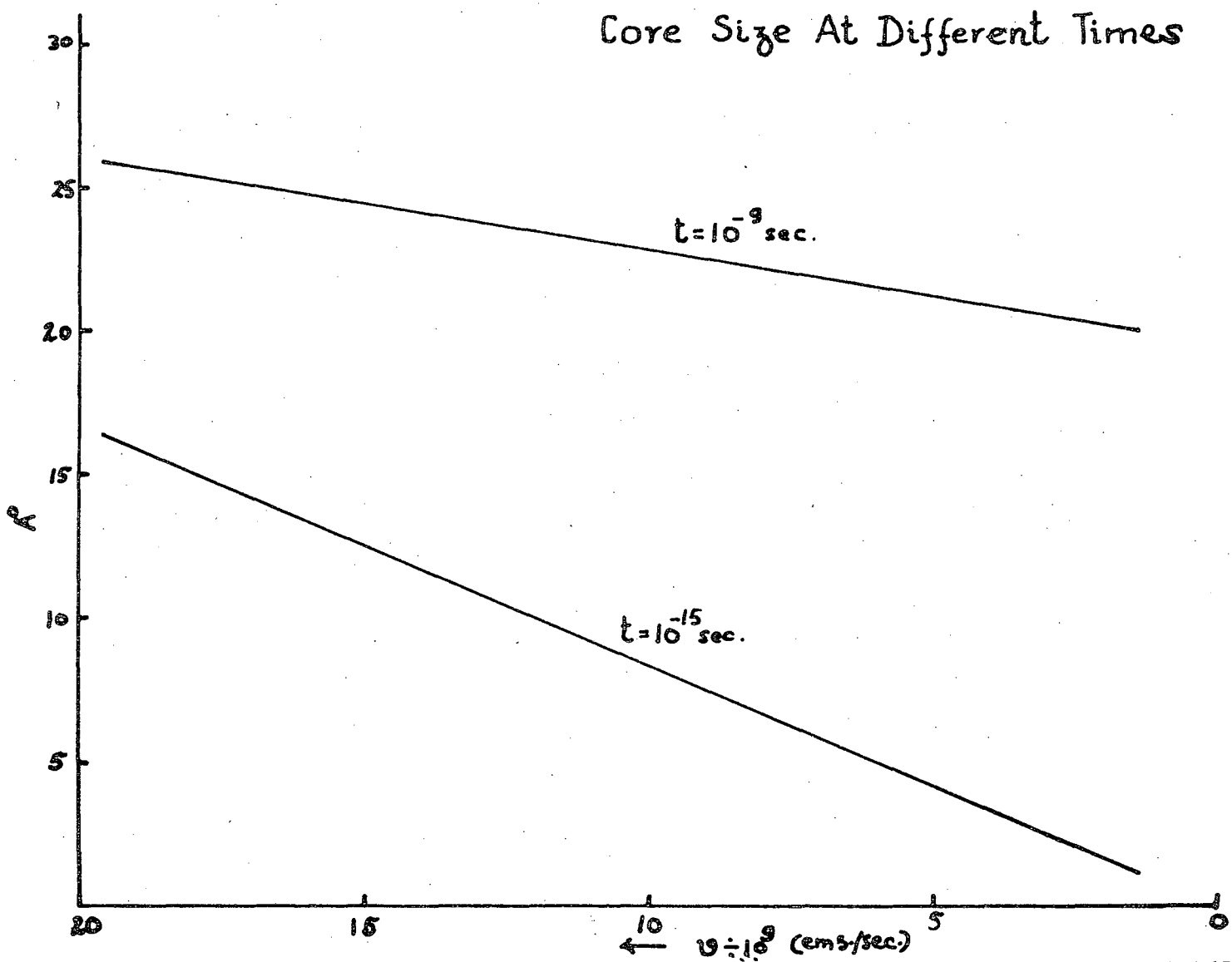

XBL 735-565

Figure 1

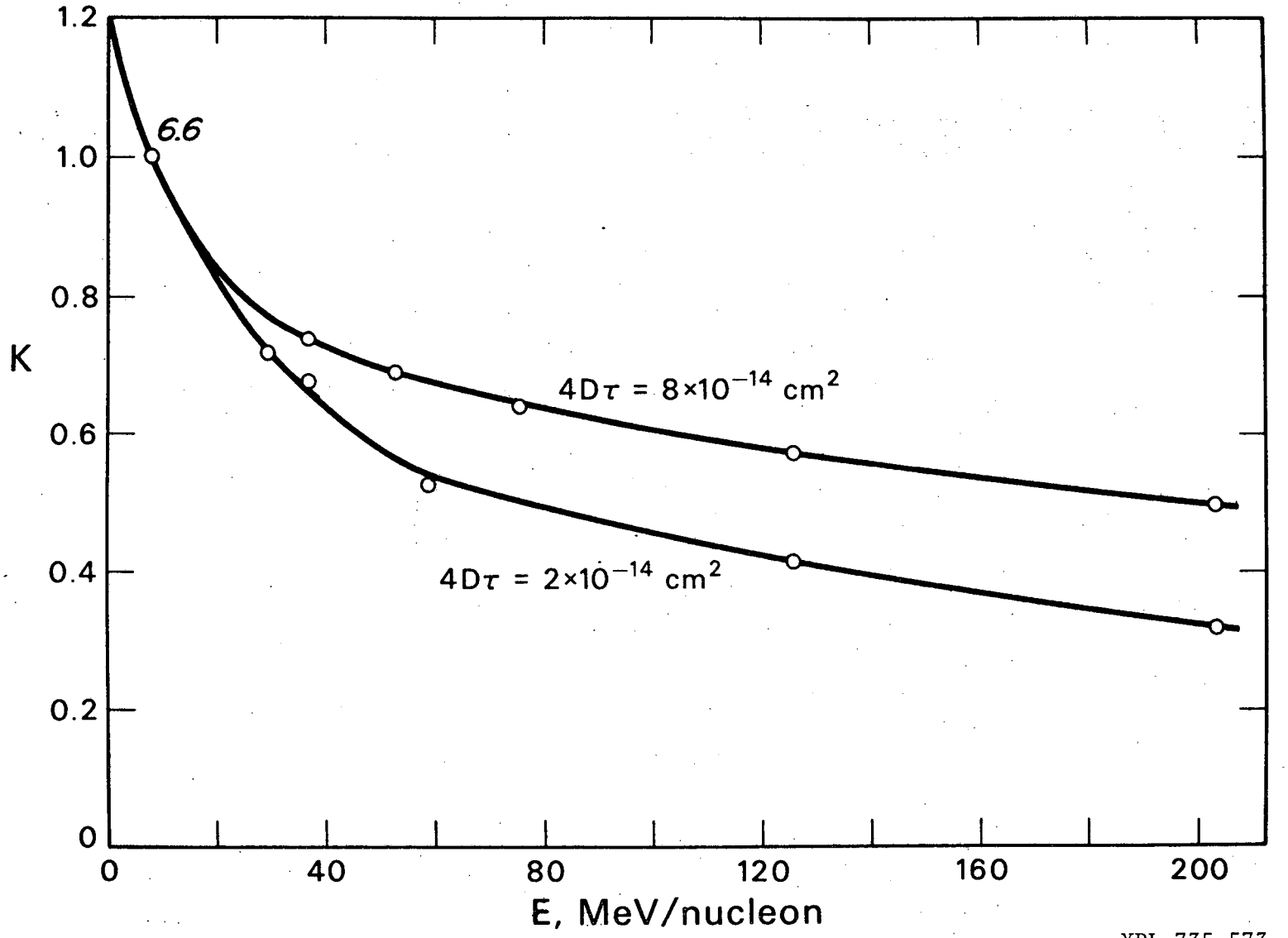

XBL 735-573

Figure 2

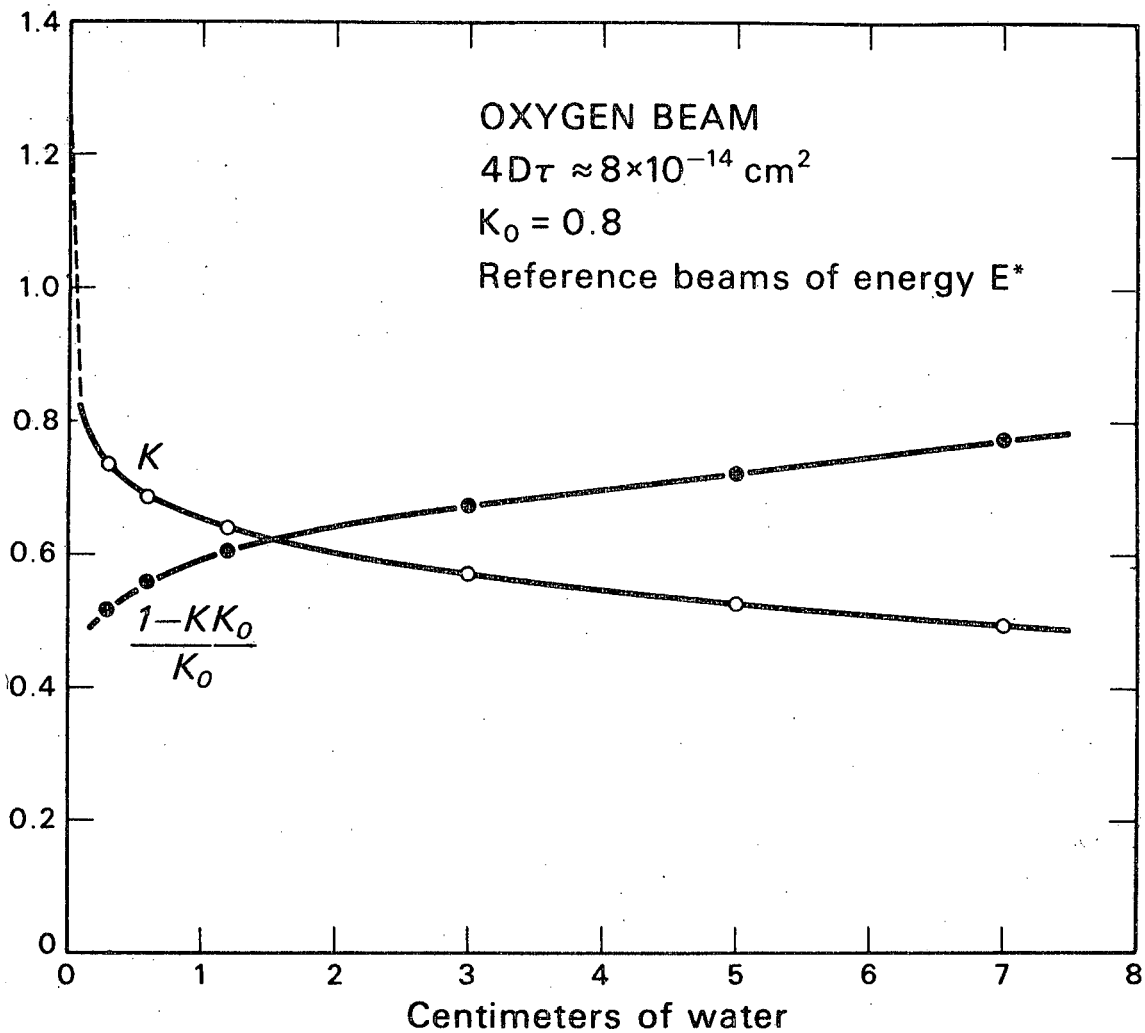

XBL 735-561

Figure 3

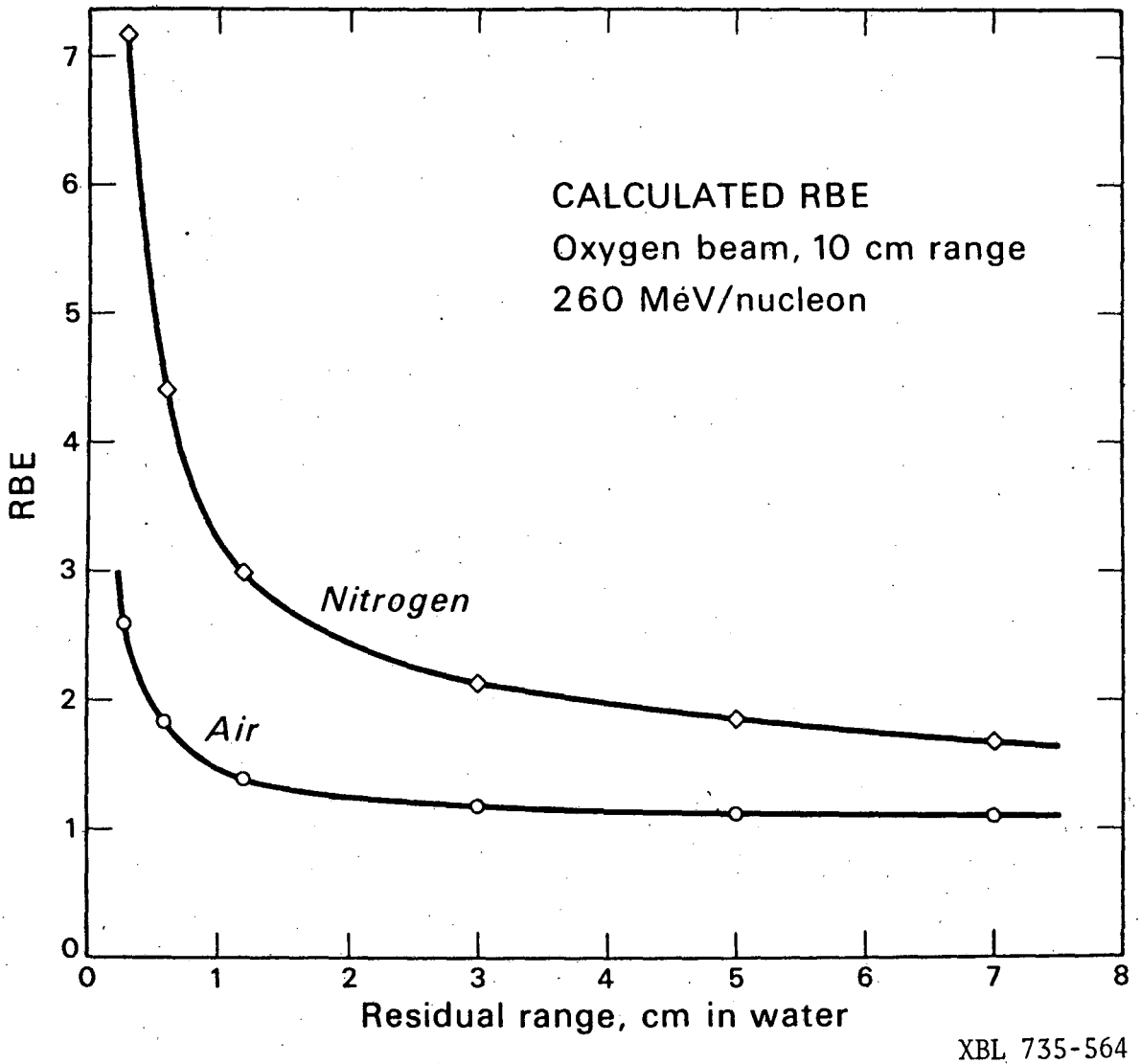
CALCULATED RBE
Oxygen beam, 10 cm range
260 MeV/nucleon
Nitrogen
Air
RBE
Residual range, cm in water
0
1
2
3
4
5
6
7
8
XBL 735-564

Figure 4

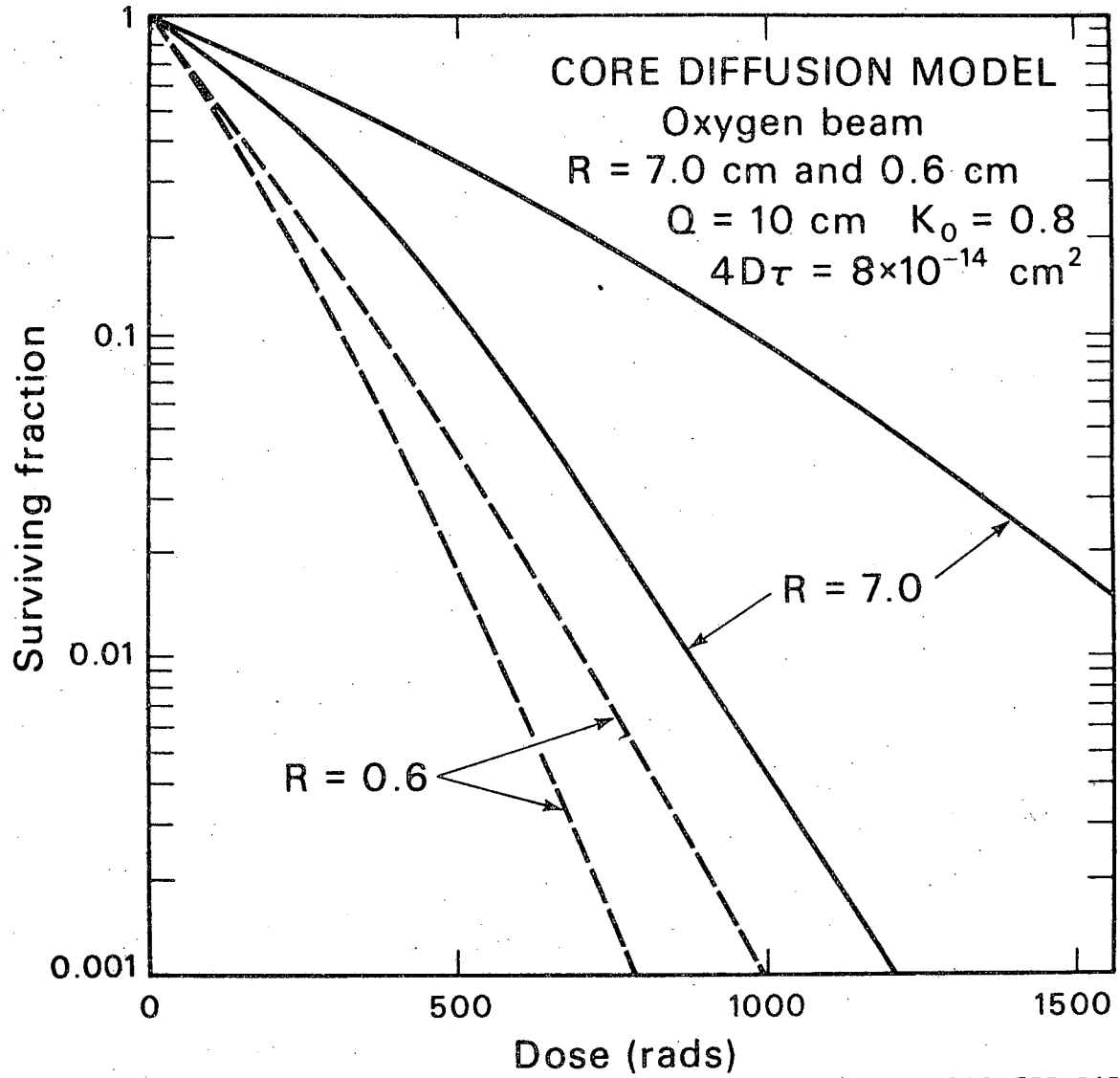

XBL 735-563

Figure 5

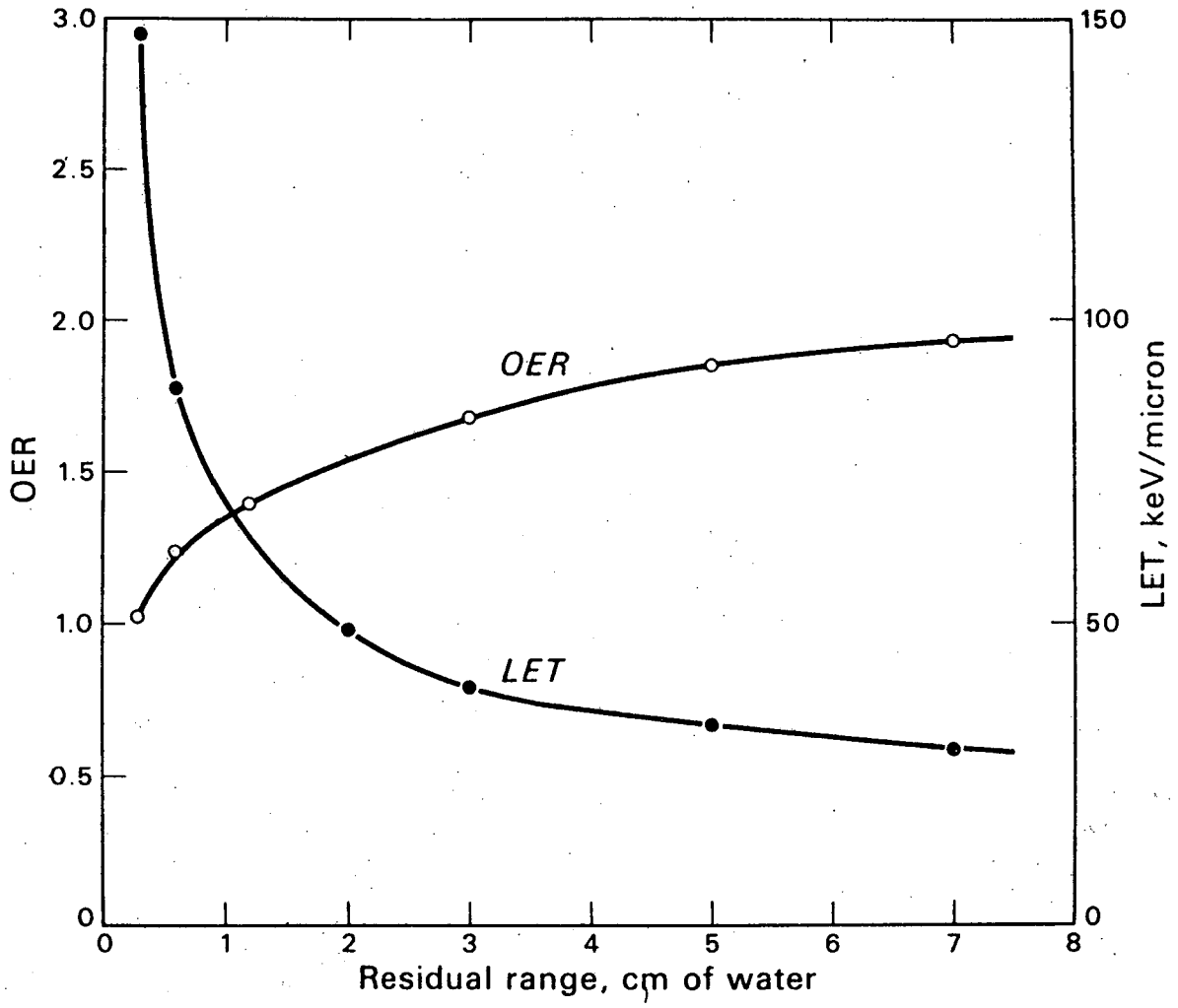

XBL 735-562

Figure 6

0 0 0 0 4 0 0 1 5 2 5

CELL SURVIVAL AS A FUNCTION OF DEPTH FOR A 220-MeV/NUCLEON OXYGEN-ION BEAM

Robert Roisman, Bambino I. Martins, Dionysios Kalofonos, and Cornelius A. Tobias

Donner Laboratory—Lawrence Berkeley Laboratory
University of California, Berkeley, Ca. 94720

Abstract.

T-1 human kidney cells were exposed to a 226-MeV/nucleon oxygen-ion beam in a tissue-equivalent exposure phantom, in order to study fractional survival as a function of depth in growth media. Cells were exposed under aerobic and anaerobic conditions, which were obtained by bubbling air or nitrogen, respectively, through the growth media in the phantom. Phantoms were exposed to unmodified beams, as well as beams in which the Bragg peak had been broadened by use of a ridge filter. Fractional survival as a function of depth and oxygen enhancement ratios for the beams indicate their potential for tumor therapy.

Ideally, in the therapy of cancer with radiation, one would like to do maximum destruction to the tumor while at the same time sparing from harm the normal healthy tissues of the body. Because of their favorable depth-dose distribution and low oxygen enhancement ratio, heavy ions such as nitrogen, oxygen and neon seem to have promise for minimizing healthy tissue destruction during radiation therapy. We are interested in this problem and have made use of the high-energy, heavy-ion beams available at the Berkeley Bevatron to study the survival of cells as a function of depth in tissue after exposure to heavy-ion radiation. To do this we have built a phantom as a model for tumor therapy in which we have exposed cultured human kidney cells.

Figure 1 shows the Bragg curve for an oxygen-ion beam. The relative dose is low at the entrance, or plateau, and rises sharply in the region of the Bragg peak. This kind of distribution should have benefits for radiation therapy. Considering a deep-seated tumor, we would expect that such a beam would do a relatively small amount of tissue destruction at the skin, or plateau region, and a relatively large amount of destruction at the tumor or peak region. In order to determine whether or not this actually occurs with real cells, we would want to have an experimental system with the following characteristics.

We would want the system, or phantom, to absorb the radiation as tissue would absorb it. We would want to be able to change the milieu in the phantom with respect to media, oxygen tension, and temperature, with precision. We would want the system to provide a milieu for the cells which is not too different from their natural condition.

Recently some articles have been written about the leaking of oxygen by plastics (1). Because of the possibility that plastics might leak and thus prevent the attainment of anaerobic conditions, we would want our phantom to be made without plastics. Also, much work has been reported where cells have been exposed on a glass or plastic dish at the interface between air and the surface of the dish (2, 3). We feel this is not physiological enough, and we would want a system which more closely represents the situation in tissue.

With these ideas in mind we have built the phantom which can be seen in Fig. 2. The phantom is made from a 25-cm. length of 70 mm standard wall borosilicate tubing. One end of the pipe is sealed off with a glass sheet of uniform thickness which acts as an entrance window for the beam. The other end

is closed with a removable glass cap which contains a gas inlet and outlet, a scintered glass bubbler, and a temperature probe. The cells, which are plated on thin glass coverslips, are held in line with the beam by a removable glass rack which locks into position in the phantom. The phantom is filled with nutrient media through which is bubbled either air or nitrogen to control the degree of oxygenation.

Others have made systems for measuring the same phenomena. For example, Paul Todd made a plastic device in which he used a high concentration of radiation-killed cells to consume dissolved oxygen and thus obtain anaerobic conditions. We feel that, at this stage of knowledge, a method such as this could introduce spurious factors, the results of which would be difficult to determine. The radiation-killed cells could result in the release of enzymes, nucleic acids, and other factors, which might influence the normal behavior of cells. Also Sutherland (4) has reported a method of exposing cell spheroids in suspension cultures, and Burki (5) has related work in which he exposed cell spheroids in agar. We feel that in these methods it would be difficult to control accurately the oxygen concentration that the cells would be exposed to.

For our experiments we used a line of T-1 human kidney cells originally obtained from G. Barendsen and group* and cultured in our laboratory for the past ten years. We have chosen to work with these cells because much work has already been done with them, by Todd (2) with low-energy heavy ions, by Barendsen (6) with helium ions, and also by Bird (7) using synchronous cell populations.

Our procedure for exposure was the following: twenty-four hours prior to exposure, cells from an 18-hr. log phase culture were plated onto 25-mm-diameter round glass coverslips. Each coverslip received a 0.2 ml aliquot of suspension containing 70,000 cells; the cells were deposited with a 1-ml pipette so that they uniformly covered a 1-cm. circle in the center of the coverslip. This plating of the cells into a small circle was necessary due to the small diameter uniform beam presently available at the Bevatron. After plating, the cells were allowed to incubate at 37° for four hours to allow them to attach to the glass, and then additional nutrients media was added to the cells.

---

*Rijswijk Institute TNO, The Netherlands.

One hour prior to exposure the coverslips were removed from the incubator and placed in the glass rack of the phantom. Loading of the rack took about five minutes, and, during this time, in order to prevent drying out of the cells, one of us dripped media onto the coverslips with a pipette while the other continued with the loading. After the loading the rack was slid into the phantom, which was then filled with media, and the cap of the phantom was sealed in place with silicone grease and a bakelite clamp. Gas was then bubbled through the media at a rate of 400 cc/minute for 45 minutes, and then throughout the exposure time, which lasted between ten to thirty minutes.

Figure 3 shows the exposure setup in the biomedical cave at the Bevatron. The beam enters from the left, passes through alignment scintillators, a monitoring ionization chamber, a variable thickness water absorber, a 3-cm. ionization chamber, a 1-cm. ionization chamber, and, finally, into the phantom.

After the exposure the coverslips were removed and treated with versene (Microbiological Associates, concentration-1:5000) for five minutes and broken into single cells. The cells were counted on a coulter counter, diluted, and plated into 35-mm. or 60-mm. plastic petri dishes to give, respectively, 200 or 600 clonogenic cells per dish. Each exposed phantom contained 15 to 18 coverslips, and each control phantom contained four coverslips. For each coverslip, 10 dishes of clonogenic cells were plated out to assure reliable statistics. The cells were then allowed to incubate at 37° for 12 days and then were stained with 1% methylente blue. Visible colonies were counted and fractional survival was determined. Throughout the experiment the cells were grown and kept in Minimum Essential Media (Microbiological Associates) supplemented with 12% fetal calf serum (Grand Island) plus 1-glutamine and penicillin/streptomycin.

Because the physics of the heavy-ion beam is still being studied, our dose determinations are not absolutely accurate. We have, however, made special attempts to keep the beam exposing the cells as uniform as possible. The beam profile has been measured by quantitative photodensitometry. J. Lyman and J. Howard (8, 9, 10) of our laboratory have determined by this method that the dose received by the cells varies by less than 20%. We are aware of the problems associated with this method, but these results on the

beam profile were confirmed with a pair of ionization chambers, as well as by particle track analysis using etched plastic sheets. This last method, developed by E. Benton (11), tells us the flux of particles that the cells received, and is not sensitive to X rays. We plan to use this method of dosimetry more fully in the future.

Results and discussion.

As a control for the heavy-ion experiment we exposed cells in the phantom to Cobalt-60 gamma rays. Figure 4 shows the results of this experiment, as well as the ionization curve for Cobalt-60 gamma rays. The dose at the entrance of the phantom was 850 rads. For gamma rays, the depth-dose distribution is such that the dose is highest at the entrance and falls off exponentially with depth. Thus we would expect lowest survival at the entrance and steadily increasing survival with depth. The results in Fig. 4 are consistent with this. Due to OER effect, survival for the anaerobic cells is considerably higher than for the aerobic ones. For the aerobic exposure, survival at the entrance is about 10% and rises to about 80% at 15-cm. depth. For the anaerobic exposure, survival at the entrance is about 50% and rises to about 90% at 15-cm. depth.

Figure 5 shows the results of exposure of anaerobic and aerobic phantoms to 170 rads of 220-MeV/nucleon oxygen ions. Above the survival curves is plotted a Bragg ionization curve for the oxygen ions. Cell survival is high in the region of the plateau, but falls off sharply to a low value in the region of the peak. Also, survival is about 100%, a small distance beyond the peak. In addition, in the plateau region, the aerobic and anaerobic curves are clearly separated due to the OER effect, but, in the peak region, the two curves merge together, which is consistent with other data showing that the OER approaches 1 near the peak.

We call survival curves of the type in Fig. 5, "Bragg survival curves". Error bars on both curves indicate uncertainty in fractional survival. We have not plotted error bars for depth, that is, along the x-axis, though at our present state of ability for positioning the Bragg peak over the cells, there is some uncertainty as to the exact position of each sample.

During our most recent series of experiments at the Bevatron, we did our first cell survival experiments with a spread-out Bragg peak, using a

ridge filter developed by Dr. Lyman. The Bragg ionization curve for the modified oxygen beam can be seen in Figure 6, as well as a schematic of the filter which is made of copper. Dr. Lyman designed the filter so that, in the peak region, the dose would fall with increasing LET and thus the RBE would remain constant. Figure 6 shows aerobic and anaerobic Bragg survival curves for the modified beam. The two curves are separated in the region of the plateau and come closer together in the region of the peak. Again survival after the peak is about 100%.

Initially it was our intention to calculate OER from these experiments as well as determine survival profiles. At this point we have not obtained good quantitative OER data from this method; we would need many more curves at a number of different dose levels to do this. But the OER that we have observed by this method is not in disagreement with OER we have obtained by other methods. These other methods indicate an OER of 1.6-1.9 at the plateau and 1.25 in the peak region. These survival profiles and OER measurements indicate the potential of heavy ions for radiotherapy.

In the future we plan to continue these experiments in several ways. We believe that the state of cell division is an important variable which needs to be controlled, and so we plan to determine survival profiles for synchronized cells. Also we wish to study repair with this device under aerobic and anaerobic conditions (12, 13). In addition we wish to determine Bragg survival curves for various cell lines including tumor cells.

Our results indicate that the device is a good tool for rapid evaluation of cellular response in radiobiology.

Acknowledgments.

We wish to thank Dr. J. Lyman for the dosimetry for these experiments, and for developing the ridge filter. Also we wish to acknowledge the help of D. Anderberg, P. Henrikson, and N. Davis for engineering and building the exposure phantom, as well as the help of P. Dowling and F. Upham for designing and building essential accessories. In addition we wish to thank the Bevatron crew for their generous help throughout the exposure periods.

Research described here is supported by the AEC and NASA.

REFERENCES

1. Boag, J.W. Oxygen diffusion and oxygen depletion problems in radiobiology, in: Current Topics in Radiation Research (M. Ebert and A. Howard, eds.), Vol. 5, North Holland, Amsterdam (1969), p. 143-195.
2. Todd, P.W., Radiat. Res. Suppl. 7, 196-206 (1967).
3. Martins, B., Roisman, R., Raju, M.R., and Tobias, C.A., Studies of the effects of an $N7^+$ ion beam on cultured human kidney cells in the presence of air and nitrogen, in: Initial Radiobiological Experiments with Accelerated Nitrogen Ions at the Bevatron, LBL-529 (1971), p. 81-92.
4. Sutherland, R.M., McCredie, J.A. and Inch, W.R., J., Nat'l. Cancer Inst. 46, 113 (1971).
5. Dalen, H. and Burki, H.J., Exptl. Cell Res. 65, 433-438 (1971).
6. Barendsen, G.W., Walter, H.D.M., Fowler, J.F., and Bewley, D.K., Radiat. Res. 18, 106-119 (1963).
7. Bird, R. and Burki, H.J., Sensitivity of Synchronized Chinese Hamster Cells to High-LET Radiation (presented at 20th Radiation Research Society Mtg., May, 1971).
8. Lyman, J. et al., Bragg Curve Measurements of the Oxygen-Ion Beam at the Bevatron (presented at American Physical Society, Ann'l. Mtg., April, 1972).
9. Lyman, J.T. et al., Experimental setup and physical measurements of heavy-ion beam for initial biological irradiations at the Bevatron in: Initial Radiobiological Experiments with Accelerated Nitrogen Ions at the Bevatron, LBL-529 (1971), p.1-19.
10. Tobias, C.A., et al., Science 174, 1131-1134 (1971).
11. Tobias, C.A. and Benton, E.V., Additional Techniques for Heavy-Ion Radiography and Laminography, UCID-3593 (1972).
12. Koch, C.J., Kruuv, J. and Frey, H.E., Radiat. Res. 53, 33 (1973).
13. Koch, C.J., Kruuv, J. and Frey, H.E., Radiat. Res. 53, 43 (1973).

FIGURE CAPTIONS

Fig. 1. Bragg curve for oxygen-ion beam. The relative dose is low on the plateau and rises sharply in the region of the peak. A short distance after the peak, the dose is found to be nearly equal to zero.

Fig. 2. Diagram of the exposure phantom. Cultured cells plated on glass coverslips are placed at various distances along the long axis of the phantom. The phantom is exposed so that the Bragg peak falls about midway in the phantom.

Fig. 3. The exposure setup in the biomedical cave at the Bevatron. The beam enters from the left, passes through various scintillators, ionization chambers and a variable-thickness water absorber before striking the phantom.

Fig. 4. An ionization profile for Cobalt-60 gamma-rays as well as results of the exposure of aerobic and anaerobic phantoms. Except for a buildup factor, the dose falls of exponentially with depth. For the survival curves, survival is lowest at the entrance and increases with depth.

Fig. 5. Bragg ionization curve and Bragg survival curves. Cell survival is high in the region of the plateau but falls off sharply to a low value in the region of the peak. Also, survival is about 100% at a small distance beyond the peak.

Fig. 6. Ridge filter Bragg ionization curve and Bragg survival curves. Survival is relatively high in the plateau region and falls off in the region of the peak but not as sharply as with the unmodified Bragg peak.

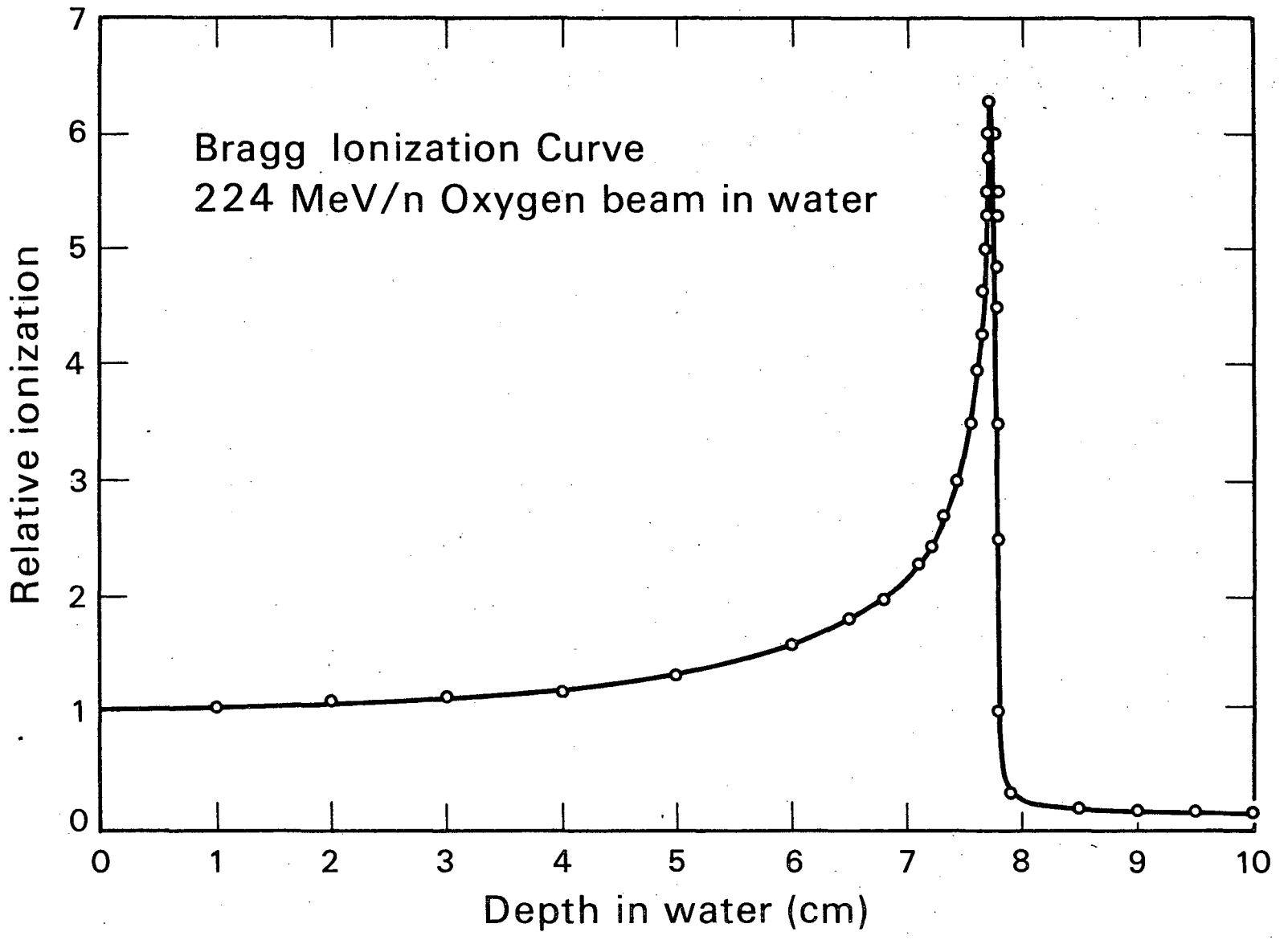

DBL 731-5035

Figure 1

0 0 0 0 1 0 0 1 2 9

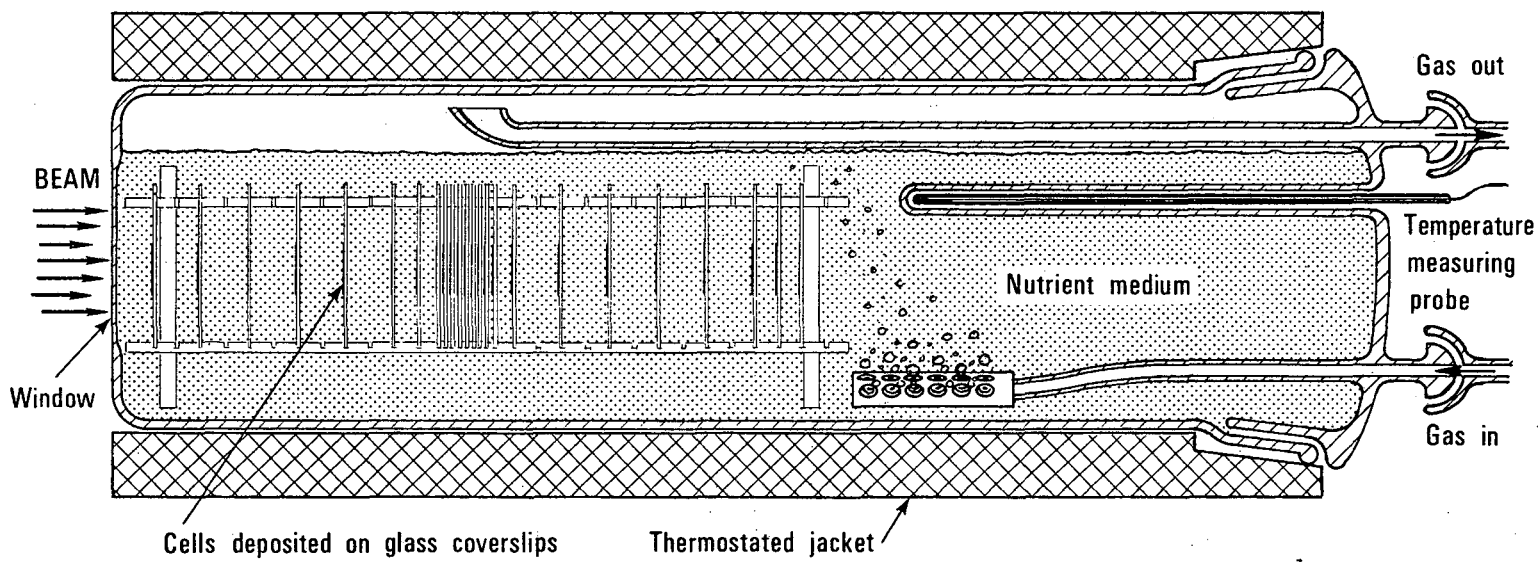

SUBMARINE CULTURE FOR PARTICLE BEAM RADIOBIOLOGY

DBL 7210-5502

Figure 2

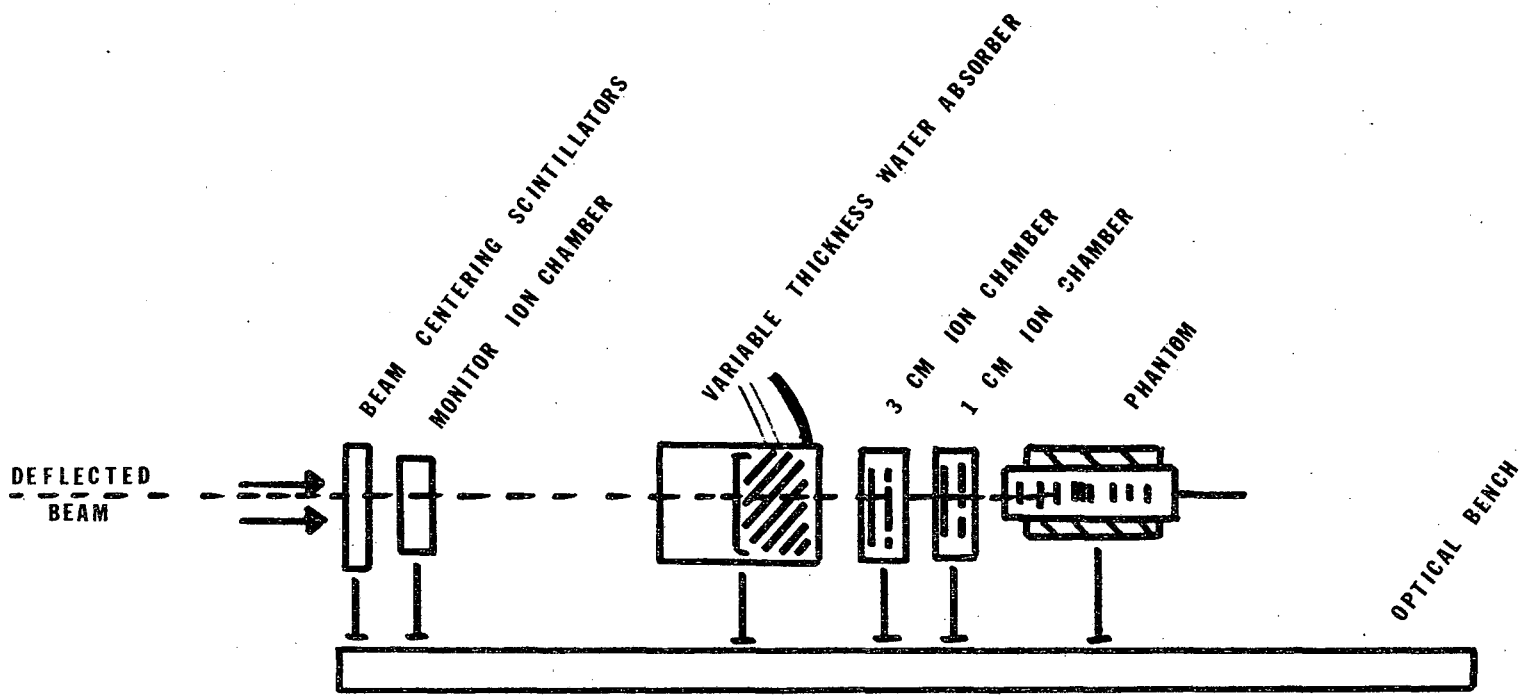

XBL 734-513

Figure 3

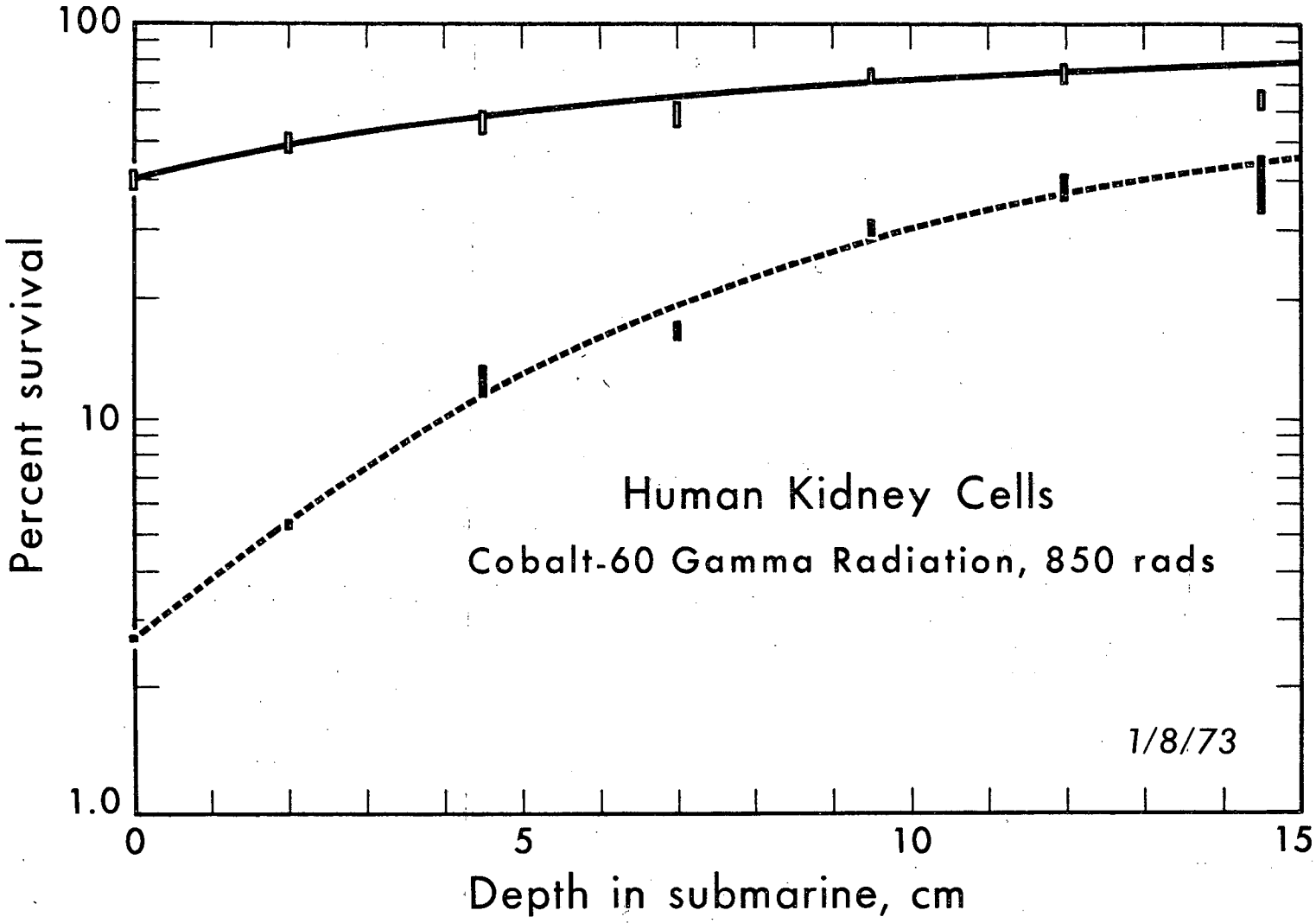

DBL 731-5040

Figure 4

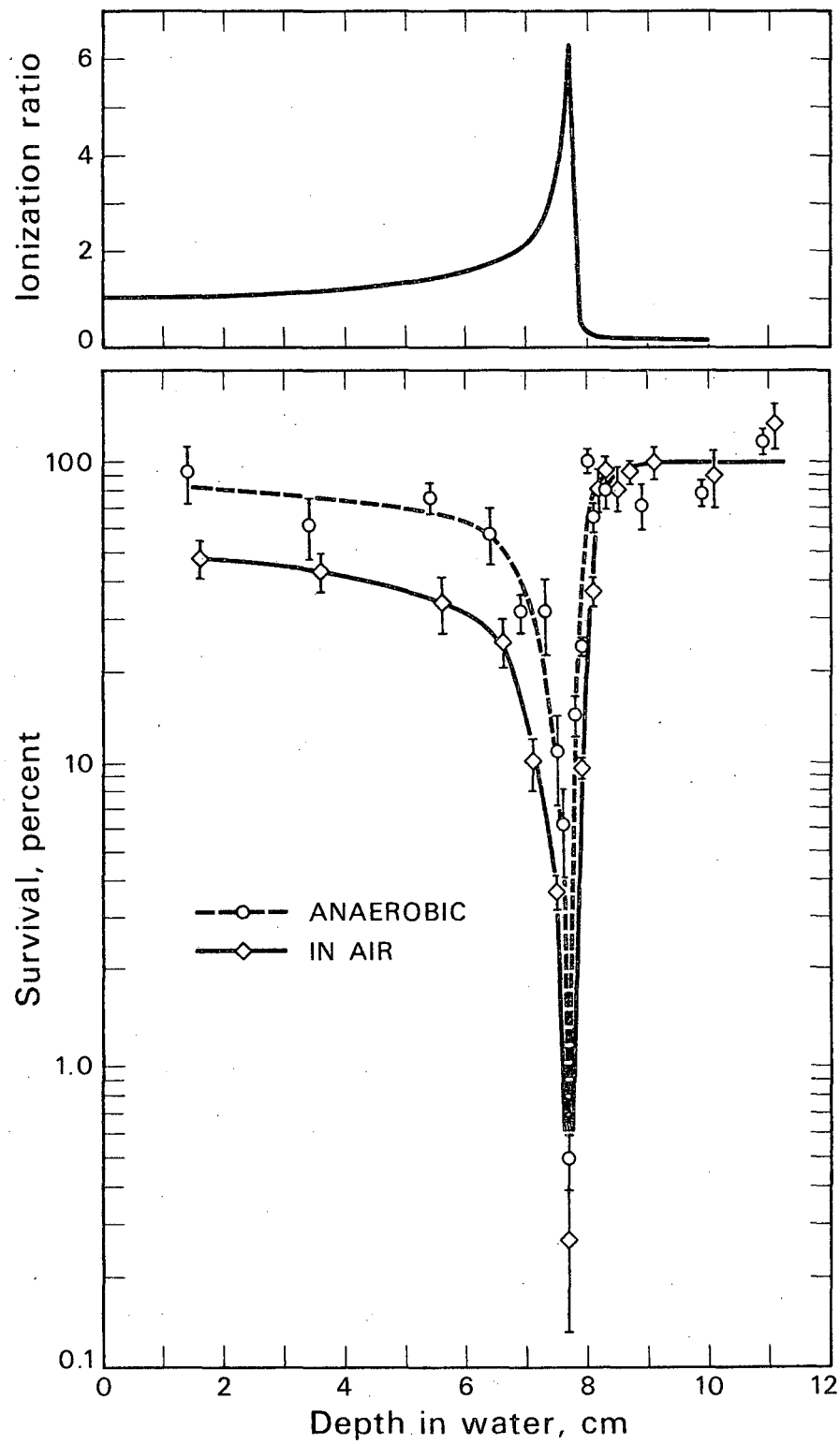

DBL 733-5080

Figure 5

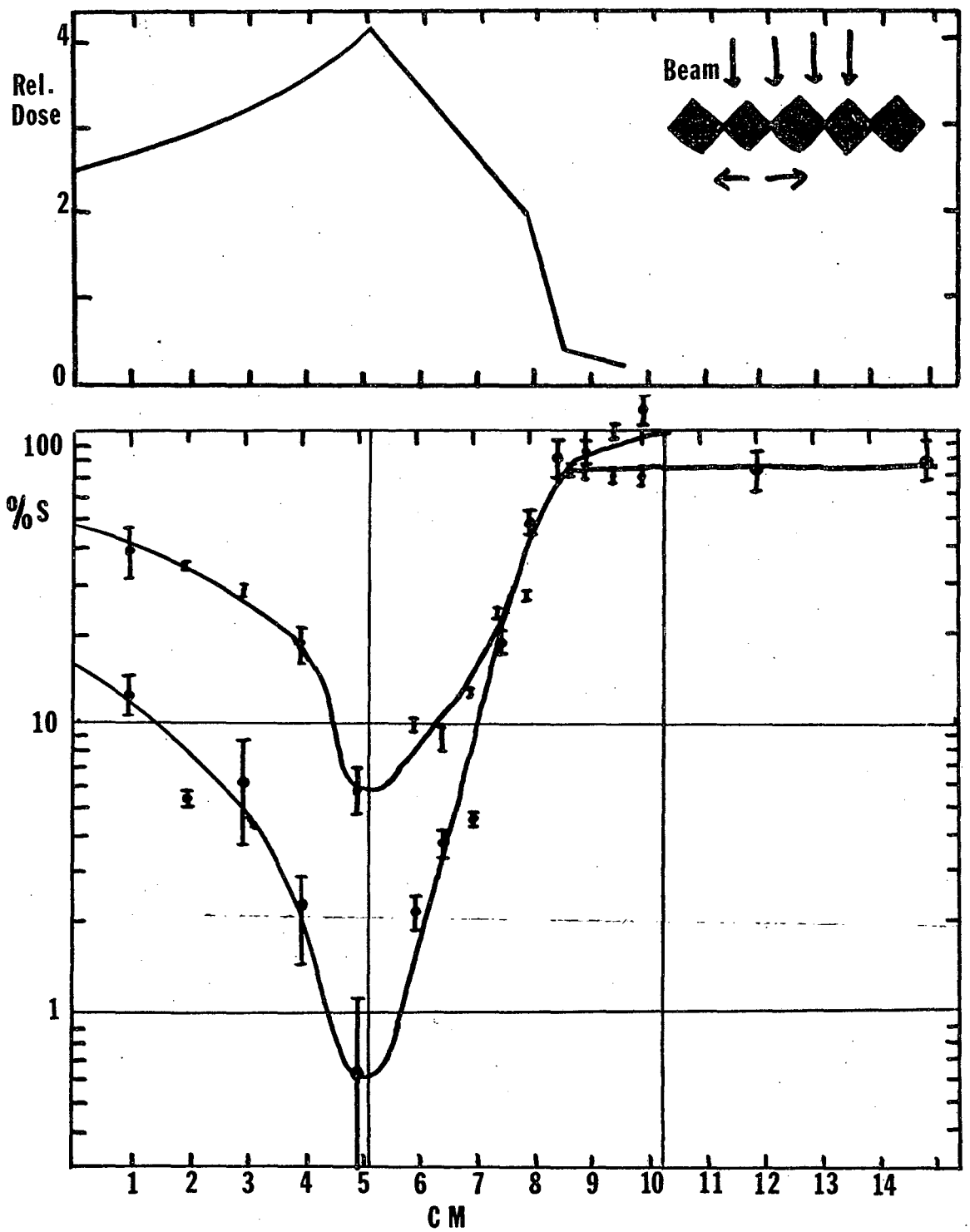

XBL 734-514

Figure 6

EFFECTS OF HEAVY-ION, HIGH-ENERGY PARTICLES UPON THE RETINAL VASCULATURE OF THE RHESUS MONKEY

Fred N. Beckman, David M. Hunter, and Charles H. Bonney
USAF School of Aerospace Medicine (AFSC)
Brooks Air Force Base, Texas 78235

Abstract.

The left eyes of five rhesus monkeys were exposed to a 250 MeV/nucleon oxygen (+8) beam with a total flux of 3.1×10^8 particles extracted from the Lawrence Radiation Laboratory Bevatron. Fundus photography and fluorescein angiography were performed serially following irradiation. Damage was seen within twenty-four hours. Changes included retinal hemorrhage, increased capillary permeability, ischemic necrosis of the retina, development of vascular shunts and neovascularization. Comparison is made with a series of eyes exposed to 3,000 rads of 200 kvp X-rays.

Introduction.

Although heavy-particle interaction with the retina to produce a visual response was hypothesized as early as 1952 (8), and the possibility of heavy particle damage to biologic subsystems consisting of highly differentiated non-regenerating tissues has been discussed in the literature (1, 2, 4), only recently has investigation of the biologic interaction of high-Z, high-energy particles in a laboratory environment been technically feasible (5).

The Radiobiology Division of the USAF School of Aerospace Medicine utilizing the heavy-ion accelerating capabilities of the Lawrence Radiation Laboratory Bevatron, has undertaken a series of experiments which attempt to demonstrate the effects of high-Z, high energy particles on nonregenerating tissues of the central nervous system, and especially the retina.

The retina of the rhesus monkey was chosen as a suitable model for this investigation because it is a highly organized lamellar structure, the vast majority of whose components are nonregenerating, and because it may be viewed and photographed directly in the intact animal. Further, two studies (7, 9) utilizing accelerated nitrogen (+7) have demonstrated susceptibility of the retina to heavy particle damage and thereby suggested that this might be a fruitful area of investigation.

Materials and Methods.

A total of 7 male and female adolescent Macaca mulatta monkeys weighing 3.5 to 5.5 kg were utilized during this series of experiments. Five were exposed to the 250 MeV/nucleon oxygen (+8) beam of the Bevatron with a total flux of 3.1×10^8 particles, while two monkeys were exposed to 200 kvp x-ray and acted as irradiated controls.

The Bevatron exposures were accomplished in the following manner: Immediately prior to exposure the animal selected was immobolized with 1 mg/kg Sernalyn; a venous catheter was placed in a saphenous vein, and an initial dose of Nembutal 25 mg/kg was administered. The anesthetized animal was then fixed in a David-Kopf visual stereotaxic apparatus which had been mounted on a cast-iron table moveable in three translation axes. The table in turn was bolted to a section of optical bench which duplicated the optical bench utilized in the high-Z beam exposure area. The optical axis of

a Zeiss fundus camera was then positioned in relation to that optical bench section such that the camera's axis aligned with the optical bench section exactly as the axis of the high-Z beam aligned with the optical bench in the exposure area. Thus, by viewing the monkey's retina through the fundus camera and by moving the cast iron table through its vertical and horizontal axes, it was possible to position the macular area of the retina in the beam path. The anterior-posterior distance from the surface of the eyelid to the anterior surface of the retina was measured to the nearest 0.5 mm by utilizing an A-Scan Echoline-20 ultrasound unit. The depth of a water column in the beam path was then set so that the previously calculated Bragg peak fell 0.5 mm behind the anterior retinal surface.

The Zeiss fundus camera had been previously modified with a Kodak 15 and 47 filter combination and a rapid sequence power pack to permit fluorescein angiography. Fundus photographs were taken using Kodachrome II 35 mm film processed in the usual manner, while fluorescein angiograms (3, 6) were taken following an I. V. dose of 10% sodium fluorescein (0.75 ml) at a nominal rate of one per second on Kodak Tri-X Pan film developed to 1600 A. S. A.

A series of fundus photos and fluorescein angiograms were taken immediately prior to exposure, immediately following exposure, at twenty-four hours, at one week, at two weeks and at five weeks.

An exactly analogous series of fundus photographs and fluorescein angiograms were taken on two animals exposed to 3,000 rads of 200 kvp X-rays with a half value layer of 1.0 mm copper. Dose rate for the X-ray animals was 65 rads/min. based on ion-chamber measurements in plastic and TLD measurements in an Alderson primate phantom.

Results.

Heavy-ion exposures.

Of the five animals which were exposed to a flux of 3.1×10^8 particles, three showed severe damage to the retina while two showed no retinal lesions whatever. During the first weeks following exposure, eye lid radiation effects (dry and moist desquamation, erythema and edema) were quite marked in the three monkeys that demonstrated retinal change while the two without retinal damage also evinced no eye lid change. However, one of these two did develop a lesion over the bridge of the nose which appeared to be secondary to radi-

ation and was of the same type as those appearing on the lids of the three animals that did demonstrate retinal lesions. Because of this marked hiatus in biologic effect (severe retinal damage vs. no damage whatever), and because of the placement of what appeared to be a radiation burn on the bridge of the nose of one monkey, it was concluded that, for the two monkeys that demonstrated no retinal lesions, the beam placement system failed.

Fluorescein angiograms taken immediately prior to and immediately following beam exposure demonstrate no fluorescein leakage in choroidal, arterial, arteriovenous or late venous phases. Fundus photographs taken immediately following beam exposure, however, do demonstrate a single small, flame hemorrhage in the peri macular area of one animal.

At twenty-four hours fluorescein angiograms demonstrate severe alteration of retinal vessel permeability. In the early arteriovenous phase, dye leaks appear in the capillary bed on both the arterial and venous sides of the circulation. These lesions are initially punctate and discrete, but as the angiogram progresses there is coalescence and increased concentration of dye in the more severely involved areas. In the late venous phase marked residual staining is apparent.

At one week large areas of ischemic infarction and edema with loss of retinal transparency are present. Flow through major vessels in the area of the infarction is either greatly slowed or blocked. Dye leakage occurs at the periphery of the infarction--which is now sharply demarcated from undamaged retina--and in the late venous phase fluorescein staining at the periphery persists.

At two weeks there is partial resolution of retinal edema and the smaller vessels in the area of the infarction reappear. Fine capillary detail, however, remains obliterated. Capillary permeability at the margin of the infarction is still greatly altered as evidenced by the continued presence of fluorescein stain in arteriovenous and late venous phases.

At six weeks there is further resolution of retinal edema and improvement in retinal transparency with concomitant improved visualization of the retinal vasculature. Noticeable in the early arterial phase are multiple small discrete punctate areas which do not fill with fluorescein. These changes probably represent retinal pigment epithelium damage and loss of pigment. Ischemic areas are still present, however, with zones of complete capillary absence. Later studies at eleven and sixteen weeks demonstrate the presence

of arteriovenous shunts around these zones and neovascularization.

X-ray exposures.

In sharp contrasts to the heavy-ion exposures, fluorescein angiograms and fundus photographs of X-ray-exposed eyes demonstrate no evidence of retinal vasculature pathology. There is no capillary permeability change, no loss of retinal transparency, no development of retinal ischemia, and no change in retinal pigment epithelium. There is, however, marked anterior segment damage, which at two weeks causes a clouding of the vitreous following an outflow of fluorescein dye from anterior uveal structures.

Discussion.

Retinal damage produced by heavy ions at 3.1×10^8 flux is quite severe and extends through the full thickness of the retina as evidenced by vessel obliteration, capillary permeability changes and pigment epithelial damage. In sharp contrast, 3,000 rads of X-rays at the retina appears to be well below threshold for vascular damage demonstrable with fluorescein angiograms and fundus photography. Even this gross qualitative comparison would seem to indicate that the heavy-ion beam evinces a predilection for retinal vasculature damage. Because the damage produced by the heavy-ion beam is initially in the form of small discrete foci of capillar disruption with a sharp margin of demarcation about the lesion periphery, it could then be argued that damage to the retinal vasculature occurs microscopically at discrete points as a highly localized, discontinuous process, and, as in diabetic and hypertensive retinopathy, nerve fiber and ganglion cell damage follows the initial vascular lesion.

Acknowledgments.

Research described here is supported by the AEC and NASA.

Certificate.

The animals involved in this study were maintained in accordance with the "Guide for Laboratory Animal Facilities and Care" as published by the National Academy of Sciences--National Research Council.

REFERENCES

1. Comstock, G.M., R. L. Fleischer, W.R. Giard, H.R. Hart, Jr., G.E. Nichols and P. B. Price. Cosmic ray tracks in plastics: The Apollo helmet dosimetry experiment. Science, 172: 154-157, 9 April 1971.
2. Haymaker, W.O., O.T. Bailey, E.V. Benton, F.S. Vogel, and W. Zeman. Brain study in balloon-borne monkeys exposed to cosmic rays. Aerospace Med. 41: 989-1002, 1970.
3. Justice, H.J., Jr. and R. J. Sever. Technique of fluorescein fundus photography, in: Neuropathalmology Symposium of the University of Miami and the Bascom Palmer Eve Institute. J. Lawton Smith ed., C.V. Mosby Co.; St. Louis, 1965, pp. 82.
4. Langham, W.H. (ed.) Radiobiological Factors in Manned Space Flight. Report of the Space Radiation Study Panel of the Life Sciences Committee, Space Science Board, National Academy of Sciences National Research Council. Washington D.C., 1967.
5. Lyman, J.T., J. Howard, H.D. Maccabbee, M.R. Raju, J. Sperinde, R. Walton, G.P. Welch, and C.A. Tobias. Experimental set-up and physical measurements of a heavy ion beam for initial biological irradiations at the Bevatron. In: Initial Radiobiological Experiments with Accelerated Nitrogen Ions at the Bevatron. LBL-529, Technical Information Division, Lawrence Berkeley Laboratory, University of California, December 1971.
6. Pettit, Thomas H. Special tests in the evaluation of retinal disease. In: Retinal Diseases Symposium of Differential Diagnostic Problems of Posterior Uveitis. Samuel J. Kumira and Wayne M. Caygill eds., Lea and Febiger; Philadelphia, 1966, pp. 109-112.
7. Philpott, D.E., R. Corbett, S. Black, and C. Turnbill. Ultrastructural investigation of the "light flash" phenomenon seen by our astronauts. 30th Ann. Proc. Electron Microscopy Soc. Amer., Los Angeles, Calif. 1972, C. J. Arceneaux (ed).

8. Tobias, C.A. Radiation Hazards in high altitude aviation. Journal of Aviation Med., 23, 345 (1952).

9. Zeevi, Y. Y., C.A. Tobias, and E.R. Lewis. Initial studies on vertebrate retinal interaction with the nitrogen beam. In: Initial Radiobiological Experiments with Accelerated Nitrogen Ions at the Bevatron. LBL-529, Technical Information Division, Lawrence Berkeley Laboratory, University of California, December 1971.

FIGURE CAPTIONS

Fig. 1. Animal 959. Heavy-ion exposure. Fluorescein angiography of left eye (from left to right and top to bottom) immediately prior to exposure, immediately following exposure, at twenty-four hours, at one week, at two weeks and at five weeks.

Fig. 2. Animal 959. Heavy-ion exposure. Fundus photography of left eye (from left to right and top to bottom) immediately prior to exposure, immediately following exposure, at twenty-four hours, at one week, at two weeks and at five weeks.

Fig. 3. Animal 989. X-ray exposure. Fluorescein angiography of left eye (from left to right and top to bottom) immediately prior to exposure, immediately following exposure, at twenty-four hours and at two weeks. Bottom photograph: Animal 886. X-ray exposure. Fluorescein angiography of right eye at five weeks.

Fig. 4. Animal 989. X-ray exposure. Fundus photography of left eye (from left to right and top to bottom) immediately prior to exposure, immediately following exposure, at twenty-four hours and at two weeks. Bottom photograph: Animal 886. X-ray exposure. Fundus photography of right eye at five weeks.

0 0 0 0 4 0 0 1 5 3 6

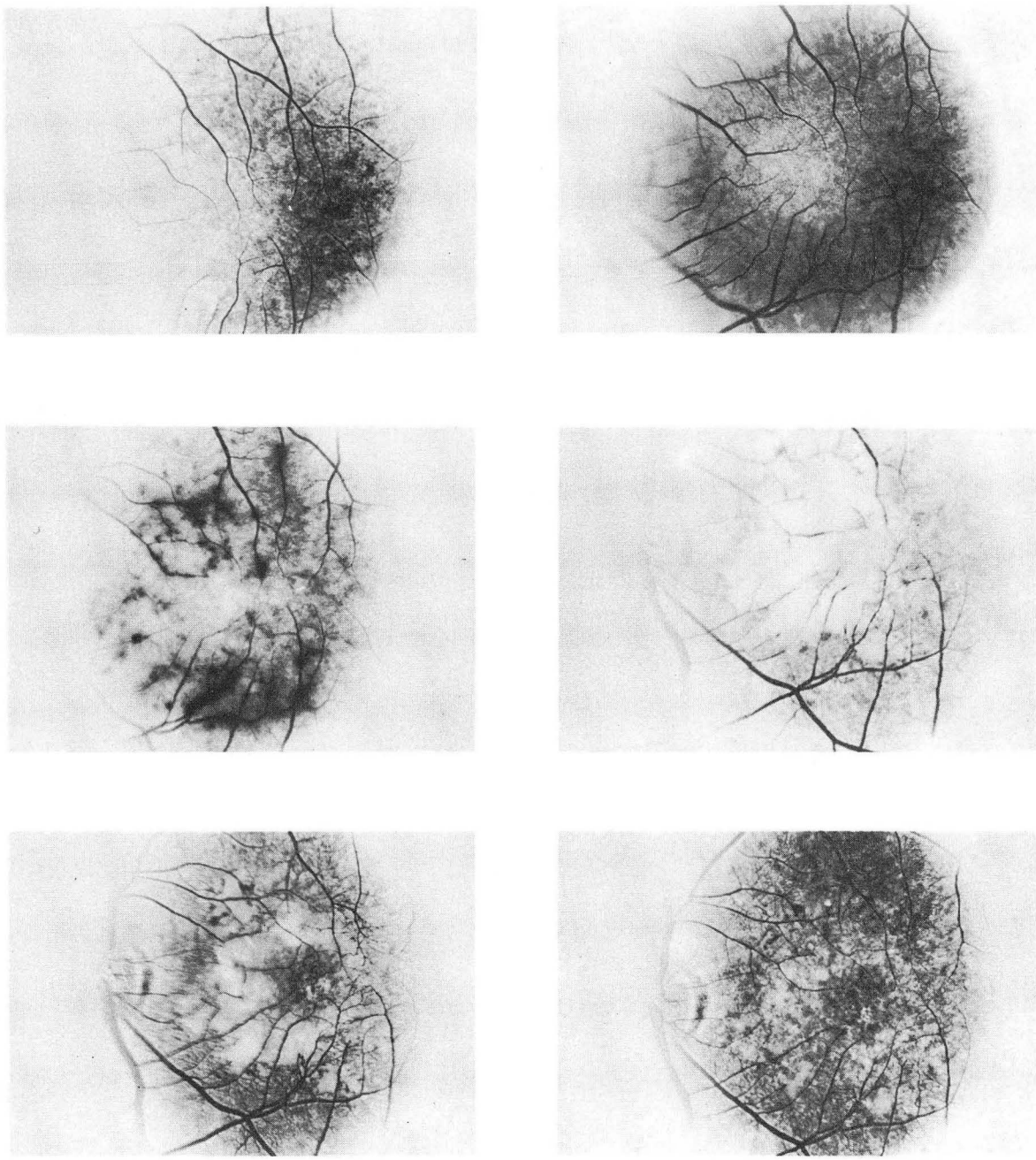

Figure 1

XBB 736-3586

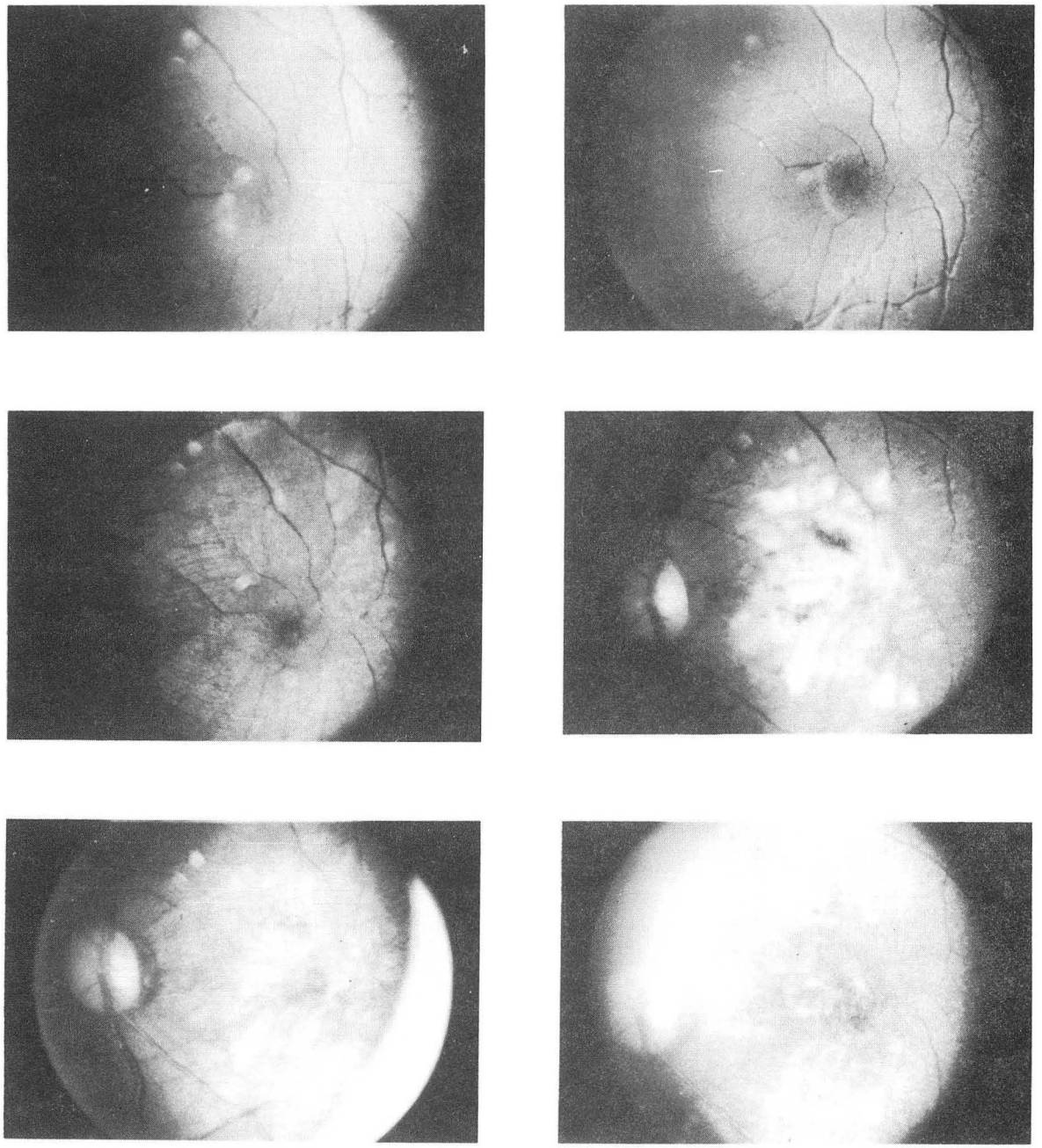

Figure 2 XBB 736-3587

0 0 0 0 4 0 0 1 5 3 7

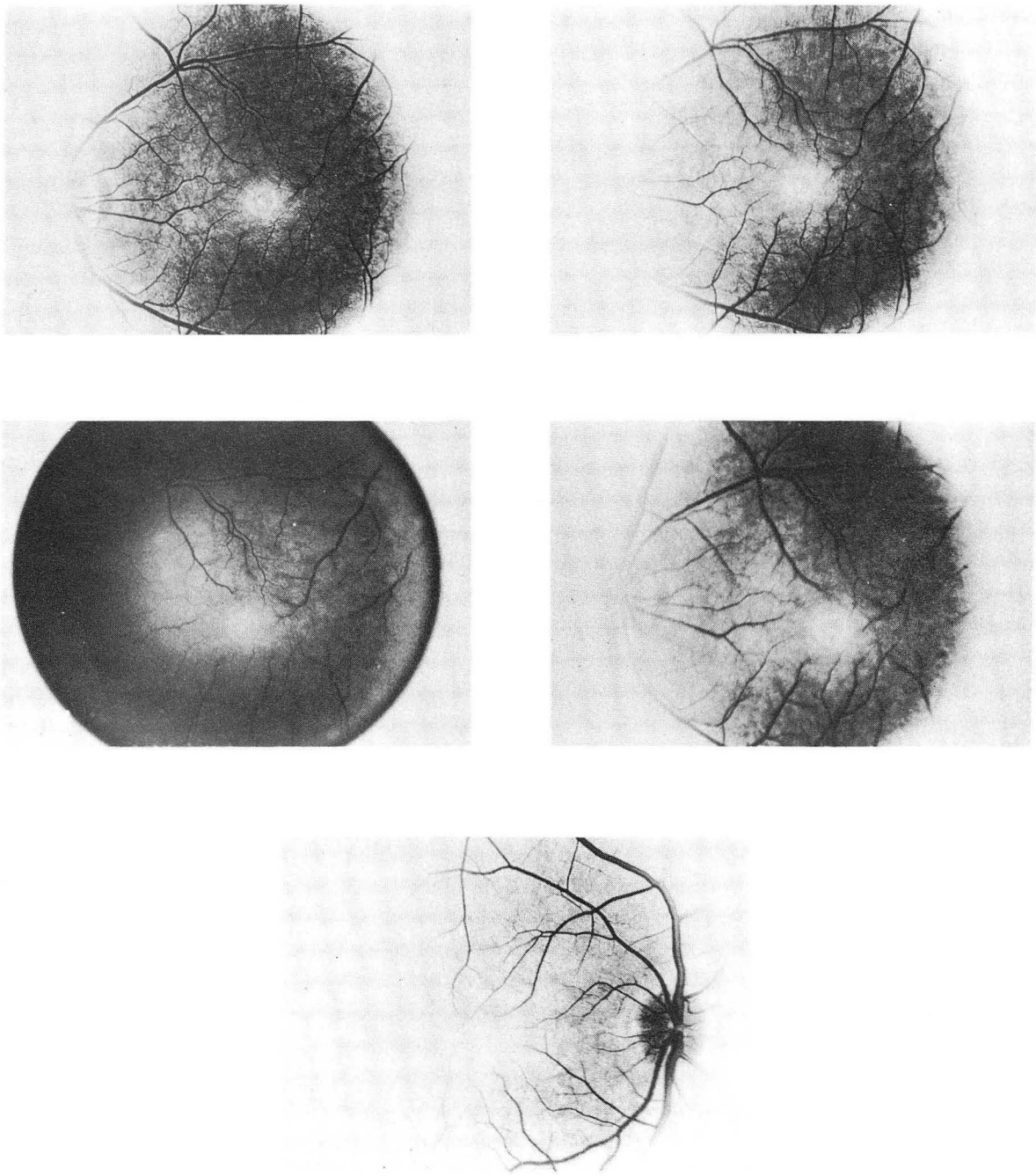

Figure 3

XBB 736-3588

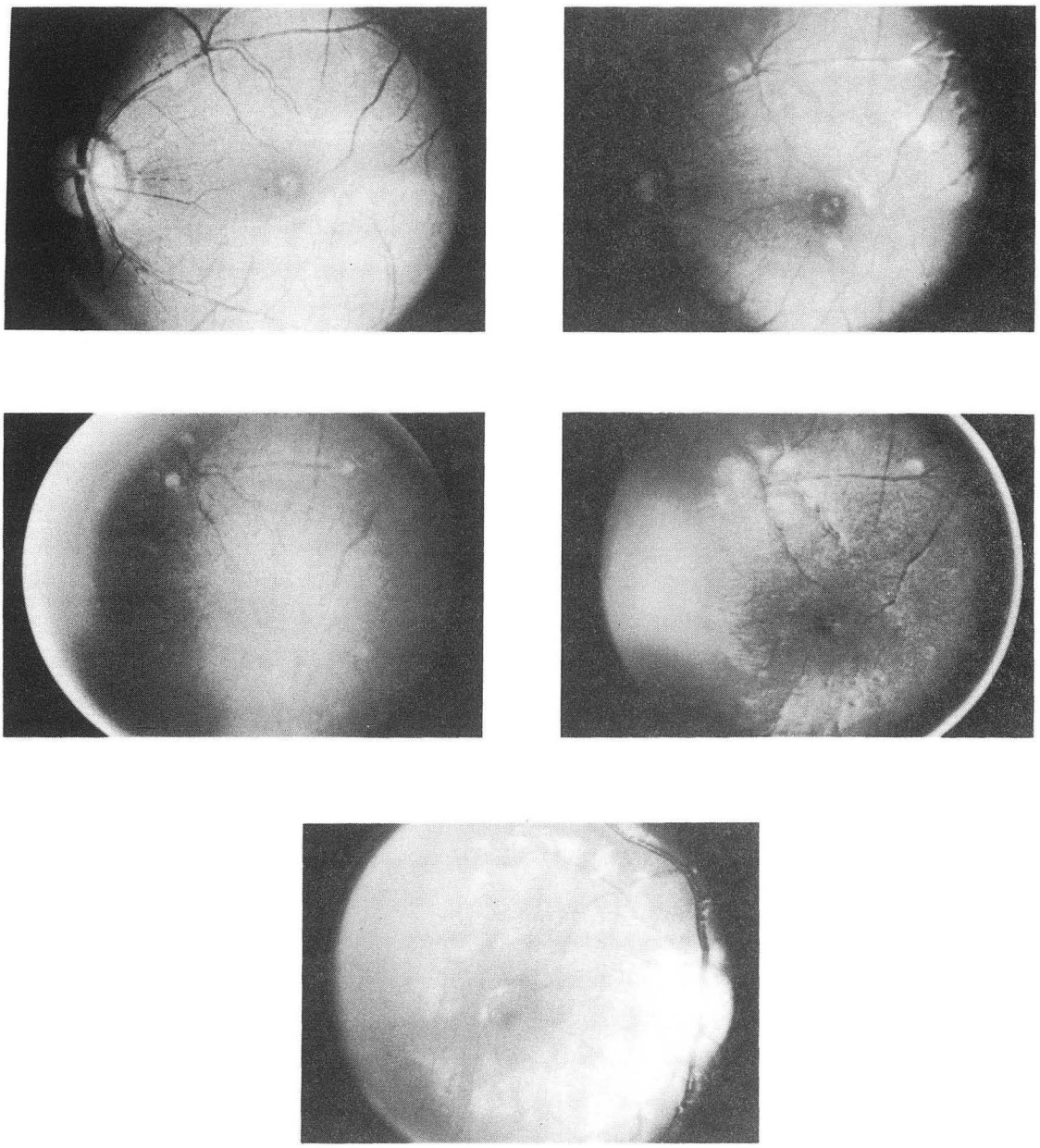

Figure 4 XBB 736-3589

FRAGMENTATION OF HIGH-ENERGY, OXYGEN-ION BEAMS IN WATER

Howard D. Maccabbee and Mark Ritter
Donner Laboratory—Lawrence Berkeley Laboratory
University of California, Berkeley, Ca. 94720

Abstract.

Silicon semiconductor detector systems have been used to measure the energy-deposition spectra of oxygen-ion beams of up to 250-MeV/nucleon at the Lawrence Berkeley Laboratory Bevatron. The removal of primaries and their fragmentation into nitrogen, carbon, and boron ions have been measured. The mean free path of fast oxygen ions in water is 19.4 ± 1.3 cm, corresponding to a total cross section of 1.55 barns "per molecule." The partial cross sections for production of fragments are 331 ± 140 mb for nitrogen, 324 ± 64 mb for carbon, and 102 ± 14 mb for boron.

Calculations of fluence and depth-dose distributions based on our fragmentation data are in good agreement with experiment. Also presented are measurements of energy deposition of oxygen beams stopping in silicon and germanium, and measurements of the effect of nuclear interactions in semiconductor detectors.

Introduction.

High-energy, heavy-ion beams are currently in use in biomedical research, and are being considered for tumor therapy (1). Other possible applications, where a highly penetrating, well-defined particle beam of definite range might be useful, include deep-lesion production in neurological research and several new diagnostic techniques including laminography and radiography (2)

(In each of these applications it is necessary to understand the phenomenon of fragmentation of high-energy heavy-ions due to nuclear interactions with atoms of the medium, particularly tissue.)

We have, therefore, measured several characteristics of the fragmentation process using water to simulate tissue. We have used the oxygen-ion beams of up to 250-MeV per nucleon available at the Lawrence Berkeley Laboratory Bevatron, and have obtained data on the mean-free path, cross sections for production of secondaries of various types, and fragmentation parameters. We compare these data with results from other experiments and theoretical calculations, and discuss the implications.

This paper is one in a series of publications on heavy-ion beams for biomedical research (3, 4) and is a direct continuation of our previous work on composition of high-energy heavy-ion beams(5).

Materials and Methods.

The basic method involves the use of semiconductor detectors to measure energy-deposition spectra of the fast ion beams, and observing the changes in these spectra with varying thickness of water absorber, to study the fragmentation process as a function of absorber depth. The fundamentals of the method have been described previously (5), but several refinements were added for the work described below.

Figure 1 gives a schematic diagram of the revised system. The most important change was the addition of detector No. 1, a lithium-drifted silicon detector in the "top-hat" configuration, with 5 mm sensitive diameter and 3 mm sensitive thickness, placed 50 cm upstream of detector No. 3, and just upstream of the water absorber. Its output pulses are analyzed by an "energy window" to determine whether the transmitted particle was an

oxygen primary. If so, a delay-coincidence system is triggered, allowing analysis of the associated events in detector No. 3.

Thus, energy deposited by a charged particle in the "analyzing" detector No. 3 is collected as a charge signal, and is then converted to a voltage pulse by the charge-sensitive preamplifier. It then passes through the pileup rejector system and a linear amplifier and pulse-shaping system. It is then allowed through a linear gate to the 400-channel pulse-height analyzer if the coincidence system has verified that: first, it was caused by a particle identified as an oxygen primary in detector No. 1; secondly, that it was properly aligned in detector No. 2; and thirdly, that it was not accompanied by a "pile-up" pulse.

We use the good approximations that the analyzed pulse-height is directly proportional to the energy deposited, and that the "straight-ahead" secondary fragments produced by collision in the water absorber have velocities differeing little from the primary (i.e., $\Delta\vec{v} = 0$). Thus, the pulse-height distributions are similar to thin-absorber energy loss frequency distributions, for particles with similar velocities but differing effective charge. Since the average energy loss of a heavy-charged particle in a thin absorber is proportional to Z^2, the various peaks in the pulse-height spectra are interpreted as being due to different values of the nuclear charge; thus, secondaries such as nitrogen ($z^2 = 49$), carbon ($z^2 = 36$), boron ($z^2 = 25$), etc., can be distinguished from fast primary oxygen ions ($z^2 = 64$).

As the water absorber thickness is increased from zero, more primaries will have nuclear interactions with target nuclei of hydrogen or oxygen, resulting in a decrease in the remaining number of primaries under the oxygen peak, and growth in the number of secondaries, tertiaries, etc., under the various fragment peaks of the spectra.

Results.

We have previously shown that incident oxygen ion beams are relatively clean, with contamination of the order of 1% due to carbon ions (see Ref. 5). In the present experiments, signals, due to contamination or any other fragmentation process upstream of our water target, are eliminated by virtue of the single-channel-analysis for oxygen primaries in detector No. 1. A typical energy deposition frequency spectrum is shown

in Fig. 2. This was measured for an oxygen-16 ion beam incident on detector No. 3, a 3-mm silicon (0.7 g/cm^2) analyzing detector, after passing through 3.0 cm of H_2O in the variable absorber and the equivalent of 0.88 cm of H_2O in the absorber windows, etc. (i.e., total 3.88 g/cm^2). The energy incident upon the absorber assembly was 215 ± 2 MeV/nucleon.

The closed circles represent data points which are originally obtained in the form of counts per channel versus channel number. The semi-logarithmic plot is used to enhance visualization of peaks which differ in height by over two orders of magnitude. A smooth curve (with no particular analytical form) has been drawn through the data to guide the eye. The peak, due to the oxygen primaries and nitrogen, carbon and boron fragments are clearly distinguishable. The present system is unable to resolve the smaller contributions from Be, Li, He, or H secondaries. The small "shoulder" on the right side of the 0 peak may be attributed to 0-15 ions which, even if produced at the same velocity as the 0-16 primary, slow down "faster" in the succeeding absorber and, therefore, have a lower velocity (and, therefore, a higher LET) in the analyzing detector.

The data are processed in a straightforward fashion to yield the number of particle counts under each peak. This is done by numerically integrating the area under each peak after fitting by hand.

The results of a series of such runs, with varying water thickness, are given in Table I. The numbers have been normalized using a factor of the ratio of oxygen primary counts in the detector No. 1 scaler in the first run (0.88 g/cm^2 absorber) to the number in each succeeding run. This normalization procedure compensates for geometrical effects and fluctuations of beam intensity between runs.

The numbers describing the attenuation of the oxygen primaries were fitted by least squares to the well-known exponential attenuation equation of the form:

$$\Phi_0(x) = \Phi_0(0) \exp\left(-\sum_0 x\right) \qquad (1)$$

where

$\Phi_0(x)$ ≡ fluence of oxygen ions at penetration x

$\Phi_0(0)$ ≡ incident fluence of oxygen primaries

$\sum_0$ ≡ macroscopic total cross section for removal of oxygen primaries from beam

and

x ≡ penetration, in cm.

Implicit in the use of this expression is the approximation that the cross-section does not vary with penetration (i.e., it is constant despite the slowing down of the projectile). The slope of the best fit line yields a value of:

$$\sum_0 = 0.0516 \pm 0.0033 \text{ cm}^{-1}$$

which is equivalent to

$$\lambda = 19.39 \pm 1.26 \text{ cm}$$

and

$$\sigma_0^{H_2O} \text{ (total)} = 1.55 \pm 0.10 \text{ barns}$$

where λ and $\sigma_0^{H_2O}$ are, respectively, the mean free path and the microscopic total cross-section for an oxygen ion incident on a "water molecule". The chi-square value for goodness of fit was 5.56.

The tabulated numerical data on the rise of the secondary fragments as a function of depth are plotted in Fig. 3. The experimental data for nitrogen, carbon, and boron fragments are represented by the squares, circles, and triangles respectively.

This data was used to calculate weighted mean fragmentation cross sections ($\Sigma_{0\to f}$) for production of each type of fragment. This was done by assuming that an expression of the following form describes fragment

fluence:

$$\Phi_f(x) = \Phi_0(0)\left[\exp(-\sum_f x) - \exp(-\sum_0 x)\right]\left[\sum_{0\to f} / \left(\sum_0 - \sum_f\right)\right] \qquad (2)$$

where $\Phi_f(x) \equiv$ fluence of fragment type f at penetration x.

$\sum_f \equiv$ macroscopic total cross sections for removal of fragment f from beam

and $\sum_{0\to f} \equiv$ macroscopic partial cross section for production of secondary fragment f in a collision of an oxygen primary.

This expression was derived in ref. (4), and is the second approximation to the "dome distribution" of the nuclear secondaries from high-energy oxygen beams.

The value of Σ_0 from above, and values of Σ_f obtained by geometrical [$(A)^{2/3}$ law] scaling from Σ_0, were utilized, and the weighted mean values of the partial cross sections for fragment production were obtained, using the inverse of the variance of each data point as a weighting factor. These cross sections are shown in Table II.

These values were then applied in Eq. (2) to yield what are approximate-fit curves to the data. These are plotted in Fig. 3, the curves for the N, C, and B fragment production being represented by the dashed, solid, and dash-dotted lines respectively.

Comparison with other Data.

Our experimental value of the mean free path of fast oxygen ions in water, 19.4 cm, is in excellent agreement with 19.3 cm, the value which we calculate from Waddington's $\lambda(0 \text{ on H}) = 6\ g/cm^2$(6) and $\lambda(0 \text{ on } 0) = 26.7\ g/cm^2$ from Bradt and Peter's summary of the cosmic ray data (7). Our corresponding value of the total cross section, 1.55 ± 0.10 barns is in good agreement with the value, 1.59 barns, the result of a theoretical calculation by Swiatecki, based upon his model of "abrasion and ablation" in high-energy heavy-ion collisions (8).

Our values for the partial cross sections can be compared with data measured by Greiner et al. for 2.1 GeV/nucleon oxygen ions in hydrogen and carbon targets (9). Our extrapolation of these data to a water target yields calculated values of 254 mb, 273 mb, and 142 mb for the production cross sections for N, C, and B respectively. These are in reasonable agreement with our values of 331 ± 140 mb, 324 ± 64 mb, and 102 ± 14 mb respectively, which were measured at 0.21 GeV/nucleon. This lends some confidence to our approximation that the fragmentation cross sections are relatively constant with projectile kinetic energy (above some minimum energy).

Another method of evaluating these results is by comparison of current dosimetric measurements with predictions based upon our fragmentation data. For biomedical irradiations, two of the most important dosimetric considerations are the shape of the depth-dose distribution and the "number-distance" relation (differential range curve). Using our fragmentation parameters (Table II), and a total cross section equivalent to our value, John Lyman has used the computer code, BRSEC* (10) to calculate the number-distance relation for an oxygen-ion beam of 233.2 ± 0.7 MeV/nucleon penetrating a water absorber. Results are shown in Fig. 4. The solid lines give the predicted fluence of primaries, secondaries, and total particles, based on the assumption that the fragmentation parameters for Be and Li production are equivalent to our B value, and that the values for He and H are 0.19 each (i. e., total = 1.0, chosen somewhat arbitrarily). The open squares represent experimental data measured by the biomedical group at the Lawrence Berkeley Bevatron. Both data sets are normalized to unity at entry. The agreement between the calculation and the experiment is good.

Multiplication of the fluence of each species at depth by the corresponding LET yields a value for density of energy transferred (i.e., absorbed dose), so that a depth-dose relation can be calculated from fluence information. Such a calculation has been made (10) for the same case as above, and is shown in Fig. 5 as the solid lines. The ordinate is normalized to average LET per unit incident particle fluence, in MeV-cm^2/g, so

---

*BRSEC is a modification of code BRAGG, outlined by G. M. Litton in U.C. Lawrence Radiation Laboratory Report UCRL-17392, University of California, Berkeley (1967).

that dose in rads may be obtained by multiplication by the actual incident fluence in No./cm^2 with the conversion factor 1.60×10^{-8} g-rads MeV. The open squares give the values for an experimental measurement at the Bevatron. Agreement between calculation and experiment is satisfactory, and tends to confirm our overall understanding of the phenomena involved.

Discussion and Related Measurements.

There are several physical phenomena which tend to modify the peaks in energy deposition spectra of the type shown in Fig. 2. These effects, such as nuclear interactions in the silicon detectors and energy straggling, affect the resolution of our present system for the study of fragmentation processes, and, in fact, make it nearly impossible to obtain identifiable peaks for water-absorber thicknesses greater than 8 cm. We have discussed these phenomena qualitatively in Ref. (5), and present here some examples of measurements of these effects.

The shape and width of the upper part of the 0 peak in Fig. 2 is dominated by the effects of straggling of energy loss in the detector and fluctuations of the momentum of the incident beam, but a "shoulder" corresponding to lower than expected) energy deposition is clearly seen on the left side of the peak. We suggest that a principal cause of this effect is fragmentation occurring in the analyzing detector, resulting in secondaries with total Z^2 values less than the $Z^2 = 64$ for the incoming primary.

In order to measure this effect, an experiment was performed which used detector No. 1 just downstream of detector No. 3, and the associated energy window to determine whether the outgoing particle was a transmitted oxygen primary or something else (e.g., fragmentation products of an interaction in the silicon of detector No. 3). Figure 6 shows the results for a 215-MeV/nucleon oxygen ion beam (with no absorber) incident on 0.7 g/cm^2 Si. The channel number is linear with energy deposited; energy calibrations are indicated by the pulser mark (P 100 → 100 MeV).

The broader peak is the "normal" pulse spectrum in the analyzing detector including all pulses that are not pile-ups, and correspond to "straight-ahead" particle alignment. The narrower peak is the spectrum observed when the single-channel analyzer and associated coincidence logic are set to eliminate any pulse corresponding to a transmitted particle which

is not identified (by pulse-height in detector No. 1) as oxygen.

The difference between the spectra (i.e., the lower-energy deposition "tail") is interpreted as being caused by nuclear interactions of primaries in detector No. 3. The frequency of these events appears to be much greater than the 2% value expected from simple calculations of the geometric cross section for oxygen or silicon (5). This discrepancy remains unexplained.

Another phenomena, which modifies energy deposition spectra, is fluctuations of kinetic energy of beam particles and straggling of energy loss in absorbers and detectors. The straggling of heavy ions is relatively smaller than for light ions, which largely accounts for the narrowness of the Bragg peak as seen in Fig. 5. The fact that range straggling is insignificant is also seen in the steepness in the drop-off of the primary fluence as shown in Fig. 4. Range straggling and thick absorber straggling are well understood theoretically, but there are virtually no measurements for high-energy heavy ions (11).

Of particular interest is the beam particle kinetic energy distribution at the location of the Bragg peak, which largely determines the LET spectrum and, therefore, the biological effectiveness. We present here a measurement of the energy deposition of an oxygen ion beam at its peak ionization.

The data are shown in Fig. 7, with a logarithmic ordinate scale. In this case, the beam energy is adjusted, using the variable water absorber, so that the maximum number of particles are just stopping at the downstream edge of the sensitive region of the silicon detector (0.70 g/cm^2). This results in a narrow peak in energy deposition, whose leading edge drops off steeply to zero. We call this effect "the cliff", and account for its shape as follows: The cliff occurs at the maximum possible energy which can be deposited by a particular kind of ion in a planar detector of a given thickness; in this case it is 790-MeV, the kinetic energy of an oxygen ion whose range is 3 mm of Si. Any oxygen ion entering the detector with less energy will stop before the back edge, and deposit all of its energy, which is less than the maximum. An oxygen ion entering the detector with more energy will <u>not</u> stop in the detector; since its rate of energy loss at every point in the detector is less than the slower ion which is just stopping, its total energy deposition will also be less than the maximum.

The loss of cliff steepness is determined by two factors: variability the thickness of the sensitive region of the detector, and fluctuations of the energy corresponding to the fixed range in the detector. (This is the reverse of the usual range straggling distribution which is the fluctuation of range corresponding to a fixed energy.). That these effects are small is shown by the drop-off of a factor of 100 in frequency in an energy range of about 25 MeV, versus a peak energy of 790 MeV. The width of the peak itself is a measure of the fluctuations of the incident beam energy representing contributions from both the "stoppers" and a small contribution from the transmitted particles. The lower frequency contribution below 600 MeV is probably due to transmitted fragments lighter than oxygen, resulting in smaller energy deposition.

The cliff effect is also extremely useful for obtaining absolute calibrations in an energy region where there are no natural radioactive sources; for example, a factor of 100 would be necessary to extrapolate from an 8-MeV alpha source to the energies of interest here.

Because of loss of identification resolution of the present system at large absorber thicknesses, a different method is necessary for fragment identification in the Bragg peak region. An alternative to the multiple-detector telescope technique described by Greiner (12) is the analog identifier technique developed by Goulding et al. (13). This method depends upon a measurement of the total energy of the particles as well as the energy deposited in a thin detector. Since a 250-MeV/nucleon oxygen ion has a range of 11.84 g/cm^2 in Si (i.e., 51 mm), [see Appendix of Ref. (5)] it requires seventeen 3-mm Si(Li) detectors to stop and measure its total energy. Alternatively, high-purity germanium detectors have been developed which are thick enough to make them useful for total energy measurements of high-energy heavy ions (14).

We have used 2 such Ge detectors of 1.5 cm thickness each, which, when placed back to back, yield a total thickness of 16 g/cm^2. With this system we have measured the total energy deposition spectrum of a stopping 4-GeV oxygen-ion beam. The data are shown in Fig. 8 in terms of logarithmic frequency (counts/channel) versus channel number (linear with energy). The pulser numbers are not equivalent to energy in MeV in this case. The rightmost peak from the oxygen-16 primaries is clearly resolved, as are major peaks which we identify as nitrogen-14 and carbon-12 from fragmentation of

the primaries in the germanium.

Although we expect roughly the same number of carbon fragments as nitrogen fragments from our experience with water targets, the maximum frequency of the ^{12}C peak is much lower than it is for the ^{14}N peak. However, the ^{12}C peak is spread out over more channels; this is probably due to greater energy fluctuations in the "more violent" collision associated with carbon production, and more broadening due to energy deposited by the remaining or escaping associated fragments of total charge 2. There are also smaller "bumps" which we tentatively identify with ^{15}O, ^{13}N, and ^{11}C and which are apparently produced in significant quantities.

Note that if the $\Delta\vec{v} = 0$ approximation were an exact description of the fragmentation collision, and all the energy remaining with the non-forward fragment of the projectile were undetected (due to escape, etd.), the forward fragment would have the same velocity as the primary (e.g., same MeV/nucleon), and the total energy spectrum would be equivalent to a mass spectrum. That this is not true is evident from the data. The major peaks, however, still contain useful mass information. It is also clear that the germanium system itself is <u>not</u> a total energy detector for all the beam particles because of the escape of energy carried off by light-fragments produced within the germanium whose residual range after formation is greater than the residual thickness of the detector. This defect can be remedied by the use of an additional detector and associated coincidence logic to monitor those fragments which escape.

Conclusions.

1. Energy deposition spectra in silicon semiconductor detectors are useful for studying the fragmentation process for high-energy heavy-ion beams of biomedical interest.

2. Measurements of total cross sections and mean-free paths (for removal of fast oxygen ions in water are in excellent agreement with values calculated from geometric models and cosmic-ray data.

3. Partial cross sections for fragment production at 215-MeV/nucleon are consistent with data obtained at relativistic energies in targets other than H_2O.

4. Fragmentation parameters (indicating the frequency of production of a fragment type from a collision removing an oxygen primary) are about 0.21 for nitrogen, 0.21 for carbon, and 0.07 for boron. These make up nearly half of the total collision probability.

5. Calculations of fluence and depth-dose distributions, based upon our data, are in good agreement with experimental measurements.

6. Measurements of the effects of nuclear interactions in detectors, the energy deposition of stopping beams, and total energy spectra in Ge can shed further light on the fragmentation process.

Acknowledgments.

This work is dedicated to the memory of Dr. Gerad J. Neary, who died of cancer late in 1972. As Director of the Biophysics Group at the MRC Radiobiology Unit, Harwell, England, he established an admirable tradition of clear and precise thinking, and provided many powerful insights into radiation biophysics at the molecular and cellular level.

We thank the following people for their contribution to this work: John Lyman for the calculation and measurements of fluence and dose spectra, Jerry Howard and Graeme Welch for collaboration on the experiments, Doug Greiner and W. Swiatecki for the use of their unpublished data, Walter Schimmerling for the idea of the measurement of nuclear interactions within the detectors, Stan Curtis and Al Smith for several useful discussions, Fred Goulding, Don Landis, Dick Pehl, Jack Walton, and E. Haller for help with detectors and electronics, M. R. Raju for the idea of the "cliff" measurement, the Bevatron group for production of high-energy heavy-ion beams, C. A. Tobias, and James Born for their continued support, and Grace Walpole for her secretarial assistance.

This work is supported by the United States Atomic Energy Commission.

REFERENCES

1. See in particular other articles in this report (Biomedical Research with Accelerated Heavy Ions, LBL-2016, University of California, Berkeley (1973)).

2. E. V. Benton, R. P. Henke, and C. A. Tobias. Heavy particle radiography. Submitted to Science (1973).

3. C. A. Tobias, J. T. Lyman, A. Chatterjee, J. Howard, H. D. Maccabee, M. R. Raju, A. R. Smith, J. M. Sperinde, and G. P. Welch. Radiological physics characteristics of the extracted heavy ion beams of the Bevatron. Science 174, 1131-1134 (1971).

4. C. A. Tobias, H. D. Maccabee, and A. Chatterjee. The "Dome Distribution" of nuclear secondaries from high-energy heavy-ion beams. Submitted to Rad. Res. (1973).

5. H. D. Maccabee. Composition of high-energy heavy-ion beams: Preliminary measurements. Rad. Res. 55 (In press, 1973).

6. C. J. Waddington. Composition of the primary cosmic radiation. In Progress in Nuclear Physics (O. R. Frisch, Ed.) Vol. 8, p. 32, Pergamon, New York, 1960.

7. H. L. Bradt and B. Peters. The heavy nuclei of the primary cosmic radiation. Phys. Rev. 77, 54-70 (1950).

8. W. Swiatecki. Private communication. Lawrence Berkeley Laboratory, Berkeley, California (1973).

9. D. E. Greiner, H. H. Heckman, P. J. Lindstrom, and F. S. Bieser. Private communication. Lawrence Berkeley Laboratory, Berkeley, California (1973).

10. J. T. Lyman, Private communication. Lawrence Berkeley Laboratory, Berkeley, California (1973).

11. C. Tschalar and H. D. Maccabee. Energy-straggling measurements of heavy charged particles in thick absorbers. Phys. Rev. B1, 2863-2869 (1970).

12. D. E. Greiner. A versatile high-resolution particle identifier theory. Nucl. Instr. Methods 103, 291-308 (1972).

13. F. S. Goulding, D. A. Landis, J. Cerny, and R. H. Peak. A new particle identifier technique. Nucl. Instr. Methods 31, 1-12 (1964).

14. R. H. Pehl, R. C. Cordi, and F. S. Goulding. High-purity germanium: detector fabrication and performance. IEEE Trans. Nucl. Sci. NS-19 [1] 265-269 (1972).

Table I

Normalized counts under primary and secondary fragment peaks as a function of increasing water absorber thickness

Total H_2O Equivalent: (g/cm^2)	0.88	1.88	2.88	3.88	4.88	5.88
O-ions (primaries)	25,729	23,971	23,789	22,034	21,760	19,620
N-ions	236	553	822	824	1145	1484
C-ions	306	490	745	897	1048	1296
B-ions	70	192	212	318	382	-

Table II

Cross sections and parameters for fragmentation of 215-MeV/nucleon oxygen beam in water

Fragment produced	Macroscopic Cross Section $\Sigma_{o\to f}$	Microscopic Cross Section $\sigma_{o\to f}^{H_2O}$	Fragmentation Parameter $\Sigma_{o\to f}/\Sigma_o$
Nitrogen	$0.0111 \pm .0047\ cm^{-1}$	331 ± 140 mb	0.21
Carbon	$0.0108 \pm .0021\ cm^{-1}$	324 ± 64 mb	0.21
Boron	$0.0034 \pm .0005\ cm^{-1}$	102 ± 14 mb	0.07

FIGURE CAPTIONS

Fig. 1. Schematic diagram of Si(Li) semiconductor detector system.

Fig. 2. Frequency spectrum of energy deposition in 3 mm (0.7 g/cm^2) Si by a 215-MeV/nucleon oxygen-ion beam after passing through 3.88 g/cm^2 H_2O equivalent.

Fig. 3. Frequency of fragments generated by 215-MeV/nucleon oxygen-ion beam penetrating water.

Fig. 4. Number-distance curves for 233-MeV/nucleon oxygen-ion beam in water. Solid lines represent calculations. Open squares are experimental measurements.

Fig. 5. Depth-dose curves for 233-MeV→nucleon oxygen-ion beam in water. Solid lines represent calculations. Open squares are experimental measurements. Dose is in rads.

Fig. 6. Energy deposition spectra measured for 215-MeV/nucleon oxygen in 3 mm Si, with no absorber. Broader peak is "normal" spectrum. Narrow peak is spectrum measured with additional detector and logic to eliminate events not verified as oxygen ions transmitted through the analyzing detector.

Fig. 7. Energy deposition spectrum of oxygen ion beam just stopping in 3 mm Si; "cliff" corresponds to maximum total-energy of 790-MeV.

Fig. 8. Energy deposition spectrum of 4-GeV oxygen ion beam stopping in 3 cm germanium detector.

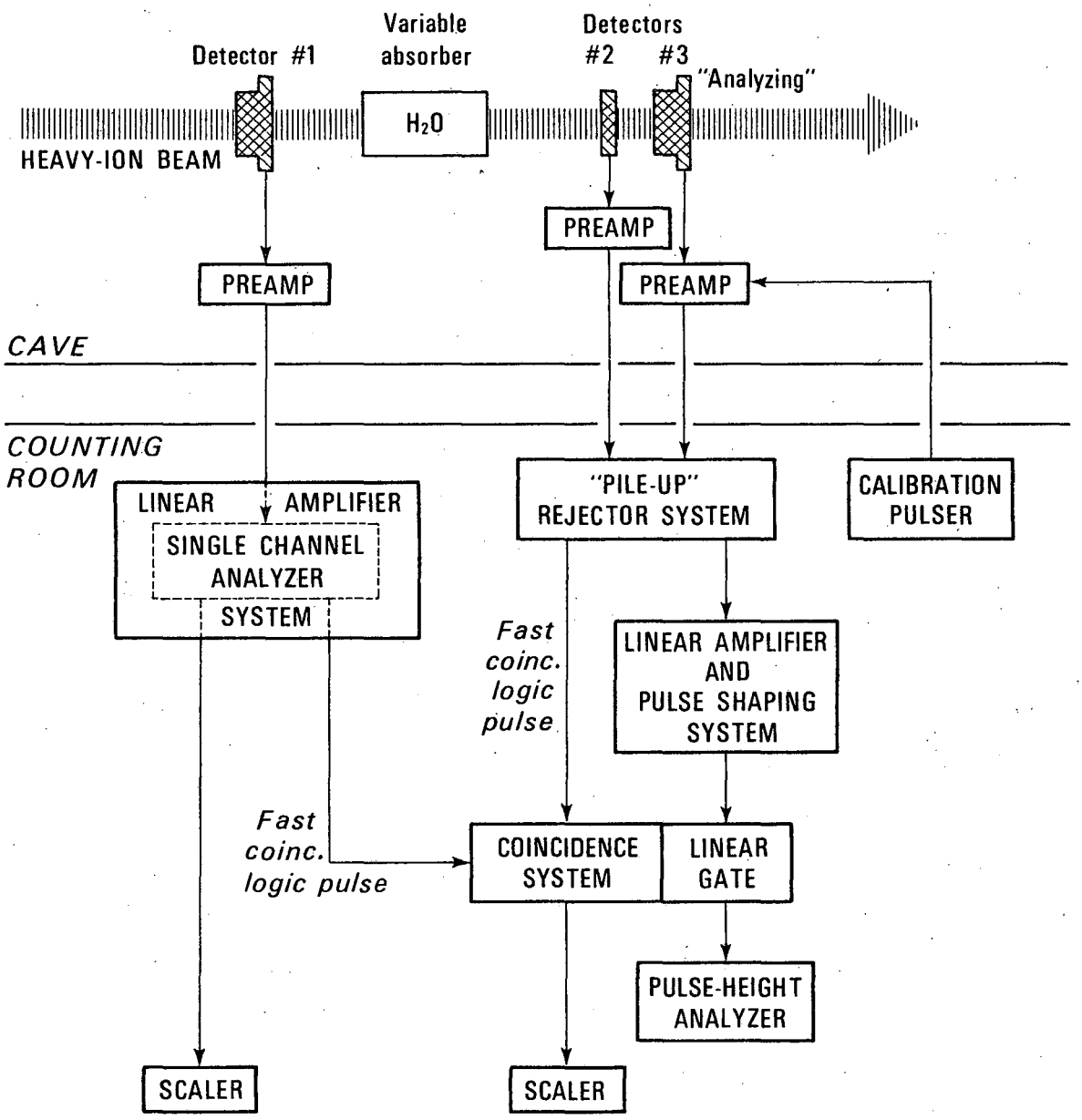

DBL 736-5232

Figure 1

0 0 0 0 4 0 0 1 5 4 7

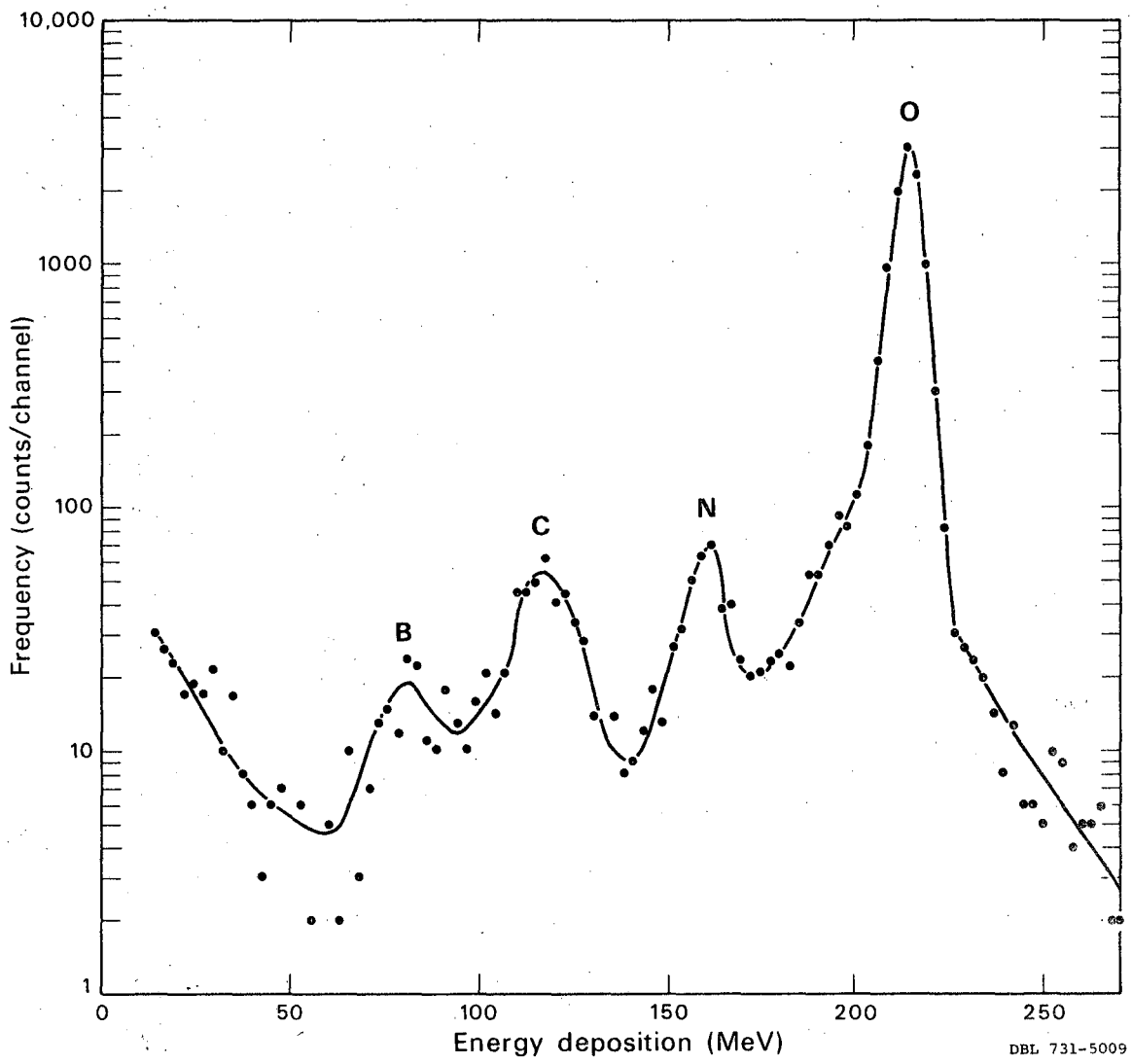

Figure 2

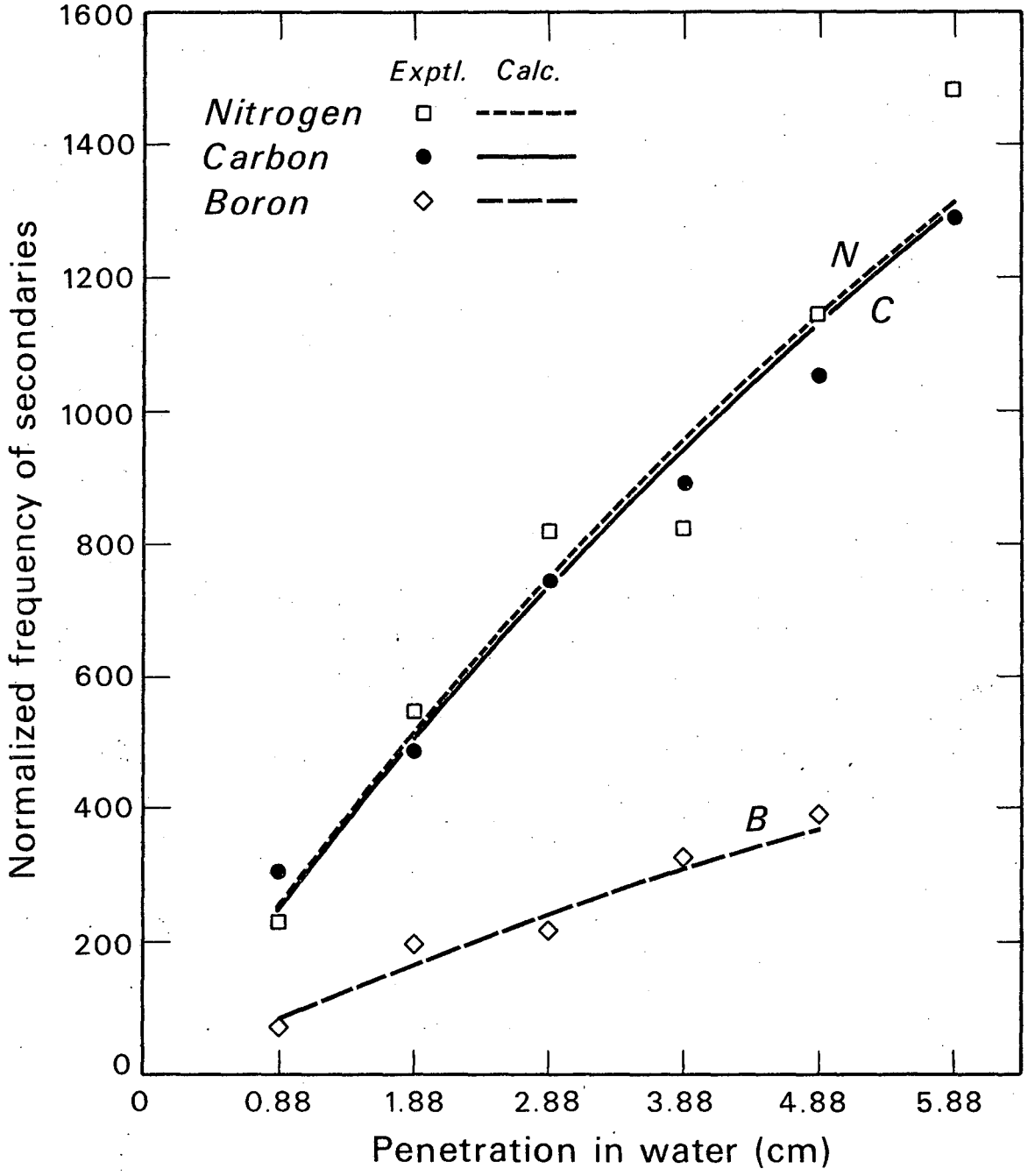

DBL 736-5233

Figure 3

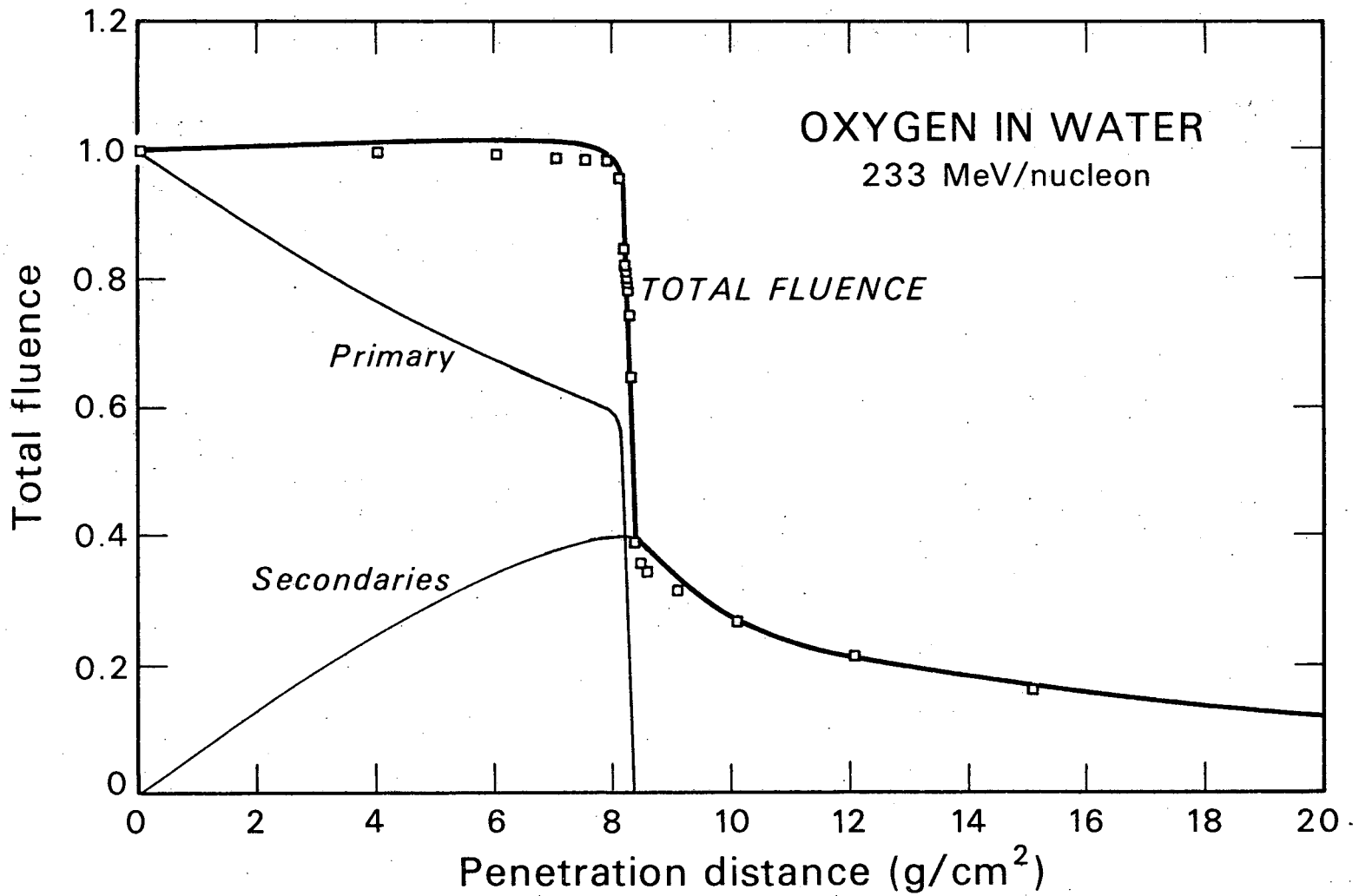

Figure 4

DBL 736-5216

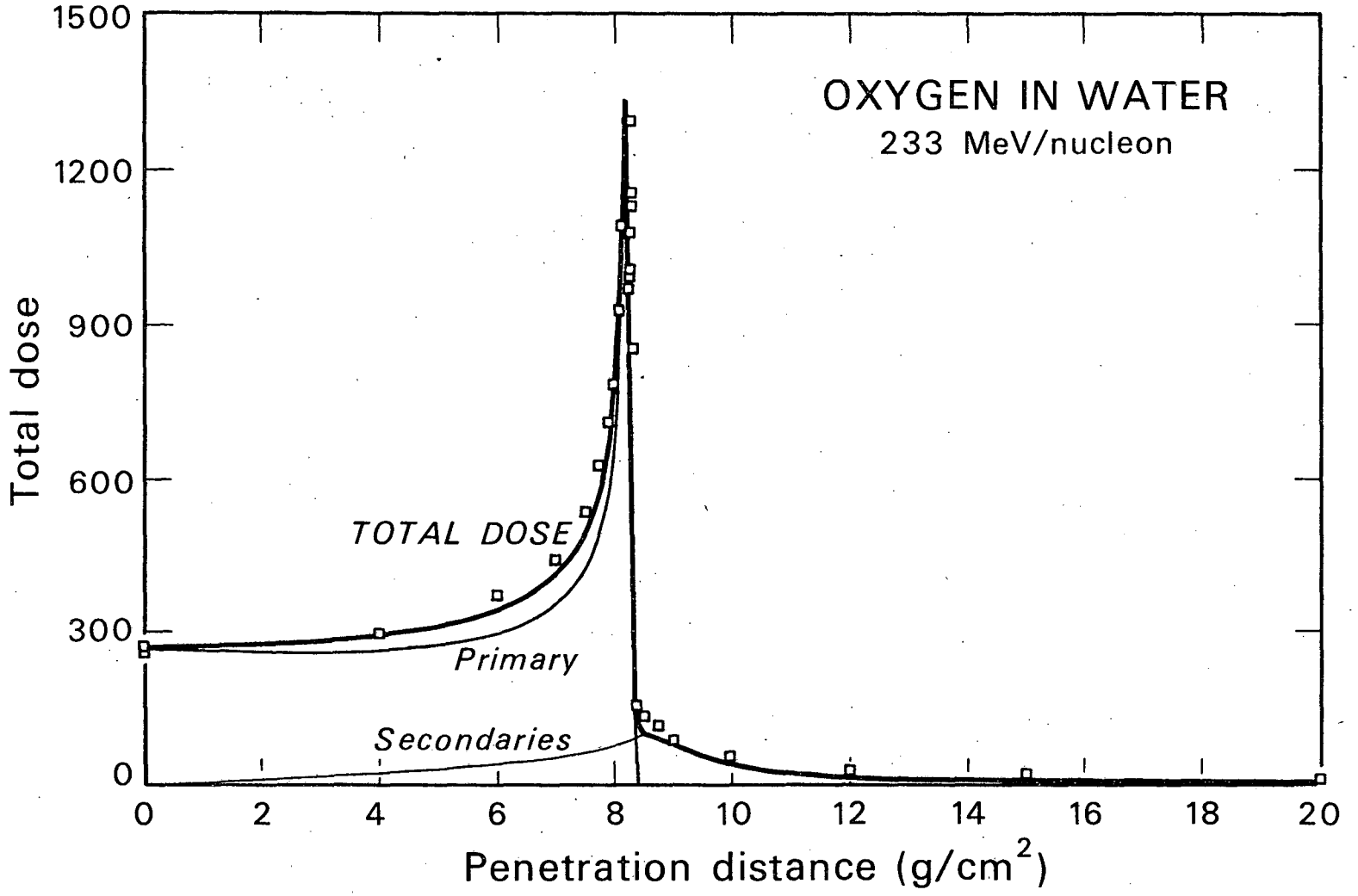

DBL 736-5215

Figure 5

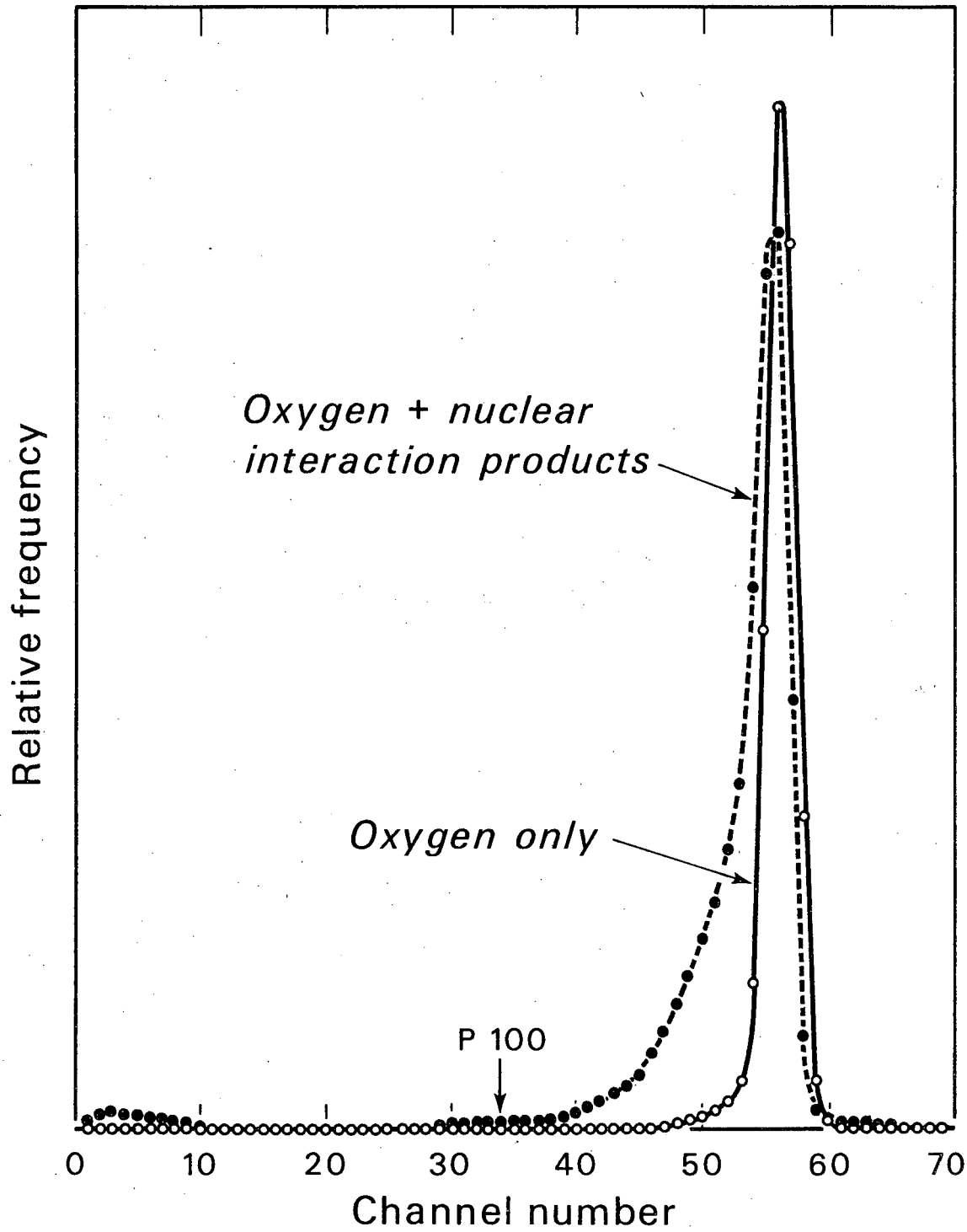

DBL 736-5229

Figure 6

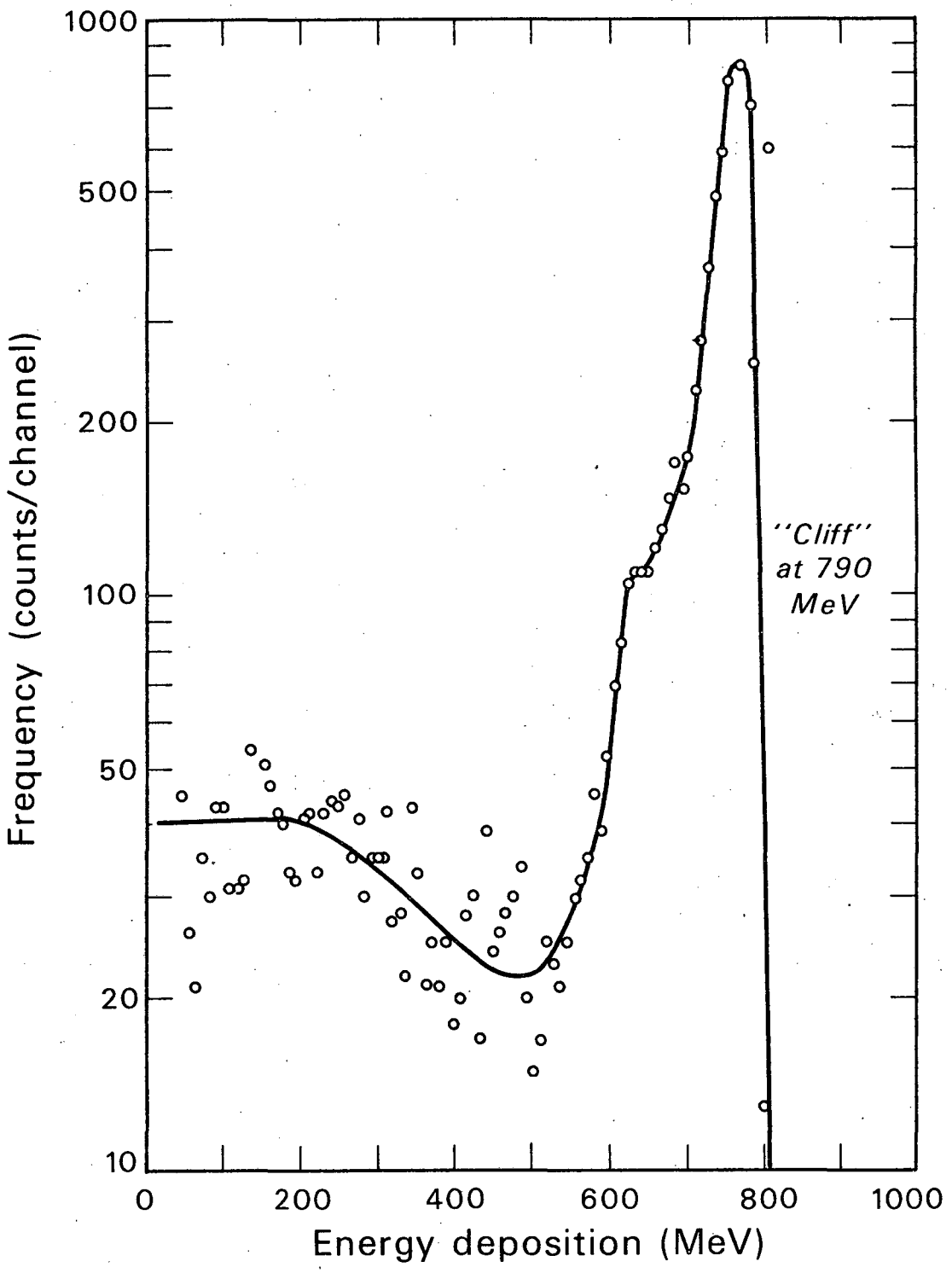

DBL 736-5230

Figure 7

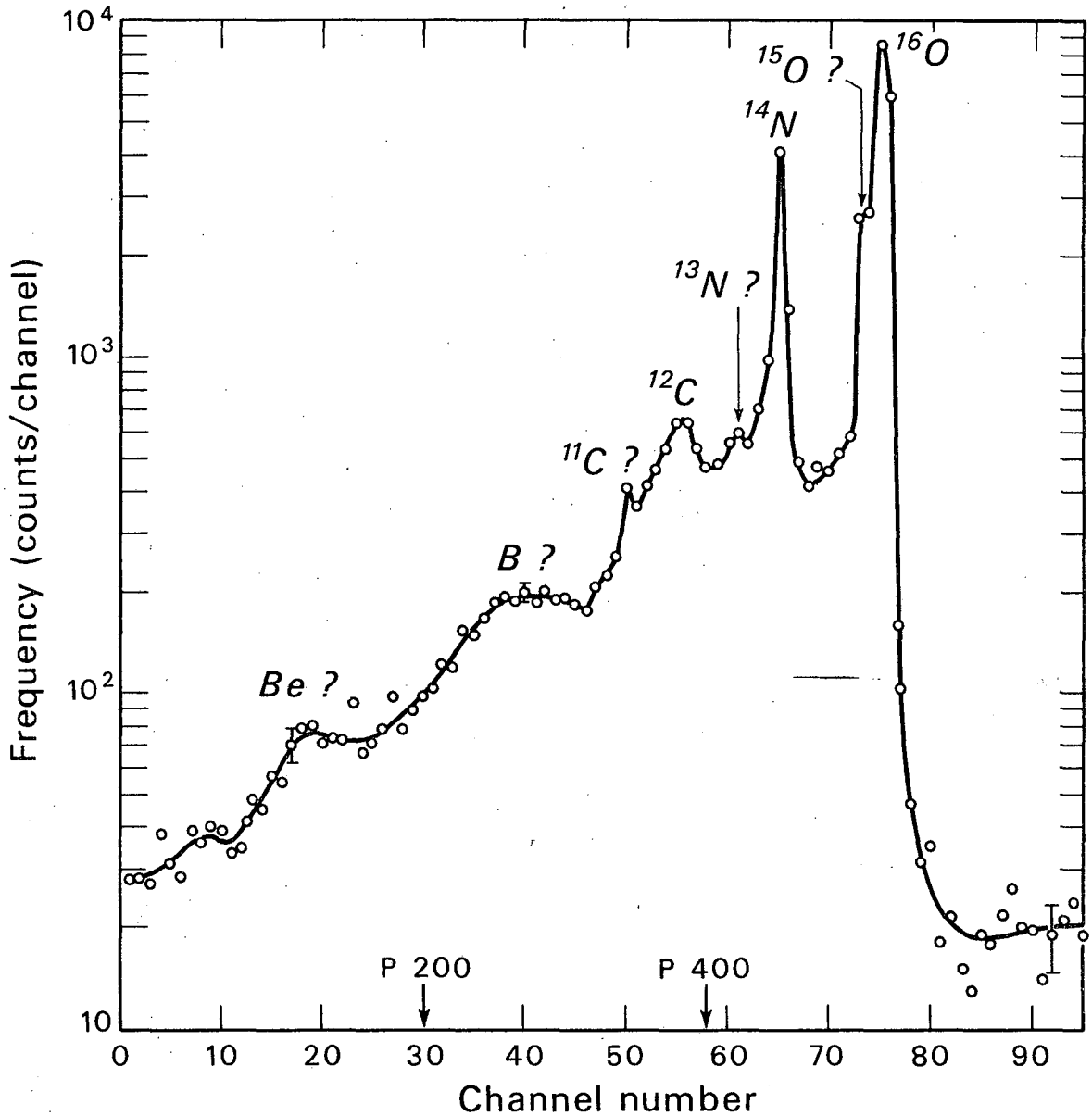

DBL 736-5231

Figure 8

EXPERIMENTAL SETUP AND PHYSICAL MEASUREMENTS OF THE HEAVY-ION BEAMS USED FOR BIOLOGICAL IRRADIATIONS

John T. Lyman, Jerry Howard, Graeme P. Welch, Walter Schimmerling and Cornelius A. Tobias

Donner Laboratory—Lawrence Berkeley Laboratory
University of California, Berkeley, CA 94720

Abstract.

This report describes the physical set up, beam characteristics and dosimetry of heavy-ion beams, for biological experiments at the Bevatron. Bragg curves for oxygen-16 and neon-20 beams were obtained. Present limitations on beam size vs. uniformity and dose rate are also discussed.

TABLE I

EQUIPMENT CUSTOMARILY LOCATED IN BEAM PATH

Items	Material and Thickness in Inches	Equivalent Thickness in g/cm^2 Water
Secondary Emission Monitors (2)	2×11× 0.00025" Al	0.0293
Bevatron Exit Window	0.005" Al	0.0266
F1 Air Gap	22.0" Air	0.0629
Scintillation Counter	0.125" Pilot B	0.3304
	0.002" Al	0.0107
	0.024" Paper	0.0452
EPB Entrance Window	0.005" Al	0.0266
EPB Channel II Exit Window	0.0135" Mylar	0.0445
Multiwire Proportional Counter	2×0.001 Mylar	0.0047
Monitor Scintillation Counter	0.0625 Pilot B	0.1652
	0.002" Al	0.0107
	0.024" Paper	0.0452
Quadrant Scintillation Counter Windows*	2×0.002" Al	0.0213
Split Ionization Chamber 1	3×0.002" Al	0.0320
	2×0.002" Kapton H	0.0132
Monitor Ionization	5×0.002" Al	0.0533
Water Absorber (Minimum Thickness)	2×0.125 Lucite	0.7337
	0.040" Water	0.1016
Main Ionization Chamber	3×0.002" Al	0.0320
	2×0.002" Kapton H	0.0132
Split Ionization Chamber II	3×0.002" Al	0.0320
	2×0.002" Kapton H	0.0132
Air Path from EPB Exit Window to Primary Sample Position	110." Air	0.3143

*The counters are not normally positioned so as to be in the central portion of the beam area.

FIGURE CAPTIONS

Fig. 1. Schematic plan view of Bevatron.

Fig. 2. Schematic plan view of biomedical irradiation area.

Fig. 3. Plot of focusing magnet current (X2Q5A) vs. "beam diameter".

Fig. 4. Bragg curve of Oxygen-16 ions.

Fig. 5. Bragg curve of an Oxygen contaminated (~20%) Neon ion beam.

Introduction.

A beam of Oxygen-16 was accelerated at the Bevatron in January and beams of Carbon-12, Oxygen-16 and Neon-20 were made available in September 1972. The nominal energy of these beams at extraction from the synchrotron ring was approximately 250 MeV/amu.

The Biophysics Group of Donner Laboratory measured the beam characteristics and provided dose data for most of the biological experiments. This report describes the experimental setup, instrumentation, and salient results obtained. Results obtained with a Nitrogen-14 ion beam in 1971 have been reported elsewhere (1, 2).

A plan view of the Bevatron is shown in Figure 1. The biomedical experimental area, located in Beam Channel 2, is shown schematically in Figure 2. Biological samples were installed on an optical bench using especially designed holders, precisely positioned.

At the biological sample irradiation positions, the energy was less than the extracted energy due to various amounts of material in the beam line between the point of extraction and the biological specimen. Table 1 is a list of items, most of which were in the beam path at any one time and would therefore affect the residual range of the particles. Whenever a change was made, and before an experiment requiring the range to be precisely known, the range was determined from several points near the peak of a Bragg curve.

Beam intensity measurements.

The wide range of beam intensities encountered required two monitoring systems. At low intensities, a one-inch square (Jan '72) or a two-inch square (Sept. '72) scintillation counter was used to count single particles. At intensities above approximately 10^5 particles/pulse, the fine structure of the 300 msec beam spill resulted in significant counting losses. Therefore, ionization chambers were used to measure beam intensity. These were parallel-plate transmission chambers with gold plated electrodes on Kapton-H. The diameter of the collector electrode was one-centimeter and the cavity was continuously flushed with nitrogen gas. The total charge collected was measured using Tomlinson Beam Current Integrators and scalers.

The maximum number of particles per beam pulse was about 5×10^4, with typical operation about 2×10^4/pulse during the Jan. '72 run. A larger beam current was obtained during the Sept. '72 run due to the installation of an improved vacuum pumping system. Typical operation was approximately

2×10^6/ pulse, with a maximum intensity of approximately 10^7 particles/pulse.

Beam intensity distribution.

Since dose rate is proportional to flux density and not to beam fluence, maximum dose rates will be obtained with minimum beam sizes. The limited dose rate available from the Bevatron required focusing of the beam to the smallest size compatible with the biological sample being irradiated. The quadrupole doublet X2Q5A and X2Q5B, the final pair of focusing magnets (see Fig. 2), was used to focus the beam. These are 32 inches long, 8 inches diameter quadrupoles, with a maximum field of 12 kG at the pole tips. In order to maintain a round beam, both magnet currents were changed proportionally. Initially, the beam size was determined with Type-57 Polaroid film and later with Dupont NDT 45 Industrial X-ray film. The latter were scanned densitometrically. Figure 3 shows a plot of the beam diameters at an optical density level 80% of the maximum plotted vs. the current in X2Q5A. In the linear region of the film response, this represents the maximum size target that could be irradiated with ±10% uniformity.

A figure of merit of the beam which is independent of its size can be given in terms of dose rate times beam area. This quantity improved from less than 1 in January, to about 40-70 rad-cm^2/min. in September. For the beam sizes shown in Figure 3, this is equivalent to a maximum dose rate of 8-14 rad/min. for a 1-in.-diam. beam with a uniformity of ±10%. This is a useful beam for many biological experiments involving small samples and animals.

Beam position measurements.

Beam position monitoring was only required for horizontal position, since our previous experience (2) had been that the beam did not wander vertically but did wander horizontally, probably due to inadequate regulation of the final bending magnet power supply. Two ionization chambers were used, one near each end of the optical bench. Each one had two "D"-shaped collecting electrodes back-to-back along the vertical center line, separating the chamber into "right" and "left" halves. The four collecting electrodes of the two ionization chambers were connected to electrometers, and these to sum and difference circuits, so that upstream and downstream balance conditions as well as the total beam current from the four electrodes were displayed on meters.

The same information was also displayed on an oscilloscope (3). The "x" position of the display indicated the left-right position of the beam downstream, and the "y" position similarly upstream. A sine-wave was added to each oscilloscope input, with the amplitudes determined by the total beam current from each ionization chamber. The pattern displayed was an ellipse, with eccentricity determined by the relative beam current from the two ionization chambers (equal currents displayed a circle). The desired alignment of the beam was obtained when, with each pulse of the machine, an ellipse appeared at the center of the oscilloscope screen; any motion away from the center indicated that the beam was not coming down the axis of the optical bench. The area of the ellipse was proportional to the total beam current.

A quadrant scintillator system was also used to indicate beam position with respect to the axis of the optical bench and to monitor the beam position during exposures of biological specimens. The output of the system, besides indicating beam position, also indicated the number of particles which had passed through a given area of the monitor scintillator. Thus, it was possible to record the total number of particles passing through the monitor scintillator, the number of particles within a defined central area, and the number of particles outside this area.

Bragg curves.

The Bragg curve of the Oxygen-16 ions obtained in Jan. '72 had a peak-to-plateau ratio of 6.0, and the residual range to the Bragg peak was 8.17 cm. of water. This indicates that, as far as the biological exposures were concerned, we were using a beam which had a residual energy (after passing through vacuum windows, scintillators, ionization chambers, etc.) of 233 MeV/amu (4, 5), whereas the initial beam energy was 250 MeV/amu.

The Bragg curve of the Oxygen-16 beam was checked several times during the September run. Figure 4 is a composite of data from seven Bragg curves. The peak-to-plateau ratio is 6.3 and the residual range to the Bragg peak was 7.73 cm., which corresponds to a residual energy of 226 MeV/amu.

A Neon-20 beam was also accelerated in September. From beam composition measurements it was determined that the major contaminating particle was oxygen (approximately 20%). A Bragg curve for this contaminated beam is shown in Figure 5. The peak at 5.93 cm. is the Neon-20 Bragg peak; the peak at 7.9 cm. is due to the contaminating Oxygen-16 ions.

REFERENCES

1. Radiological physics characteristics of the extracted heavy-ion beams of the Bevatron. C. A. Tobias, et al. Science 174:1131-1134 (1971).
2. Experimental set up and physical measurements of a heavy-ion beam for initial biological irradiations at the Bevatron, J. T. Lyman et al., in: Initial Radiobiological Experiments with Accelerated Nitrogen Ions at the Bevatron, LBL-529 (1971), p. 1-19.
3. Particle irradiation Methods M. R. Raju, J. T. Lyman, and C. A. Tobias, UCRL-20226 (1971).
4. Penetration at High-Energy Heavy Ions with Inclusion of Coulomb, Nuclear, and Other Stochastic Processes, Gerald M. Litton, John Lyman and C. A. Tobias, UCRL-17392, Rev., (1968).
5. Stopping Power and Range for Any Nucleus in the Specific Energy Interval 0.01-500-MeV/amu in any Non Gaseous Material, Palmer G. Steward (Ph. D. Thesis, Univ. of California, Berkeley) UCRL-18127 (1968).

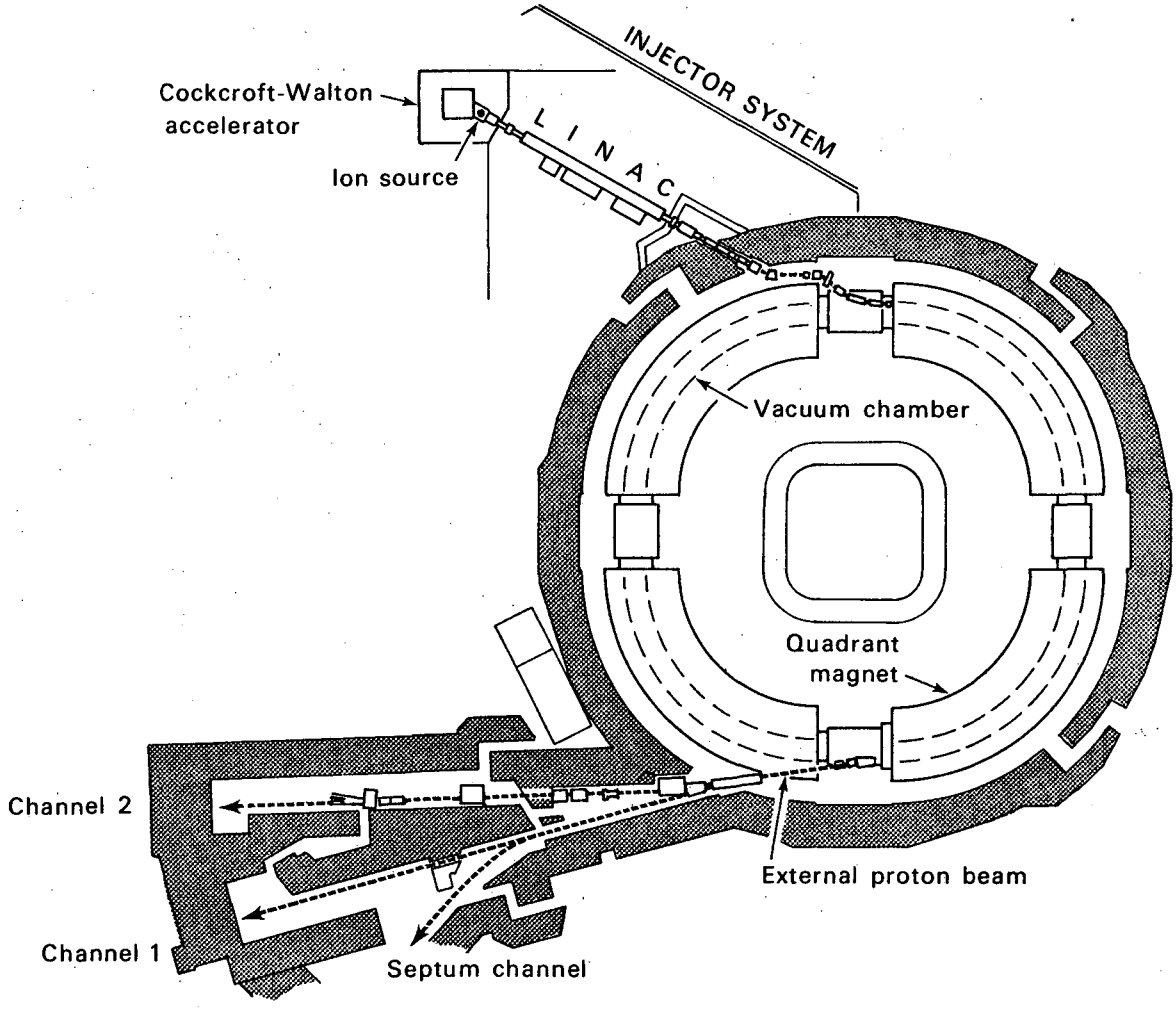

DBL 721 5108

Figure 1

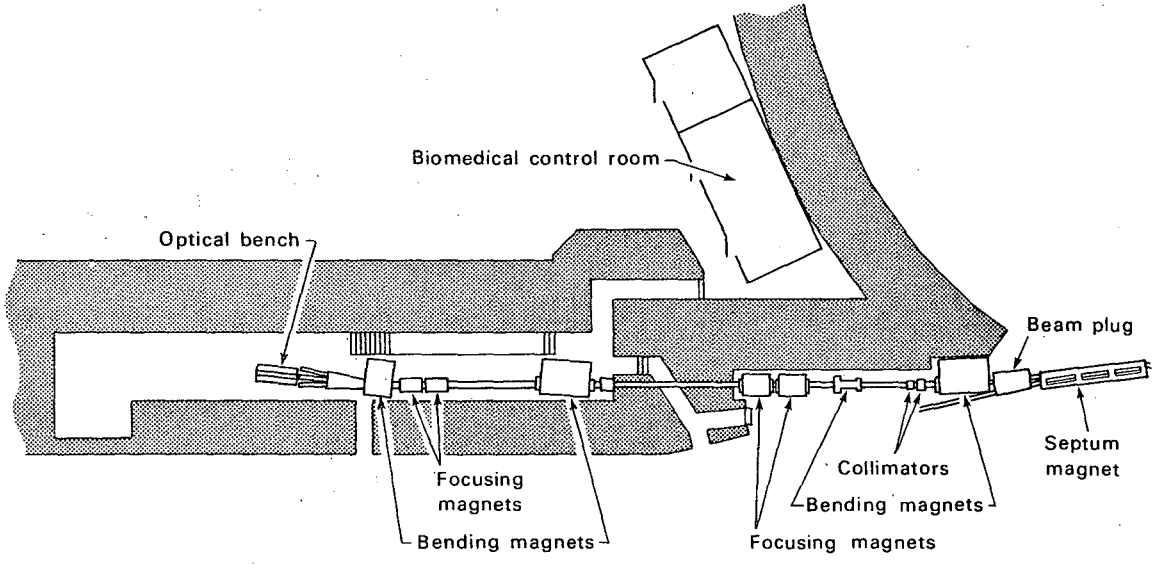

DBL 721 5107

Figure 2

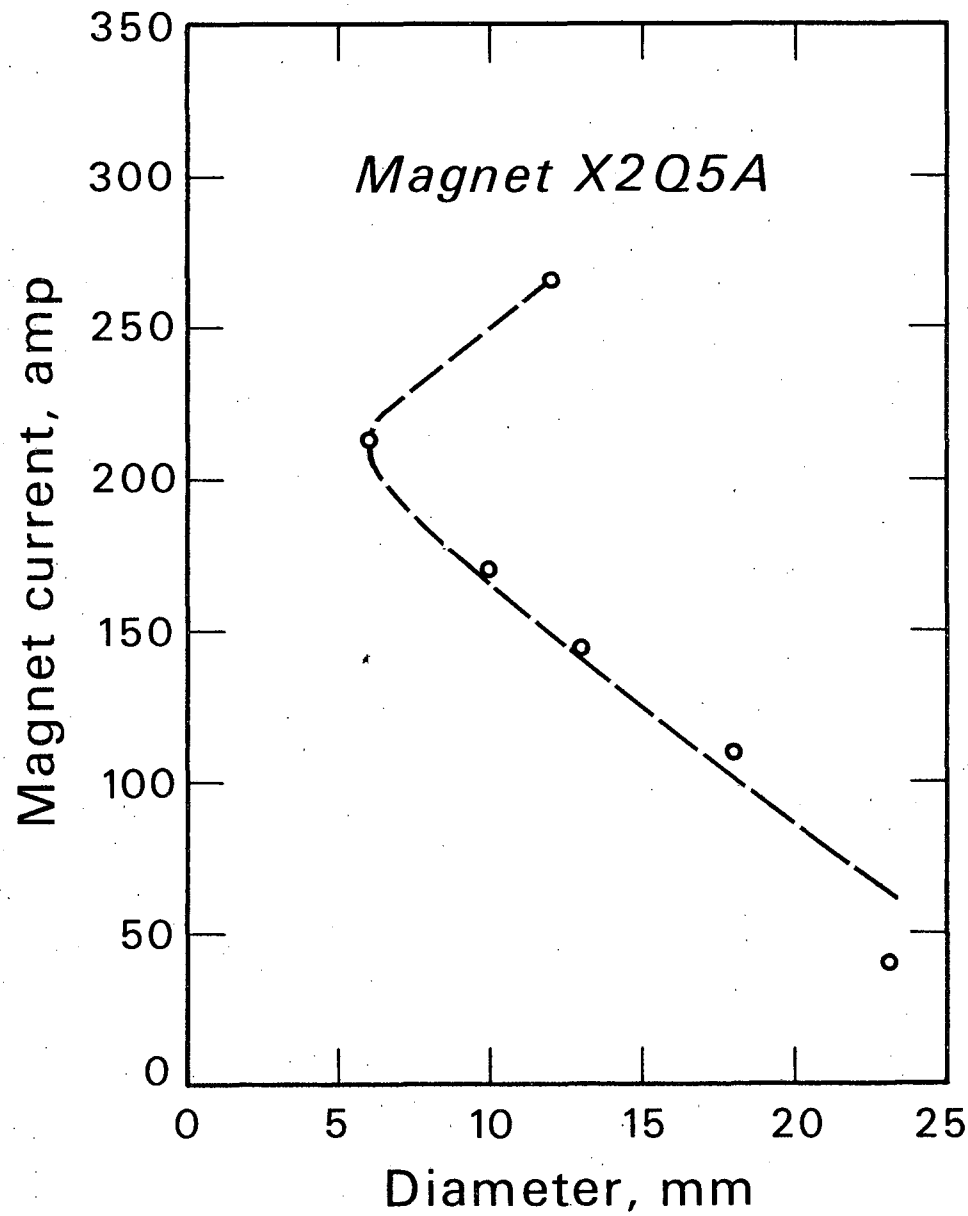

DBL 731-5015

Figure 3

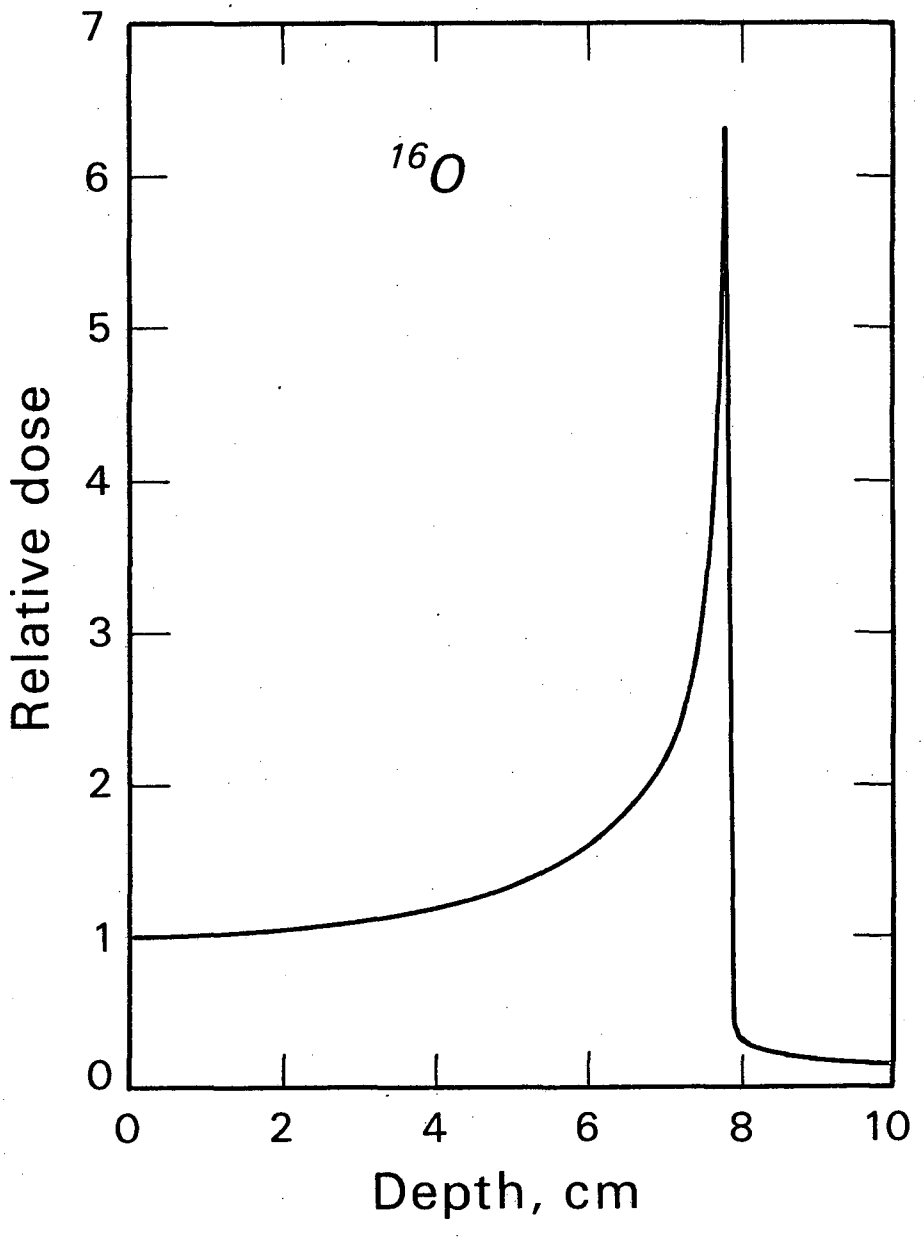

DBL 731-5016

Figure 4

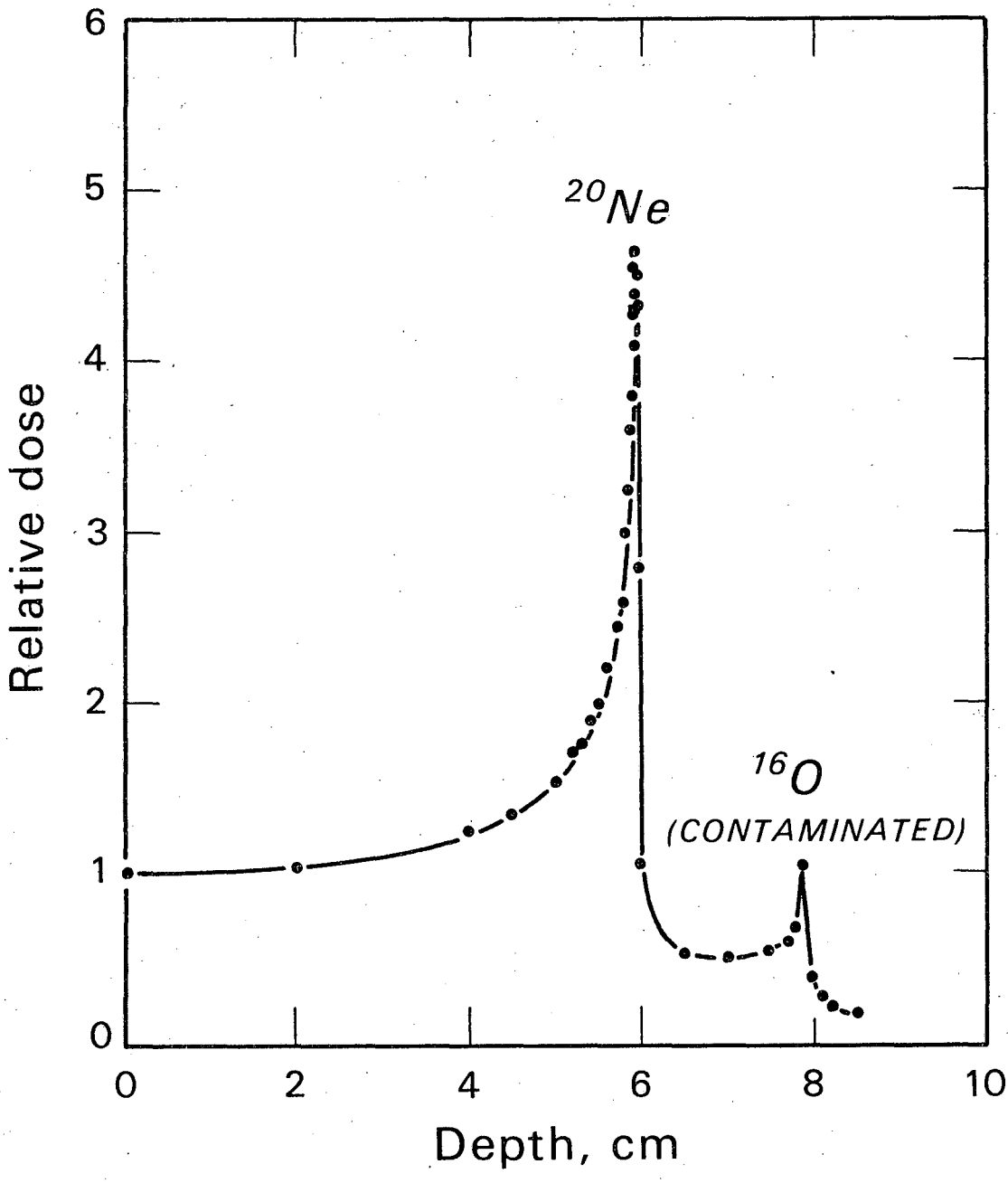

DBL 731-5014

Figure 5

INITIAL STUDIES ON OER, RBE, AND DEVELOPMENT OF *TRIBOLIUM* EGGS USING AN OXYGEN BEAM

Chui-hsu (Tracy) Yang, Laurie Craise, Graeme P. Welch, and Cornelius A. Tobias

Donner Laboratory — Lawrence Berkeley Laboratory
University of California, Berkeley, Ca. 94720

Abstract.

An investigation on OER and RBE in an embryonic system at various positions in the depth-dose curve of an oxygen-ion beam was made. The value of OER decreases with an increase of LET in the range studied, from 27 keV/μ to 53 keV/μ. RBE varies with LET and increases more rapidly for eggs irradiated in nitrogen. The detrimental effects of oxygen ions on the development of Tribolium at various stages of the life cycle were observed.

Introduction.

About a year ago Tribolium confusum eggs were used as a test system to examine the effects of N^{7+} ions on biological development at very low doses, less than ten thousand particles, in the interests of space radiobiology. Some permanent damage due to heavy-ion irradiation was seen early embryo development, late matamorphosis of larvae, and the gross structure of adults (e.g. antennal deformity) (1). With recent improvements in dosimetry of heavy-ion beams generated at the Bevatron in this Laboratory, a further investigation of OER and RBE with different LET in living organisms has become feasible. The purpose of the present study has been to determine the OER and RBE at various positions in the depth-dose curve of an oxygen-ion beam, using an embryonic system and to obtain more quantitative information about the lasting effects of heavy ions on the development of Tribolium.

Materials and Methods.

The general methods of collecting Tribolium confusum eggs have been reported elsewhere (2). For this experiment Tribolium eggs were collected during eight hours at 23°C from 1-month-old adults and irradiated before blastoderm stage. Under a dissecting microscope, about eighty healthy-looking eggs were chosen and placed in a polyethylene tube with I.D. of one-sixteenth of an inch. Eggs were kept at 23°C and R. H. ~30% before, during, and after irradiation. The number of larvae hatched was checked twice a day in order to determine the effects of radiation on embryo development, and hatched larvae were transferred to a separate dish containing several milli-liters of flour-yeast media until they became pupae, which were then sexed. About one week after eclosion, adults were examined under a dissecting microscope to determine the type and number of abnormalities.

The setup used in our oxygen-ion beam irradiation of Tribolium confusum eggs is illustrated in Figure 1. In brief, about eighty eggs were put in a section (about 0.5 cm) of a polyethylene tube, which was then placed in the hole of a polyethylene rod (2.5 cm ×10 cm). A small piece of cotton plugs was placed on each end of the section containing eggs in order to hold the eggs in position during irradiation. Seven holes of equal size were drilled at different angles and positions along the lucite holder so that eggs were

always lined up at the center of the oxygen beam and exposed to radiation of various LET (front view, Fig. 1). Gas (air or nitrogen was passed continuously through a gas washing bottle, maintaining a constant relative humidity, and then through eggs at a flow rate of about 1 ml/min. before and during irradiation. To ensure a hypoxic condition when nitrogen gas was used, eggs were gassed for at least 15 minutes continuously before the exposure. The oxygen-ion beam used for this experiment had a cross-section geometry of about 1×1 cm^2 and a relatively uniform distribution of oxygen ions (220 MeV/amu). No water absorber was placed between the beam and the biological samples. The entrance doses of the beam were measured by ionization chambers and fast scintillation counters, which were placed before the lucite holder. The actual doses that would be absorbed by the target in question, the eggs, were calculated by using Bragg ratios. For a detailed description of the dosimetry setup and the physical properties of the oxygen beam see Ref. (3), p. 100 of this report.

A dose rate at about 50 rads/min generated from a Philips x-ray unit was used for the X-irradiation experiment, and the same gassing procedure was followed. Physical conditions of irradiation were 220 kV, 15 mA; and a 1.0 mm Al filter was used.

At the end of irradiation, eggs were transferred from the polyethylene tube to a glass petri dish to evaluate hatchability.

Results and Discussion.

Figure 2 shows the effects of oxygen ions on the development of *Tribolium* eggs irradiated with different entrance doses at various points along the polyethylene holder in the presence of oxygen. The hatchability changed gradually along the first three points and dropped very rapidly along the next four. Four different doses, ranging from 60 rads to 200 rads, were used, and the survival of eggs decreased accordingly at all points.

Similar results were obtained while eggs were irradiated in nitrogen, as shown in Figure 3. In the same figure, the Bragg curve for the polyethylene holder, calculated from data determined with a water absorber, is given. Because of the sharpness of the Bragg peak, it was quite difficult to place eggs exactly at the point of maximum irradiation, and eggs in positions 6 and 7 were not irradiated at the peak. A correlation, however, between the Bragg curve is observed. Hatchability tends to decrease as the Bragg ration increases.

A comparison of egg survival as a function of depth in the presence of oxygen with egg survival in nitrogen, as shown in Figure 4, indicates that there is an oxygen effect. In order to determine the oxygen enhancement ratio (OER), dose-response curves have been plotted and are shown in Figures 5 and 6. It can be seen that the slope of the curve becomes steeper as the depth increases. The extrapolation number, $\tilde{n}$, $\simeq 2$, determined from survival curves of γ-irradiated eggs. Based on the limited quantitative dose data we have, we can say that a small initial shoulder appear to exist in some survival curves. An OER value of about 2.62 at LD_{63} (mean lethal dose) was obtained for X-rays from the survival curves presented in Figure 7. For oxygen ions, the value of OER decreased from about 2.61 at Position 2 to 1.73 at Position 6. When LET is plotted versus OER, as shown in Figure 8, OER tends to reach a value of about 1.0 at LET around 100 keV/μ.

An attempt was also made to determine the relative biological effectiveness (RBE) for different LET from the present experimental data, and results are given in Table 1 and Figure 8. In the presence of oxygen, an increase of RBE from about 1.70 at Position one, with LET about 27 keV/μ, to 2.58 at Position six, with LET of about 51 keV/μ, was observed. Under hypoxic conditions the RBE changed more rapidly with LET, from about 2.2 at 33 keV/μ to 3.9 at 51 keV/μ, for example. Since survival at Positions 1 and 2 remained high, RBE values for these positions were determined by using LD_{30} (the dose required to reduce survival by 30%) and could be higher than the true values. However, the general shape of the RBE vs. LET curve should be valid. Since most Tribolium eggs were irradiated at the intermediate positions on the Bragg curve, the value of LET which will give a maximum RBE cannot be determined from this experiment, and further investigations are needed.

The effects of oxygen ions on early embryonic development as well as on late metamorphosis in Tribolium were checked, and results are summarized in Table 2. Injuries induced at early egg stage clearly persisted through some of the later development stages. The decrease of pupation parallels that of hatchability, indicating that radiation injurieis remain in Tribolium through the larval stage. Observable gross structure changes in irradiated adult groups were found, and some major types of abnormalities frequently appearing in this experiment are shown in Figure 9. The antennal deformity (fused segments), which was observed in an earlier nitrogen-ion irradiation experiment (1), was also found in the oxygen-ion irradiated

groups but at a substantially higher frequency. Out of 62 adults, for example, 3 showed fused antennal segments in the group receiving 60 rads in air, in contrast to the control group, which showed no such abnormalities. No consistent and significant influence, however, on eclosion due to heavy ions was found. Whether the control mechanism for eclosion is repaired at larval stage or is relatively radioresistant, or both cannot be answered at present; more studies are required.

The induction of gonad mutation by heavy-ion irradiation at egg stage is presently under investigation, and results will be reported in the near futrue.

Acknowledgments.

We wish to acknowledge the technical assistance of the Bevatron crew. This work is supported by the U. S. Atomic Energy Commission and the National Aeronautics and Space Administration.

REFERENCES

1. Yang, T. C., Heinze, B.D., Maccabee, H., and Welch, G., Effect of nitrogen ions on biological development. LBL-529, 109-120 (1971).

2. Yang, T.C., Silver, I.L., and Heinze, B.D., Tribolium Information Bulletin 13, 90-93 (1970).

3. Lyman, J.T., J. Howard, G.P. Welch, W. Schimmerling, and C.A. Tobias, Experimental setup and physical measurements of the heavy-ion beams used for biological irradiations, p.100 of this report, LBL-2016 (1973).

Table 1. OER and RBE for oxygen ion irradiated *Tribolium confusum* eggs.

Radiation	Sample Position	Bragg Ratio	Energy (Mev/nucleon)	Average LET (kev/u)	Gas	Entrance Dose (rads) MLD	Entrance Dose (rads) LD_{30}	Corrected Dose* (rads) MLD	Corrected Dose* (rads) LD_{30}	OER	RBE
X-rays (220 kV)	----	-----	-------	0.27	air	500	280	---	---		
					N_2	1310	870	---	---	2.62	---
Oxygen ions	1 (0.25cm)	1.00	224	27	air	---	165	---	165	----	1.70
	2 (5.00cm)	1.33	128	33	air	---	115	---	153		1.83
					N_2	---	300	---	399	2.61	2.18
	3 (6.01cm)	1.52	103	37	---	---	---	---	---	---	---
	4 (6.79cm)	1.84	79	42	air	140	---	258	---		1.94
					N_2	320	---	589	---	2.28	2.22
	5 (7.18cm)	2.11	64	47	air	105	---	222	---		2.25
					N_2	212	---	447	---	2.01	2.93
	6 (7.41cm)	2.36	55	51	air	82	---	194	---		2.58
					N_2	142	---	335	---	1.73	3.91
	7 (7.61cm)	2.73	44	58	air	82	---	194	---		2.58
					N_2	125	---	341	---	1.76	3.85

* Calculated by (Entrance Dose) x (Bragg ratio).

Table 2. Effects of oxygen ion radiation on the development of Tribolium at different stages of life cycle.

Gas	Entrance Dose (rads)	Position	No. Eggs	Hatchability (%)	Pupation (%)	Eclosion (%)	Abnormalities (%)
Air	0	--	609	89.83	95.98	100.00	0.00
	60	1	76	77.93	92.86	95.38	9.68
		2	78	70.13	93.65	100.00	8.47
		3	76	63.45	89.47	98.04	8.00
		4	79	63.45	84.21	100.00	6.25
		5	76	52.32	85.11	97.50	10.25
		6	75	47.87	74.42	100.00	9.37
		7	79	37.85	73.53	88.00	18.18
	99	1	77	69.02	90.32	94.64	13.21
		3	75	57.89	76.92	95.00	10.53
		4	75	40.08	77.78	100.00	17.86
		5	66	28.94	76.92	100.00	35.00
		6	74	16.00	66.67	---	---
		7	71	5.57	40.00	---	---
	150	1	78	55.66	76.00	94.74	8.33
		2	77	50.10	86.67	76.92	20.00
		4	78	26.72	66.67	100.00	18.75
		5	79	13.36	50.00	100.00	16.67
		7	75	7.79	28.57	100.00	0.00
	200	1	75	48.98	81.82	100.00	11.11
		3	76	18.93	47.06	100.00	37.50
		5	75	6.68	66.67	100.00	25.00
		6	80	2.23	50.00	100.00	0.00
		7	69	2.23	50.00	100.00	0.00
N_2	100	1	60	81.67	95.91	95.74	2.22
		2	73	100.00	91.78	94.03	3.17
		3	55	82.27	95.83	97.83	6.67
		4	70	65.71	86.96	100.00	10.00
		5	74	82.43	86.89	98.11	13.46
		6	76	46.05	---	----	---
		7	76	46.05	65.71	95.65	18.18
	226	1	75	85.33	92.19	98.30	15.52
		2	80	73.75	94.91	98.21	7.27
		3	74	72.97	77.78	95.24	12.50
		4	75	40.00	73.33	100.00	18.18
		5	77	29.87	56.52	100.00	30.77
		6	77	18.18	42.86	100.00	50.00
		7	78	7.69	50.00	100.00	0.00
	302	1	74	74.32	90.91	94.00	8.51
		2	49	75.51	78.38	93.10	11.11
		3	73	63.01	78.26	100.00	16.67
		4	65	38.46	76.00	78.95	13.33
		5	70	18.57	23.08	100.00	0.00
		6	77	7.79	50.00	100.00	0.00

FIGURE CAPTIONS

Fig. 1. An illustration of the setup used for oxygen-ion beam irradiation of *Tribolium confusum* eggs.

Fig. 2. Survival of *Tribolium* eggs irradiated at different entrance doses of oxygen ions at various points along the polyethylene holder in the presence of oxygen.

Fig. 3. The effect of oxygen ions on the development of *Tribolium* eggs irradiated at three different entrance doses in the presence of nitrogen at various points along the depth-dose curve of the oxygen beam. A Bragg curve for the polyethylene holder is given at bottom of the figure.

Fig. 4. A comparison of the survival of Tribolium eggs as a function of depth in the presence of oxygen with survival nitrogen.

Fig. 5. Dose-response curves for *Tribolium* eggs irradiated with oxygen ions in air. Entrance doses are given.

Fig. 6. Dose-response curves of *Tribolium* eggs irradiated with oxygen ions in the presence of nitrogen. Entrance doses are given.

Fig. 7. Survival curves for *Tribolium* eggs irradiated in air or nitrogen with X-rays.

Fig. 8. RBE and OER of Tribolium eggs for radiations of different LET.

Fig. 9. An illustration of abnormalities observed in *Tribolium confusum* adults irradiated with oxygen ions at egg stage.

SETUP USED IN HEAVY PARTICLE IRRADIATION OF T. CONFUSUM EGGS

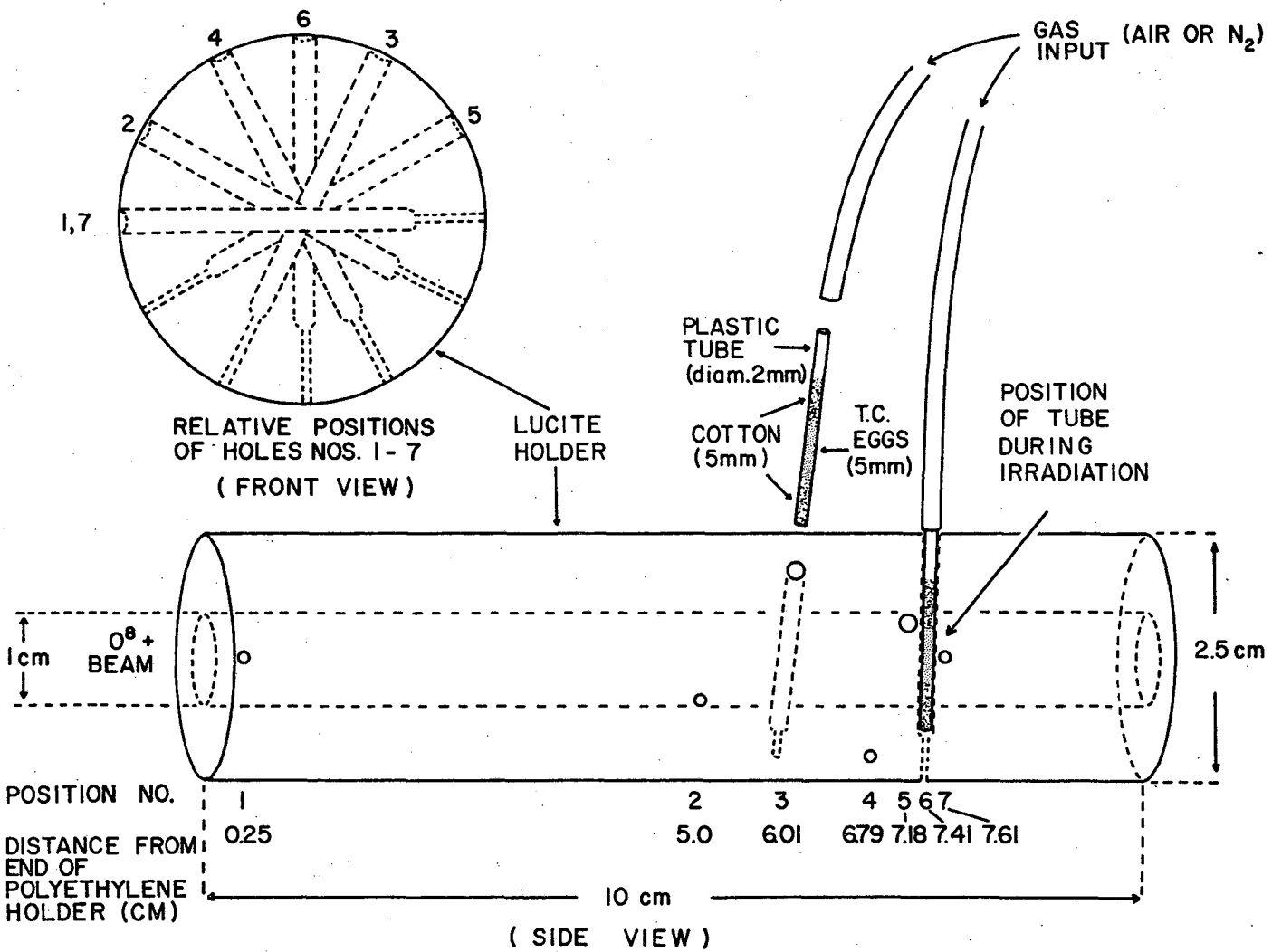

XBL 731-62

Figure 1

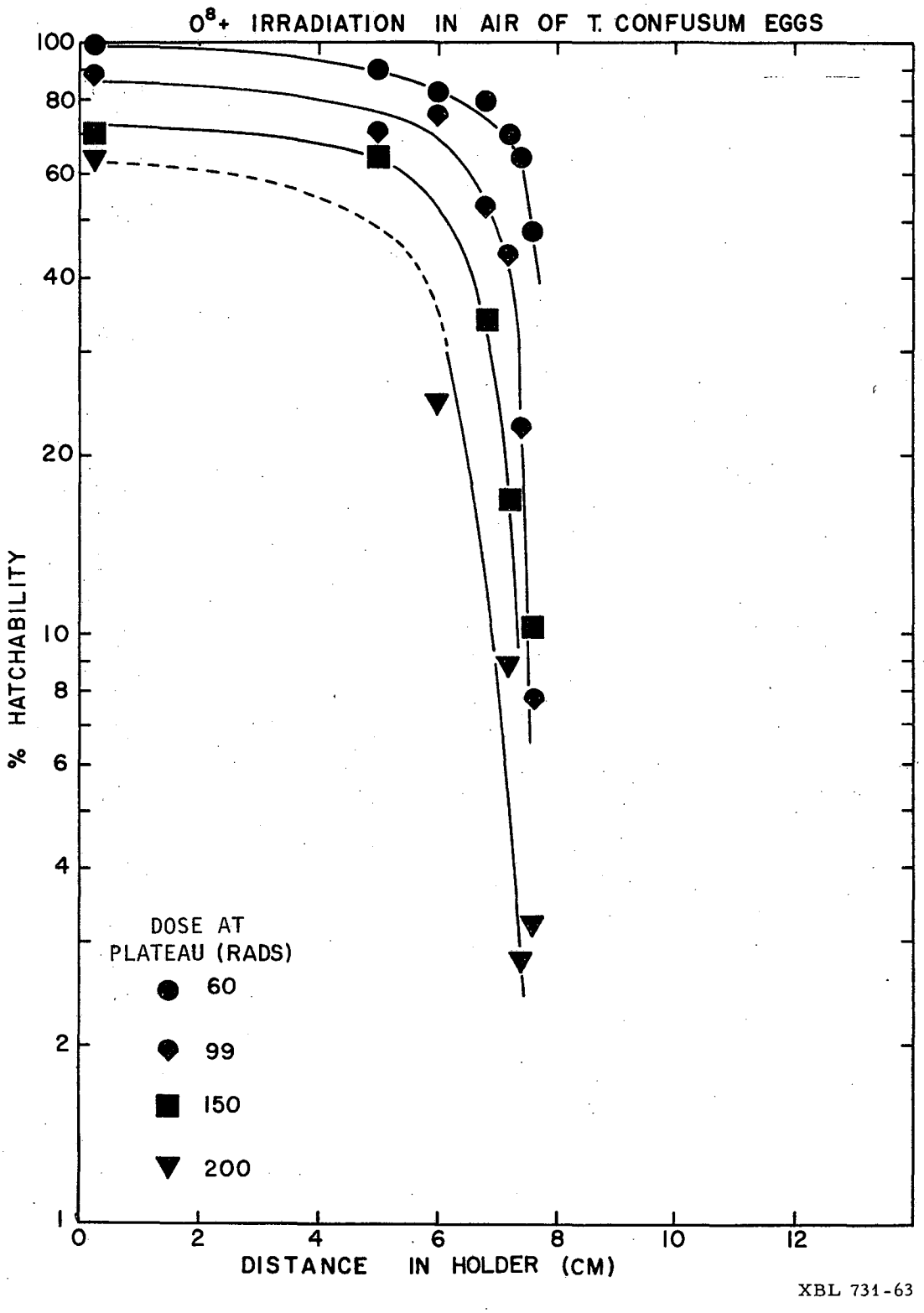
O^{8+} IRRADIATION IN AIR OF T. CONFUSUM EGGS
% HATCHABILITY
100
80
60
40
20
10
8
6
4
2
1
0
2
4
6
8
10
12
DISTANCE IN HOLDER (CM)
DOSE AT PLATEAU (RADS)
60
99
150
200
XBL 731-63

Figure 2

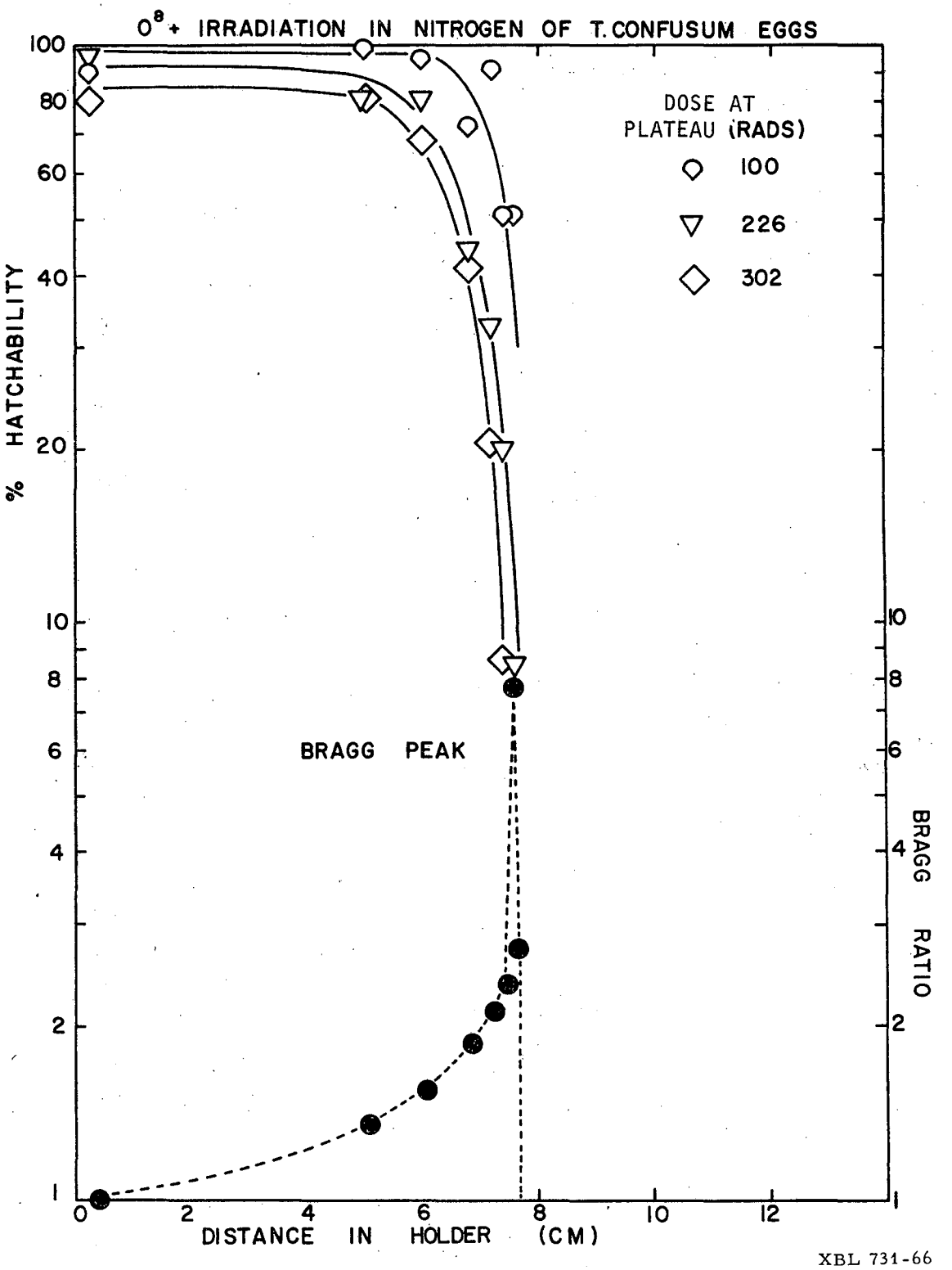
O8+ IRRADIATION IN NITROGEN OF T.CONFUSUM EGGS
% HATCHABILITY
BRAGG RATIO
DISTANCE IN HOLDER (CM)
DOSE AT PLATEAU (RADS)
100
226
302
BRAGG PEAK
XBL 731-66

Figure 3

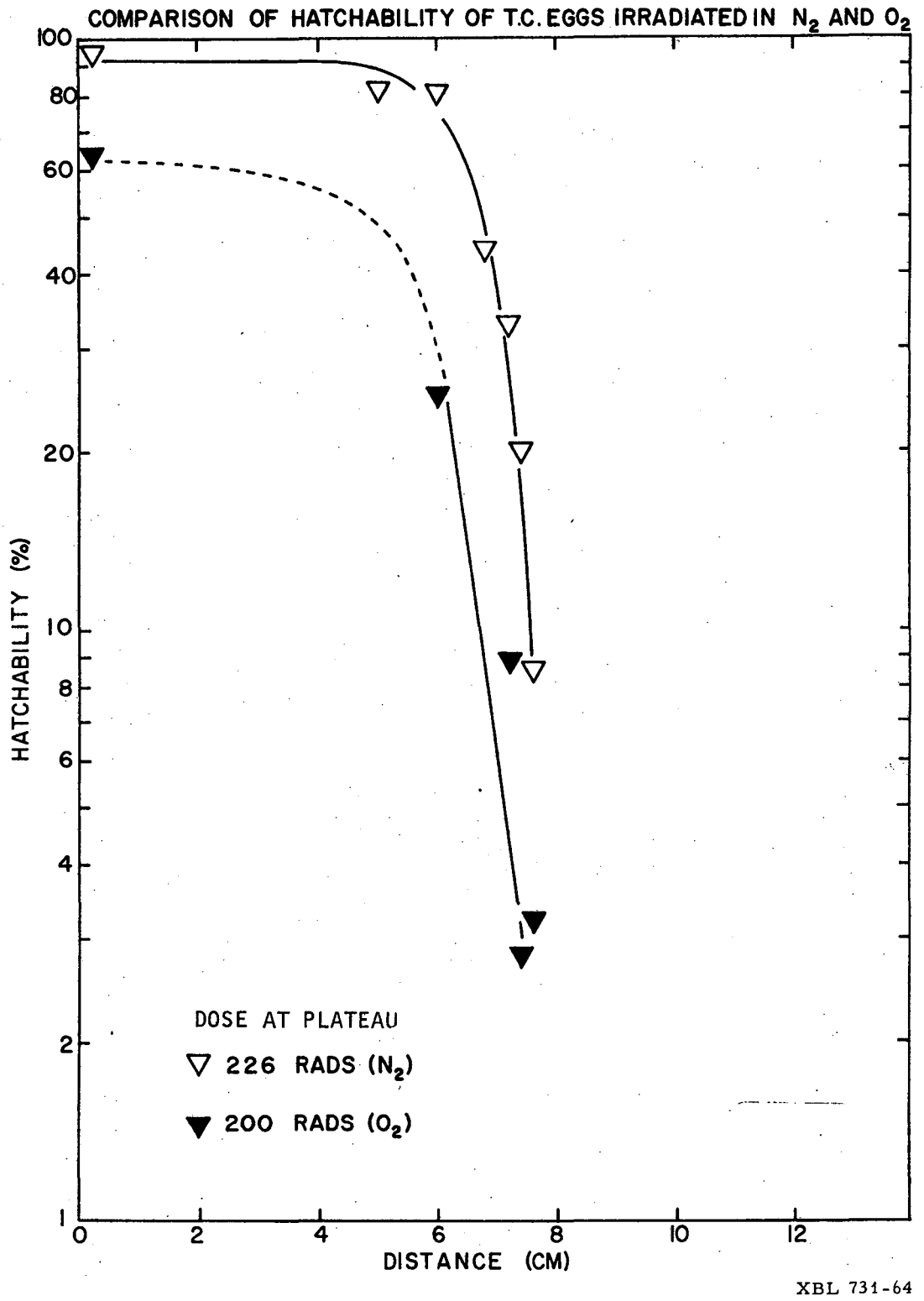
COMPARISON OF HATCHABILITY OF T.C. EGGS IRRADIATED IN N_2 AND O_2
HATCHABILITY (%)
100
80
60
40
20
10
8
6
4
2
1
0
2
4
6
8
10
12
DISTANCE (CM)
DOSE AT PLATEAU
226 RADS (N_2)
200 RADS (O_2)
XBL 731-64

Figure 4

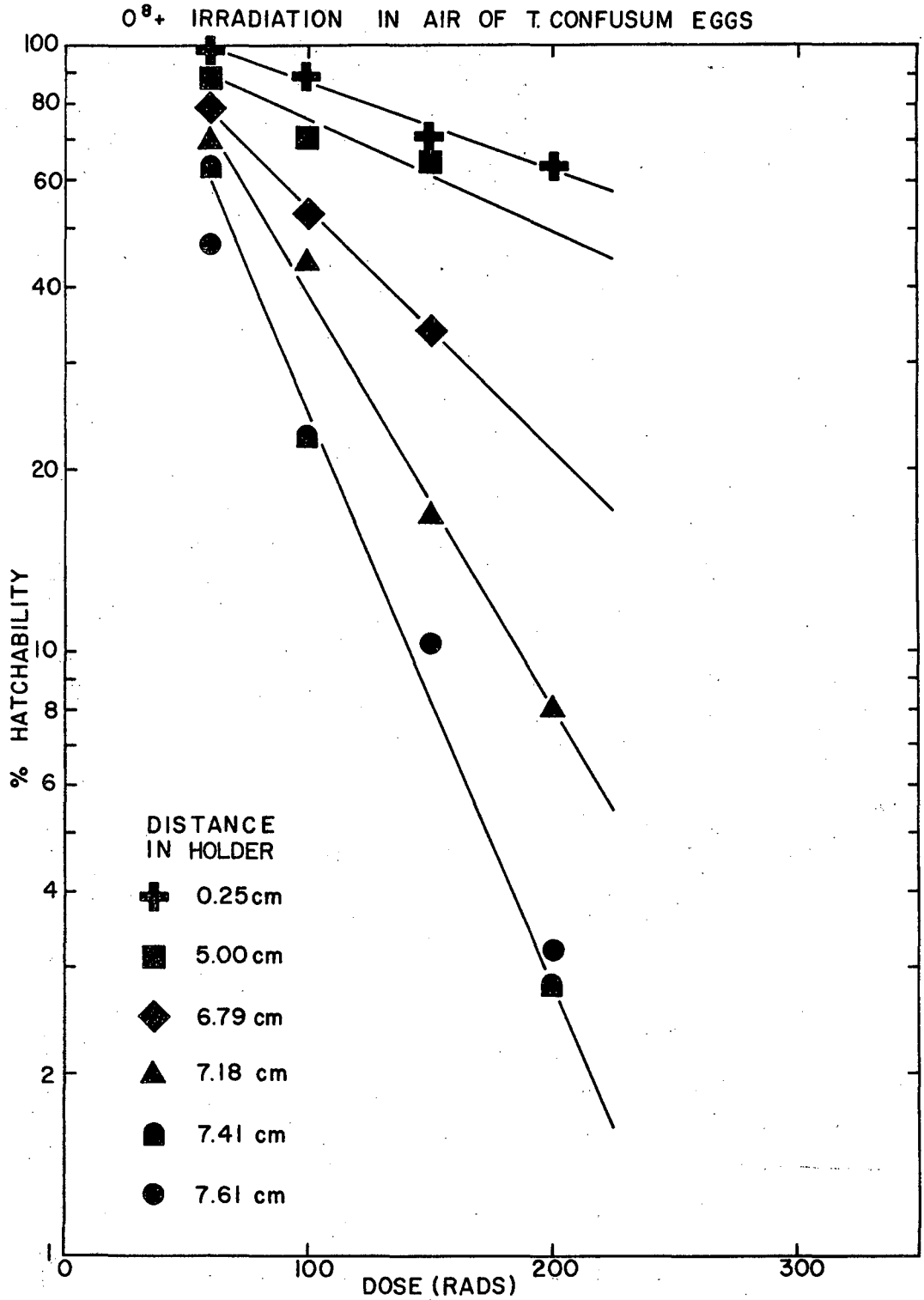

XBL 731-70

Figure 5

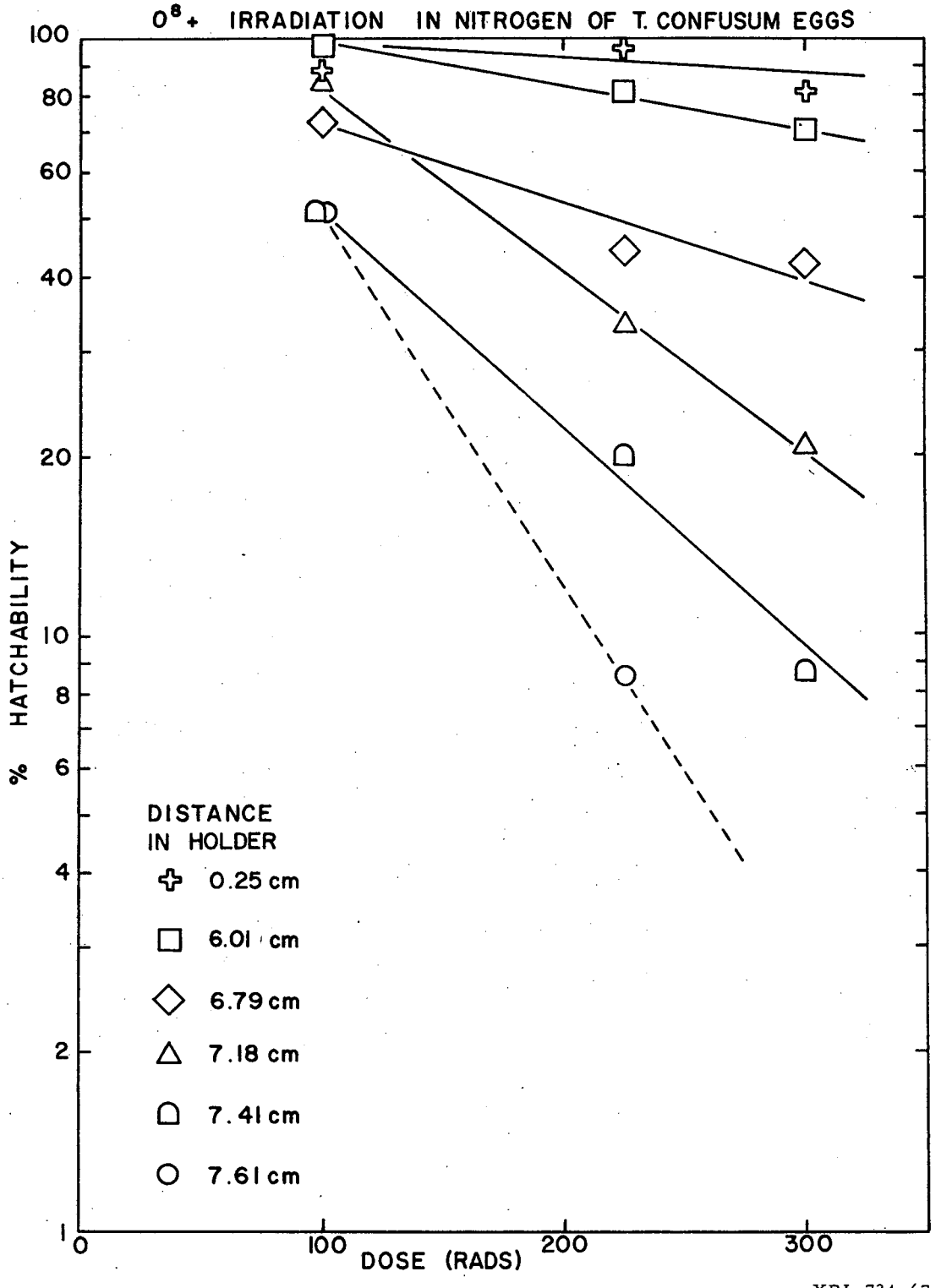

XBL 731-67

Figure 6

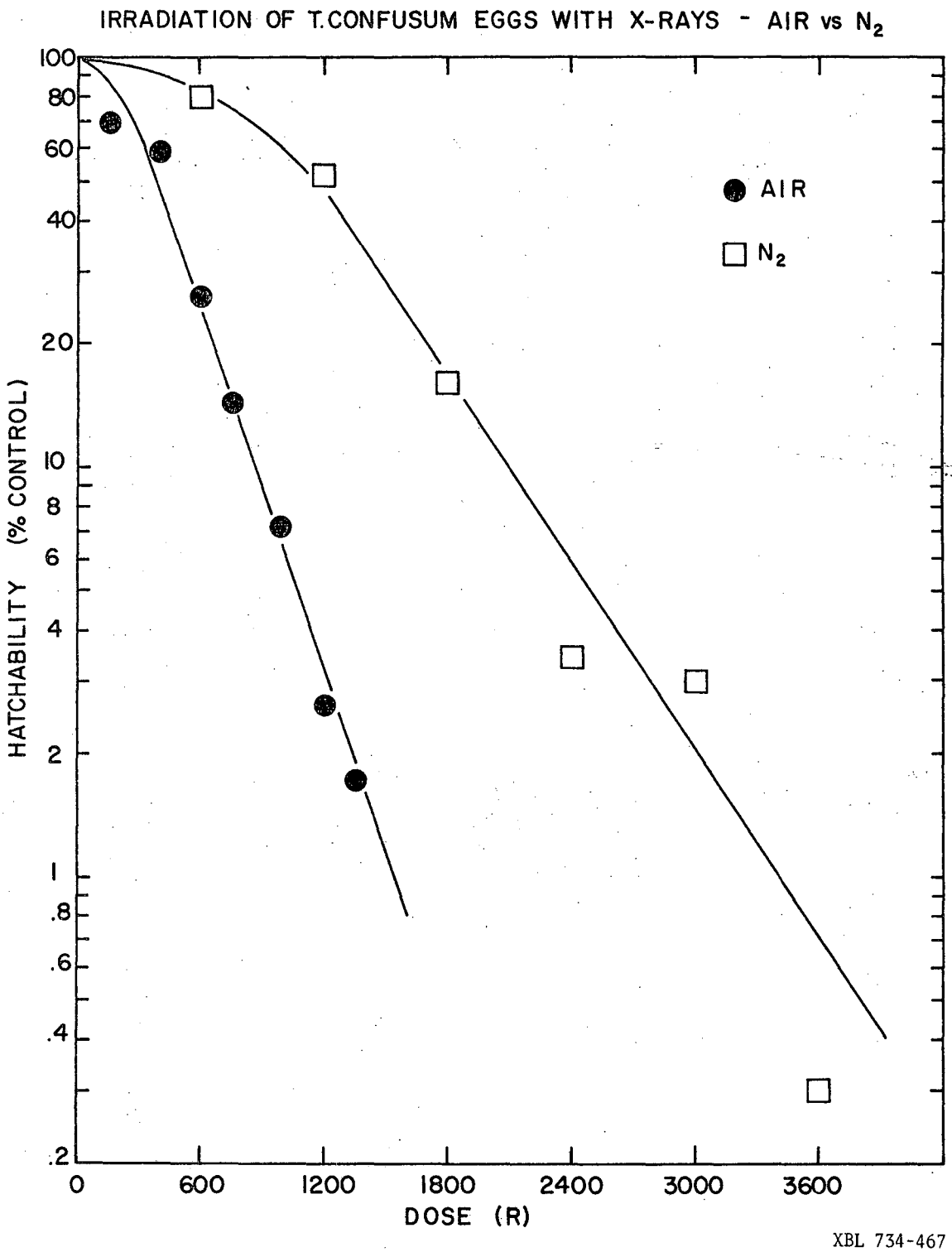
IRRADIATION OF T.CONFUSUM EGGS WITH X-RAYS - AIR vs N2
HATCHABILITY (% CONTROL)
100
80
60
40
20
10
8
6
4
2
1
.8
.6
.4
.2
0
600
1200
1800
2400
3000
3600
DOSE (R)
AIR
N2
XBL 734-467

Figure 7

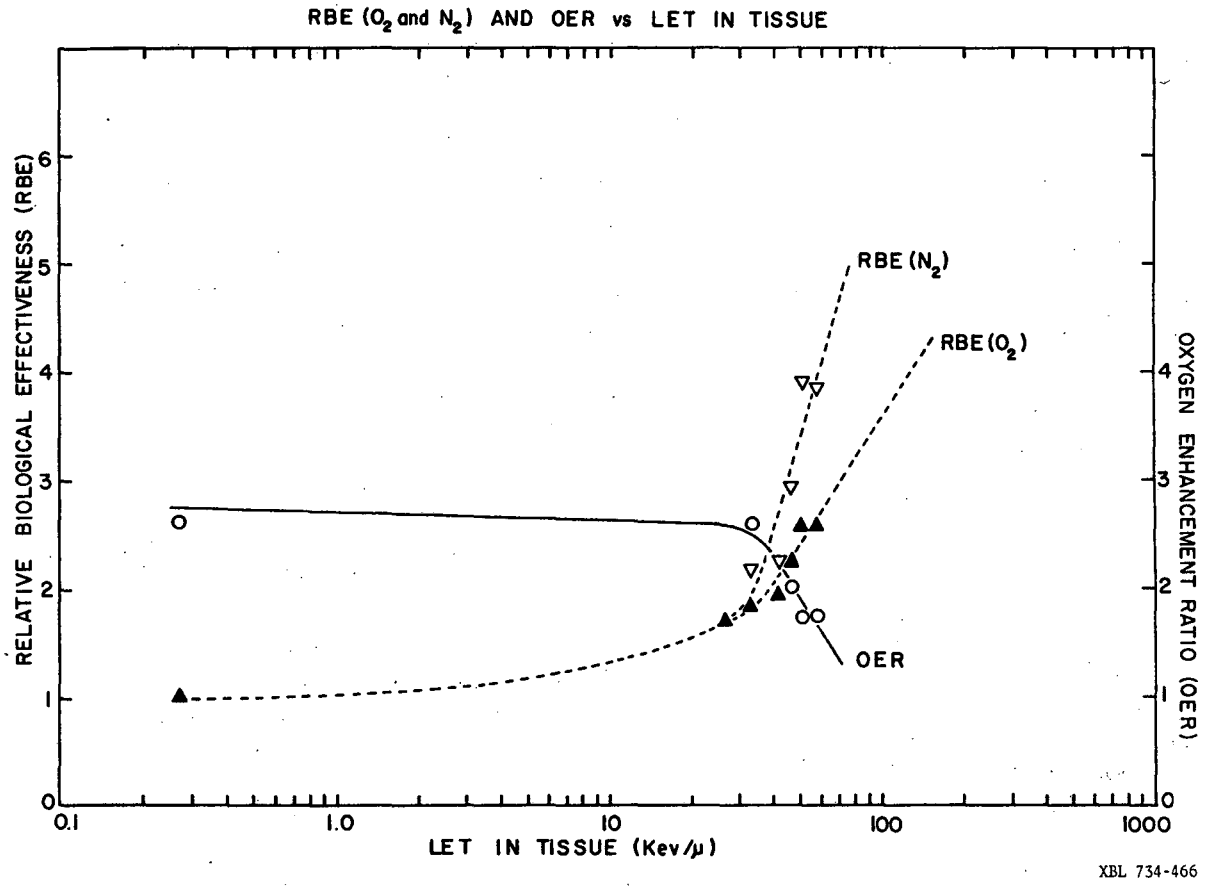
RBE (O_2 and N_2) AND OER vs LET IN TISSUE
RELATIVE BIOLOGICAL EFFECTIVENESS (RBE)
OXYGEN ENHANCEMENT RATIO (OER)
LET IN TISSUE (Kev/μ)
RBE (N_2)
RBE (O_2)
OER
0
1
2
3
4
5
6
0.1
1.0
10
100
1000
XBL 734-466

Figure 8

0 0 0 0 4 0 0 1 3 6 1

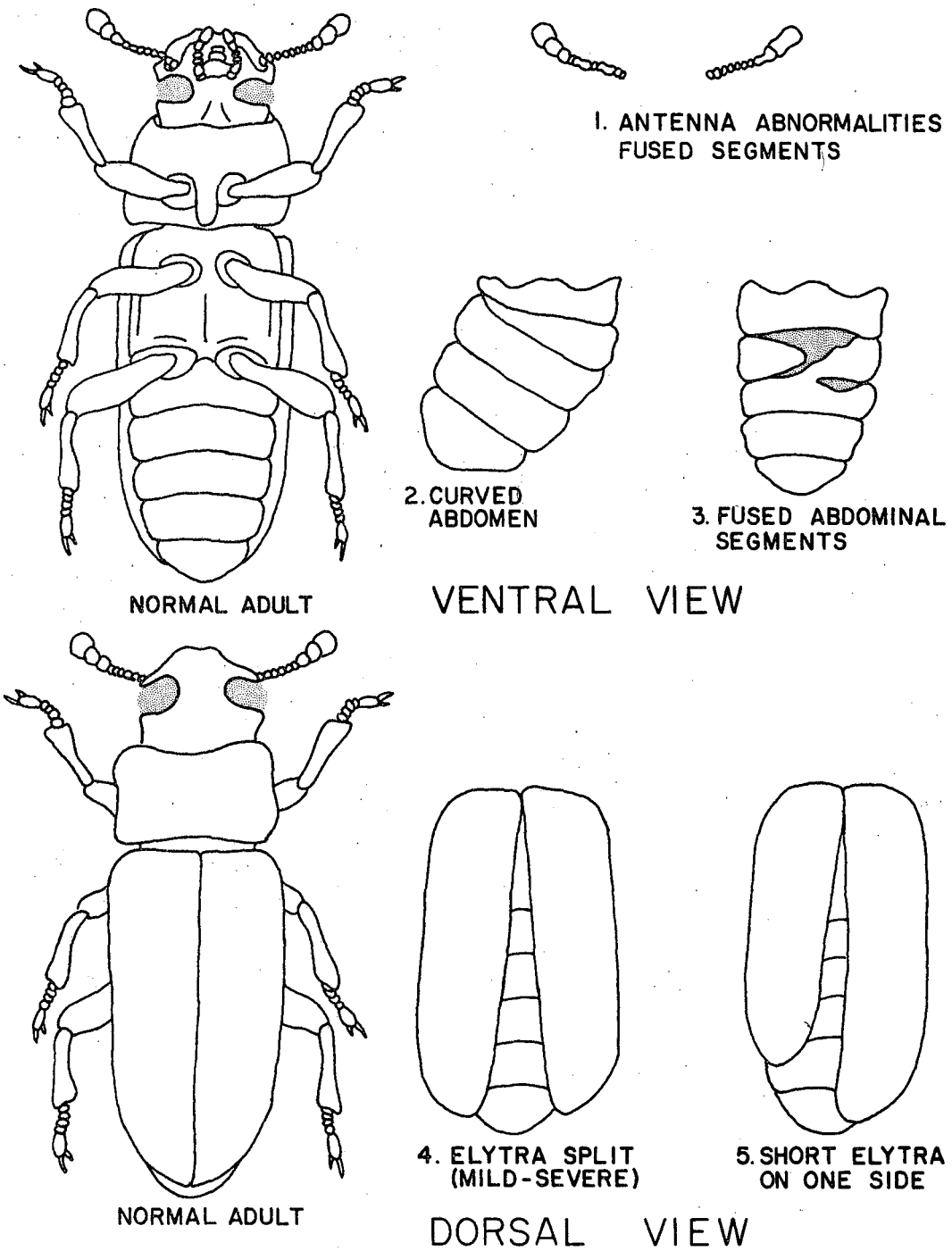

ADULT ABNORMALITIES FOUND IN T. CONFUSUM AFTER EGGS IRRADIATED WITH O^{8+}

XBL 731-68

Figure 9

STUDIES OF THE DEVELOPMENT OF *ZEA MAYS* IRRADIATED WITH ACCELERATED OXYGEN IONS

Chui-hsu (Tracy) Yang, Eugene V. Benton, Laurie Craise, and Cornelius A. Tobias

Donner Laboratory—Lawrence Berkeley Laboratory
University of California, Berkeley Ca. 94720

Abstract.

The effects of high-LET oxygen ions on growth, differentiation, morphogenesis, and mutation were investigated. Leaf growth appeard to be much more sensitive to oxygen ions than to gamma rays; a shoulder was found in the dose-response curve. Arrest in pigmentation, irregular morphogenesis, and visible streaks were observed in the oxygen-ion irradiated group. The ratio of total stripe length to leaf length reflected linear increase with dose, at a rate about 0.05% per rad of oxygen-ion irradiation. The stripe became more prominent in later leaves. The number of oxygen particles stopped in the corn seeds was monitored with a special method. Some of the experimental observations indicate that heavy-ion irradiation can be very useful in solving certain fundamental biological problems.

Introduction.

The effects of cosmic radiation on seed differentiation and development were first studied and reported by Slater and Tobias (1). Arrests in pigmentation, irregular morphogenesis, and visible streaks in leaves were found in seeds recovered from a high-altitude balloon flight. Using corn seeds of a speical genetic stock, Curtis and Smith (2) observed a slight increase in chromosomal deletions and also in sector frequency in corn recovered from a satellite flight when compared with controls. Since the number of particles absorbed by corn seeds was extremely small, both results suggest that cosmic rays can be very effective in inducing biological damage. The recent success in accelerating heavy ions to very high energies (several hundred MeV/amu) at the Bevatron in Berkeley provides an opportunity to evaluate the effects of heavy ions on biological development under controlled conditions and at sea level. The purpose of the present experiment has been to determine the effects of high-LET radiation on growth, differentiation, morphogenesis and mutation in dry corn seeds.

Materials and Methods.

Corn seeds, consisting of one-third homozygous yellow kernels (genotype $Lw_1 Lw_1$) and two-thirds heterozygous yellow kernels ($Lw_1 Lw_1$), were obtained from Ratio Seeds Co., Champaign, Illinois. Before treatment all seeds were kept in a desiccator at 5% relative humidity. Corn seeds were placed, six at a time, with embryos facing up and towards the center, in a special holder (I.D. = 2.5 cm) and were covered with a layer of cellulose nitrate (type USF4b, thickness of about 110 1) which serves as the dosimetry monitor. The seeds were held in place with double-sided Scotch tape and were numbered clockwise, starting with the seed stained with black ink. The layer of cellulose nitrate has three or four reference holes, as well as a number to identify the particular set of corn seeds. The exposure was made so that the oxygen beam entered the monitor layer first, then the seeds, the Scotch tape and the holder itself. Prior to disassembling them for further processing, the holders were photographed. The prints were made to the original dimensions of the individual seed arrangements. In this manner a record of the exact geometrical relationship between the seeds and their monitor layer was obtained. Before this layer was etched to enlarge the particle tracks to microscopic size, it was superimposed

and aligned on its life-sized photograph, and the outline of the seed(s) was scratched into the plastic for each seed whose exposure was to be determined. The etching was done in a 6.25 N solution of NaOH in H_2O at 40° C. The etch times are shown in Table 1. The monitor layers were immersed in individual test tubes containing 100 ml of the etchant. No stirring was possible or deemed necessary in view of the short etch times anticipated. The track counting was performed under a magnification of 650X. The sampling area was centered on the outline of the corn embryo enscribed onto the monitor. (A number of adjacent sites were sampled to ascertain the uniformity of the track distribution over the area of the embryo.) With the particular eyepiece used, the field of view appears subdivided into 100 squares of $(20\ \mu)^2$. The number of these squares within which the tracks were counted was chosen so as to keep the counting statistics about the same in all cases (four squares for very high track densities, up to 36 for the lowest ones).

The oxygen-ion beam, with an energy of 220 MeV/amu and a beam spot of 2 cm × 4 cm, was generated at the Bevatron. The Bragg peak of the beam was placed 2 mm below the surface of the seeds, so that the whole embryo would be irradiated in the Bragg peak region. For a full description of the parameters see Lyman, and etc. (3).

The gamma rays were generated by a 1500-Curie Co^{60} source and seeds were exposed to different doses at a dose rate of 48 rads/min.

All seeds were sown in a greenhouse in flats (18" × 24" × 3"), with 15 seeds per flat. Greenhouse conditions during a 24-hour period provided sixteen hours of light at approximately 25° C and eight hours of darkness at approximately 23° C. Flats of the control group were placed side by side with those of irradiated groups.

Leaf length was measured from the base to the tip of the blade, and width of leaf was measured at the leaf mid point. No streak was recorded in this experiment unless readily observable from both sides of the leaf. Leaf area was calculated by multiplying (3/4) times (leaf length × leaf width), and the area of stripe by multiplying (Σ stripe length) times (Σ stripe width). All measurements were taken from the third leaf of the plants after the fifth leaf had begun to grow out.

Results and Discussion.

In this experiment doses ranging from 75 rads to 1000 rads (entrance dose) of oxygen ions were used. Table 1 lists the dosimetry data for some of the seeds exposed to oxygen ions and showed large white stripes on later leaves. The observed track densities vary from about 3 to 30 million per cm^2, as determined with a counting error of about 6%. The monitor layers from seed sets 112 and 113 were overetched by about 35 minutes, as compared with seed set 114, so that the tracks overlap sufficiently to render a count subject to errors several times $(N)^{1/2}$. However, there is good uniformity in the cross-section of the ^{16}O beam, which can be seen from the track counts in seed sets 121, 126, and 141. In each case the various seeds within the holder were subject to the same exposure, well within the counting error ($\sqrt{N}$). In fact, the same is true for holders no. 121 and 126 which were exposed to the same dose (at different times of course). Therefore, once can assume with reasonable certainty that the track density found in the nomitor layer of seed set 114 is also the track density which one would have found in monitors 112 and 113, were they not overetched. Counting tracks in the neighborhood of $30 \times 10^6/cm^2$ borders on the practical limits of the current method, so that in many trials only one reliable count could be obtained. This is the reason why the dosimetry data for holder no. 114 is shown in parentheses. The dosimetry data in Table 1 is graphed in Figure 1 to show the correlation between the observed track density and the ionization chamber reading from the Bevatron. As expected, the correlation is linear within the experimental error (counting statistics).

The uniformity of the oxygen-ion beam and the sharpness of Bragg peak can be determined with a stack of cellulose nitrate. Although there were no beam-profile stacks exposed during or after the corn seed exposures, some stacks were exposed just before the Bevatron was adjusted for these runs. The cellulose nitrate layer from one of these stacks has been etched and appears to be evenly "fogged", i.e., turned partially opaque to transmitted light, due to scattering by the track enlarged by etching, as shown in Figure 2. The x-y distribution of the oxygen beam seems, therefore, to be quite uniform. In Figure 3 is shown a Bragg peak from 220 MeV/amu oxygen ions stopping in a stack of cellulose nitrate. While several cm of degrader are used to stop the particles, the width of the peak is less than one millimeter. Since the exposure conditions (length of water column) were

changed between the beam-profile and the corn-irradiation exposures, it is difficult to know exactly where the Bragg peak is located in the corn exposures. Therefore, the track densities determined from the monitors indicate the number of particles that entered the corn embryos with LET higher than the cellulose nitrate threshold (0.1 MeV/μ). This number does not include those particles, if any, that have LET's smaller than this threshold and which therefore do not leave tracks. Since the stopping power of the corn is much like that of the tissue-equivalent Lexan, and since the seed is much thicker than the distance required to stop the Bragg peak in Lexan, all of the particles seen entering a seed also stop in the seed, and this number is proportional to the actual number stopping in the seed.

The effects of high-LET radiation on the growth of plants were observed, and a dramatic reduction in plant height and leaf size is shown in Figure 4. Comparing the length, width, and area of third leaves in oxygen-irradiated groups and control groups, as depicted in Figure 5, retardation in development of the third leaf is evidently dose-dependent, and a dose of 800 rads caused a 50% decrease in leaf area. It is worthwhile to notice that the change in width and length of leaves with dose remains the same, indicating there is a constant ratio between width and length of leaf. The control mechanism for this ratio, although possibly a genetic one, is unknown at the present time. The fact that this control mechanism is so insensitive to radiation when compared to plant growth is an interesting problem for both the radiobiologist and the development biologist. In the gamma-irradiated group, no significant change in leaf area was detected with doses up to 1000 rads, except at 75 rads a small but significant increase was found. The question of whether a small dose of gamma-rays can stimulate plant growth or not needs further study. A statistical analysis of the above results is summarized in Table 2.

Arrest in pigmentation, irregular morphogenesis, and visible streaks showed up in the embryonic and first leaves, and the size of streaks and depigmentation became more prominent in the second and third leaves, as shown in Figure 6. Drastic, large white stripes were found in the fourth and fifth leaves, as shown in Figure 7. In addition to stripes, many ridges appeared on the surface of leaves of oxygen-ion irradiated plants, and some leaves failed to spread flat or showed asymmetric growth. An example is shown in Figure 8.

The increase in size of stripes in the later leaves is not unexpected, since the number of embryonic cells in the seed which will produce the third, fourth, and fifth leaves is comparatively much smaller than the number for the first and second leaves. Heavy-ion-induced damage to the gene (Lw_1) in embryonic cells of the fourth or fifth leaf, containing an albino gene (lw_1), will produce a large white stripe corresponding to the particular combination of number of target cells in the embryo initially and the amount of cell division and expansion that occurs in subsequent growth.

The length and width of the stripes appearing on the third leaves were measured, and results are given in Figure 9. This figure clearly shows that both the total length and the total area of stripes with respect to leaf length and area in oxygen-irradiated groups is a linear function of dose. The ratio of stripe length to total leaf length increases about 0.05 per rad. No significant difference between the gamma-irradiated group and control group was found. A statistical analysis of the data, as shown in Table 3, indicates that a dose of 75 rads of oxygen ions produces a highly significant increase ($P < 0.001$) in the ratio of total stripe length to leaf length.

The percentage of plants showing stripes corresponding to various doses on the third leaves is plotted in Figure 10, and an exponential curve is shown for the oxygen-ion irradiated groups. This result suggests that a single hit by a heavy ion may be enough to cause mutation and that cells in seeds may not be able to repair the radiation damage induced by high-LET oxygen ions.

The main reason for choosing the third leaf to measure the effectiveness of high-LET oxygen ions in inducing stripes in this study is that the size of stripes on the third leaf was found to be relatively large and the number of stripes not too numerous to record. To detect the effects of heavy ions at very low doses, however, it may be better to choose the first leaf than the third one for recording purposes, since more than several times the number of stripes, even though small, appeared on the first leaf.

Since the Bragg peak of accelerated oxygen ions was located about 2 mm below the surface of the corn seeds, there is a good chance that an oxygen particle will pass through and will damage many layers of cells in the embryo and stripes on different leaves of the same plant consequently might be induced by a single ionization track. In fact, it was observed in this experiment that many plants did show an overlapping of stripes between

different leaves of the same plant while the leaves were young. Figure 11 shows the top view of an oxygen-ion-irradiated plant, and large white stripes can be seen on the third, fourth and fifth leaves. Because the leaf is constantly changing its position while it is growing, the overlapping of stripes among different leaves is not evident in this picture. However, the cells that did develop into stripes on these leaves could have been located adjacent to each other in the embryo.

This experimental observation shows the heavy-ion irradiation can circumvent conventional techniques and can be very useful in solving many fundamental problems in developmental biology, e.g., mapping the three-dimensional structure of the embryo in seeds, determining the number of leaf premordia in embryo, examining the dynamic relationship between cells during plant development, and studying the control mechanisms of growth.

Acknowledgments.

We thank the Department of Genetics, University of California, Berkeley, for their generosity in providing the greenhouse necessary for these experiments, and the staff of the Photography Department, Lawrence Berkeley Laboratory, for providing the photographs. We also wish to acknowledge the technical assistance of the Bevatron crew. This work is supported by the U. S. Atomic Energy Commission and the National Aeronautics and Space Administration.

0 0 0 0 4 0 0 1 5 6 5

REFERENCES

1. Slater, J. V., and C. A. Tobias. Effects of Cosmic Radiation on Seed Differentiation and Development. Radiat. Res. 19: 218 (1963).

2. Curtis, H. J., and H. H. Smith. Corn Seeds Affected by Heavy Cosmic Ray Particles. Science 141: 158-159 (1963).

3. Lyman, J. T., J. Howard, G. P. Welch, W. Schimmerling, and C. A. Tobias. Experimental Setup and Physical Measurements of the Heavy-Ion Beams Used for Biological Irradiations, p.100 of this report, LBL-2016 (1973).

TABLE 1. SUMMARY OF DOSIMETRY INFORMATION FOR THE CORN SEEDS EXPOSED TO ^{16}O BEAMS IN SEPTEMBER, 1972.

Holder number	Seed number	Bevatron dose (rad)	Scanned area (10^{-4} mm^2)	Observed no. of tracks in scanned area	Track density (10^6/cm^2)	Error, $\sqrt{N}$	Error, %	Etch time (hours)	Thickness removed (μ)	Surface etch rate (μ/hr)
98	1	300	64	583	9.1	24	4.2	2.58	2.8	0.54
112	3	1000	Monitor layer was overetched, resulting in considerable track overlap					2.58	2.9	0.56
	5									
	6									
113	2	1000						2.58	2.9	0.56
	4									
	6									
114	1	1000	(4)	(126)	(31.5)	(11)	(8.8)	1.75	12.2	3.48
	2									
	4									
	5									
121	1	600	16	300	18.7	17	5.8	1.75	1.5	0.43
	3		16	321	20.0	18	5.6			
126	5	600	16	294	18.4	17	5.8	1.75	3.4	0.97
	6		16	298	18.6	17	5.8			
132	2	150	64	261	4.08	16	6.2	2.00	1.9	0.47
141	4	75	144	387	2.68	20	5.1	2.00	1.9	0.47
	6		144	381	2.64	20	5.1			

Table 2. EFFECT OF RADIATION ON THE GROWTH OF THIRD LEAF.

Radiation	Dose (rads)	Number of Plants	Ave. leaf Area (cm^2)	Standard Error	t	Probability
Oxygen ion						
	0	75	94.26	2.89	----	-----
	75	48	91.88	2.53	0.619	$0.6 > P > 0.5$
	150	45	89.15	2.75	1.281	$0.3 > P > 0.2$
	300	52	75.54	1.98	5.355	$P \ll .001$
	600	47	58.83	2.20	9.749	$P \ll 0.001$
	1000	46	36.03	2.06	16.404	$P \ll 0.001$
Gamma-rays (Co^{60})	0	142	95.87	1.96	-----	-----
	75	40	104.97	3.57	2.233	$0.05 > P > 0.02$
	150	41	96.53	3.09	0.181	$0.9 > P > 0.8$
	300	45	93.62	2.90	0.641	$0.6 > P > 0.5$
	600	46	92.96	2.18	0.989	$0.4 > P > 0.3$
	1000	46	97.92	3.69	0.491	$0.7 > P > 0.6$

TABLE 3. EFFECT OF RADIATION ON THE RATIO OF THE STRIPS LENGTH AND THE LEAF LENGTH.

Radiation	Dose (rads)	Number of Plants	(Stripe Length / Leaf Length %)	Standard Error	t	Probability
Oxygen ion						
	0	75	0.821	0.496	--	----
	75	48	6.868	1.718	3.382	$P < 0.001$
	150	45	7.236	1.963	3.168	$0.001 < P < 0.01$
	300	52	22.318	3.407	6.244	$P \ll 0.001$
	600	47	19.748	3.955	4.748	$P \ll 0.001$
	1000	46	39.242	4.192	9.102	$P \ll 0.001$
Gamma-rays (Co^{60})	0	142	0.391	0.209	--	----
	75	40	0.304	0.213	0.292	$0.7 < P < 0.8$
	150	41	0.312	0.308	0.212	$0.8 < P < 0.9$
	300	45	1.435	0.805	1.255	$0.2 < P < 0.3$
	600	46	0.928	0.526	0.949	$0.3 < P < 0.4$
	1000	46	2.069	1.577	1.055	$0.2 < P < 0.3$

FIGURE CAPTIONS

Fig. 1. A layer of oxygen-ion-irradiated cellulose nitrate after etching. Notice the plastic is evenly "fogged".

Fig. 2. Relative detectivity of the cellulose nitrate monitors.

Fig. 3. Bragg peak of oxygen beam monitored by a stack of cellulose nitrate.

Fig. 4. Photograph of corn plants showing the effects of high-LET oxygen ion irradiation on plant growth and development. The plant on the right is a control; the three small plants on the left were irradiated with 1000 rads of oxygen ions. Embryonic, first, second, and third leaves have developed, and the fourth leaf is starting to come out in the control plant.

Fig. 5. Effect of radiation on the growth and development of the third leaf.

Fig. 6. A photograph of young corn plants showing stripes and arrest in pigmentation of embryonic, first, second, and third leaves. Plants were irradiated with 1000 rads of oxygen ions.

Fig. 7 (A) Photograph of growing leaves of a corn plant having received 1000 rads of oxygen ions. A large white strips can be seen on the fifth leaf.
(B) Illustration of the same plant showing white stripes on leaves.

Fig. 8. Photograph of third leaves. The leaf on the right was irradiated with 1000 rads of oxygen beam. Note the ridges, asymmetrical growth, and the small size of the irradiated leaf as compared to the control on the left.

Fig. 9. Effects of oxygen-ion irradiation on the size of stripe in third leaves.

Fig. 10. Percentage of plants showing stripes as a function of radiation.

Fig. 11. Photograph of a corn plant viewed from above. The plant was irradiated with 1000 rads of oxygen ions. Large, white stripes appeared on third, fourth, and fifth leaves.

D 0 0 0 4 0 0 1 5 6 7

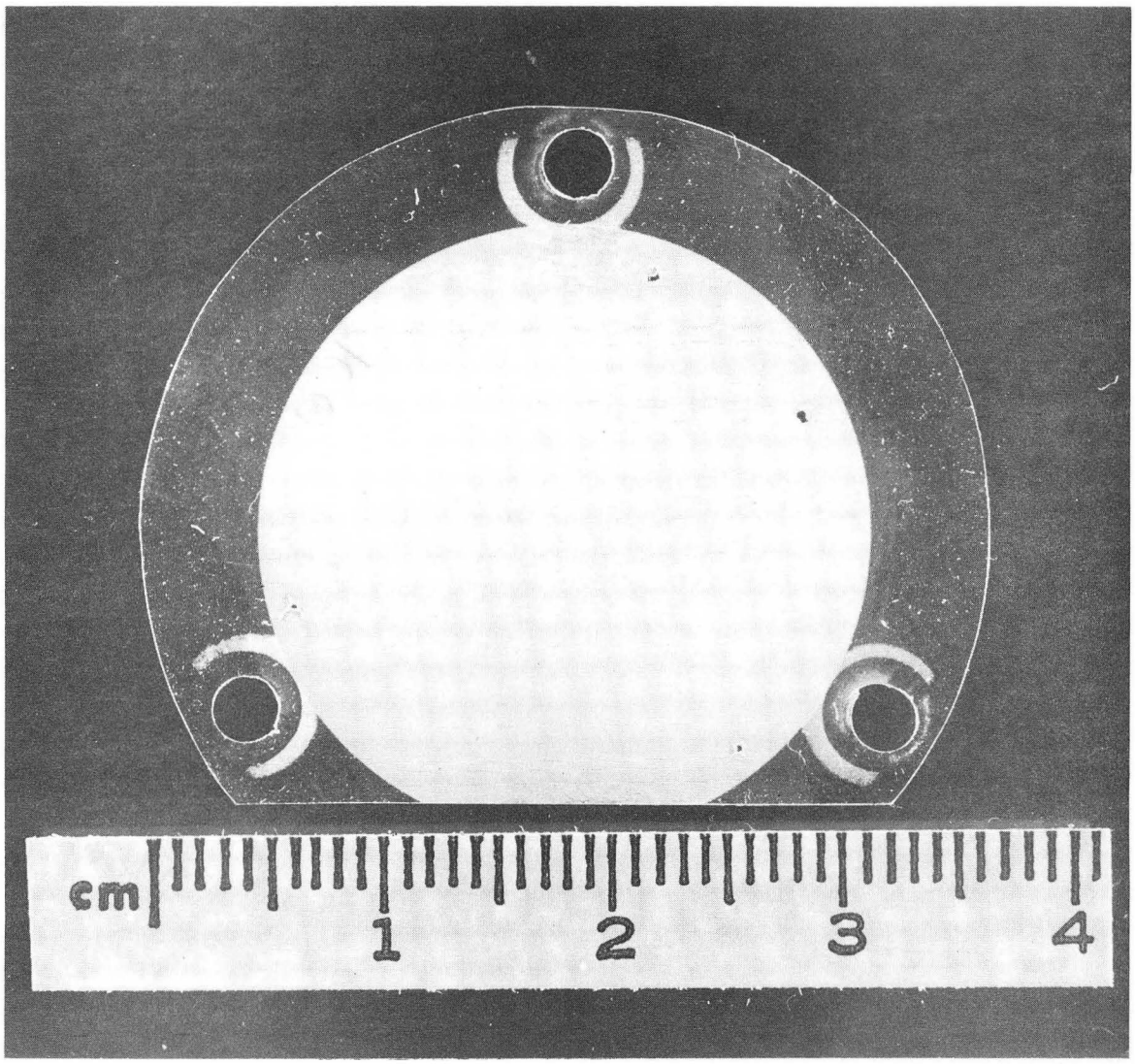

XBB 737-4154

Figure 1

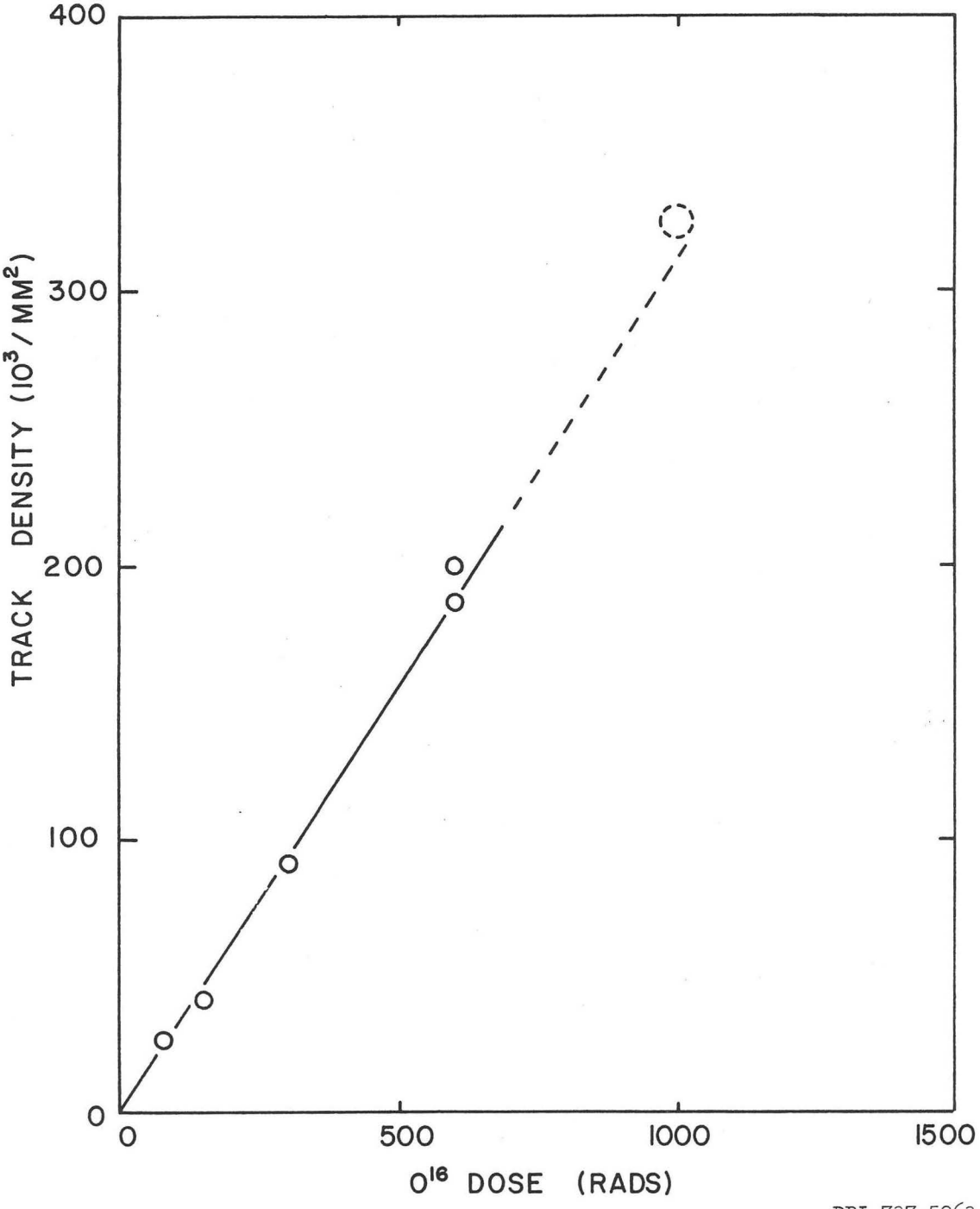

DBL 737-5263

Figure 2

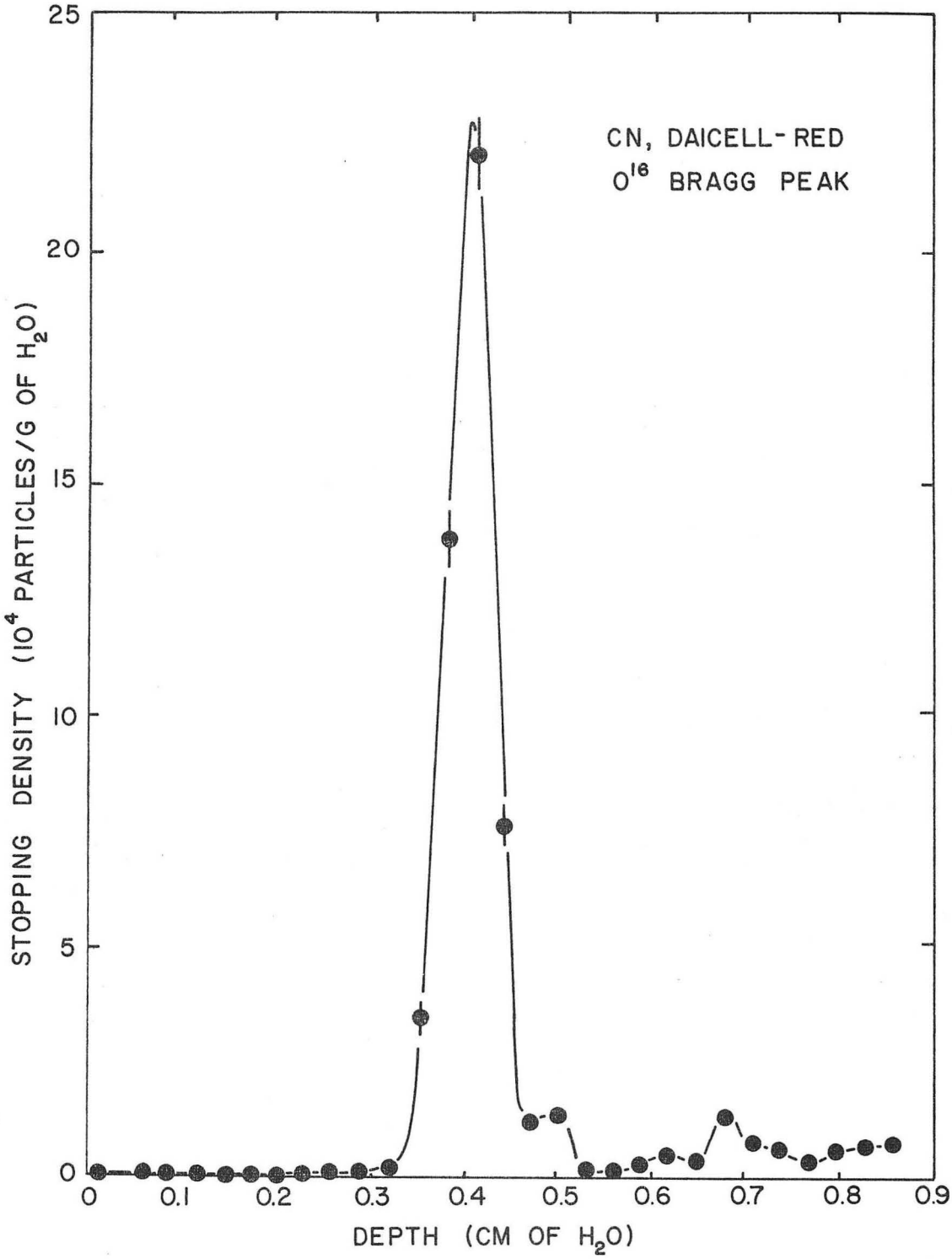

DBL 737-5264

Figure 3

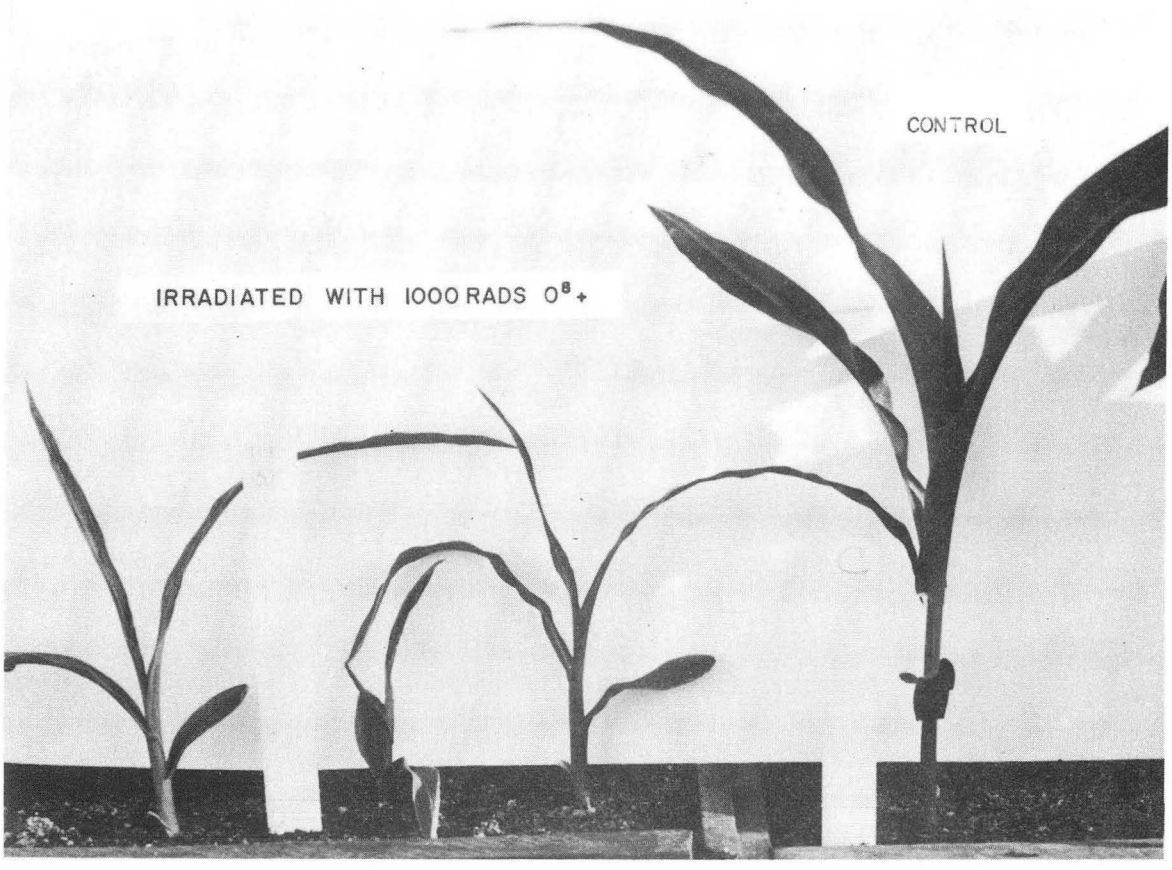

EFFECT OF HEAVY ION IRRADIATION ON PLANT GROWTH AND DEVELOPMENT

CBB 736-3590

Figure 4

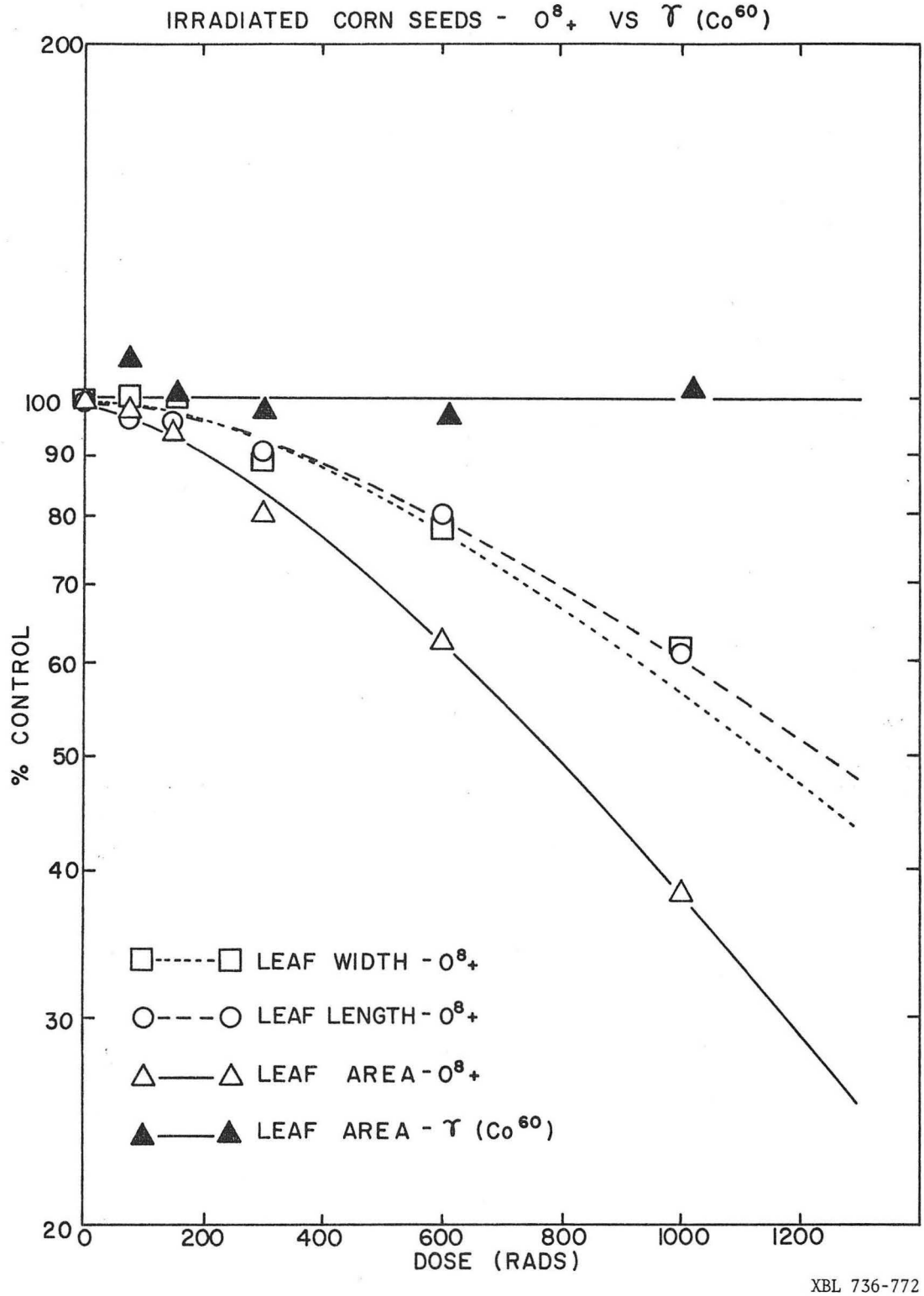
IRRADIATED CORN SEEDS - O^{8+} VS γ (Co^{60})
200
100
90
80
70
60
50
40
30
20
% CONTROL
0
200
400
600
800
1000
1200
DOSE (RADS)
LEAF WIDTH - O^{8+}
LEAF LENGTH - O^{8+}
LEAF AREA - O^{8+}
LEAF AREA - γ (Co^{60})
XBL 736-772

Figure 5

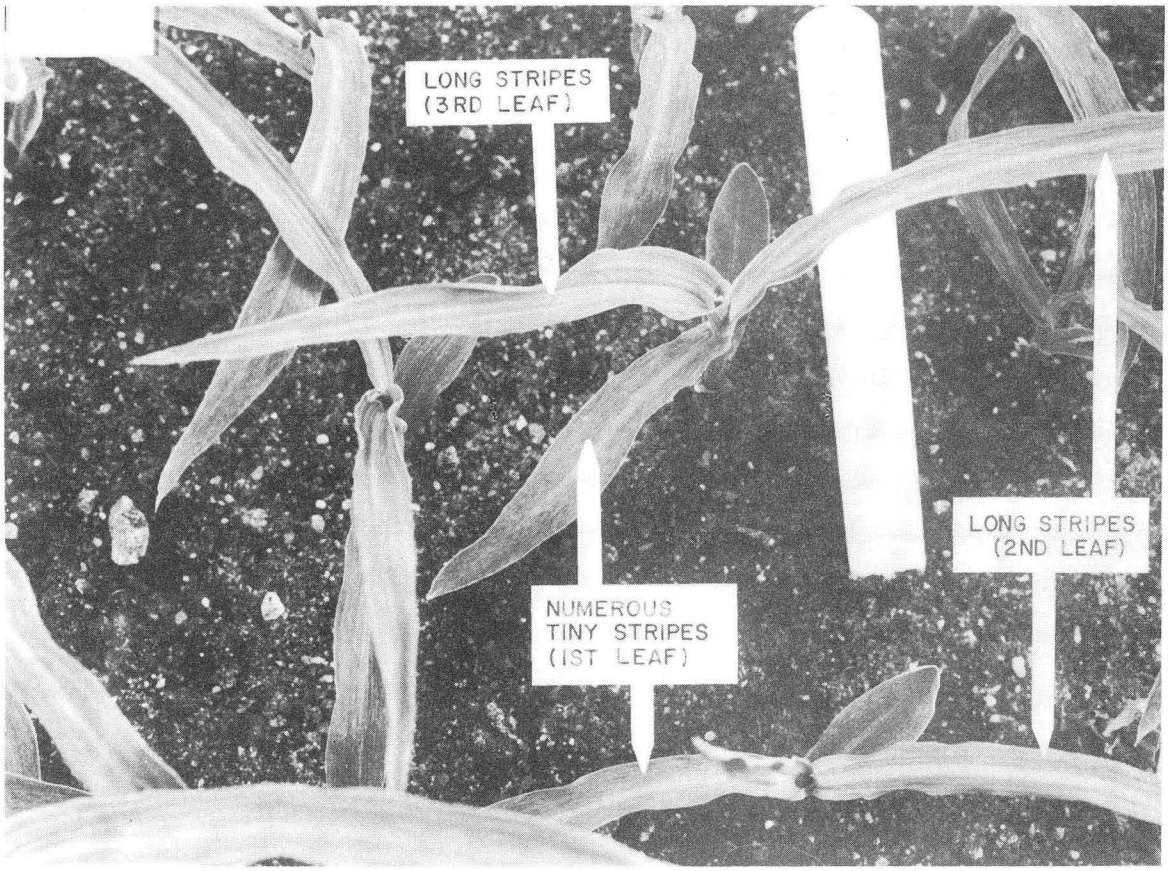

DIFFERENT STRIPE EFFECTS IN YOUNG CORN PLANTS (1000RADS O^{6}+)

CBB 736-3594

Figure 6

0 0 0 3 4 0 0 1 3 6 9

CBB 736-3596

Figure 7(A)

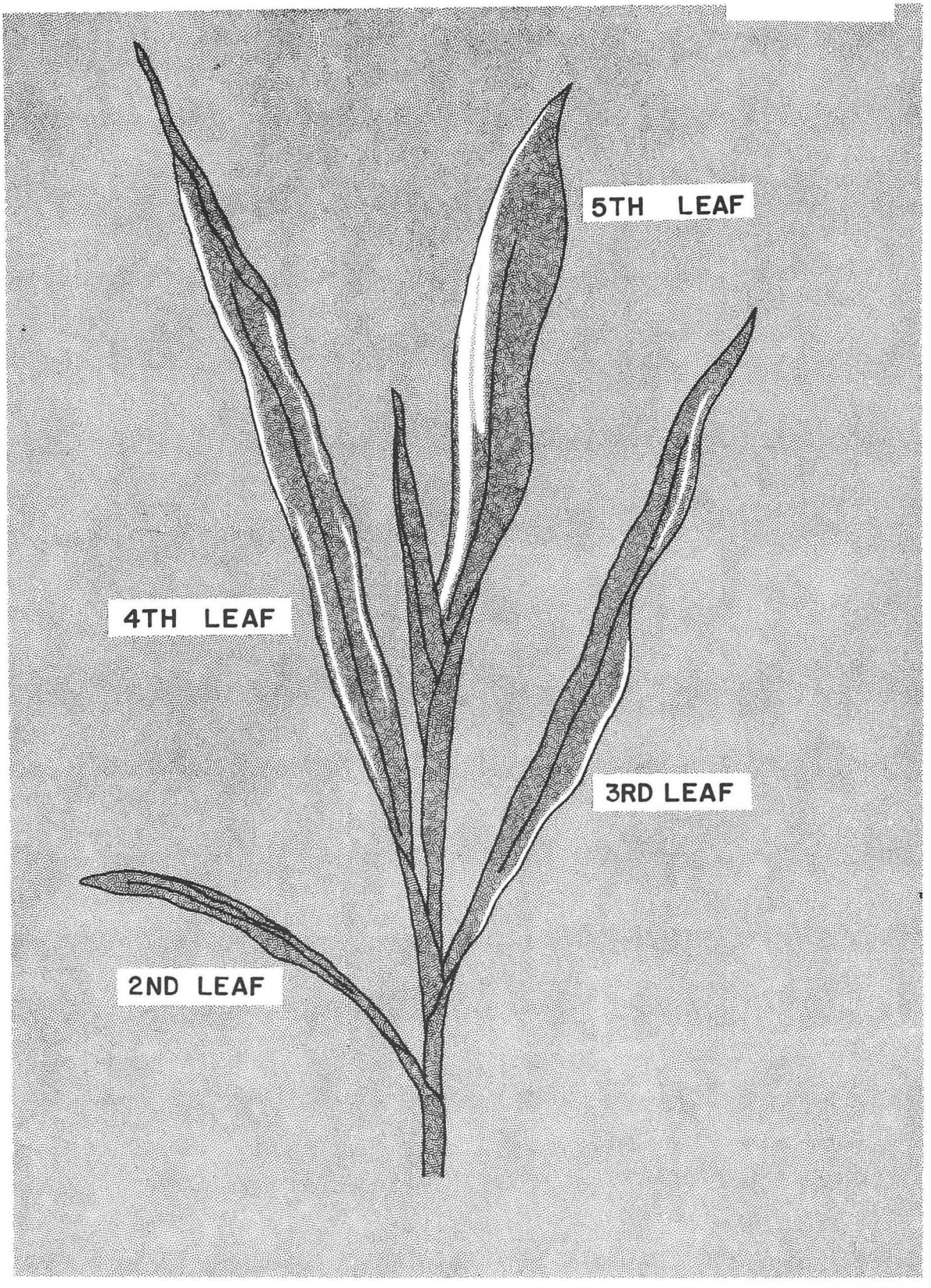

AN EXAMPLE OF THE INCREASE IN STRIPING WITH LATER LEAVES

XBB 736-3600

Figure 7(B)

0 0 0 0 4 0 0 1 5 7 0

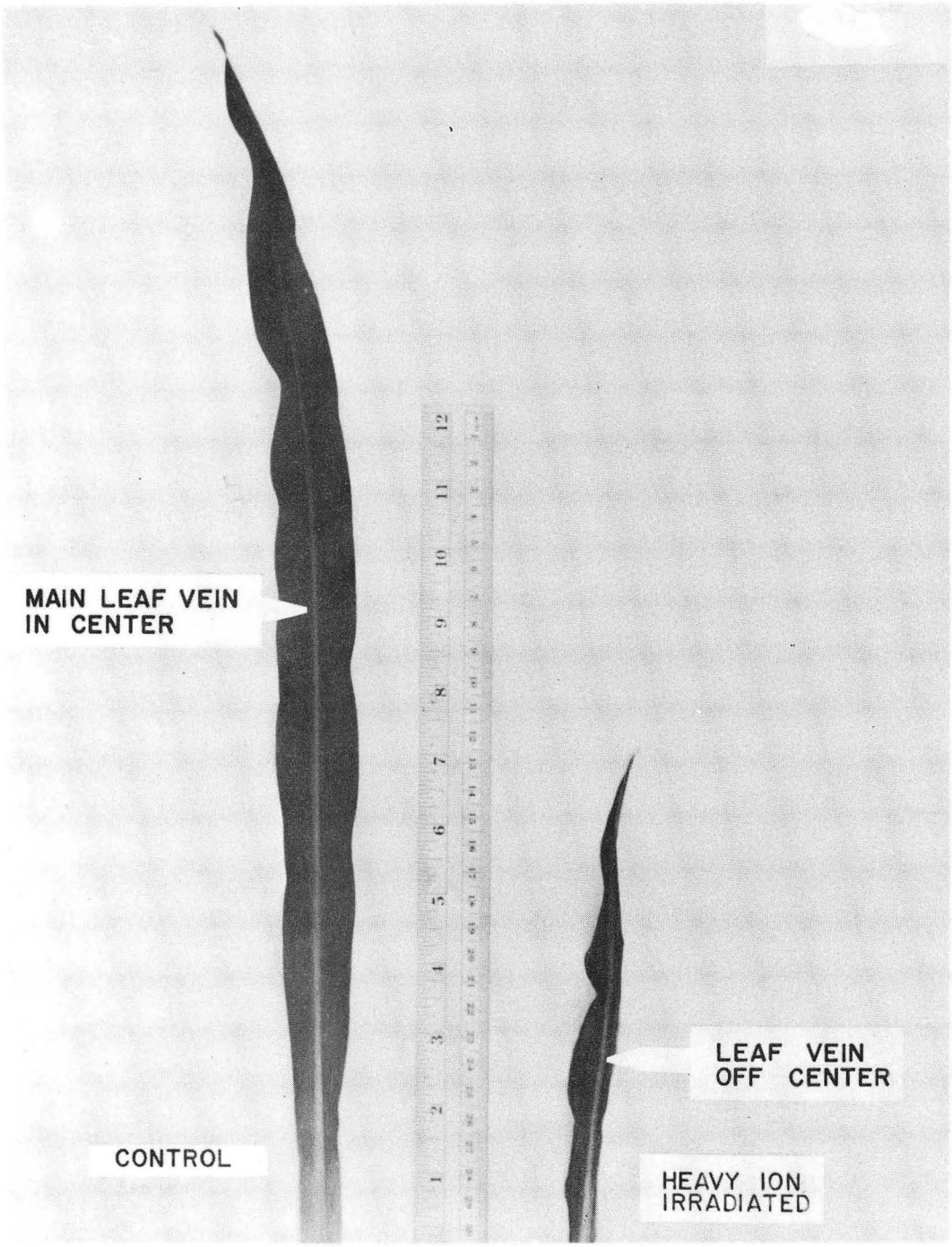

UNSYMMETRICAL AND ARRESTED GROWTH IN LEAF FROM IRRADIATED PLANT

CBB 736-3592

Figure 8

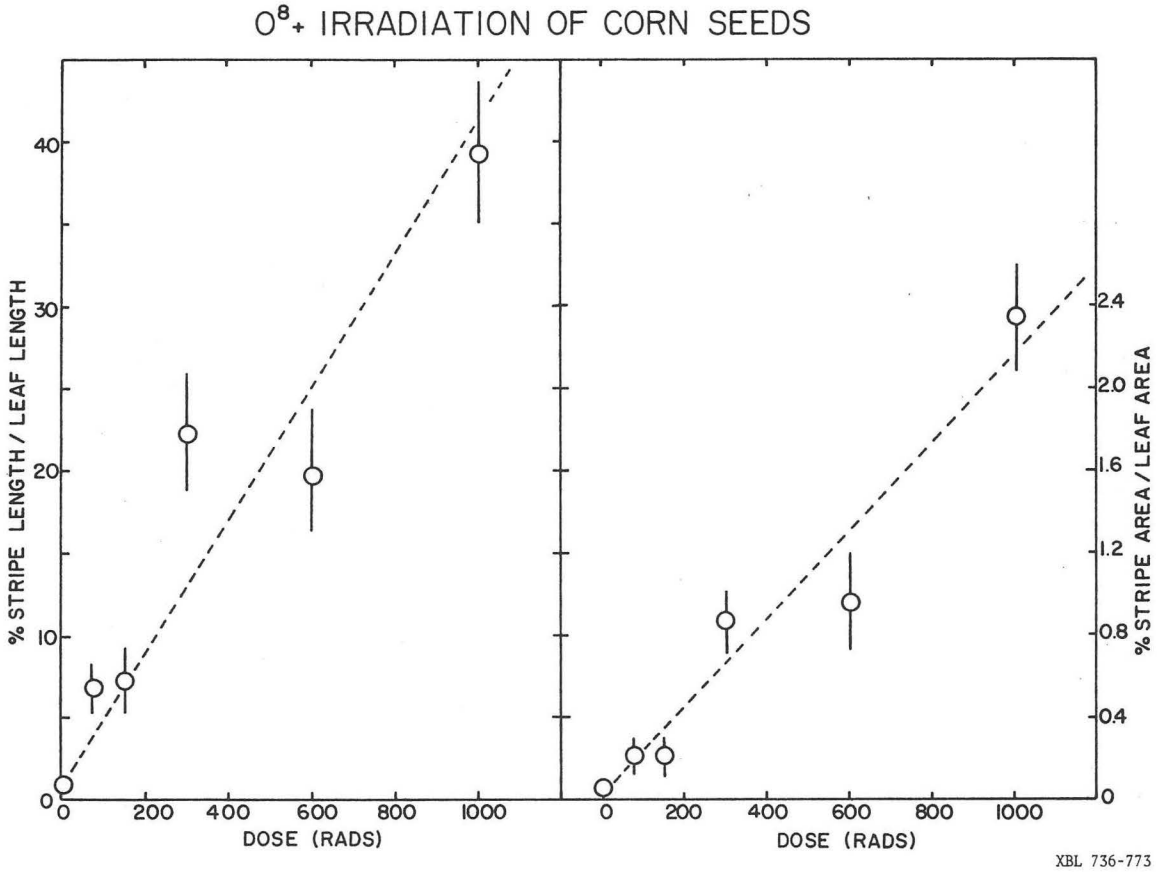
O^{8+} IRRADIATION OF CORN SEEDS
% STRIPE LENGTH / LEAF LENGTH
% STRIPE AREA / LEAF AREA
DOSE (RADS)
DOSE (RADS)
0
10
20
30
40
0
0.4
0.8
1.2
1.6
2.0
2.4
0
200
400
600
800
1000
XBL 736-773

Figure 9

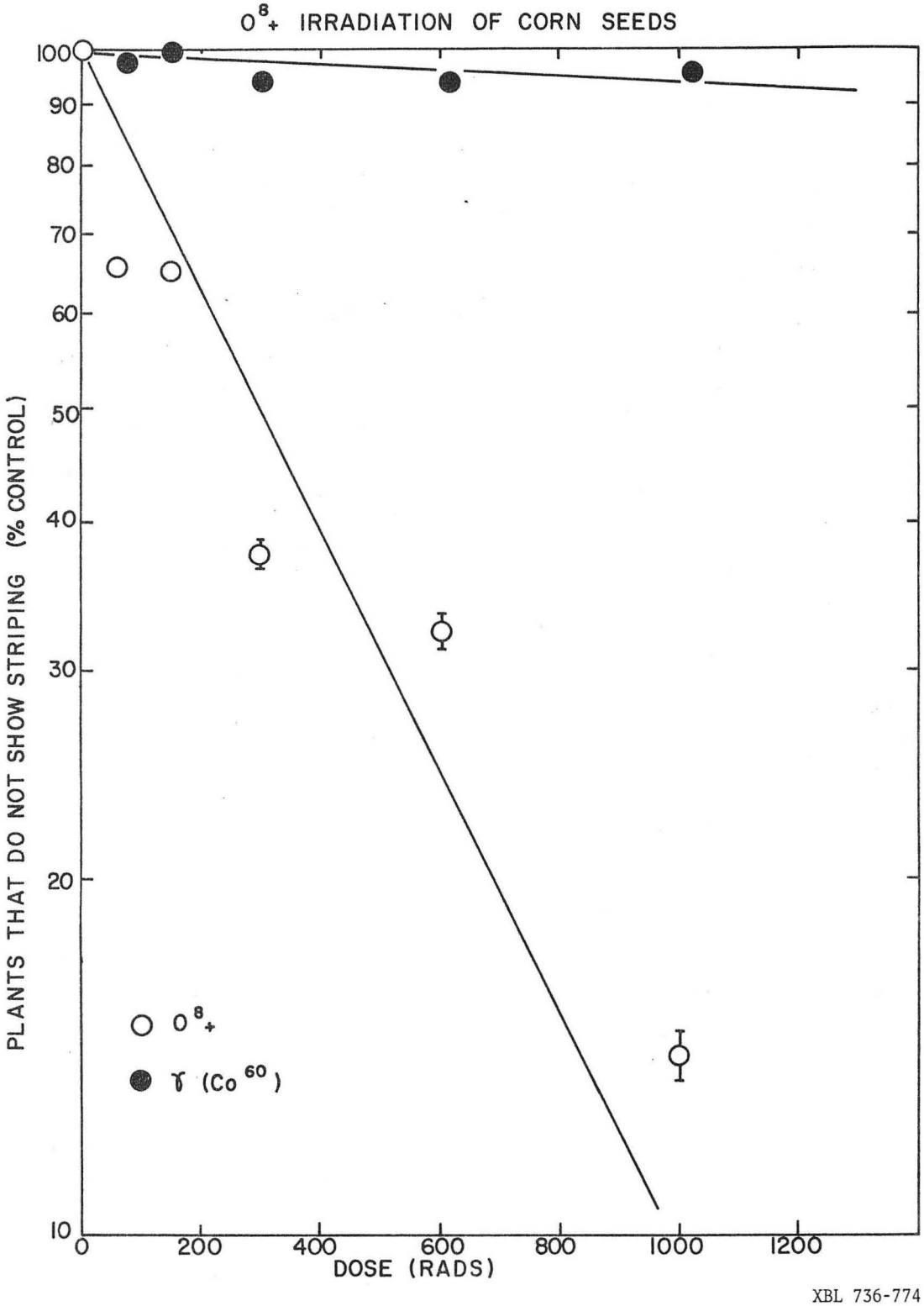

XBL 736-774

Figure 10

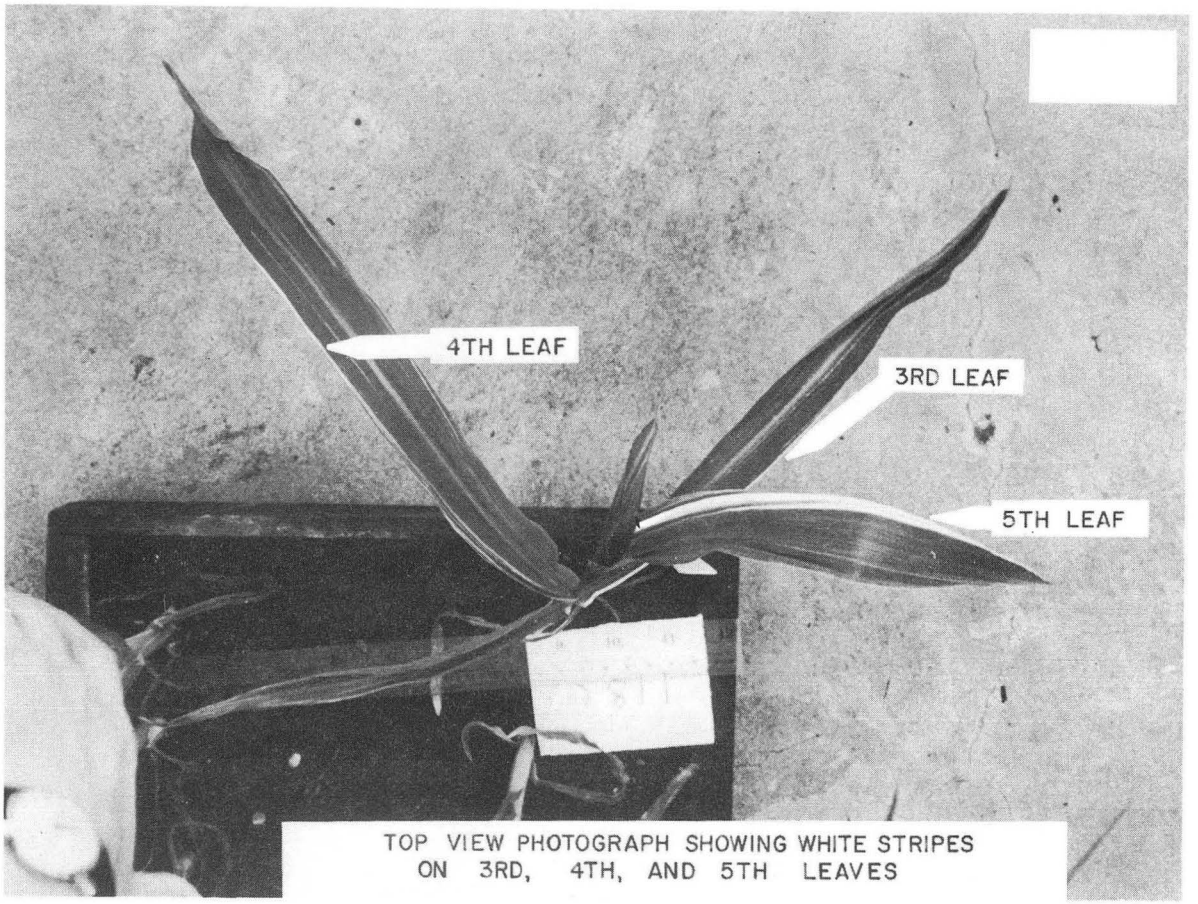

TOP VIEW PHOTOGRAPH SHOWING WHITE STRIPES ON 3RD, 4TH, AND 5TH LEAVES

CBB 736-3598

Figure 11

0 0 0 0 4 0 0 1 5 7 2

COMPARATIVE EFFECTS OF IRRADIATION OF THE SKIN OF MOUSE LEG WITH X RAYS, HELIUM IONS OR OXYGEN IONS

John T. Leith, Wolfgang A. Schilling, John T. Lyman, Jerry Howard, Graeme P. Welch and Walter Schimmerling

Donner Laboratory—Lawrence Berkeley Laboratory
University of California, Berkeley, CA 94720

and

Donald G. Baker

Claire Zellerbach Saroni Tumor Inst. —Mount Zion Hospital
Divisadero Street, San Francisco, CA

Abstract.

The acute responses of the skin of the legs of mice (erythema, dry and moist desquamation) have been studied after single doses of X rays, helium ions, or oxygen ions. The average 30-day response after oxygen or helium-ion irradiation has been used to obtain RBE values versus X-ray responses. The RBE values obtained were dependent on dose level and increased with increasing dose. For helium ions, the RBE increased from 1.23 to 2.63 over the dose interval of 750 to 1500 rads. The RBE for oxygen ions increased from 1.56 to 2.43 over the dose interval of 750 to 2000 rads. The data indicate that particle irradiations have a significantly greater RBE with respect to production of acute damage than do X rays, and that the RBE is dependent on dose level. Further research is necessary for complete evaluation of the particle beams.

Introduction.

The tolerance of normal tissues in an irradiation field is a major limiting factor for radiation therapy. Before any new type of radiation can be used for patient treatment, the RBE (relative biological effectiveness) for that radiation must be known for the normal tissues at risk.

We have begun to evaluate skin responses in the legs of mice following different types of radiation. This type of experiment is well known and has been used for evaluation of the RBE of skin for single doses of fast neutrons (1), electrons (2), helium ions (3), radioprotective agents (4); and for fractionated doses of X-rays (5) or neutrons (6).

In this report we present data on the responses of mouse skin to oxygen ions and helium ions relative to X-ray responses.

Materials and methods.

Animals. Mice used were C3H/HeJ females, obtained from the Jackson Laboratories, Bar Harbor, Maine. They were housed, five per cage, until irradiation, at which time they were switched to individual housing, using pint Mason jars. One day before irradiation, the right hindlimbs were depilated using a commercial depilatory agent. Animals were irradiated at approximately 70 days of age and were anesthetized for the exposures. They were given food and water *ad libitum*, with the water slightly chlorinated to inhibit growth of *Pseudomonas* organisms.

Irradiation procedures - X rays. Mice were irradiated, four at a time, using a lead shield with cutouts for the right hindlimbs. Dose was delivered at a rate of approximately 150 rads per minute; irradiation factors were: intrinsic filtration 1.1 mm Al, added filtration 0.25 mm Cu and 1.0 mm Al, FSD 25 cm, HVL 1.2 mm Cu, 15 mA, and 230 kV. The dose was measured with a Victoreen probe in conjunction with a Victoreen r-meter, and a Roentgen to rad conversion factor of 0.96 was used.

Irradiation procedures - helium ions. Mice were irradiated four at a time, with the trunks of the animals shielded by a 1.5 mm thickness of lead. The initial energy of the beam used in these experiments was 910 MeV and this was subsequently reduced by a series of energy degrading absorbers. A variable-thickness water column placed in front of the mice provided exact positioning of the helium-ion Bragg peak. As the width of the Bragg peak for helium ions is too narrow to permit irradiation of large volumes (i.e., the mouse leg or a tumor) at a constant dose rate, the Bragg curve was widened

by inserting a moving copper ridge filter into the beam path (7-10). This variable absorber transformed the Bragg peak portion of the ionization curve into a plateau with relatively constant dose. A portion of the modified Bragg curve is shown in Figure 1. Respective doses of 750, 1000, and 1500 rads of helium ions were given at a dose rate of 350 rads per minute. Dosimetry was performed with a plane parallel plate ionization chamber (7).

Irradiation procedures - oxygen ions. The first experiment involving irradiation of the skin of the legs of mice was done in March of 1973. The initial energy of the oxygen-ion beam was approximately 265 MeV/nucleon, and this initial energy was degraded by interposition into the beam path of various absorbers, scintillation chambers, and a variable-thickness water column. When the beam emerged at the position of the sample, it had a residual range of 8.77 cm, with a peak-to-plateau ionization ratio of 6.05. The unmodified Bragg curve of the oxygen ions was modified by inserting a moving ridge filter into the beam path. The modified and unmodified Bragg curves are shown in Figure 2. The surface of the mouse leg was placed at 4 mm behind the ridge filter peak. The beam diameter was 28 mm; a densitometry tracing of the beam profile obtained from X-ray films is shown in Figure 3. The number of mice used and doses received are shown in Table 1. The mice were irradiated at a dose rate of approximately 50 rads per minute. The surface of the mouse skin was 1.62 cm from the end of the range of the primary oxygen-ion beam. The minimum linear energy transfer at this point was calculated to be about 51 keV/micron.

Scoring of the skin reactions. Scoring of acute skin reactions was done according to the criteria discussed by Lowy and Baker (4); these criteria are listed in Table 2.

At 100 days postirradiation, when it was felt that the acute skin injury had reached a more or less constant scoring level, the mice irradiated with oxygen ions and X rays were sacrificed and the irradiated and nonirradiated legs were amputated and limb weight measured. The data obtained provide an indication of late occurring fibrosis and muscle atrophy which lessen the weight of the leg. Samples were fixed in Bouin's solution for future histological analysis. Weights of the legs are shown in Table 3.

Results and discussion.

The development of skin reactions following the helium-ion irradiations is shown in Figure 4, and following X-irradiation in Figure 5. As the

oxygen ions produce skin reactions not different in their temporal development from those produced by helium ion and X-ray reactions, these are not shown. As a means of comparing the two modes of irradiation, averaged thirty-day skin reactions have been calculated. This was done by taking the area under the curve of skin-reaction development versus time, for each mouse at each dose level between 1 and 30 days postirradiation, and dividing by the number of days, to give the average reaction per day (1). These values for oxygen ions, helium ions and X rays are listed in Table 4, together with the times of maximum skin reaction. In Table 5, the scoring of acute skin reactions is presented in terms of the proportion of mice at each dose level for each type of irradiation showing a particular level of skin response (complate moist desquamation; patchy moist desquamation; moderate dry desquamation) occurring within 21 days postirradiation (5). From these data the doses needed to produce a given level of skin response in half of the irradiated mice were approximated. In figure 6, skin reactions averaged over the 30-day postirradiation period are plotted and have been fitted to first- and second-degree polynomial equations for purposes of comparison.

For doses of 750 rads, the duration of maximal involvement of skin in an acute reaction is: 12.5 - 13.5 days (helium ions), 7.0 - 22.0 (oxygen ions), and 16.0 - 23.0 days (X rays). At 1000 rads duration is 12.5 - 13.5 days (helium ions), 9.0 - 14.0 (oxygen ions), and 10.0 - 20.0 days (X rays). At 1250 rads involvement lasts 19.5 - 20.5 days (oxygen ions) and 11.5 - 17.5 days (X rays). For 1500 rads duration is 15.0 - 19.5 days (helium ions), 19.5 - 23.5 days (oxygen ions), and 16.0 - 22.5 days (X rays); and for 2000 rads, 19.5 - 22.5 days (oxygen ions), and 16.5 - 20.5 days (X rays). At the lower doses (750 to 1500 rads), the time of maximal involvement is not well defined, however, it is felt that there is not significant difference between the temporal skin reactions occurring after different modalities of irradiation (when corrected for RBE). This has also been suggested by Denekamp et al. (1), who compared neutrons to X-rays for production of skin reactions using an identical assay system. Both results, and the results of Denekamp et al. (1), then suggest that the rates of cellular repopulation in irradiated skin are not significantly different for low-LET (X-rays) or high-LET (neutrons, helium ions, oxygen ions) radiations.

The averaged 30-day postirradiation skin reactions after a dose of 750 rads are not significantly different for helium-ion versus X-irradiation.

However, the 750 rad dose-effect point for the oxygen-ion irradiations is significantly greater than for helium-ion or X-ray responses. Also the rate of increase of skin involvement as shown by the 30-day average is greater for increasing helium-ion and oxygen-ion dose than for increasing X-ray dose (Figure 6). The thirty-day average reactions at the 1000-rad dose level for oxygen ions (1.67), helium ions (1.58), and 250 kVp X rays (1.46) are significantly different at the 0.05 level of significance using a two-tailed t-test.

Values for relative biological effectiveness (RBE's) are displayed in Figure 6. Taking a thirty-day averaged skin response level of 1.5 for comparison, the ratio of doses needed to produce this response level is 1140 rads (X-rays)/960 rads (helium ions), or an RBE of 1.19. For oxygen ions at this response level, the ratio is 1140 rads/880 rads, or an RBE of 1.30. Similarly, for an averaged thirty-day skin reaction level of 2.0, the RBE is 1960/1230 rads, or an RBE of 1.59 for helium ions; for oxygen ions the ratio is 1960 rads/1425 rads, giving an RBE of 1.38. For an averaged thirty-day skin reaction level of 2.5, the RBE is 3180/1460 rads for helium ions, giving an RBE of 2.18; for oxygen ions this ratio is 3180/1967 rads, giving an RBE of 1.62. This data is plotted in Figure 7. It therefore appears that the RBE for helium ions and for oxygen ions, relative to X rays, increases with increasing dose in the interval from 750 to 2000 rads. This type of response has been previously shown for skin responses following single doses of neutrons (1), and has been interpreted as being due to a small proportion of hypoxic cells in the skin (11). In Figure 7, the increase of RBE for increasing neutron doses is plotted (data from Reference 1), together with the increasing RBE found for helium-ion and oxygen-ion irradiations in the present experiments. It appears that that there is no significant difference between the neutron, helium-ion, and oxygen-ion RBE data. Whether or not this similarity would also be found for late changes in irradiated skin and for short-term recovery between fractions of heavy-particle irradiation remains to be evaluated. Also it must be remembered that the most penetrating components of the helium-ion and oxygen-ion beams as modified by the ridge filter produce a very broad LET spectra at the surface of the skin. The appropriate method for comparison of neutron (1), helium-ion, and oxygen-ion radiations would probably involve a comparison of their LET spectra. At the present time this information is unavailable; however, minimum LET values for helium-ion and oxygen-ion irradiations are around 7 and 51 keV/micron, respectively.

REFERENCES

1. Denekamp, J., Fowler, J. F., Kragt, K., Parnell, C. J., and Field, S. B., Recovery and repopulation in mouse skin after irradiation with cyclotron neutrons as compared with 250-KV X-rays or 15. MeV electrons. Radiat. Res., 29, 71-84, (1966).
2. Fowler, J. F., Kraft, K., Ellis, R. E., Lindop, P. J., and Berry, R. J., The effects of divided doses of 15 MeV electrons on the skin response of mice. Int. J. Radiat. Biol., 9, 241-252, (1965).
3. Leith, J. T., Baker, D. G., Lyman, J. T., and Howard, J., Acute skin reactions in mice after irradiation with cyclotron-accelerated 910 MeV helium ions in the Bragg peak region of ionization as modified by use of a ridge filter (submitted to: International Journal of Radiation Biology.)
4. Lowy, R. O., and Baker, D. G., Protection against local irradiation injury to the skin by locally and systemically applied drugs. Radiol., 105, 425-428 (1972).
5. Suit, H. D., and Howard, T. C., Normal tissue damage and tumor cure probability for irradiation given under different conditions of tissue oxygenation in hybrid mice. Radiol., 89, 720-726 (1967).
6. Fowler, J. F., Denekamp, J., Page, A. L., Begg, A. C., Field, S. B., and Butler, K., Fractionation with X rays and neutrons in mice: response of skin and C3H mammary tumors. Brit. J. Radiol., 45, 237-249 (1972).
7. Karlsson, B. G., Methoden zur Berechnung und Erzielung einiger fuer die Tiefentherapie mit Hochenergetischen Protonen guenstiger Dosisverteilungen. Strahlentherapie, 124, 481 (1964).
8. Raju, M., Heavy-particle studies with silicon detectors. Radiat. Res. Suppl. 7, 43 (1967).
9. Raju, M. R., The use of the miniature silicon diode as a radiation dose meter. Phys. Med. Biol., 11, 371 (1966).
10. Raju, M. R., Lyman, J. T., Brustad, T., and Tobias, C. A., Heavy-charged-particle beams. In: Radiation Dosimetry, Vol. 3 (E. H. Attix, W. C. Roesch, and E. Tochilin, Eds.), Academic Press, New York (1969).
11. Field, S. B., and Hornsey, S., RBE values for cyclotron neutrons for effects on normal tissues and tumors as a function of dose and dose fractionation. Europ. J. Cancer, 7, 161-170 (1971).

TABLE I.

DOSES OF OXYGEN IONS GIVEN TO THE SKIN OF MICE DURING BEVATRON EXPERIMENT OF MARCH, 1973

Mouse Number	Dose (rads)
1	749
2	747
3	1003
4	1006
5	1250
6	1254
7	1254
8	1500
9	1494
10	1503
11	2005

TABLE II.

GRADING SYSTEM FOR ACUTE SKIN IRRADIATION REACTIONS

Tissue Grades and Appearance In Acute Injury Phase	Tissue Grades and Appearance In Recovery Phase
1.0 no difference from controls	1.0 no difference from controls
1.5 slight erythema	1.5 limb appears normal except for presence of hair depigmentation
2.0 distinct erythema	2.0 hair is depigmented and there is sparse regrowth of hair
2.5 suggestion of dry desquamation	2.5 sparse regrowth of hair, probably no edema, the skin dose not appear as thin as in a 3.0 recovery state
3.0 dry desquamation, powdery appearance of skin on close observation with small cracks and flaking of skin. Usually edematous	3.0 marked epilation, skin is thin appearing and presents a tight appearance, may be a reduction in the size of the limb
3.5 dry desquamation with suggestion of incipient skin breakdown	3.5 very thin, shiny skin, usually edematous
4.0 moist desquamation of moderate extent, patchy appearance	4.0 focal areas of moist desquamation with extensive scab formation
4.5 major percent of limb is involved in moist desquamation, may find small areas of necrosis	4.5 small, non-healing areas
5.0 significant amount of necrosis with loss of dermis, similar to a third degree burn	5.0 open, but non-draining wound

TABLE III.

WEIGHTS OF THE LEGS OF MICE AT 100 DAYS POSTIRRADIATION

Radiation Modality	Dose (rads)	Weight of irradiated legs expressed as a percent of unirradiated legs (%)
X-ray	2000	97.0 ± 21.0[a]
	3000	94.0 ± 12.0
	3500	98.0 ± 16.0
	4000	78.0 ± 20.0
Oxygen-16	750	88.0 ± 7.0
	1000	89.0 ± 17.0
	1250	109.0 ± 11.0
	1500	109.0 ± 10.0
	2000	100.0 ± 0.0

[a]The values are the mean values and the standard deviation of the mean value.

TABLE IV.

AVERAGE SKIN IRRADIATION REACTIONS OVER AN INTERVAL OF 1 TO 30 DAYS POSTIRRADIATION

Dose (rads)	Thirty day postirradiation averaged skin reaction			Time of maximal acute skin involvement (days)		
	X-rays	Helium Ions	Oxygen Ions	X-rays	Helium Ions	Oxygen Ions
750	1.24(0.09)[a]	1.23(0.08)	1.56(0.02)	16.0-23.0[b]	12.5-13.5	7.0-22.0
1000	1.46(0.12)	1.58(0.27)	1.67(0.14)	10.0-20.0	12.5-13.5	9.0-14.0
1250	1.53(0.10)	——	1.72(0.29)	11.5-17.5	——	19.5-20.5
1500	1.80(0.09)	2.63(0.06)	2.09(0.13)	16.0-22.5	15.0-19.5	19.5-23.5
1750	1.85(0.12)	——	——	15.5-19.0	——	——
2000	1.88(0.15)	——	2.43(0.00)	16.5-20.5	——	19.5-22.5
2500	2.38(0.17)	——	——	16.0-19.0	——	——
3000	2.47(0.18)	——	——	20.5-24.0	——	——
3500	2.61(0.11)	——	——	20.0-23.5	——	——
4000	2.65(0.10)	——	——	18.0-22.5	——	——
4500	2.72(0.12)	——	——	19.5-21.5	——	——

[a]Value in parentheses is the standard deviation of the mean value.

[b]The range of days for the maximal involvement of the skin in an acute reaction is taken as the time when the skin reactions are equal to, or greater than, 95 percent of the maximum skin reaction, to the nearest 0.5 day.

TABLE V.

PROPORTION OF MICE PRESENTING CERTAIN LEVELS OF SKIN REACTION AS A FUNCTION OF X-RAY, HELIUM ION OR OXYGEN ION IRRADIATION DOSE LEVEL.

Dose (rads)	Proportion of mice showing complete moist desquamation[a]			Proportion of mice showing patchy moist desquamation			Proportion of mice showing moderate dry desquamation			Proportion of mice showing strong erythema		
	X-rays	Helium Ions	Oxygen Ions	X-rays	Helium Ions	Oxygen Ions	X-rays	Helium Ions	Oxygen Ions	X-rays	Helium Ions	Oxygen Ions
750	0/8	0/8	0/2	0/8	0/8	0/2	0/8	0/8	0/2	0/8	1/8	1/2
1000	0/8	0/8	0/2	0/8	0/8	0/2	0/8	6/8	0/2	5/8	8/8	1/2
1250	0/8	—	0/3	0/8	—	0/3	0/8	—	0/3	7/8	—	3/3
1500	0/8	0/3	0/3	0/8	3/3	0/3	2/8	3/3	3/3	8/8	3/3	3/3
1750	0/8	—	—	0/8	—	—	3/8	—	—	8/8	—	—
2000	0/8	—	0/1	0/8	—	0/1	5/8	—	1/1	8/8	—	1/1
2500	0/7	—	—	2/7	—	—	6/7	—	—	7/7	—	—
3000	0/8	—	—	5/8	—	—	8/8	—	—	8/8	—	—
3500	1/7	—	—	5/7	—	—	7/7	—	—	7/7	—	—
4000	2/7	—	—	7/7	—	—	7/7	—	—	7/7	—	—
4500	2/2	—	—	2/2	—	—	2/2	—	—	2/2	—	—

[a]Skin reactions are scored as positive responses if they occur within 21 days postirradiation.

FIGURE CAPTIONS

Fig. 1. A schematic showing a portion of the modified Bragg curve used for irradiation of mouse legs with helium ions.

Fig. 2. Profiles of the oxygen-ion Bragg curves. The position of the surface of the mouse leg is indicated.

Fig. 3. Isodose contours for irradiation of mouse leg. Radiation intensities were determined using X-ray film with subsequent densitometric measurements.

Fig. 4. Temporal development of skin reactions after helium-ion irradiation.

Fig. 5. Temporal development of acute skin reactions after X-irradiation.

Fig. 6. Skin reactions after irradiation with oxygen ions, helium ions or 250 kVp X rays. The values are the skin reactions averaged over the time period of one to 30 days postirradiation. The error bars for the helium-ion and X-ray data points are the standard errors of each 30-day average value. The oxygen ion responses may be fitted with a linear least squares regression equation of $Y = 0.69 + 0.92 \times 10^{-3} X$.

The helium-ion responses may be fitted with a linear least squares regression equation of $Y = -0.245 + 1.90 \times 10^{-3} X$, or a quadratic least squares regression equation of $Y = 0.88 - 2.33 \times 10^{-4} X + 9.33 \times 10^{-8} X^2$ (the units of X are rods).

The X-ray skin responses may be fitted with a linear least squares regression equation of $Y = 1.104 + 4.057 \times 10^{-4} X$ or a quadratic least squares regression equation of $Y = 0.605 + 0.029 \times 10^{-4} X - 9.602 \times 10^{-8} X^2$.

The dashed lines for the helium-ion and X-ray data are the quadratic fits and the dashed line for the oxygen-ion data is a linear fit.

Fig. 7. Variation of relative biological effectiveness (RBE) for fast-neutron, helium-ion, oxygen-ion and fast-electron irradiation of the skin of mouse leg. The neutron and fast-electron data have been taken from Denekamp et al. (1), and the bars on the neutron points represent the ranges of dose and RBE for each point as reported by Denekamp, et al. (1).

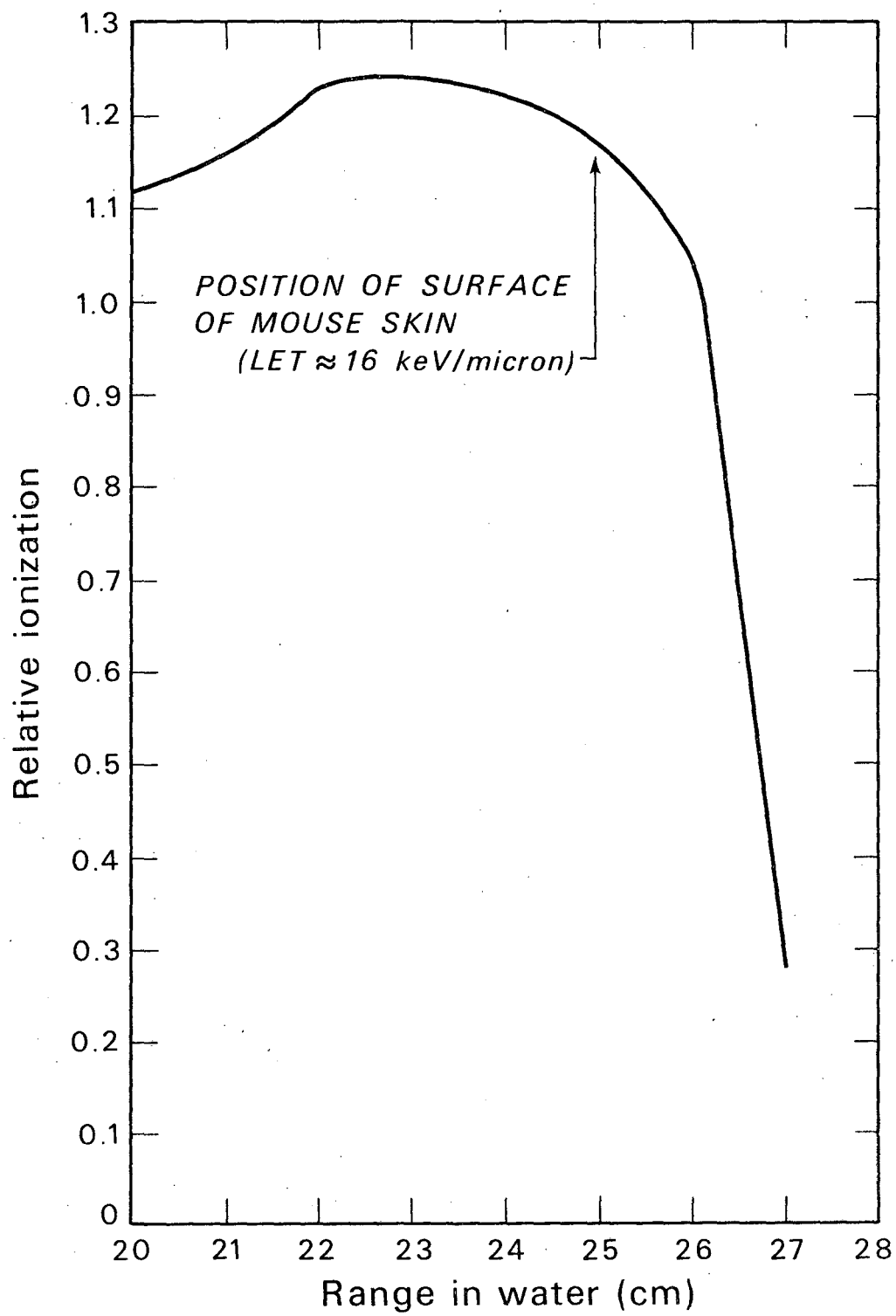

DBL 732-5058

Figure 1

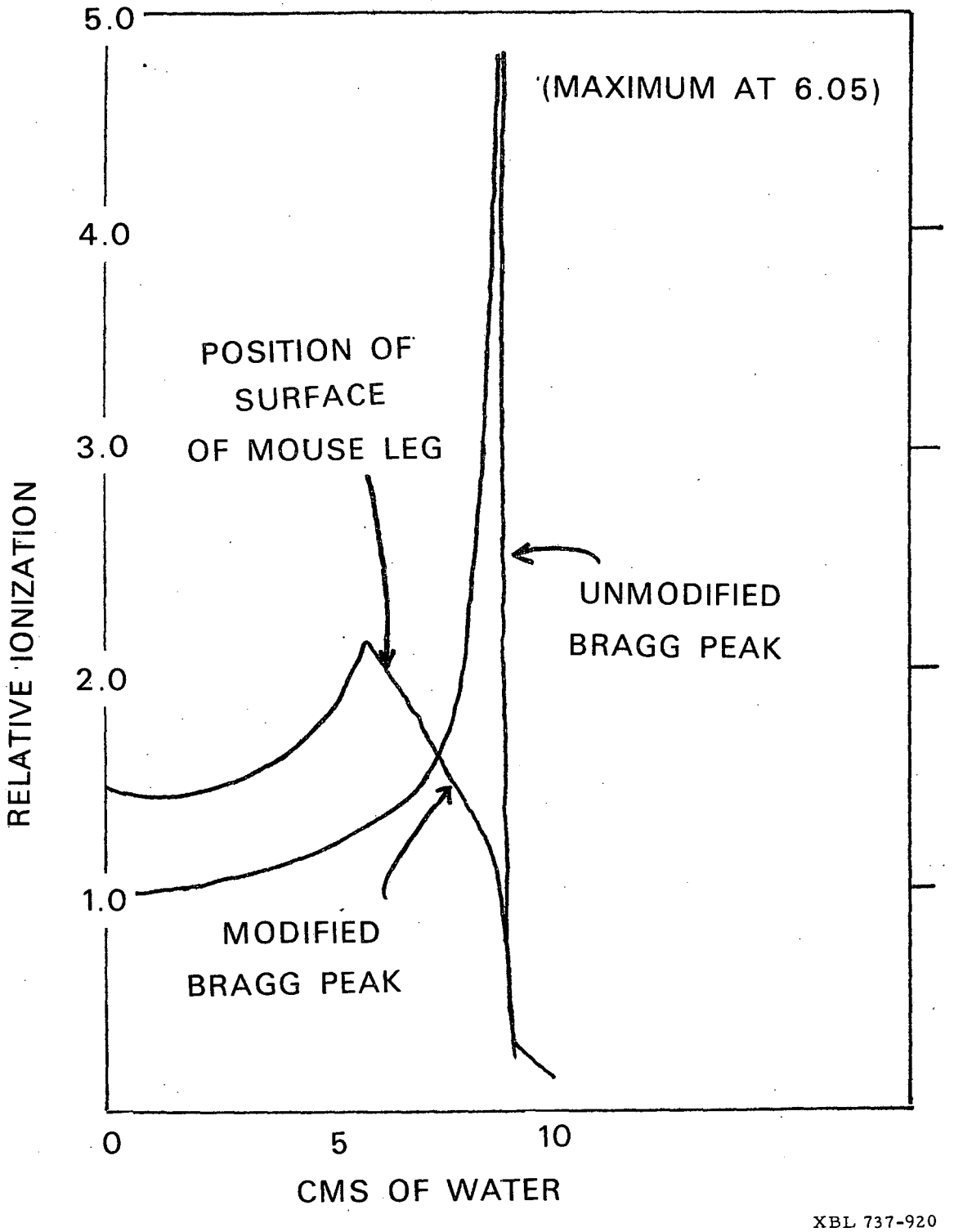

XBL 737-920

Figure 2

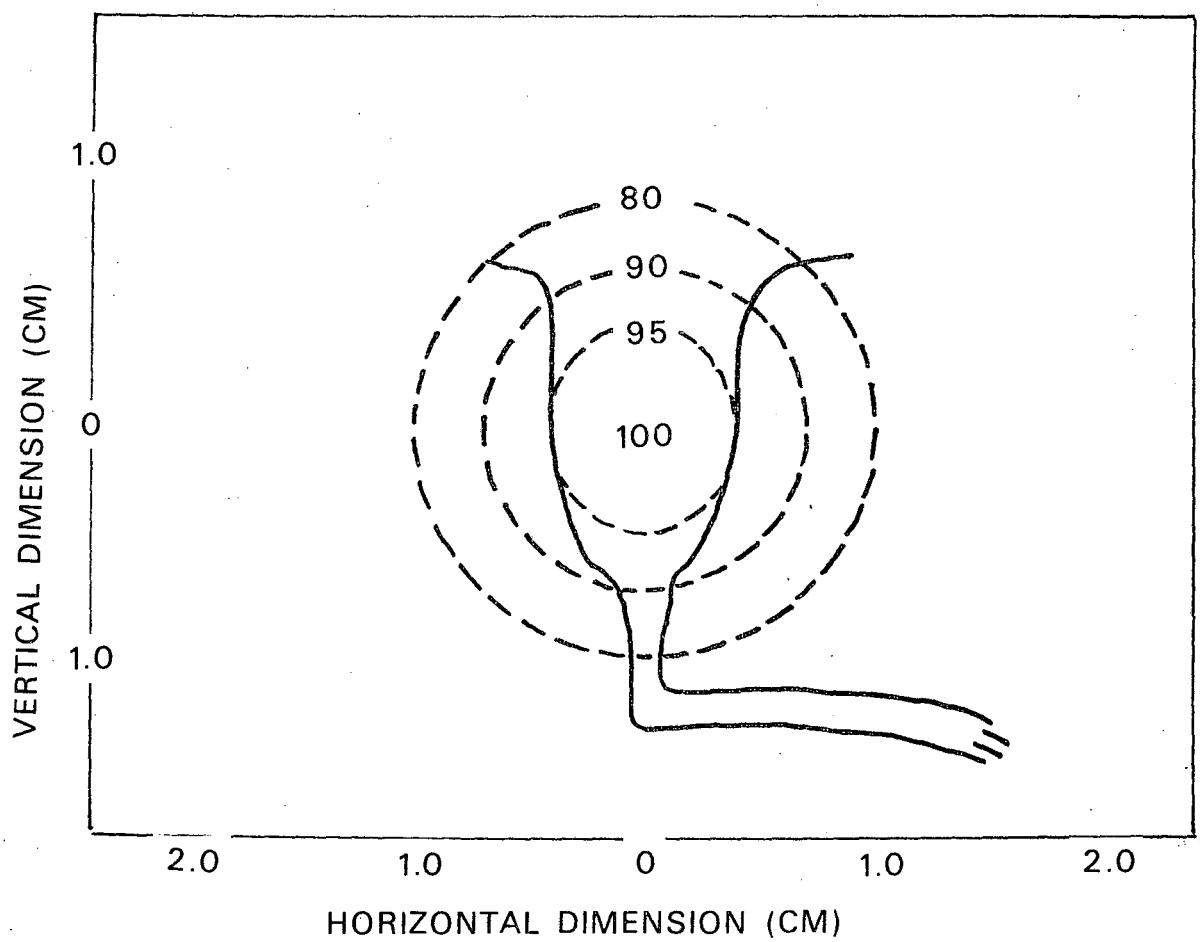

XBL 737-921

Figure 3

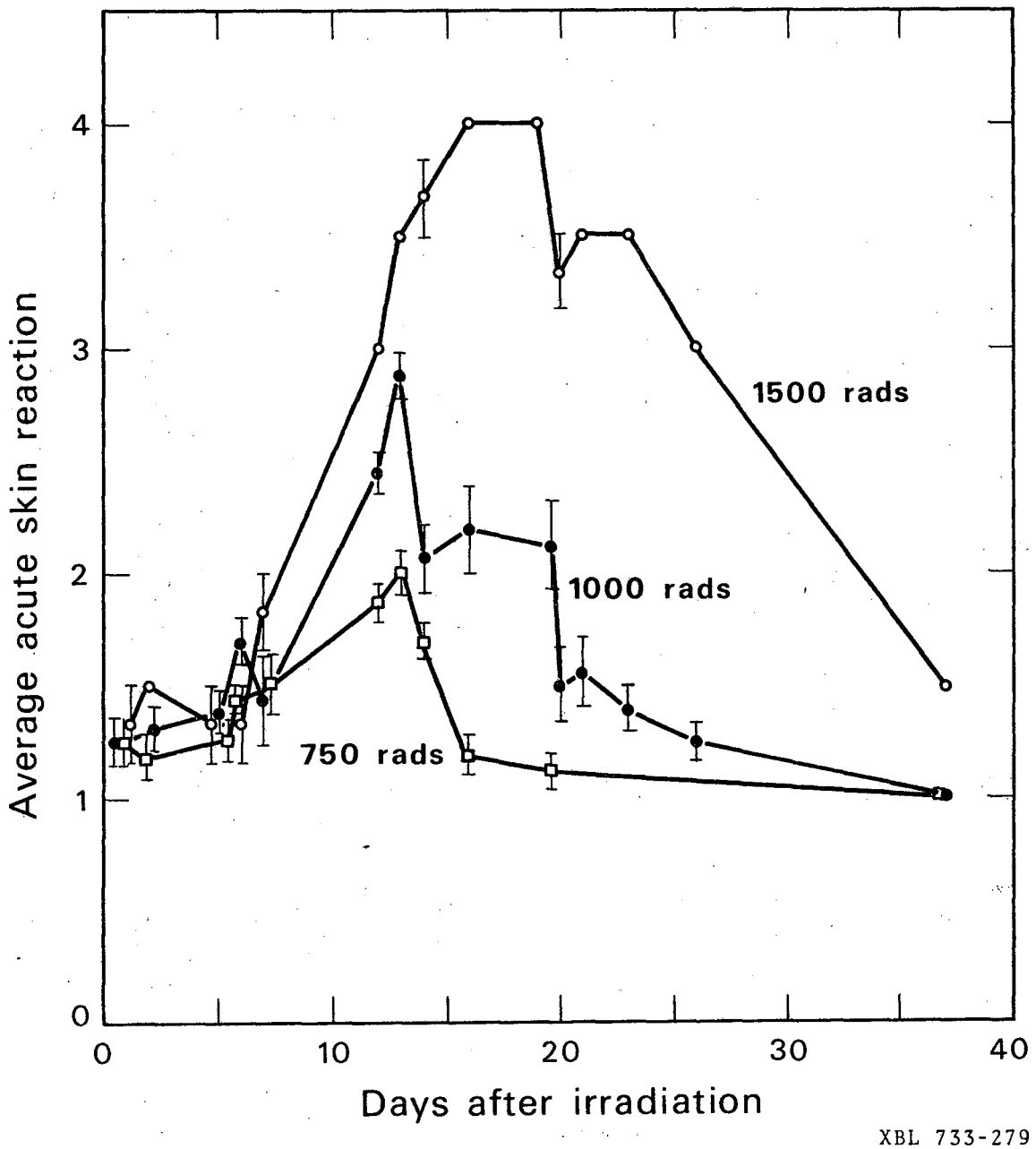
Average acute skin reaction
Days after irradiation
1500 rads
1000 rads
750 rads
0
1
2
3
4
0
10
20
30
40
XBL 733-279

Figure 4

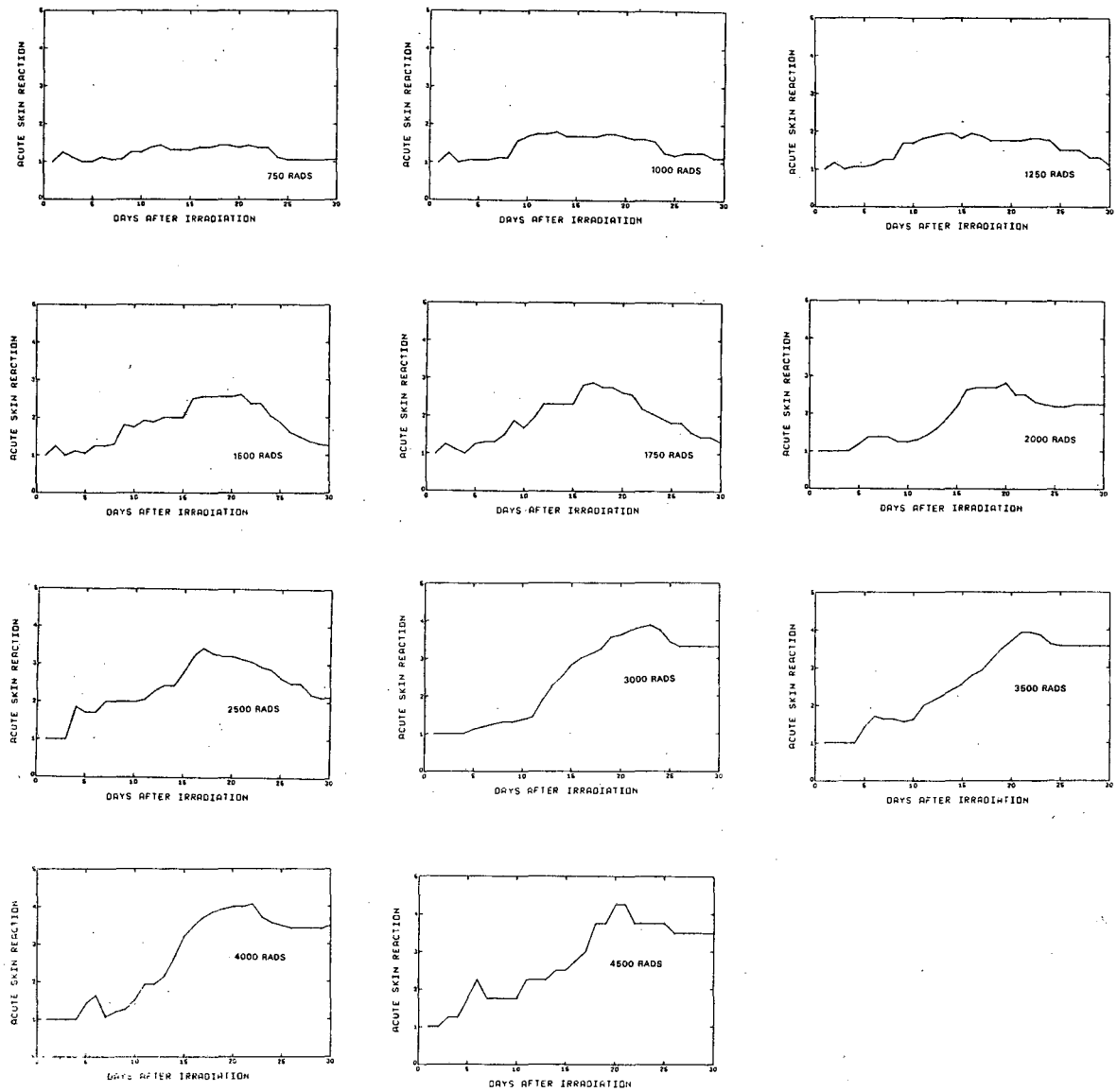

XBL 736-754

Figure 5

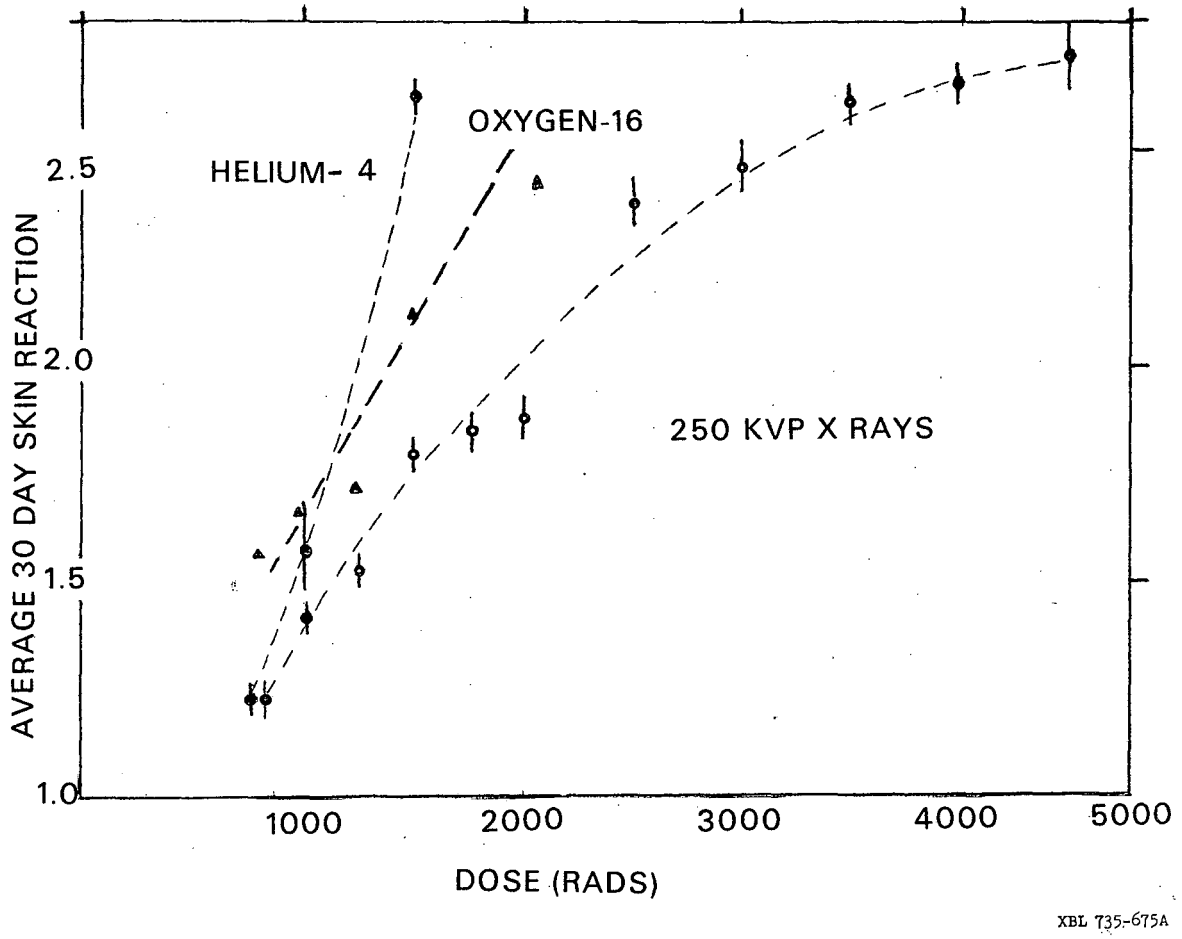
HELIUM- 4
OXYGEN-16
250 KVP X RAYS
AVERAGE 30 DAY SKIN REACTION
2.5
2.0
1.5
1.0
1000
2000
3000
4000
5000
DOSE (RADS)
XBL 735-675A

Figure 6

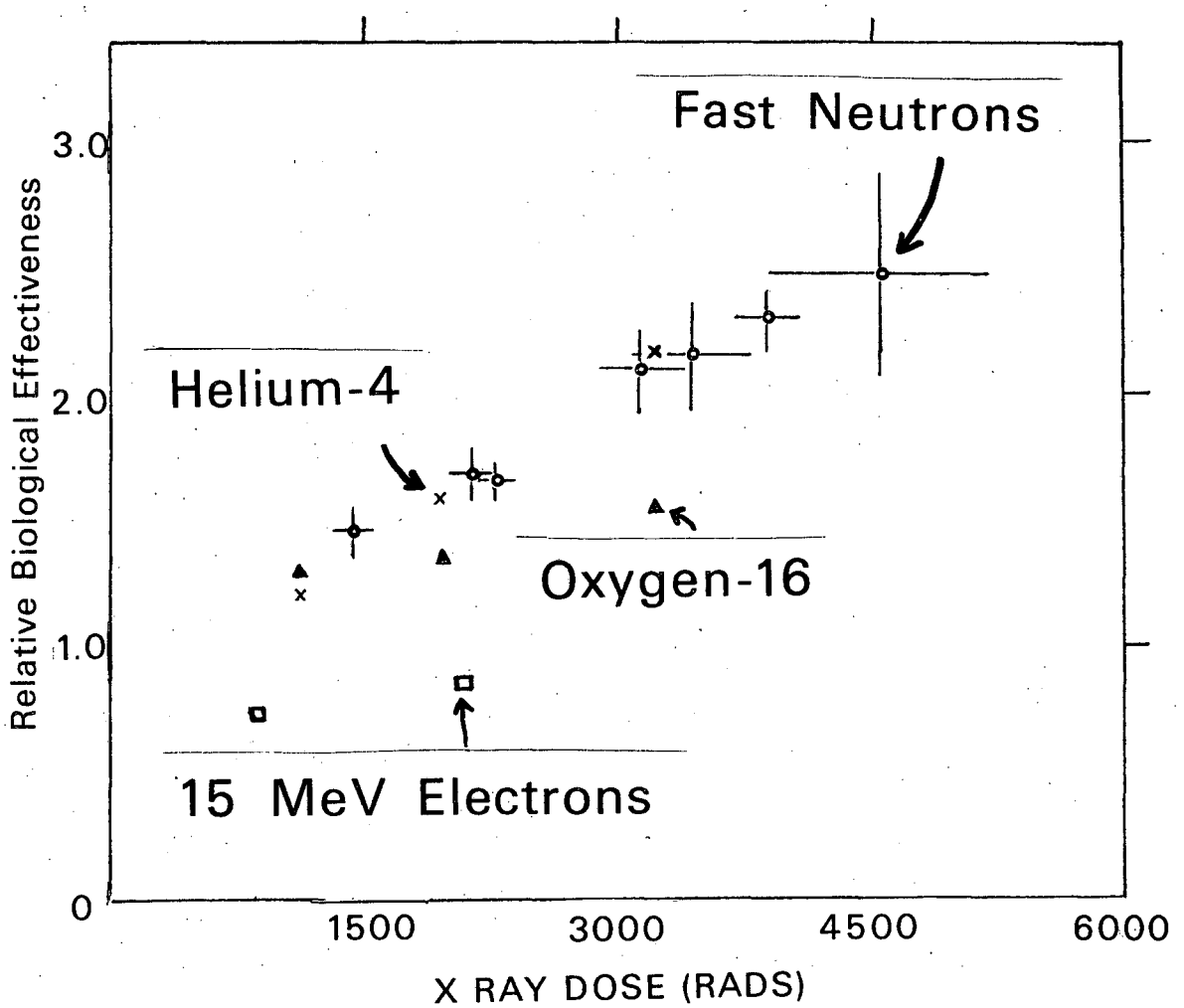

XBL 735-744A

Figure 7

ULTRASTRUCTURAL INVESTIGATION OF THE "LIGHT FLASH" PHENOMENON SEEN BY OUR ASTRONAUTS THROUGH EXPOSURE OF POCKET MOUSE AND RABBIT RETINA TO X-RAY, NITROGEN AND OXYGEN IRRADIATION

Delbert E. Philpott, R. Corbett, Sam Black,
and Charles Turnbill

NASA-Ames Research Center
Moffett Field, California 94035

Abstract.

The light flashes seen by astronauts on their flights to the moon are believed to be caused by "heavy primaries" passing through the eyes. In order to learn more about this phenomenon and its effect on the retina, pocket mouse retinas were exposed to nitrogen beams and oxygen beams at the Bevatron, Lawrence Berkeley Laboratory. The evoked response from X rays in rabbit eyes was also observed.

The Experiments.

Pocket mouse retinas were exposed to nitrogen beams for the first time at the Berkeley Bevatron. The pocket mice were positioned so as to expose one eye while the other eye was left unexposed. Both eyes were compared with controls (Fig. 1). The dose rate for eight pairs of mice was 2, 4, 6, and 8 million nitrogen particles/cm^2. One of the mice in each pair was sacrificed at 63 hours and the other one in five days. Fixation by perfusion with glutaraldehyde was performed.

Definite ultrastructural alterations occur in the pocket mouse retina exposed to 8 million particles 2 days after exposure, and there are indications of changes at somewhat lower doses. The outer segments respond in a patchy fashion, producing areas of alteration scattered amongst normal-appearing receptors (Fig. 2). The rods are swollen near the inner segments and, although the outer membrane surrounding the rods appears intact in most places, the disks or flattened membrane sacs within the rods appear disrupted. The radiation damage could be to these membranes or to the precursor material necessary for membrane formation. The pigment epithelium also shows general signs of alteration with vacuole formation in the cytoplasm. This patchy response of the outer segments has also been seen using the SEM. Figure 3 shows a rabbit retina 48 hours after exposure to 2000 r. Localized swelling and membrane rupture can be observed which corresponds to the TEM observations (1).

Pocket mouse retinas and one rabbit eye were also exposed to the oxygen beam at the Bevatron in an effort to compare these results with the nitrogen run. The rabbit-eye exposure was done to elicit, if possible, an electroretinogram (ERG) from oxygen particles and compare the response to an ERG produced by a flash of light. Despite several technical problems, tracings were obtained which were typical of an ERG. In addition, an electroretinogram (ERG) was recorded from a dark-adapted rabbit eye using X rays. If the ERG is followed by successive X-ray doses, the electrical response is abolished and can be shown to regenerate much the same as following exposure to light. Since this indicates the effect is on the outer segments, where the visual pigment is located, and not in some other part of the retina or in the brain, a similar response was looked for with the oxygen beam. Although the response was abolished, technical problems make any

conclusion difficult. This will be repeated when more time can be allowed for the experiment.

A lexan stack was also exposed and later examined by G. V. Benton, and this lexan stack confirmed the predicted Bragg peak for the run. The retinas of the mice and rabbit have been embedded and are being examined.

Acknowledgments.

This work is supported by NASA and the U.S. Atomic Energy Commission.

REFERENCES

1. Philpott, Delbert E., R. Corbett, Sam Black and Charles Turnbill, Ultrastructural investigation of the "light flash" phenomenon seen by our astronauts, Proc., Electr. Microscope Society of America, Vol. 30, p. 52-53 (1972).

FIGURE CAPTIONS

Fig. 1. Control. Pocket mouse retina.

Fig. 2. Pocket mouse retina exposed to 8 million nitrogen particles/cm^2.

Fig. 3. Scanning electron micrograph of rabbit retina outer segments after X-irradiation.

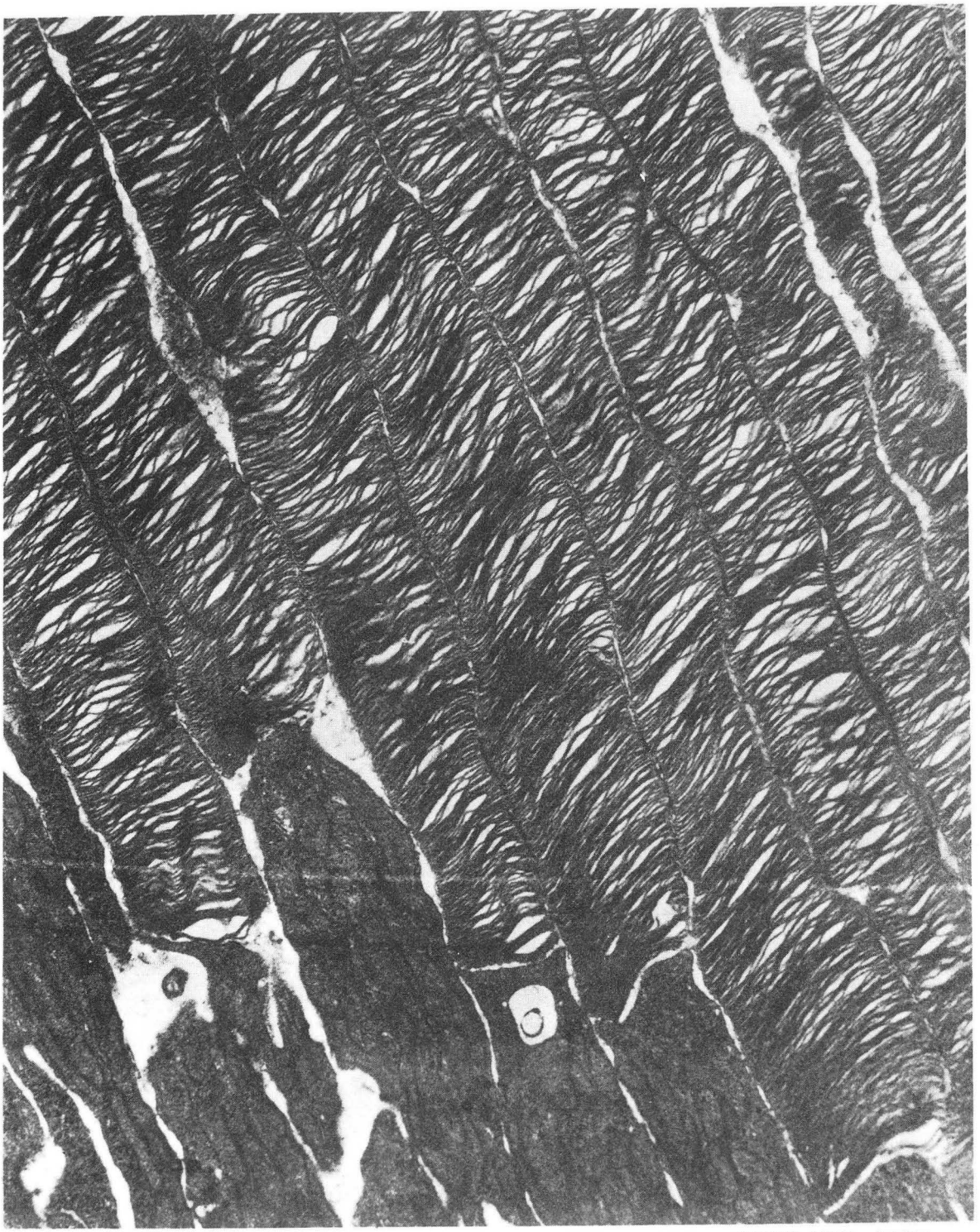

XBB 737-4597

Figure 1

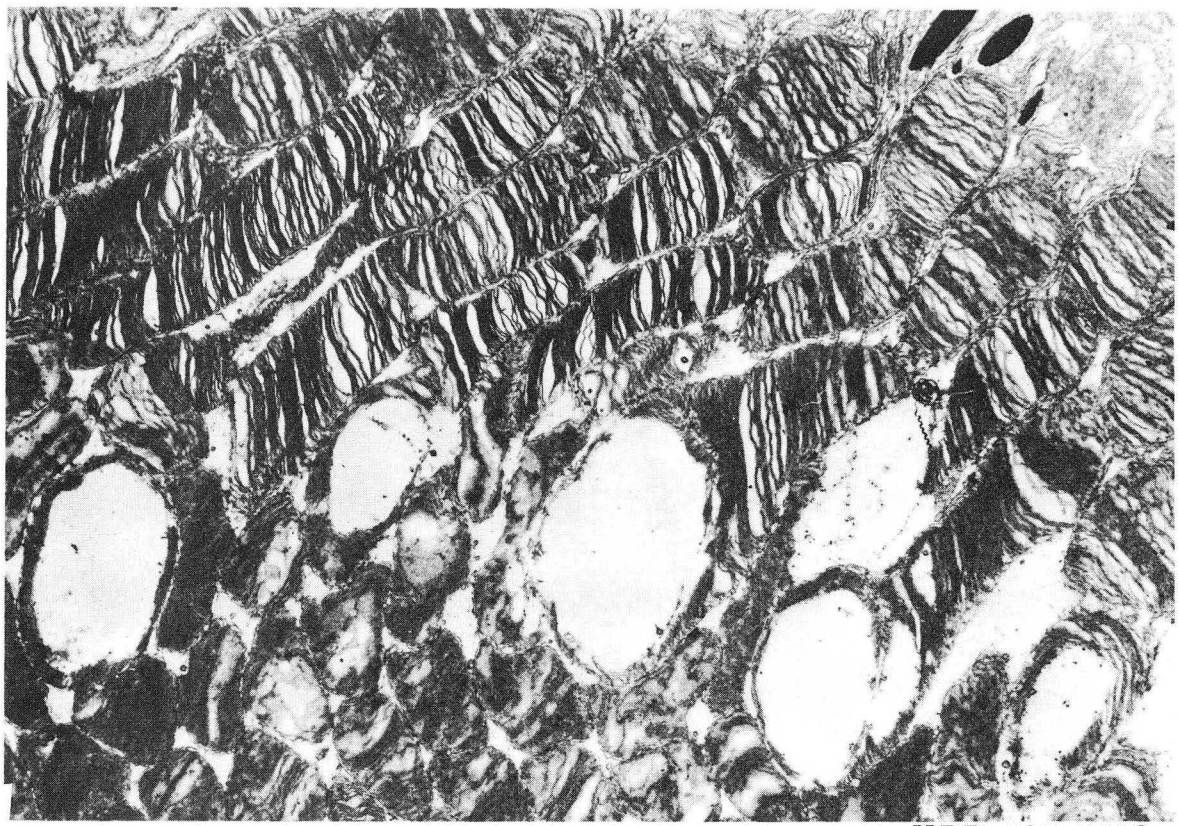

XBB 737-4598

Figure 2

XBB 737-4599

Figure 3

LEGAL NOTICE

This report was prepared as an account of work sponsored by the United States Government. Neither the United States nor the United States Atomic Energy Commission, nor any of their employees, nor any of their contractors, subcontractors, or their employees, makes any warranty, express or implied, or assumes any legal liability or responsibility for the accuracy, completeness or usefulness of any information, apparatus, product or process disclosed, or represents that its use would not infringe privately owned rights.

TECHNICAL INFORMATION DIVISION
LAWRENCE BERKELEY LABORATORY
UNIVERSITY OF CALIFORNIA
BERKELEY, CALIFORNIA 94720